

THE AGES OF COMPACT EARLY-TYPE GALAXIES

by

Stephanie Keating

A thesis submitted in conformity with the requirements
for the degree of Doctor of Philosophy
Graduate Department of Astronomy & Astrophysics
University of Toronto

Copyright © 2015 by Stephanie Keating

Abstract

The Ages of Compact Early-Type Galaxies

Stephanie Keating

Doctor of Philosophy

Graduate Department of Astronomy & Astrophysics

University of Toronto

2015

Most massive galaxies are compact at high redshifts, but similarly compact massive galaxies are rare in the local universe. The most common interpretation of this phenomenon is that massive galaxies have grown in size by a factor of about five since redshift $z = 2$. An alternative explanation is that recently-formed massive galaxies are larger (a ‘progenitor bias’). In this thesis we explore the importance of progenitor bias by looking for systematic differences in the stellar populations of compact early-type galaxies in the DEEP2 survey as a function of size. Our analysis is based on exploiting a statistical technique we apply for the first time characterizing the distribution of stellar populations in co-added spectra. The light-weighted ages of compact early-type galaxies at redshifts $0.5 < z < 1.4$ are compared to those of a control sample of larger galaxies at similar redshifts. We find that massive compact early-type galaxies selected on the basis of red color and high bulge-to-total ratio are younger than similarly-selected larger galaxies, suggesting that size growth in these objects is *not* driven mainly by progenitor bias, and that individual galaxies grow as their stellar populations age. However, *compact early-type galaxies selected on the basis of image smoothness and high bulge-to-total ratio are older than a control sample of larger galaxies*. Progenitor bias will play a significant role in defining the apparent size changes of early-type galaxies if they are selected on the basis of the smoothness of their light distributions.

“Who are we? We find that we live on an insignificant planet of a hum-
drum star lost in a galaxy tucked away in some forgotten corner of a
universe in which there are far more galaxies than people.”

-CARL SAGAN

Acknowledgements

It almost goes without saying – but of course it deserves to be said! – that this thesis would not have been possible without the enduring support, guidance, care, and enthusiasm of my Ph.D. advisor, Roberto Abraham. Bob, thank you for believing in me always – especially during those times when I didn't believe in myself. Thank you for sharing your passionate quest for understanding the universe with me, for indulging in all those side-tracked conversations we had along the way, and for knowing when going for beers is the best course of action. I've been fortunate in so many ways to have had you in my corner.

Thanks to Ricardo Schiavon and Genevieve Graves for sharing their expertise over so many telecons, especially in the early stages of the project. I also thank my Ph.D. committee members, Raymond Carlberg and Howard Yee, for their helpful suggestions and feedback.

I am also forever grateful to Michael Reid: for the many times a knock on the door across the hall led to chats about Doctor Who and cat video distractions, for the gifts of chocolate and cookies to get me through late-night dissertation writing, and for always having confidence in my abilities. Mike, it has been a true pleasure to work with you over the years.

As the saying goes, it takes a village to raise a Ph.D.¹, and so of course I must thank my some of my dear friends in the department over the years. Gregory Paciga, Nick Tacik, and Adam Atkinson, thank you for all of those coffee breaks that kept me sane. Max Millar-Blanchaer, sharing an office with you has been a joy, and I will miss our office chats. There have been many other friends, too many to list here (but you know who you are!), inside and outside the department, who have lent an ear or a shoulder when it was needed. You are all appreciated so very much.

From the bottom of my heart, I thank my family for their continued support and guidance throughout not just this degree, but also those that came before it. To my mother, Karen Keating; my stepfather, Gerry Gauthier; my nana, Carolyn Jemmett; and my brother, Daniel Gauthier: I

¹I'm sure someone has said this at some point in time.

love you and I truly could not have done this without you. Thank you for always being there for me, for listening to me, for supporting me, and for believing I could do anything.

Finally, to Kevin Kuhl, my partner in all things (and our little furry bundle of snuggles and claws, Mira): it is difficult to put my love and gratitude for you into words. Thank you for making me laugh when I needed to laugh, and letting me cry when I needed to cry. Thank you for the Netflix binges, for the long distance runs, for the hot coffees and the cold beers. Thank you for always being there and for sharing in all of these adventures over these past five years.

Contents

1	Introduction	1
1.1	Observational history of “red nuggets”	5
1.2	Size Evolution Mechanisms for Compact Elliptical Galaxies	8
1.3	Progenitor Bias	9
1.4	Stellar Population Synthesis	11
1.4.1	EZ_Ages	13
1.5	Overview of Methodology	15
1.5.1	Co-adding spectra	15
1.5.2	A Brief Overview of Bootstrap Resampling	17
1.6	Thesis Overview	20
2	Data and Samples	21
2.1	Chapter Overview	21
2.2	The DEEP2 Survey	21
2.2.1	HST Imaging from AEGIS	22
2.3	Definition of the Samples	23
2.4	Co-Addition of DEEP2 Spectra	35
2.5	Systematic Properties of the Samples	36
2.6	Summary	38

3	Methodology	51
3.1	Chapter Overview	51
3.2	Age Measurements	51
3.2.1	Velocity dispersion measurement	53
3.2.2	Determining the optimal fitting indices	53
3.3	Systematic errors on the age measurements	59
3.4	Characterizing the Homogeneity of Co-added Spectra	62
4	Results	84
4.1	Chapter Overview	84
4.2	Nominal ages and bootstrap resampling	84
4.2.1	Velocity Dispersion Shortcut	85
4.2.2	Red and Bulge-Dominated Galaxies	88
4.2.3	Smooth & Bulge-Dominated Galaxies	94
4.2.4	Red, Smooth & Bulge-Dominated Galaxies	99
4.3	Overview of the Results	99
4.4	Characterizing the contributing galaxies	104
4.5	Correlation between “smoothness” and age	107
5	Conclusions & Future Work	112
5.1	Conclusions	112
5.1.1	Defining an “early-type galaxy” and the influence of “progenitor bias”	112
5.2	Future Work and Directions	115
5.2.1	Determining the local nugget fraction	115
5.2.2	High Quality Spectra, Measuring Chemical Abundances, and Star Formation History	116
5.3	Thesis Summary	118
	Bibliography	120

Appendices	130
A	131
A.1 RBD, Compact & Heavy: Representative Galaxies	132
A.2 RBD, Compact & Heavy: non-ETGs	133
A.3 RBD, Control & Heavy: Representative Galaxies	134
A.4 RBD, Control & Heavy: non-ETGs	135
A.5 RSBD, Compact & Heavy: Representative Galaxies	137
A.6 RSBD, Compact & Heavy: non-ETGs	138
A.7 RSBD, Control & Heavy: Representative Galaxies	139
A.8 RSBD, Control & Heavy: non-ETGs	140
B	141

List of Tables

2.1	Number of galaxies remaining after consecutive cuts	27
2.2	Details of cuts for each sample	28
2.2	Details of cuts for each sample	35
2.3	Kolmogorov-Smirnov results for histogram pairs in Figures 2.4, 2.5, & 2.6 . . .	39
3.1	Sample Velocity Dispersions	54
3.2	Index Combinations Tested for EZ_Ages Fitting	56
3.3	Percent Error for EZ_Ages Indices	59
3.4	Systematics I: Effect on Age Measurements of Changing Velocity Dispersion .	63
3.5	Systematics II. Effect on Ages Measurements of Correcting Balmer Line Infill .	66
3.6	Mean Bootstrap Ages for Various Star Formation Histories	68
4.1	Measured Ages	87
4.1	Measured Ages	88

List of Figures

1.1	From Hubble (1936): the Hubble “tuning fork” galaxy classification scheme.	2
1.2	From Graves & Schiavon (2008): Example index grids for models with solar-scaled and enhanced [Mg/Fe]. <i>Top</i> : Models computed with solar-scaled abundances. <i>Bottom</i> : Models produced with supersolar [Mg/Fe].	15
1.3	Recreated from Efron & Tibshirani (1994), a schematic of the bootstrap process for estimating the standard error of a statistic $\hat{\theta} = s(\mathbf{x})$	19
2.1	The overlap of the “Red & Bulge Dominated (RBD)” samples ($B/T > 0.5$, $U - B > 0.9$) in a mass-radius diagram.	29
2.2	The overlap of the “Smooth & Bulge Dominated (SBD)” samples ($B/T > 0.35$ and $S2 < 0.075$) in a mass-radius diagram.	30
2.3	The overlap of the “Red, Smooth & Bulge Dominated (RSBD)” samples ($B/T > 0.35$, $S2 < 0.075$, and $U - B > 0.9$) in a mass-radius diagram.	31
2.4	Distributions in redshift, stellar mass, and color for the compact, control, heavy, and light subsamples of the “Red & Bulge Dominated (RBD) Sample”.	32
2.5	Distributions in redshift, stellar mass, and color for the compact, control, heavy, and light subsamples of the “Smooth & Bulge Dominated (SBD) Sample”.	33
2.6	Distributions in redshift, stellar mass, and color for the compact, control, heavy, and light subsamples of the “Red, Smooth & Bulge Dominated (RSBD) Sample”.	34
2.7	The co-added spectrum, signal-to-noise, number of contributing galaxies, average redshift, and average stellar mass for the compact and control galaxies of our “Red & Bulge Dominated (RBD) Sample”.	40

2.8	The co-added spectrum, signal-to-noise, number of contributing galaxies, average redshift, and average stellar mass for the compact and control galaxies of our “Smooth & Bulge Dominated (SBD) Sample”.	41
2.9	The co-added spectrum, signal-to-noise, number of contributing galaxies, average redshift, and average stellar mass for the compact and control galaxies of our “Red, Smooth & Bulge Dominated (RSBD) Sample”.	42
2.10	The co-added spectrum, signal-to-noise, number of contributing galaxies, average redshift, and average stellar mass for the heavy and light galaxies of our RBD Sample.	43
2.11	The co-added spectrum, signal-to-noise, number of contributing galaxies, average redshift, and average stellar mass for the heavy and light galaxies of our SBD Sample.	44
2.12	The co-added spectrum, signal-to-noise, number of contributing galaxies, average redshift, and average stellar mass for the heavy and light galaxies of our RSBD Sample.	45
2.13	The co-added spectrum, signal-to-noise, number of contributing galaxies, average redshift, and average stellar mass for the compact and light and control and light galaxies of our RBD Sample.	46
2.14	The co-added spectrum, signal-to-noise, number of contributing galaxies, average redshift, and average stellar mass for the compact and light and control and light galaxies of our SBD Sample.	47
2.15	The co-added spectrum, signal-to-noise, number of contributing galaxies, average redshift, and average stellar mass for the compact and light and control and light galaxies of our RSBD Sample.	48
2.16	The co-added spectrum, signal-to-noise, number of contributing galaxies, average redshift, and average stellar mass for the compact and heavy and control and heavy galaxies of our RBD Sample.	49

2.17	The co-added spectrum, signal-to-noise, number of contributing galaxies, average redshift, and average stellar mass for the compact and heavy and control and heavy galaxies of our SBD and RSBD Samples.	50
3.1	Percent error for various index combinations used to fit the age of a simple stellar population at various ages.	57
3.2	A continuation of Figure 3.1.	58
3.3	Index-index model grids showing the effects of changing the velocity dispersion by $\pm 20\%$ for the RBD Compact, Control, Heavy, and Light subsamples.	62
3.4	Index-index model grids showing the effects of changing the velocity dispersion by $\pm 20\%$ for the RBD Compact & Heavy, Control & Heavy, Compact & Light, and Control & Light subsamples.	64
3.5	Index-index model grids showing the effects of changing the velocity dispersion by $\pm 20\%$ for the SBD Compact, Control, Heavy, and Light subsamples.	64
3.6	Index-index model grids showing the effects of changing the velocity dispersion by $\pm 20\%$ for the SBD Compact & Heavy, Control & Heavy, Compact & Light, and Control & Light subsamples.	65
3.7	Index-index model grids showing the effects of changing the velocity dispersion by $\pm 20\%$ for the RSBD Compact, Control, Heavy, and Light subsamples.	65
3.8	Index-index model grids showing the effects of changing the velocity dispersion by $\pm 20\%$ for the RSBD Compact & Heavy, Control & Heavy, Compact & Light, and Control & Light subsamples.	66
3.9	<i>Top</i> : Star formation history used to generate the synthetic galaxy spectra: a single burst 0.5 Gyr in duration. <i>Bottom</i> : Age histograms generated from 300 bootstrap resampling of the synthetic galaxy spectra drawn from three parent populations.	69
3.10	<i>Top</i> : Star formation history used to generate the synthetic galaxy spectra: a single burst 1.0 Gyr in duration. Bottom panels as in Figure 3.9.	70

3.11	<i>Top</i> : Star formation history used to generate the synthetic galaxy spectra: exponentially declining with e -folding timescale $\tau = 0.5$ Gyr. Bottom panels as in Figure 3.9.	71
3.12	<i>Top</i> : Star formation history used to generate the synthetic galaxy spectra: exponentially declining with e -folding timescale $\tau = 1.0$ Gyr. Bottom panels as in Figure 3.9.	72
3.13	<i>Top</i> : Star formation history used to generate the synthetic galaxy spectra: exponentially declining with e -folding timescale $\tau = 1.0$ Gyr, followed by a 0.2 Gyr long single burst at $t = 3$ Gyr. Bottom panels as in Figure 3.9.	73
3.14	<i>Top</i> : Star formation history used to generate the synthetic galaxy spectra: exponentially declining with e -folding timescale $\tau = 1.0$ Gyr, followed by a 0.2 Gyr long single burst at $t = 2$ Gyr. Bottom panels as in Figure 3.9.	74
3.15	<i>Top</i> : Star formation history used to generate the synthetic galaxy spectra: exponentially declining with e -folding timescale $\tau = 0.5$ Gyr, followed by a 0.2 Gyr long single burst at $t = 3$ Gyr. Bottom panels as in Figure 3.9.	75
3.16	<i>Top</i> : Star formation history used to generate the synthetic galaxy spectra: exponentially declining with e -folding timescale $\tau = 0.5$ Gyr, followed by a 0.2 Gyr long single burst at $t = 2$ Gyr. Bottom panels as in Figure 3.9.	76
3.17	<i>Top</i> : Star formation history used to generate the synthetic galaxy spectra: exponentially declining with e -folding timescale $\tau = 0.2$ Gyr, followed by a 0.2 Gyr long single burst at $t = 3$ Gyr. Bottom panels as in Figure 3.9.	77
3.18	<i>Top</i> : Star formation history used to generate the synthetic galaxy spectra: exponentially declining with e -folding timescale $\tau = 0.2$ Gyr, followed by a 0.2 Gyr long single burst at $t = 2$ Gyr. Bottom panels as in Figure 3.9.	78
3.19	<i>Top</i> : Star formation history used to generate the synthetic galaxy spectra: exponentially declining with e -folding timescale $\tau = 0.5$ Gyr, followed by another exponentially declining burst with $\tau = 0.5$ Gyr and amplitude 0.3 at $t = 3$ Gyr. Bottom panels as in Figure 3.9.	79

3.20	Age histograms generated from 4000 bootstrap resamplings of the synthetic galaxy spectra drawn from parent populations with differing numbers of “young” (2 Gyr) and “old” (7 Gyr) spectra.	82
3.21	Age histograms generated from 4000 bootstrap resamplings of the synthetic galaxy spectra drawn from a parent population with 15 galaxies of 7 Gyrs age, 5 galaxies of 5 Gyrs age, and 5 galaxies of 2 Gyrs age.	83
4.1	Age histograms generated from bootstrapping the Compact subsample of the “Red, Smooth & Bulge-Dominated (RSBD) Sample” to demonstrate the effects of assuming a single velocity dispersion for all resamplings.	86
4.2	Age histograms generated from bootstrapping the Compact and Control galaxies in the “Red & Bulge-Dominated (RBD) Sample” 4000 times each.	89
4.3	Age histograms generated from bootstrapping the Heavy and Light galaxies in the RBD Sample 4000 times each.	90
4.4	Age histograms generated from bootstrapping the Compact & Heavy and Control & Heavy galaxies in the RBD Sample 4000 times each.	91
4.5	Age histograms generated from bootstrapping the Compact & Light and Control & Light galaxies in the RBD Sample 4000 times each.	92
4.6	Age histograms generated from bootstrapping the Compact and Control galaxies in the “Smooth, & Bulge-Dominated (SBD) Sample” 4000 times each.	95
4.7	Age histograms generated from bootstrapping the Heavy and Light galaxies in the SBD Sample 4000 times each.	96
4.8	Age histograms generated from bootstrapping the Compact & Heavy and Control & Heavy galaxies in the “Smooth, & Bulge-Dominated (SBD) Sample” and the “Red, Smooth, & Bulge-Dominated (RSBD) Sample” 4000 times each. . .	97
4.9	Age histograms generated from bootstrapping the Compact & Light and Control & Light galaxies in the SBD Sample 4000 times each.	98
4.10	Age histograms generated from bootstrapping the Compact and Control galaxies in the “Red, Smooth, & Bulge-Dominated (RSBD) Sample” 4000 times each. .	100

4.11	Age histograms generated from bootstrapping the Heavy and Light galaxies in the RSBD Sample 4000 times each.	101
4.12	Age histograms generated from bootstrapping the Compact & Light and Control & Light galaxies in the RSBD Sample 4000 times each.	102
4.13	Age histograms generated from bootstrapping the Compact and a redshift-matched subset of the Control galaxies in the RSBD Sample 4000 times each. .	105
4.14	Comparison of the age histograms generated from bootstrapping the entire set of Control galaxies and a subset of the Control galaxies which have been matched in redshift to Compact galaxies in the RSBD Sample 4000 times each.	106
4.15	The number of galaxies contributing to the co-added bootstrapped spectra for the SBD/RSBD Control & Heavy subsample for ages < 3.68 Gyr, the median bootstrap age.	108
4.16	The number of galaxies contributing to the co-added bootstrapped spectra for the SBD/RSBD Control & Heavy subsample for ages > 3.68 Gyr, the median bootstrap age.	109
4.17	DEEP ID 12016360 (image on the left, spectrum on the right) contributes strongly to the co-additions with ages greater than the median age for the RBD, SBD, and RSBD Control & Heavy subsample, and also contributes weakly to co-additions with ages less than the median age for the same subsamples. . . .	110
B.1	The number of galaxies contributing to the co-added bootstrapped spectra for the RBD Compact & Heavy subsample for all ages < 15 Gyr	142
B.2	The number of galaxies contributing to the co-added bootstrapped spectra for the RBD Compact & Heavy subsample for ages < 1.62 Gyr, the median bootstrap age.	143
B.3	The number of galaxies contributing to the co-added bootstrapped spectra for the RBD Compact & Heavy subsample for ages > 1.62 Gyr, the median bootstrap age.	144

B.4	The number of galaxies contributing to the co-added bootstrapped spectra for the RBD Control & Heavy subsample for all ages < 15 Gyr.	145
B.5	The number of galaxies contributing to the co-added bootstrapped spectra for the RBD Control & Heavy subsample for ages < 3.42 Gyr, the median bootstrap age.	146
B.6	The number of galaxies contributing to the co-added bootstrapped spectra for the RBD Control & Heavy subsample for ages > 3.42 Gyr, the median bootstrap age.	147
B.7	The number of galaxies contributing to the co-added bootstrapped spectra for the SBD/RSBD Compact & Heavy subsample for all ages < 15 Gyr.	148
B.8	The number of galaxies contributing to the co-added bootstrapped spectra for the SBD/RSBD Compact & Heavy subsample for ages < 6.69 Gyr, the median bootstrap age.	149
B.9	The number of galaxies contributing to the co-added bootstrapped spectra for the SBD/RSBD Compact & Heavy subsample for ages > 6.69 Gyr, the median bootstrap age.	150
B.10	The number of galaxies contributing to the co-added bootstrapped spectra for the SBD/RSBD Control & Heavy subsample for all ages < 15 Gyr.	151
B.11	The number of galaxies contributing to the co-added bootstrapped spectra for the SBD/RSBD Control & Heavy subsample for ages < 3.68 Gyr, the median bootstrap age.	152
B.12	The number of galaxies contributing to the co-added bootstrapped spectra for the SBD/RSBD Control & Heavy subsample for ages > 3.68 Gyr, the median bootstrap age.	153
B.13	DEEP ID 12008605 (image on the left, spectrum on the right) contributes strongly to the co-additions with ages younger than the median age for the RBD Compact & Heavy subsample.	154

B.14 DEEP ID 13034447 (image on the left, spectrum on the right) contributes weakly to the co-additions with ages older than the median age for the RBD Compact & Heavy subsample. 154

B.15 DEEP ID 12016360 (image on the left, spectrum on the right) contributes strongly to the co-additions with ages greater than the median age for the RBD, SBD, and RSBD Control & Heavy subsample, and also contributes weakly to co-additions with ages less than the median age for the same subsamples. . . . 155

Chapter 1

Introduction

The majority of visible stars in the Universe reside within *galaxies*: massive, gravitationally-bound systems containing (in addition to stars) the stellar remnants from stars that have exhausted their fuel supplies, an interstellar medium composed of gas and dust, and dark matter. Galaxies are a diverse group of astronomical objects, spanning a wide range of parameters including luminosity, stellar mass, size, surfaces brightness, color, and environment. In order to begin to understand how galaxies have formed and evolved over time, it has been useful to divide them into categories and examine the differences and similarities between the types.

Typically, luminous galaxies have been classified according to their visual shape or morphology. One of the earliest proposed visual classification schemes was developed by Reynolds (1920), who separated spiral galaxies into seven categories. More well-known, however, is the Hubble sequence (Hubble 1926; 1936), colloquially known as the “tuning fork” (see Figure 1.1). Hubble was inspired by Reynolds’ work, but interestingly opted not to reference him in the 1926 paper (Dick 2013). The Hubble scheme is still widely used today, although there have been many proposed modifications and alternatives along the way. In the sequence, the elliptical, or “early-type” galaxies (so-called because Hubble’s original hypothesis was that galaxies evolved from one form to the other, with ellipticals forming first), form the “handle” of the fork. These are further ordered by the degree of ellipticity that they demonstrate. At the centre of the fork lie lenticular galaxies, with their bright central bulges surrounded by an extended but featureless

disk. From there, two branches emerge to denote spiral galaxies: one branch to identify spirals with a bar-like structure, and one branch to describe those without a bar. This sequence, of course, does not encompass all galaxy variations, as it applies to luminous galaxies only, which tend to dominate in observations at high redshift.

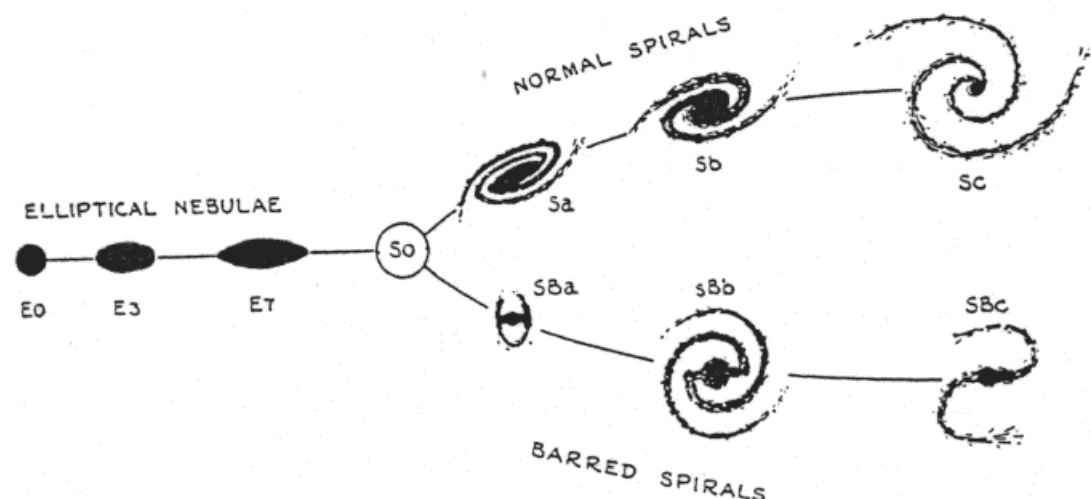


Figure 1.1: From Hubble (1936): the Hubble “tuning fork” galaxy classification scheme.

Although the Hubble classification system is based purely on visual appearance, the structural properties of luminous galaxies do correlate somewhat with other intrinsic properties such as color and gas content, which are related to the stellar population of the galaxies, and stellar mass. However, it should be noted that the values of these parameters span a wide range within any given type of galaxy (Roberts & Haynes 1994). Because the formation mechanisms for spiral and elliptical galaxies are most likely very different, a galaxy’s morphology is also related to its formation history (Mo et al. 2010). Elliptical or early-type galaxies tend to be quite red. Their spectra are characterized by stellar absorption lines and little to no nebular emission lines, signifying that a lack of recent star formation. Spiral galaxies, on the other hand, are bluer, and have spectra that indicate they are rich with gas and star formation. The correlation between visual morphology, color, and spectroscopic features exists both locally and at higher redshifts (Kauffmann et al. 2003; Abraham et al. 2007; Cassata et al. 2008; Kriek et al. 2009; Szomoru et al. 2011, e.g.).

Another important (and more quantitative) method of distinguishing between galaxy types is based on measurements of their light distributions, which are different for bulge-dominated and disk-dominated systems. The radial dependence of the surface brightness of most elliptical and spiral galaxies are generally well-described by the formulation proposed by Sersic (1968):

$$I(R) = I_e e^{-\beta_n [(R/R_e)^{1/n} - 1]} \quad (1.1)$$

where $I(R)$ is the surface brightness of a galaxy at a given circularized radius $R = a\sqrt{b/a}$, with a the scale length of the profile and b/a the axial ratio; I_e is the intensity at the effective radius, R_e (the radius within which half of the total light is emitted); and β_n is a normalization constant defined in terms of the parameter n which is a proxy for the galaxy's light profile. Spiral galaxies, whose disks have surface brightnesses with a shallow inner profile, are characterized by the $n = 1$ exponential Sérsic profile (Kent et al. 1991; Andredakis & Sanders 1994). Elliptical galaxies, on the other hand, have surface brightnesses with a steep inner profile and are often best described by a Sérsic index $n = 4$, which is also known as the de Vaucouleurs profile (de Vaucouleurs 1948).

Although the existence of the two distinct classes of spiral and elliptical galaxy was known in the 1930s, detailed formation mechanisms were not proposed until almost 30 years later. Eggen et al. (1962) described the “monolithic collapse” model, which postulates that galaxies form from collapsing gas clouds. In this model, if the cloud remains mostly gaseous during the collapse, gravitational energy can be dissipated and the cloud will shrink into a disk, forming a spiral galaxy. If instead the gas is mostly converted into stars during the collapse, the gravitational energy is not dissipated, and the infall motions then translate into random motion of stars thus forming an elliptical galaxy.

Current theories of galaxy formation, of course, must be constructed within the modern framework of Λ cold dark matter (Λ CDM) cosmology, where small initial perturbations gave rise to structure on a larger scale. Within this framework, the “hierarchical merging” model of galaxy formation, which posits that elliptical galaxies are formed by the merging of smaller

disk galaxies, emerged (e.g. Toomre & Toomre 1972; Blumenthal et al. 1984; Schweizer 1986). However, problems with this scenario quickly appeared. Ostriker (1980) pointed out that the velocity dispersion of elliptical galaxies were much too high to have been formed entirely from mergers of spiral galaxies, which typically have much lower velocity dispersions. This problem was addressed by looking at the dark halos that galaxies find themselves embedded in. The explanation finds its origin in a paper by White & Rees (1978) proposed a two-stage theory of galaxy formation, wherein dark halos first form through hierarchical clustering and the luminous galactic matter forms next, once it has condensed and cooled within the potential well of the dark halo.

Galaxy formation and evolution is a highly complex process; the star formation histories of galaxies are further complicated by dynamical processes, feedback, and active galactic nuclei (AGN), which all play a role in triggering, regulating, and suppressing star formation. For example, the correlation of the velocity dispersion and/or mass of a galaxy's bulge with the mass of its central black hole indicates that these supermassive black holes may help regulate the growth of their host galaxies (e.g. Kormendy & Richstone 1995; Magorrian et al. 1998; Ferrarese & Merritt 2000; Marconi & Hunt 2003). As matter accretes onto a black hole, it emits radiation which can drive out the surrounding gas and therefore suppress star formation (and reduce accretion onto the black hole) (e.g. Silk & Rees 1998; Fabian 2012). (It is worth mentioning that that the effect of AGN feedback may not always be negative, and that in some instances it may act to accelerate star formation. Nayakshin & Zubovas (2012) present supermassive black hole feedback simulations that find that when ambient shocked gas cools rapidly, it is compressed into then cold dense filaments, which can then undergo a burst of star formation if the quasar over-pressurizes it. Ishibashi et al. (2013) examine a scenario in which star formation is triggered by radiation pressure on dusty gas due to AGN feedback. In this picture, stars are formed in the feedback-driven outflow at increasingly large radii and build up the outer regions of the host galaxy.)

Likewise, feedback from supernovae also plays an important role in regulating the star

formation histories of galaxies (see, e.g., McKee & Ostriker (1977); Efstathiou (2000)). As a supernova explosion proceeds, it can act to evaporate the cold, dense clouds in the interstellar medium and move them to a hot, diffuse phase. Star formation will be suppressed with the hot phase fills most of the volume of the interstellar medium and is of sufficiently low density such that the radiative cooling time is long. Additionally, if the temperature of the hot interstellar medium exceeds the virial temperature of the galaxy, the gas may climb out of the galaxy's potential.

Clearly, the formation and evolution is a complicated and multivariate problem. Our understanding of these processes is being facilitated greatly as models and simulations become increasingly sophisticated. Observationally, however, the current key to understanding how galaxies form and subsequently evolve requires studying galaxies over a wide range of redshifts.

1.1 Observational history of “red nuggets”

One of the most surprising recent developments in galaxy evolution has been the discovery of a population of massive compact quiescent galaxies (‘red nuggets’) at high redshifts. These objects, which were first reported by Daddi et al. (2005), have since been the subject of dozens of observational papers. A representative subset of these would include Longhetti et al. (2007); Trujillo et al. (2007); Toft et al. (2007); Zirm et al. (2007); Cimatti et al. (2008); van Dokkum et al. (2008); Buitrago et al. (2008); Damjanov et al. (2009); Newman et al. (2010); Szomoru et al. (2010); van Dokkum et al. (2010); Mancini et al. (2010); Damjanov et al. (2011); Bruce et al. (2012); Szomoru et al. (2012); Law et al. (2012); Ryan et al. (2012); McLure et al. (2013); Chang et al. (2013); Barro et al. (2013); Newman et al. (2012); Patel et al. (2013); Damjanov et al. (2014); Belli et al. (2014b). Several of these many papers explore in detail the potential sources of systematic error which could cause sizes to be underestimated, or masses to be overestimated, or some combination of both. Examples of possible sources of error include errors in photometric redshifts, errors in conversion from light to stellar mass, undetected extended envelopes which cannot be observed because of cosmological dimming, and other

factors. Currently, having been through this crucible, there is now broad consensus that massive quiescent galaxies at high redshifts are indeed a factor of 2–5 smaller than local systems at similar mass. In this thesis, we treat red nuggets as an observationally established phenomenon.

Most attempts to understand the nature of red nuggets have assumed that they have some connection to local elliptical galaxies. In the last several years, studies have begun to challenge this basic assumption (van der Wel et al. 2011; Chevance et al. 2012; Bruce et al. 2012; Patel et al. 2013). It has become clear that the structure of high-redshift quiescent compact galaxies does not resemble that of local elliptical galaxies. While the ellipticity distribution of nuggets resembles that of massive local spheroids, their Sérsic indices are better matched to those of massive local disks. The incompatibility between the bivariate ellipticity - Sérsic index distribution of nuggets and any homogeneous local population (Chevance et al. 2012) means that the morphology of nuggets is presently a mystery. They may be a population of early-type galaxies with intrinsic shapes that differ from their local counterparts, or they may be disks with unusually massive bulges, or they may be a mix of these. They may even be a new class of galaxies unique unto themselves. An intriguing suggestion, proposed in the model of Hopkins et al. (2009a), is that they may be the dense central component of early-type galaxies, which recent observations suggest may be better described by multi-component models (Huang et al. 2013a;b).

As we have noted, many obvious sources of systematic error have been ruled out as the explanation for the observed size growth of massive galaxies. However, one systematic source of error worth a special mention is the possibility that the abundance of local analogs to the high-redshift nuggets may have been greatly underestimated. Initial studies based on data from the Sloan Digital Sky Survey (SDSS) have indicated an almost complete absence of very compact massive systems nearby (Trujillo et al. 2009; Taylor et al. 2010) lending credence to the idea that the local galaxy size-mass relation is the result of a significant amount of size evolution on the part of red nuggets. However, Valentinuzzi et al. (2010a) report little evidence for a changing fraction of very compact galaxies in rich clusters from $z = 0.7$ to $z = 0$. This result might be

understood as an environmental effect, although the role of environment is controversial¹. Using the Wide-field Nearby Galaxy-clusters Survey (WINGS), Valentinuzzi et al. (2010b) found that in nearby ($z \sim 0.05$) galaxy clusters, superdense galaxies represent nearly 22 % of all cluster members with stellar mass range $3 \times 10^{10} \leq M_{*/M_{\odot}} \leq 4 \times 10^{11}$, and have masses and sizes similar to their high- z counterparts.

Outside of the cluster environment, Saracco et al. (2011) report little change in the number density of compact quiescent galaxies from $z = 1.5$ to $z = 0$. Poggianti et al. (2013b) looked for field superdense galaxies at $z = 0.03 - 0.11$ using the Padova-Millennium Galaxy and Group Catalogue (PM2GC) and found that compact galaxies with radii and mass densities comparable to high- z massive, passive galaxies represent 4.4% of all galaxies with stellar masses $> 3 \times 10^{10} M_{\odot}$, and claim that when stellar age and environmental effects are accounted for, the size evolution of galaxies between high and low z is only a factor of ~ 1.6 . Damjanov et al. (2013) identify nine compact, quiescent galaxies from SDSS with dynamical masses $M_{dyn} > 10^{10} M_{\odot}$, initially classed photometric point sources, but with redshifts $0.2 < z < 0.6$. Also, more recently, using a sample of ~ 200 compact galaxies drawn from the Baryon Oscillation Spectroscopic Survey (BOSS), Damjanov et al. (2014) determine that at $0.2 < z < 0.6$, the abundance of compact quiescent galaxies is consistent with the number densities of the most massive compact systems at high redshift.

If the abundance of local nuggets is greatly underestimated then this opens the door to ‘progenitor bias’ being the dominant source of the observed size growth. The central idea here is that galaxies forming at later times (and ultimately joining the red sequence) may be systematically larger because they are less gas rich (van Dokkum & Franx 2001). Gas-rich systems forming earlier are losing total energy through dissipative processes while conserving

¹Raichoor et al. (2012) investigated the mass-size relation at $z \sim 1.2$ for morphologically-selected early-type galaxies in field, cluster, and group environments, and found that for masses $10 < \log(M/M_{\odot}) < 11.5$, field galaxies appear to be larger than cluster galaxies at fixed stellar mass. However, using DEEP3 at lower redshift but the same stellar mass range, Cooper et al. (2012) find the opposite trend: cluster galaxies appeared larger. Using CANDELS data, Papovich et al. (2012) also find larger galaxies in the cluster environment at $z = 1.62$. Furthermore, studies by Maltby et al. (2010) and Rettura et al. (2010) find no trend with environment at $z < 0.4$ and $z \sim 1.2$ respectively. Recently, looking at galaxies in the COSMOS survey, Huertas-Company et al. (2013) found that the galaxy size-mass relation and size growth do not depend on environment.

mass, so the final galaxy is more compact. This important idea is explored in more detail in 1.3.

1.2 Size Evolution Mechanisms for Compact Elliptical Galaxies

Most authors have assumed that the evolving sizes seen in the red nugget population are due to the physical expansion of individual galaxies, although as early as 2001, van Dokkum et al. noted that galaxies forming (and ultimately joining the red sequence) at later times may be systematically larger because they are less gas rich.

Various mechanisms have been proposed to explain the physical expansion. One such mechanism is adiabatic expansion (e.g. Fan et al. 2008; Damjanov et al. 2009; Fan et al. 2010). This model proposes that the size growth is caused by extreme mass loss due to feedback within the galaxy. For massive ($M_* > 3 \times 10^{10}$) galaxies, the nature of the feedback is related to quasar activity. For smaller galaxies ($M_* \lesssim 2 \times 10^{10}$), stellar winds and/or supernova feedback is thought to drive the size evolution. In either situation, the feedback acts to remove large amounts of cold gas from the centre of the galaxy, which then leads to a redistribution of stellar content of the galaxy. However, adiabatic expansion occurs within a relatively short timescale, which conflicts with the old ages that have been measured for compact early-type galaxies at high redshifts (Damjanov et al. 2009; Ragone-Figueroa & Granato 2011).

Another proposed size growth mechanism is that of mergers (e.g. Khochfar & Silk 2006; Naab et al. 2007; Hopkins et al. 2009b; Bezanson et al. 2009). Dissipationless major mergers occur between gas-poor galaxies with similar masses, and produce massive quiescent galaxies without additional star formation. Such ‘dry’ mergers were the one of the first mechanisms to be considered to explain the increase of quiescent galaxy radii. However, as discussed in Shankar et al. (2010), the number of major dry mergers expected from N-body Λ CDM simulations are too low to produce the observed size growth. They find that although major dry mergers add most of the stellar mass, the growth in size is due primarily to minor dry mergers (with mass

ratios $< 1 : 3$), which outnumber major mergers by a factor of ~ 5 at $M_* > 10^{10.5}$ and by a factor of 10 at lower stellar masses.

This idea has taken hold, and minor dry (gas-poor) mergers are now the currently favored model (Hopkins et al. 2010; Naab 2013; Trujillo et al. 2012; McLure et al. 2013, Lopez-Sanjuan et al. 2012). However, the number of mergers required to explain the size evolution is much larger than what is predicted by Λ CDM models, which creates many more massive galaxies than are seen in the local universe (Saracco et al. 2011). Shankar et al. (2010) used semi-analytic models based on a hierarchical growth of galaxies that are driven by an initial major, wet merger and followed by a number of late, minor, dry mergers and showed that compact galaxies at high- z can grow on to the same local size-age relation; however, the models provide a poor match to the local size-mass relation. Perhaps the greatest challenge to the idea that dry minor mergers alone can explain the observed size growth has come from Newman et al. (2012), who have used very deep CANDELS data to demonstrate that there are simply not enough companions around high- z galaxies to account for the very rapid size growth seen from $z = 2.5$ to $z = 1$. It seems that a two-phase mechanism is needed in which rapid early size growth is later augmented by a more gradual growth from minor mergers (Oser et al. 2010; 2012).

As noted earlier, an alternative explanation for the apparent size growth of ‘red nuggets’ has also been proposed: progenitor bias. This idea will be explored in more detail in the section below.

1.3 Progenitor Bias

The central prediction of progenitor bias is that younger galaxies are larger at a fixed mass because they are less gas rich. At low redshifts there appears to be some support for this prediction (Shankar & Bernardi 2009; van der Wel et al. 2009). Interestingly, there appears to be considerable morphological dependence in any putative age-mass relation: Bernardi et al. (2010) find little evidence for age-dependent sizes at fixed mass for elliptical galaxies, but show that large S0 and Sa galaxies tend to be younger at a fixed dynamical mass, suggesting that progenitor

bias might be more important for early-type systems with disks. In the phenomenological picture of Huang et al. (2013b;a), the innermost component of massive, early-type galaxies has a low Sérsic index. Furthermore, at high redshift, the disk fraction of compact galaxies appears to be over 50% (e.g. van der Wel et al. 2011). This suggests that the early-phase of the nugget phenomenon is associated with disk galaxies, which appears to be consistent with the suggestion that many of the nuggets are indeed disks (e.g. van der Wel et al. 2011; Chevance et al. 2012; Bruce et al. 2012; Patel et al. 2013).

On the other hand, at higher redshifts there appears to be no evidence for age-dependent galaxy sizes at fixed mass (Trujillo et al. 2011; Whitaker et al. 2012). Perhaps this is because outside the local universe it is difficult to tell the difference between sub-classes of early-type galaxies. Existing investigations make no attempt to distinguish elliptical galaxies from the S0/Sa-like systems that may be an important component of the population of nuggets. It is therefore of considerable interest to look for trends in galaxy age as a function of redshift with an eye toward understanding the importance of the morphological ‘fine structure’ used to distinguish elliptical galaxies from other types of objects in the early-type galaxy family (e.g. S0 and Sa galaxies).

The importance of progenitor bias has been explored in detail in a number of papers, with most authors concluding that it is unlikely to be the dominant effect (e.g. van Dokkum & Franx 2001; van Dokkum et al. 2008; van der Wel et al. 2009; Hopkins et al. 2009a; Szomoru et al. 2011; Whitaker et al. 2012; López-Sanjuan et al. 2012; Bruce et al. 2012). However, Newman et al. (2012) note that if the evolution of the mass-size relation is not driven at least in part by progenitor bias, the merger rate falls even further short of explaining the observed size growth. Carollo et al. (2013) have recently suggested that many compact galaxies may be missing from local catalogs due to misclassification as stars and/or intra-sample inconsistency in the definition of compactness. These authors use data from the COSMOS survey to argue that progenitor bias is the dominant source of observed size growth, noting that the ‘*apparent disappearance of Q-ETGs [quenched early-type galaxies] at later epochs may thus be a false reading of a reality*

in which earlier populations of denser Q -ETGs remain relatively stable in terms of numbers through cosmic time, but become less and less important, in relative number, at later and later epochs’.

We will explore these ideas in this thesis. But first, we must digress to consider some of the fundamental tools used to determine the ages of galaxies. These are stellar population synthesis, co-addition of spectra, and the statistical technique of bootstrap resampling. We will briefly describe each of these in turn before showing in the next chapter how they can be combined into a methodology for explore the evolving properties of high redshift galaxies.

1.4 Stellar Population Synthesis

Given that galaxies are primarily composed of stars, an ideal way to study them would naturally be to examine the individual stellar components. Unfortunately, from the ground we cannot resolve, and therefore cannot study, individual stars within galaxies outside the local group (although with *HST* we can go somewhat further, out to ~ 10 Mpc depending on stellar density). This is particularly true for galaxies at high redshift. Instead, we observe the integrated light from a galaxy: the sum of the light from all of the stars within it. In order to take the information contained within this light and recover meaningful physical parameters, we require a model of what kinds of stars are present, and how many of those stars there are. Stellar population synthesis provides a method for us to link the integrated light that we observe from galaxies with the stellar populations that they are composed of.

Stellar evolution and stellar atmospheres are largely (although not completely) understood. If the number density of stars as a function of mass, evolutionary stage, and chemical composition is known, one can compute the spectral energy distribution of a galaxy by superposing the corresponding stellar spectra. A single stellar population (i.e. a population whose stars were all formed at the same time, and with the same chemical composition) can be evolved forward in time, and snapshots of their positions in the Hertzsprung-Russell (HR) diagram at various points in time will map out an isochrone. The relative number of stars along the isochrone reflects the

initial mass function (IMF). Adding together the absolute flux-spectra of the stars along a given isochrone in the proportions dictated by the IMF will produce the spectrum (the power radiated per unit wavelength per unit mass):

$$S_{\lambda}[t', \xi(t-t')] \quad (1.2)$$

for a simple stellar population of age t' and metallicity $\xi(t-t')$. The IMF in this case is an adjustable parameter. Taking into account the star formation rate, $\psi(t)$, the spectral energy distribution of a stellar population at time t is characterized by the following (Bruzual & Charlot 2003):

$$F_{\lambda}(t) = \int \psi(t-t') S_{\lambda}[t', \xi(t-t')] dt' \quad (1.3)$$

Comparisons of galaxy spectral observations with such population synthesis models allows us to characterize and constrain the ages and star-formation histories of these galaxies. The EZ_Ages IDL code package (Graves & Schiavon 2008), described below in Section 1.4.1, provides a convenient and largely automated way of determining the age of a galaxy by comparing its observed spectrum with a library of model spectra. Colors alone are insufficient for inferring meaningful ages, in large part because of the problem of age-metallicity degeneracy: both increasing age and increasing metallicity can make a galaxy appear redder (the former because more stars have moved off the main-sequence and onto the giant branch, and the latter because a higher metallicity will increase the opacities in stellar photospheres, decreasing the effective temperatures of the stars. Worthey (1994) identified the “2/3” rule: if two populations have a percentage change $\delta\text{age}/\delta Z = 3/2$, they will appear identical in most indices. In other words, the effect on the spectral indices caused by an increase or decrease in the age of a stellar population by a factor of three is nearly indiscernible from the effects caused by an increase or decrease in metallicity by a factor of two. However, Worthey (1994) also pointed out that there are several indices which do not follow this trend of degeneracy, noting that $H\beta$ and higher Balmer lines were promising for being more sensitive to age, while Fe4668 and Fe5015

were more sensitive to metallicity. EZ_Ages uses Balmer lines and iron lines to disentangle the effects of age and metallicity; a brief description of the procedure is presented in the next section.

1.4.1 EZ_Ages

The ages of galaxies in this thesis will be calculated using the EZ_Ages IDL code package (Graves & Schiavon 2008), which computes the mean, light-weighted stellar population age, $[\text{Fe}/\text{H}]$, and abundance enhancements $[\text{Mg}/\text{Fe}]$, $[\text{C}/\text{Fe}]$, $[\text{N}/\text{Fe}]$, and $[\text{Ca}/\text{Fe}]$ for unresolved stellar populations. The following description of the EZ_Ages routine draws heavily from Schiavon (2007).

The code takes as input the measured Lick index line strengths of a spectrum and compares them to the stellar population synthesis models of Schiavon (2007). The Lick index line strengths are measured by the automated IDL code Lick_EW, available as part of the EZ_Ages package. If they are provided, EZ_Ages uses errors in the Lick index data to estimate the uncertainties in the ages, $[\text{Fe}/\text{H}]$, and abundance ratios, and uncertainties are assumed to be dominated by measurement errors in the line strengths. The models provide a choice of solar-scaled or α -enhanced (average $[\alpha/\text{Fe}] = +0.42$) isochrones.

EZ_Ages performs a directed search through the abundance ratio parameter space by taking advantage of the fact that several Lick indices are sensitive to only a few different elemental abundances. The abundance fitting adjusts only one abundance at a time, with the next chosen Lick index introducing only one additional abundance dependency. It begins by computing a set of models using the user-chosen isochrone and solar abundance ratios for the stellar atmospheres. It then determines a fiducial age and $[\text{Fe}/\text{H}]$ by using a pair of lines that are sensitive to age and $[\text{Fe}/\text{H}]$ but relatively insensitive to other elemental abundances. The default choices for these lines are $\text{H}\beta$ for age-sensitivity and an average of Fe5270 and Fe5335 ($\langle\text{Fe}\rangle$) for $[\text{Fe}/\text{H}]$ sensitivity, though other lines can be specified by the user. A model grid of $\text{H}\beta$ vs. $\langle\text{Fe}\rangle$ is created, showing lines of constant age from 1.2 to 14.1 Gyr and lines of constant $[\text{Fe}/\text{H}]$ from

-1.3 to $+0.2$, with a square representing the observed data. The box of the grid which the data point lies in gives a bounded range in age and $[\text{Fe}/\text{H}]$ and the point is converted into a fiducial value for age and $[\text{Fe}/\text{H}]$. Figure 1.2 shows a plot of model grids for $\text{H}\beta$ and $\langle\text{Fe}\rangle$, with a sample data point for a galaxy with age ≈ 7 Gyr and $[\text{Fe}/\text{H}] \approx -0.2$.

Once the fiducial age and $[\text{Fe}/\text{H}]$ have been determined, similar grid plots are created with indices which are sensitive to non-solar abundance ratios. Thus, after fitting $\text{H}\beta$ and $\langle\text{Fe}\rangle$, a good next index choice is $\text{Mg } b$, which is dominated by Mg and Fe (which has already been set by the $\text{H}\beta$ - $\langle\text{Fe}\rangle$ grid inversion). If the chosen model determined from the $\text{H}\beta$ - $\langle\text{Fe}\rangle$ model grid is a good match to the data, then the age and $[\text{Fe}/\text{H}]$ estimated by the grid inversion of the $\text{H}\beta$ - $\text{Mg } b$ grid should match the fiducial age and $[\text{Fe}/\text{H}]$ determined from the previous plot. In the example of Figure 1.2, this is not the case: the top right panel showing $\text{H}\beta$ - $\text{Mg } b$ gives a larger value of $[\text{Fe}/\text{H}]$ than in the top left panel showing $\text{H}\beta$ - $\langle\text{Fe}\rangle$, indicating that the galaxy has a larger $[\text{Mg}/\text{Fe}]$ ratio than the solar-scaled model predicts. If the values do not match (as in this example), then the algorithm increases or decreases the input value of $[\text{Mg}/\text{Fe}]$ and then recomputes the model. Increasing or decreasing $[\text{Mg}/\text{Fe}]$ lowers or raises the value of $[\text{Fe}/\text{H}]$ that is estimated by the grid inversion of the $\text{H}\beta$ - $\text{Mg } b$ plot, which brings it into agreement with the value obtained from the first $\text{H}\beta$ - $\langle\text{Fe}\rangle$ plot. The bottom panels of Figure 1.2 show $\text{H}\beta$ - $\langle\text{Fe}\rangle$ and $\text{H}\beta$ - $\text{Mg } b$ plots for the model computed with $[\text{Mg}/\text{Fe}] = +0.3$, which brings the $[\text{Fe}/\text{H}]$ into agreement between the two plots.

The benefit of using `EZ_Ages` is that it is largely an automated procedure, which enables us to perform in-depth analysis of many sets of spectra, which are required by the bootstrap resampling technique discussed in detail in §1.5.2. The exact details of our methodology, including how we measured the velocity dispersions of the galaxies, and which indices we chose to determine the age measurements, are discussed later, in §3.2.

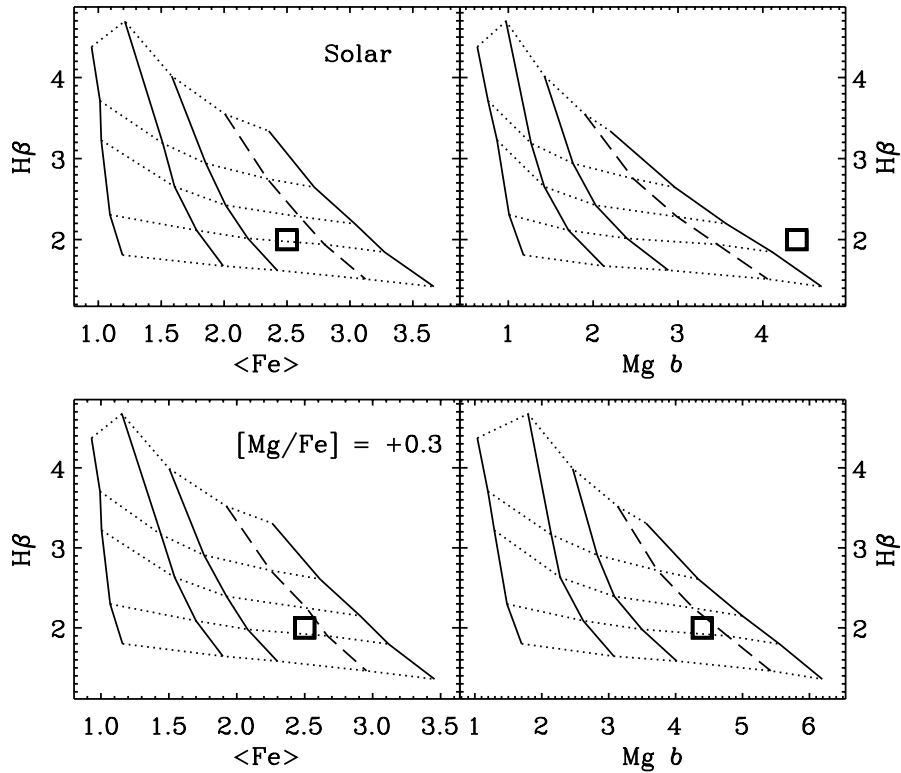


Figure 1.2: From Graves & Schiavon (2008): Grids produced by the Schiavon (2007) model illustrating the effects of supersolar $[Mg/Fe]$. Solid lines show constant $[Fe/H]$ from left to right of -1.3 , -0.7 , -0.4 , 0.0 , and $+0.2$ (the dashed line shows $[Fe/H] = 0.0$ for reference). Dotted lines show constant age from top to bottom of 1.2 , 2.2 , 3.5 , 7.0 , and 14.1 Gyr. The square shows an example data point with age ≈ 7 Gyr and $[Fe/H] \approx -0.2$. *Top*: Models computed with solar-scaled abundances. The Balmer-Fe grid gives fiducial values of $t = 7$ Gyr and $[Fe/H] = 0.2$. The Balmer-Mg b grid shows an $[Fe/H] > 0.4$ dex higher than the fiducial from the Balmer-Fe grid. This indicates that $[Mg/Fe]$ is supersolar. *Bottom*: Increasing $[Mg/Fe]$ in the models slides the grid to the right toward the Balmer-Mg b data point, lowering the estimated $[Fe/H]$. $H\beta$ is also slightly affected by the abundance change, yielding a slightly younger fiducial age. In the Mg-enhanced model, the fiducial $[Fe/H]$ from the Balmer-Fe grid matches the value of $[Fe/H]$ estimated from the Balmer-Mg b grid, indicating that $[Mg/Fe] = +0.3$ is a good fit to the data.

1.5 Overview of Methodology

1.5.1 Co-adding spectra

When conceptualizing this thesis, we were faced with a dilemma that many observational astronomers grapple with: our spectra had a much too low signal-to-noise to allow for EZ_Ages

to meaningfully measure their ages. To overcome this problem, we decided to co-add our spectra to create a representative composite for each compact and control subsample. Co-addition is susceptible to many systematic effects, the majority of which are unavoidable. Nevertheless, the usage of co-addition to measure properties of similar objects is not uncommon across various subfields of astronomy, particularly in areas where high signal-to-noise observations are rare². The key to successful use of co-addition for our present purposes is to keep careful track of potential systematics and to ensure that our conclusions are based on comparison with a control sample that shares these systematics.

The decision to co-add our spectra then introduces a new problem: namely, that simply measuring one age for each compact and control sample cannot provide us with meaningful constraints on these ages. Although EZ_Ages provides an estimate of the error on the age, which is based on the signal-to-noise of the inputted co-added spectra, our concern arises from the fact that the co-added spectra are, ultimately, composites: each co-added spectrum does not represent any one of the individual galaxies that comprise it. Thus we were faced with the question: how do we more robustly characterize the ages of these galaxies? In an ideal world, we would simply obtain extremely high-quality observations, but such observations were outside the timeline of this thesis.

In other words, we wanted to ask a question of a population: *what is the age of ultra-compact early-type galaxies?*, but we cannot answer this directly, due to our observational limitations. Instead, we must ask this question of a *sample* of the population instead. How can we be confident that the answer given by the sample is close to the answer that would be given by the population? Ideally, we would repeatedly take different samples from our parent population, ask them the same question, and then examine the variability of the answers, but it is not feasible to

²As early as 1985, Adelman & Leckrone (1985) used co-addition to study the ultraviolet and optical region of a horizontal branch star in the field. Although instrumentation has improved drastically since then, observations of faint or distant objects still often benefit from co-addition. For example, Dressler et al. (2004) utilized composite spectra to quantify general trends in star formation for galaxy populations at $z > 0.3$. In order to investigate the distribution of metals in galaxies, Gallazzi et al. (2008) used co-added spectra of galaxies with similar velocity dispersions, absolute r-band magnitude and 4000 Å-break values to probe areas of parameter space where their individual spectra had low signal-to-noise. Finally, most recently, Varga et al. (2012) used co-added image stacking to reveal a strongly reddened, faint active galactic nucleus population.

do this in a consistent fashion. Alternatively, we could make assumptions about the shape of the population, or else use the information in the sample we already have we have to learn about it. However, we prefer not to make any assumptions about a relatively unexplored population: we therefore must use the information we already have.

Thankfully, there is a statistical technique that is optimized to help answer such questions. This technique is known as bootstrap resampling.

1.5.2 A Brief Overview of Bootstrap Resampling

The bootstrap is, as far as statistical methods go, a relatively recent development. It was introduced by Efron (1979), and eventually popularized as computing power improved. The term “bootstrap” is derived from the phrase *to pull oneself up by one’s bootstrap*, widely attributed to “The Surprising Adventures of Baron Munchausen” (1781) by Rudolph Erich Raspe, although as it turns out, there is no explicit reference to bootstraps in the various versions of the Munschhausen tales. In one tale, the Baron lifts himself (and his horse) out of the mud by pulling on his own pigtail – the bootstrap variation likely arose as a variant of this story. In any case, the phrase carries the implication that one is attempting an absurdly impossible task. Indeed, initially, the bootstrap methodology was met with a great deal of mistrust. Davison & Hinkley (1997, p. 3) stated, “in the simplest nonparametric problems we do literally sample from the data, and a common initial reaction is that this is a fraud. In fact it is not.” Chernick (1999, p. 2) notes that even the publication of a *Scientific American* article that detailed the bootstrap and its applications in laypersons terms only succeeded in increasing the skepticism of scientists and engineers.

The bootstrap was developed as a method of estimating the standard error of sample estimators (the mean, median, and standard deviation are some simple examples of sample estimators). The bootstrap estimate of the standard error is useful in that it can be performed no matter how complicated the estimators may be, and it is free from theoretical calculations (Efron & Tibshirani 1994). The basic idea is that an inference about a population from sample

data can be modelled by resampling the sample data and performing the inference on the new resample.

The non-parametric bootstrap is outlined in Efron & Tibshirani (1994) and Chernick (1999) as follows: Suppose we observe a sample of n independent data points x_1, x_2, \dots, x_n , which we can denote with the vector $\mathbf{x} = (x_1, x_2, \dots, x_n)$. From this sample, we can compute a statistic of interest, $\hat{\theta} = s(\mathbf{x})$, where s is some function applied to the vector \mathbf{x} . Some typical simple examples of the statistic include the median, the mean, or the standard deviation, but it could also be something much more complex. We would like to know how $\hat{\theta}$ compares to the true value of θ - in order words, we want to get an estimate of the error in our estimation of the true value of θ .

To do this, we compute a *bootstrap sample*, $\mathbf{x}^* = (x_1^*, x_2^*, \dots, x_n^*)$, which is obtained by randomly sampling n times, *with replacement*, from the original data points x_1, x_2, \dots, x_n . This means the same values can appear more than once, and some may not appear at all. For example, with $n = 8$, we could obtain a bootstrap sample $\mathbf{x}^* = (x_2, x_7, x_5, x_8, x_7, x_3, x_1, x_4)$. A number of bootstrap samples $\mathbf{x}^{1*}, \mathbf{x}^{2*}, \dots, \mathbf{x}^{B*}$ are then generated, each of size n . According to Efron & Tibshirani (1994), typical values of B , the number of bootstrap samples, range from 50 to 200 for standard error estimation. However, more recent literature suggests that a much larger number is preferable. For example, Booth & Sarkar (1998) show that if the sampling distribution of $\hat{\theta}$ is approximately normal, $B = 800$ is required to ensure that Monte Carlo error does not affect the conclusions of a statistical analysis. In general, it seems that $B > 1000$ is preferred, and that the “ideal” number is as large as your computing power and time constraints allow.

For each bootstrap sample, we then compute $\hat{\theta}^{1*} = s(\mathbf{x}^{1*})$, $\hat{\theta}^{2*} = s(\mathbf{x}^{2*})$, \dots , $\hat{\theta}^{B*} = s(\mathbf{x}^{B*})$ – the values of the statistic s obtained by using the bootstrap samples in place of the original sample. Repeating this B times, we obtain a Monte Carlo approximation to the distribution of the estimator. The bootstrap estimate of the standard error is then the standard deviation of the bootstrap replications. This procedure is outlined in a schematic form in Figure 1.3.

The bootstrap technique is suitable for our application because the sample that we have is

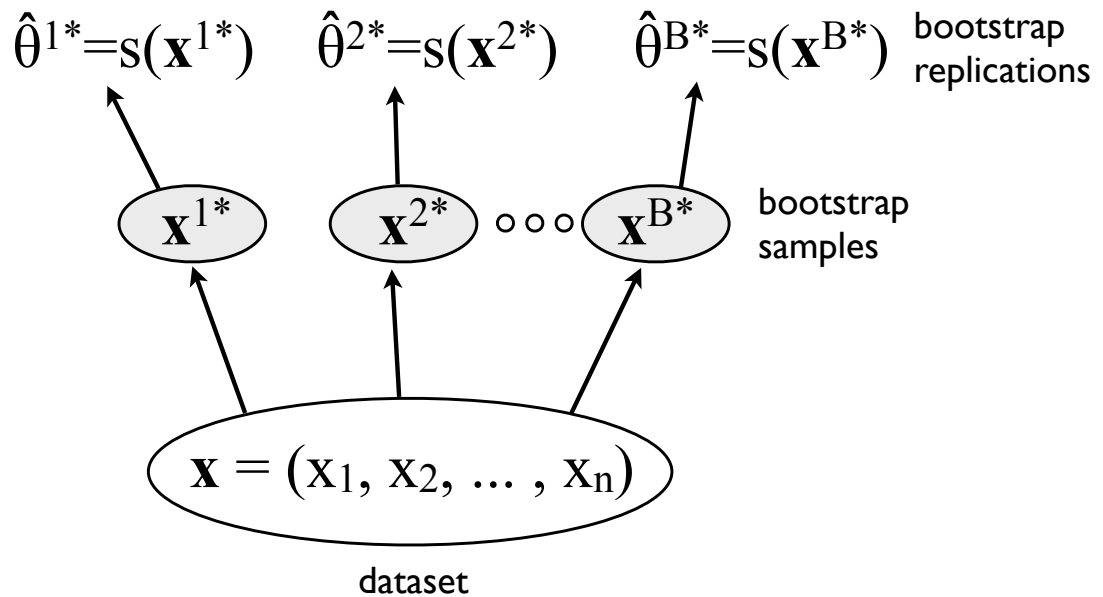


Figure 1.3: Recreated from Efron & Tibshirani (1994), a schematic of the bootstrap process for estimating the standard error of a statistic $\hat{\theta} = s(\mathbf{x})$. B bootstrap samples of n elements each are generated by sampling with replacement n times from the original data set. Bootstrap replications $\hat{\theta}^{1*}, \hat{\theta}^{2*}, \dots, \hat{\theta}^{B*}$ are obtained by calculating the value of the statistic $s(\mathbf{x})$ on each bootstrap sample.

also a population, albeit a small and discrete one. If we sample from it with replacement, we are treating this sample as though it is a population. This is justifiable because most samples, if randomly chosen, tend to look like the population that they are drawn from. Furthermore, the sample is the only information we have about what the population actually looks like. Thus the resampling is not done to provide an estimate of the population distribution, because we take our sample itself as a model of the population. Rather, resampling is done to provide an estimate of the sampling distribution of the sample statistic in question, which in our case is the age of the galaxies.

1.6 Thesis Overview

In this thesis, we aim to better characterize the link between stellar population age, galaxy size and morphology as a function of redshift. Colors alone cannot be used to infer ages because of age-metallicity degeneracies mentioned in §1.4. On the other hand, the absorption features used to characterize galaxy ages on spectra are difficult to observe at the required signal-to-noise levels at high-redshifts (except in the cases of the most extreme post-starburst systems, (e.g. Bezanson et al. 2013; Whitaker et al. 2013)). In this thesis, we describe an attempt to get around this basic difficulty by using exploiting the statistical technique of bootstrap resampling in order to explore galaxy ages using co-added spectra.

By examining the light-weighted ages of galaxies as a function of size using this technique, our goal is to explore whether the red nugget phenomenon is more closely related to the physical expansion of galaxies already established on the red sequence, or whether it is likely due to some form of progenitor bias. A measurement of younger ages for compact galaxies, as compared to larger galaxies, would indicate that the galaxy growth scenario is favoured. A measurement that finds the opposite, that compact galaxies are older than larger galaxies, would suggest that progenitor bias is the preferred model. We also seek to test whether the morphological ‘fine structure’ of galaxies (which we characterize crudely using apparent smoothness) leaves an imprint on their measured stellar populations.

A plan for this thesis follows. Chapter 2 describes our data and explains how our subsamples were defined. Chapter 3 focuses on our methodology, including the fine-tuning of our age measurements (§3.2) and our method of characterizing the homogeneity of the underlying stellar populations (§3.4). Chapter 4 describes the results of the bootstrap resampling performed on the galaxies that contribute to each co-added spectrum to generate a distribution of possible ages. Our conclusions are presented in Chapter 5. Throughout this thesis, we assume a Λ CDM cosmology with $H_0 = 70 \text{ km s}^{-1}$, $\Omega_m = 0.3$, and $\Omega_\Lambda = 0.7$.

Chapter 2

Data and Samples

Much of the material presented in this chapter, as well as Chapters 3 and 4, appears in Keating et al. 2015, ApJ, 798, 26.

2.1 Chapter Overview

This chapter describes the properties of the DEEP2 survey from which we obtained the data for this thesis (§2.2, §2.2.1). A brief overview of the selection of the galaxies is provided in §2.3. The details of our spectral co-adding procedure are described in §2.4. In §2.5, we examine the systematic properties of our co-added spectra.

2.2 The DEEP2 Survey

The Deep Extragalactic Evolutionary Probe 2 (DEEP2) (Davis et al. 2003; 2005; 2007; Newman et al. 2013) survey forms the heart of our data. DEEP2 was designed to study galaxy evolution out to redshifts of $z \sim 1.4$ and targeted > 50000 galaxies over four widely separated fields covering a total sky area of 2.8 deg^2 , observed with ~ 1 hour exposure times to a limiting apparent magnitude of $R_{AB} < 24.1$. The survey used the DEIMOS spectrograph on the 10-m

Keck II telescope with the 1200-line/mm grating which delivers high spectral resolution of $R \sim 6000$ with an observed wavelength range of $6500 < \lambda [\text{\AA}] < 9200$ (Faber et al. 2003).

Our galaxy samples are drawn from a subset of the DEEP2 sample known as the Extended Groth Strip (EGS: $\alpha = 14^h 17^m$, $\delta = +52^\circ 30'$). This field is the subject of a panchromatic study: the All-Wavelength Extended Groth Strip International Survey (AEGIS) (Davis et al. 2007), which includes *Hubble Space Telescope (HST)*/Advanced Camera for Surveys (ACS) imaging. The DEEP2 targets were selected from CFHT *BRI* imaging. The targets selected must have $18.5 \leq R \leq 24.1$ and surface brightness brighter than $\mu_R \leq 26.5$. Unlike the majority of the DEEP2 survey, in the AEGIS region there was no *BRI* photometry screening applied to remove low-redshift galaxies, and therefore the sample spans a redshift range $0 < z < 1.4$. Further details of the DEEP2 observations, catalog construction, and data reduction can be found in Davis et al. (2003; 2005; 2007) and Newman et al. (2013).

2.2.1 HST Imaging from AEGIS

In the EGS field, *HST*/ACS images in the *V* (F606W) and *I* (F814W) bands were taken between June 2004 and March 2005 over 63 tiles that cover an effective area of approximately $10.1' \times 70.5'$. For a point source, the 5σ limiting magnitudes are $V = 28.14$ and $I = 27.52$ within a circular aperture of radius $0.12''$ (~ 50 pixel area). The 5σ limiting magnitudes for an extended object are $V = 26.23$ and $I = 25.61$ for a circular aperture of radius $0.3''$ (~ 314 pixel area) (Davis et al. 2007).

The DEEP2 survey in the AEGIS field contains redshifts, rest-frame *U* and *B* magnitudes, stellar masses and error on stellar masses for ~ 17600 galaxies. We required both redshifts and morphology from *HST*/ACS images; of the galaxies in the catalogue, 2305 of met these criteria. This parent sample spans a redshift range $0.5 < z < 1.3$ and magnitude range $-20.6 < U < -17.0$.

Publicly available, quantified morphologies for the parent sample were obtained from Cheung et al. (2012): structural parameters of the *HST*/ACS images were measured using

GIM2D, a 2D bulge + disk decomposition program (Simard et al. 2002), providing bulge radii for Sérsic indices $n=4$ and $n=2$, and bulge-to-total (B/T) ratios in V (F606W) and I (F814W) bands for Sérsic indices $n=4$ and $n=2$. Stellar masses for the sample were derived by Bundy et al. (2006): using *BRIK* colors and spectroscopic redshifts, they fit the observed galaxy spectral energy distributions (SEDs) to a grid of model templates from Bruzual & Charlot (2003) with a Chabrier (2003) initial mass function, spanning a range of star formation histories, ages, metallicities, and dust content.

For this thesis, our interest lies with massive, passive compact galaxies. From our catalogue of galaxies with redshifts and morphologies, we examined several choices of cuts to select subsamples of the red, early-type galaxies of interest (by a combination of color, bulge-to-total ratio, and image smoothness; the exact properties selected are detailed in §2.3). We used the I -band, $n=4$ cases for our selection of B/T values and bulge radii.

2.3 Definition of the Samples

Of the 2305 galaxies described above, 32 galaxies had poor half-light radii estimates. Potential causes of a poor radius estimate include unreliable or failed GIM2D decompositions, which can occur for galaxies with effective radii less than half the FWHM of the PSF (2 pixels), or for galaxy models that are offset from the centre of the *HST/ACS* images by more than 3.5 pixels (Cheung et al. 2012). These galaxies were removed from further analysis. As shown by, e.g., Moresco et al. (2013), the observed properties of early-type galaxies are often highly dependent on the way in which those galaxies are defined or selected. Taking this into account, we selected our early-type galaxies in several different ways by using various combinations of the available properties. We examined three different samples of ‘early-type’ galaxies in total. These cuts, and the assumptions they are based on, are detailed in Tables 2.1 and 2.2 and further described below:

1. *Red & Bulge-Dominated (RBD)*: We based this selection on cuts for rest-frame color ($U - B > 0.9$) to select the red galaxies, and bulge-to-total ratio $B/T > 0.5$ to minimize the

- number of galaxies with disks. Before implementing a mass cut, this sample is comprised of 203 galaxies.
2. *Smooth & Bulge-Dominated (SBD)*: Simard et al. (2002; 2009) suggests that usage of a measure of image “smoothness” can aid in maximizing the number of E/S0 galaxies selected, while minimizing contamination from Sa-Irr type galaxies, by removing those with clumpy structure. The image smoothness is defined as $S = R_T + R_A$, where R_T and R_A are indices which quantify the amount of light in symmetric and asymmetric residuals (respectively) from a fitting model, expressed as a fraction of the total galaxy model flux. They are defined in detail in Simard et al. (2002). Simard et al. (2009) find that the optimal definition of an early-type galaxy is one with a limit of smoothness, S_2 (S measured within two half-light radii) of $S_2 < 0.075$ (measured in the I -band) and $B/T > 0.35$; we therefore adopted these criteria for our second selection, which is comprised of 141 galaxies before a mass cut.
 3. *Red, Smooth & Bulge-Dominated (RSBD)*: This sample was selected identically to the Smooth & Bulge-Dominated (SBD) Sample, but imposes an additional color cut of $U - B > 0.9$ to ensure that we selected the purely red galaxies. Before implementing a mass cut, this sample is comprised of 119 galaxies.

Mass and Size Selection

Each of the samples outlined above was then further subdivided by mass and half-light radius. The mass division was performed in order to separate out the effects of mass from our measurements. At masses $M > 10^{11}M_{\odot}$, there is negligible evolution of the stellar mass function from $z = 1$ to $z = 0$ (e.g. Fontana et al. 2004; Bundy et al. 2006; Borch et al. 2006; Vulcani et al. 2011). We used this threshold to divide our samples between “heavy” ($M_* > 10^{11}M_{\odot}$) and “light” ($M_* < 10^{11}M_{\odot}$) subsamples.

An ideal radius cut would be on the order of 1 kpc, which is the typical measured size of a red nugget; however, implementing such a cut on our sample resulted in too few compact

galaxies to contribute to a meaningful co-added spectrum (the RSBD Compact sample, for example, has fewer than 10 galaxies with $r < 1$ kpc). Given this constraint, we implemented a radius division at 2 kpc, which separated the above groups into “compact” ($r < 2$ kpc) and “control” ($r > 2$ kpc) subsamples. This slightly larger-than-ideal radius division is still keeping with the accepted definition of a “compact” galaxy: for example, Cassata et al. (2011) present a distinction between “ultra-compact,” “compact,” and “normal” early-type galaxies based on a galaxy’s location relative to the local mass-size relation, with a “normal” ETG having $r_e \sim 2 - 4$ kpc at $M \gtrsim 10^{10.6-8} M_\odot$.

Table 2.1 shows the number of galaxies remaining in our samples after each consecutive cut (but before removing galaxies without data in our normalization range, described in §2.4). Figures 2.1 – 2.3 show the overlap of the each of the samples in mass-radius (with a dotted line indicating the radius division between the compact and control samples), color-magnitude, color-smoothness, and smoothness-B/T. The symbols in the figures are colored according to whether the galaxy is heavy ($M_* > 10^{11} M_\odot$, in red) or light ($M_* < 10^{11} M_\odot$, in black). For all of the samples, as expected, the brighter galaxies tend to have higher mass than the lower magnitude ones. In the SBD sample, which spans a wider range of color than the RBD or RSBD samples, the galaxies that have colors $U - B < 1.0$ are all ones with $M_* < 10^{11} M_\odot$. Imposing the additional color cut of $U - B > 0.9$ on the RSBD sample removes only the low mass galaxies, therefore the SBD and RSBD compact and control samples with $M_* > 10^{11} M_\odot$ are identical.

Figures 2.4, 2.5, and 2.6 show histograms of the distribution in redshift, stellar mass, and color respectively for the each of the subsamples. The systematics of these histograms are discussed in §2.5.

A Note on our Sample Selection

We note here that in the time taken to produce this thesis, several alternative (and arguably more effective) methods of selecting compact massive galaxies have emerged. For example, it has become standard to use the slope of the mass-size relation in order to select compact

galaxies, rather than taking a simple straight cut as we have done. Furthermore, instead of the morphological selections we have used, another interesting approach would be the use of a selection in the rest frame $U - V$ versus $V - J$ diagram (i.e., the UVJ diagram). The UVJ diagram has been established as a tool to distinguish red quiescent galaxies from reddened star-forming galaxies (Williams et al. 2009; Patel et al. 2012). Selecting for quiescence, as opposed to morphology, may have eliminated many of the non-smooth “early-type spiral” galaxies in our RBD sample (see §4.5 and Appendix A for a discussion of these galaxies).

Table 2.1. Number of galaxies remaining after consecutive cuts

Cut	# Remaining
Total	2305
Remove bad radii [†]	2273
RBD	
$U - B > 0.9$	836
$B/T > 0.5$	258
$r < 2$ kpc	134
$r > 2$ kpc	124
SBD	
$B/T > 0.35$	668
$S2 < 0.075$	159
$r < 2$ kpc	73
$r > 2$ kpc	86
RSBD	
$U - B > 0.9$	836
$B/T > 0.35$	403
$S2 < 0.075$	130
$r < 2$ kpc	63
$r > 2$ kpc	67

[†]We removed galaxies which had poor half-light radii estimates caused by unreliable or failed GIM2D decompositions (see 2.3 for details).

Table 2.2. Details of cuts for each sample

Sample Name	B/T cut	S2 cut	$U - B$ Cut	Bulge Radius (R_e) cut	Mass cut ($\log M_*$)	# with data at 4130-4160 Å
RBD, compact	> 0.5	N/A	> 0.9	< 2 kpc	N/A	97
RBD, control	> 0.5	N/A	> 0.9	> 2 kpc	N/A	106
RBD, heavy	> 0.5	N/A	> 0.9	< 2 kpc	> 11	78
RBD, light	> 0.5	N/A	> 0.9	< 2 kpc	< 11	125
RBD, compact, heavy	> 0.5	N/A	> 0.9	< 2 kpc	> 11	25
RBD, control, heavy	> 0.5	N/A	> 0.9	> 2 kpc	> 11	53
RBD, compact, light	> 0.5	N/A	> 0.9	< 2 kpc	< 11	72
RBD, control, light	> 0.5	N/A	> 0.9	> 2 kpc	< 11	53
SBD, compact	> 0.35	< 0.075	N/A	< 2 kpc	N/A	61
SBD, control	> 0.35	< 0.075	N/A	> 2 kpc	N/A	80
SBD, heavy	> 0.35	< 0.075	N/A	N/A	> 11	69
SBD, light	> 0.35	< 0.075	N/A	N/A	< 11	72
SBD, compact, heavy	> 0.35	< 0.075	N/A	< 2 kpc	> 11	25
SBD, control, heavy	> 0.35	< 0.075	N/A	> 2 kpc	> 11	44
SBD, compact, light	> 0.35	< 0.075	N/A	< 2 kpc	< 11	36
SBD, control, light	> 0.35	< 0.075	N/A	> 2 kpc	< 11	36
RSBD, compact	> 0.35	< 0.075	> 0.9	< 2 kpc	N/A	54
RSBD, control	> 0.35	< 0.075	> 0.9	> 2 kpc	N/A	65
RSBD, heavy	> 0.35	< 0.075	> 0.9	N/A	> 11	69
RSBD, light	> 0.35	< 0.075	> 0.9	N/A	< 11	50
RSBD, compact, heavy	> 0.35	< 0.075	> 0.9	< 2 kpc	> 11	25

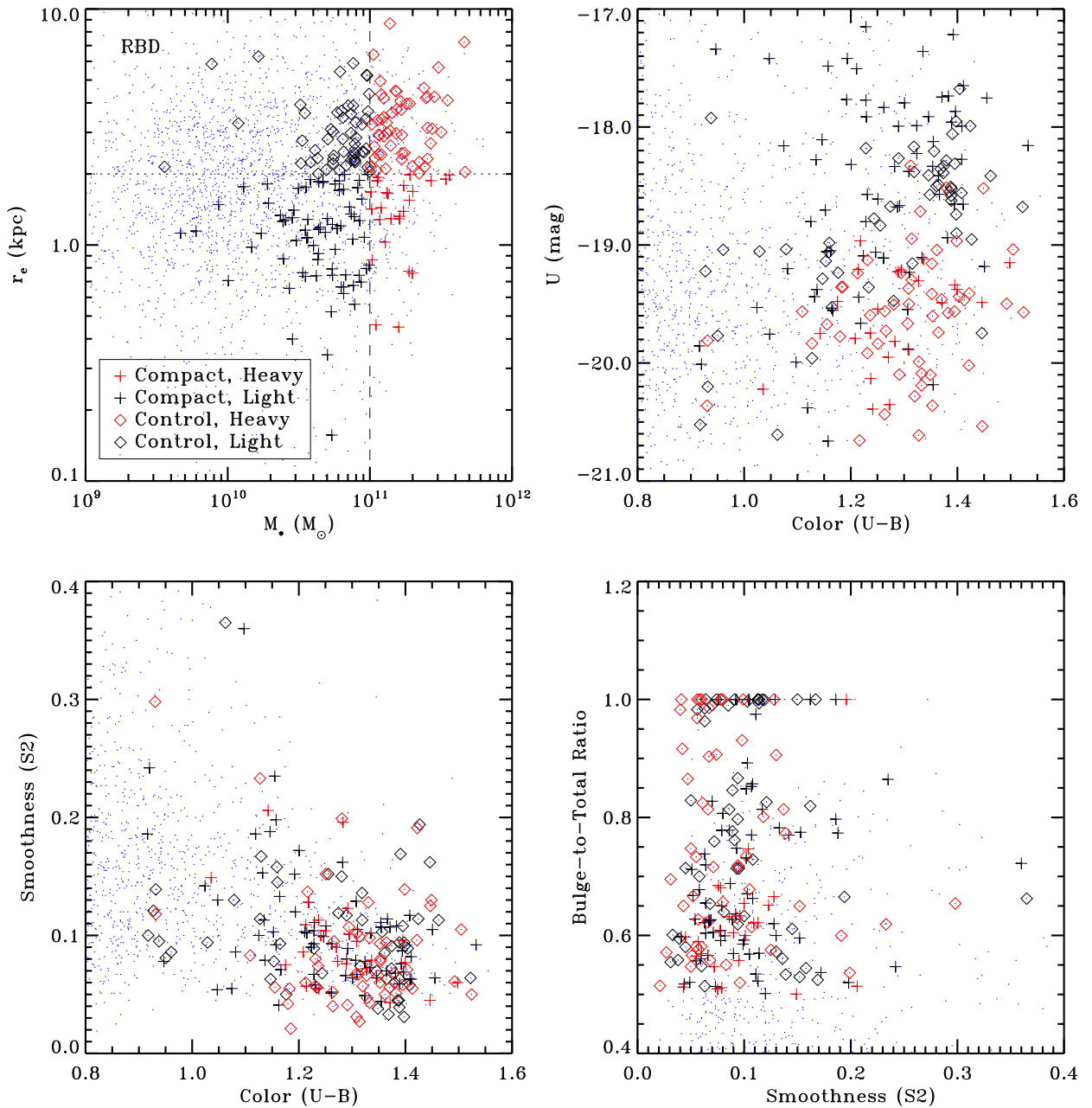


Figure 2.1: The overlap of the “Red & Bulge Dominated (RBD)” samples ($B/T > 0.5$, $U - B > 0.9$) in a mass-radius diagram (top left; dashed line indicates the radius division at $r_e = 2$ kpc, where r_e is I -band half-light radius of the bulge), color-magnitude (top right), color-smoothness (bottom left), and smoothness-B/T (bottom right). Compact galaxies are indicated with crosses, control galaxies are indicated with diamonds. The symbol color indicates whether the galaxy has $M_* > 10^{11} M_\odot$ (red) or $M_* < 10^{11} M_\odot$ (black). The blue dots indicate the whole population of galaxies that we select from.

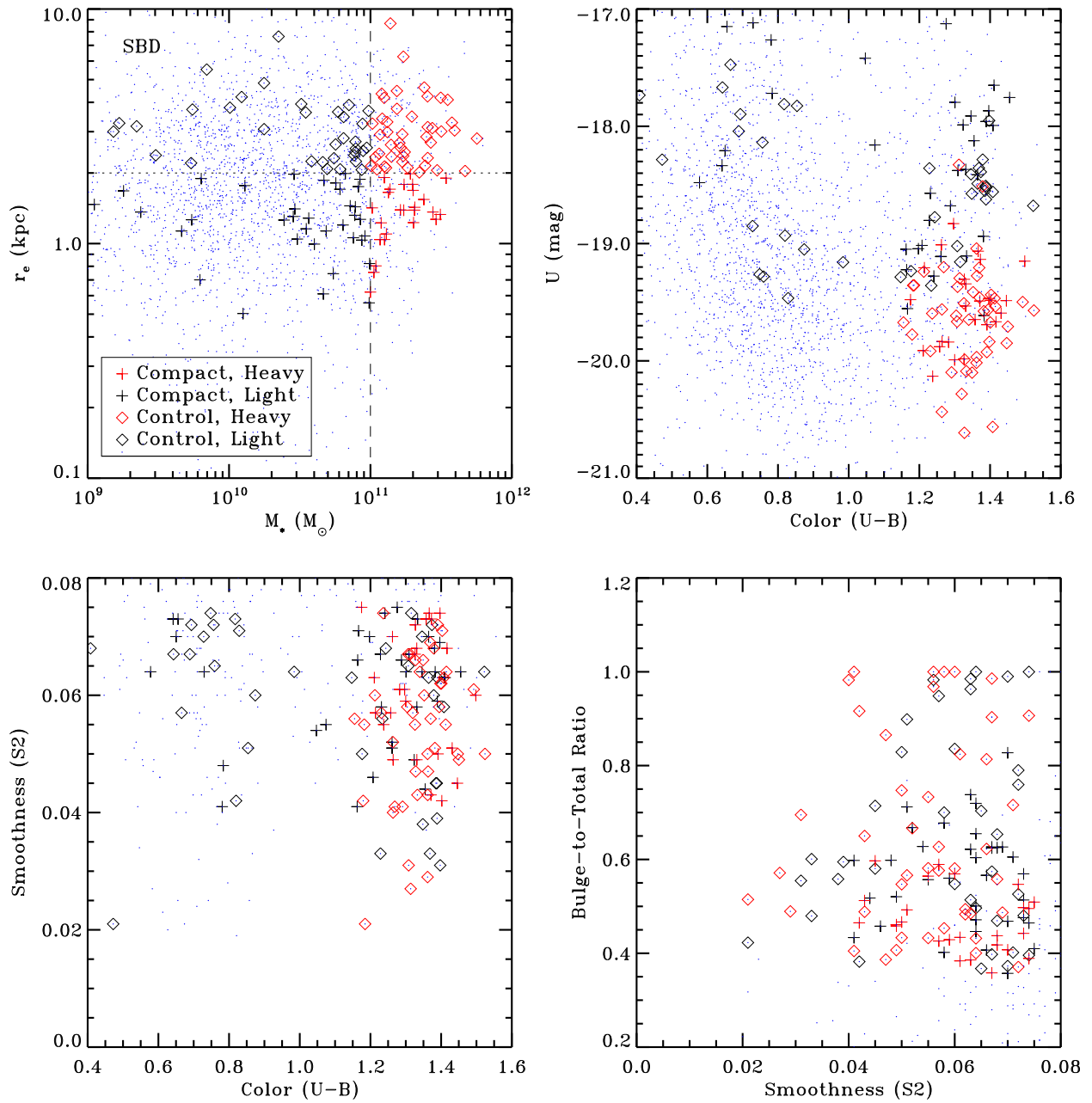


Figure 2.2: The overlap of the “Smooth & Bulge Dominated (SBD)” samples ($B/T > 0.35$ and $S2 < 0.075$) in a mass-radius diagram (top left; dashed line indicates the radius division at $r_e = 2$ kpc, where r_e is I -band half-light radius of the bulge), color-magnitude (top right), color-smoothness (bottom left), and smoothness- B/T (bottom right). Compact galaxies are indicated with crosses, control galaxies are indicated with diamonds. The symbol color indicates whether the galaxy has $M_* > 10^{11} M_\odot$ (red) or $M_* < 10^{11} M_\odot$ (black). The blue dots indicate the whole population of galaxies that we select from (in the bottom panels, many of the points have higher S2 values and/or bluer colors and as such are not displayed with the given axis range).

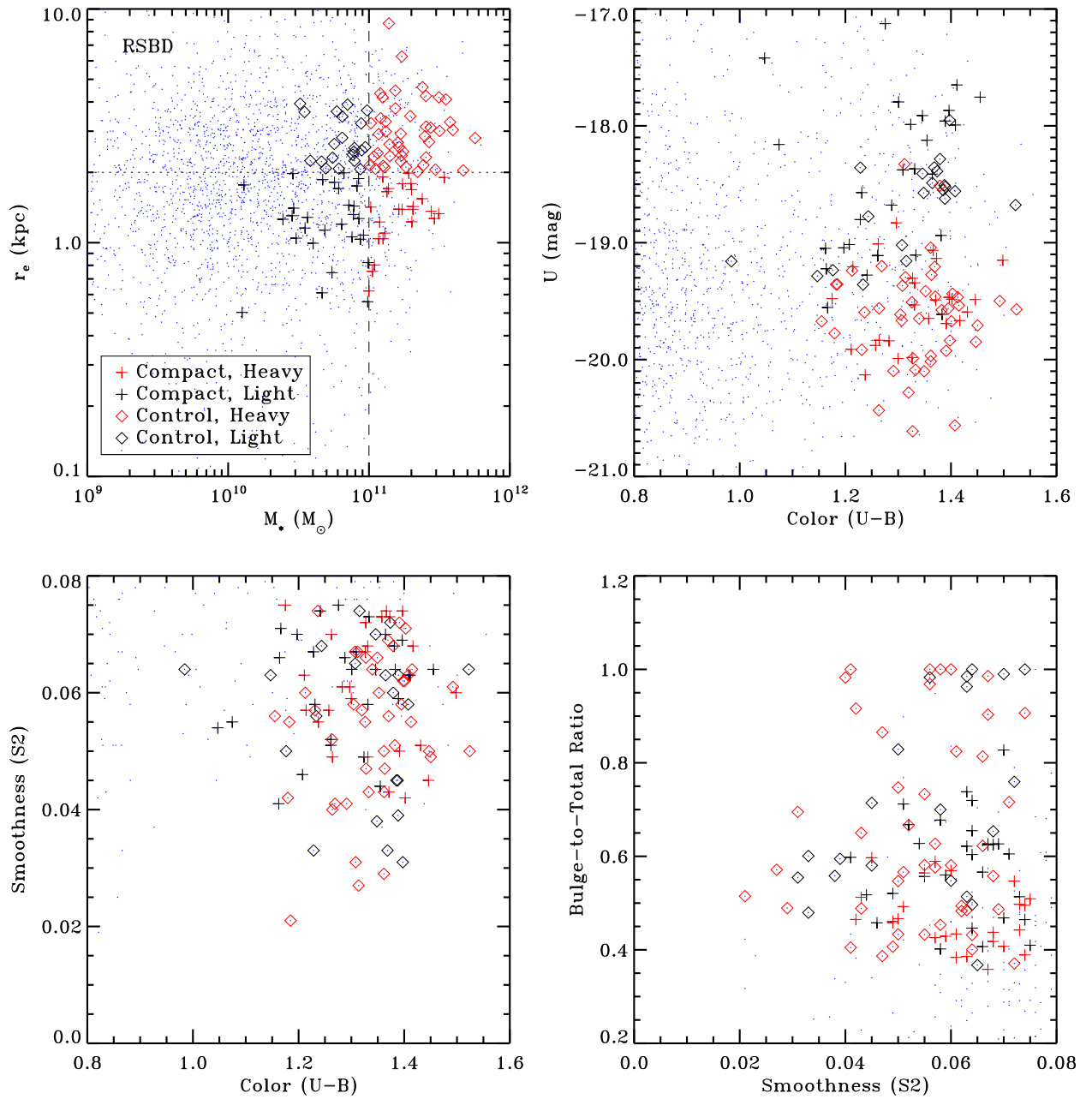


Figure 2.3: The overlap of the “Red, Smooth & Bulge Dominated (RSBD)” samples ($B/T > 0.35$, $S2 < 0.075$, and $U - B > 0.9$) in a mass-radius diagram (top left; dashed line indicates the radius division at $r_e = 2$ kpc, where r_e is I -band half-light radius of the bulge), color-magnitude (top right), color-smoothness (bottom left), and smoothness-B/T (bottom right). Compact galaxies are indicated with crosses, control galaxies are indicated with diamonds. The symbol color indicates whether the galaxy has $M_* > 10^{11} M_\odot$ (red) or $M_* < 10^{11} M_\odot$ (black). The blue dots indicate the whole population of galaxies that we select from (in the bottom panels, many of the points have higher S2 values and/or bluer colors and as such are not displayed with the given axis range).

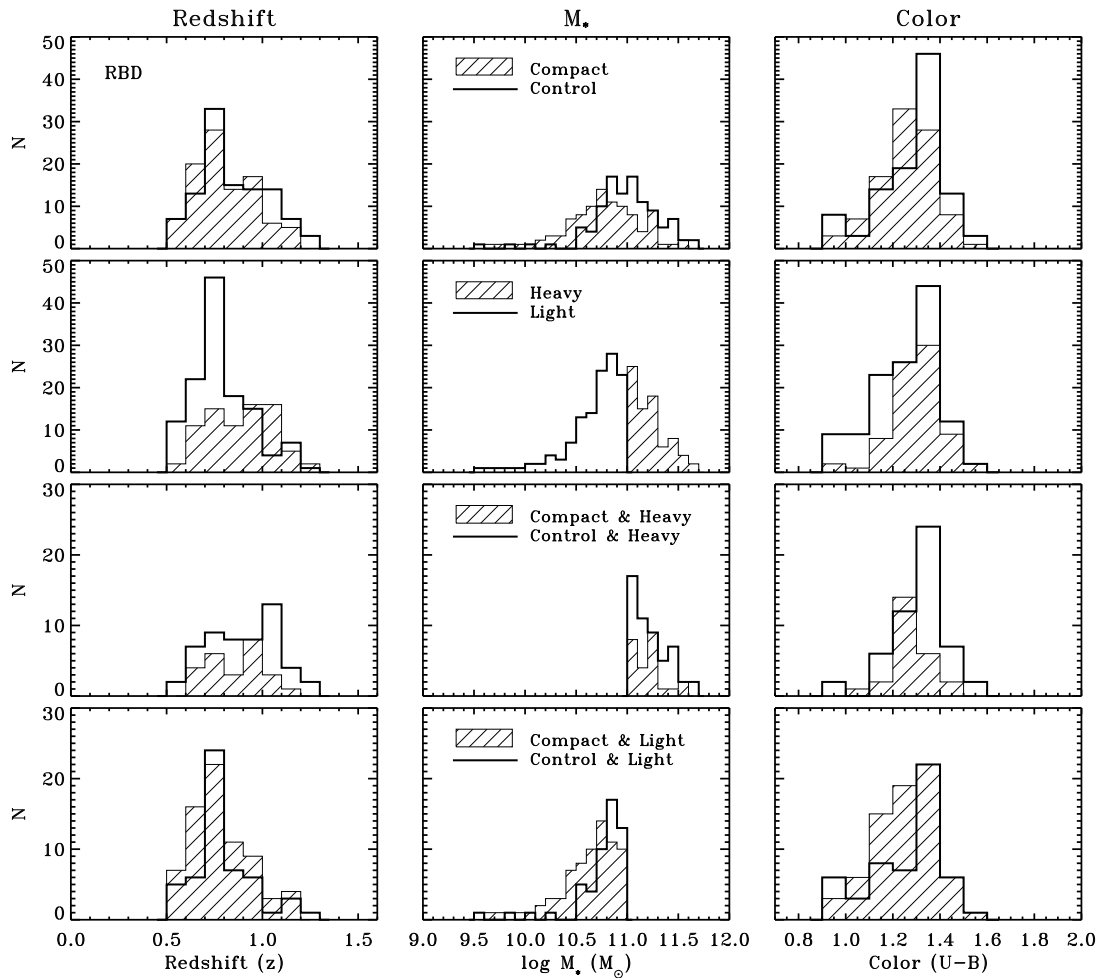


Figure 2.4: Distributions in redshift (first column), stellar mass (second column), and color (third column) for the “Red & Bulge Dominated (RBD) Sample” sample, which implements cuts for $B/T > 0.5$, $U - B > 0.9$. The compact ($r_e < 2$ kpc) and control ($r_e > 2$ kpc) subsamples are shown in the first row, and the heavy ($M_* > 10^{11} M_\odot$) and light ($M_* < 10^{11} M_\odot$) subsamples are show in the second row.

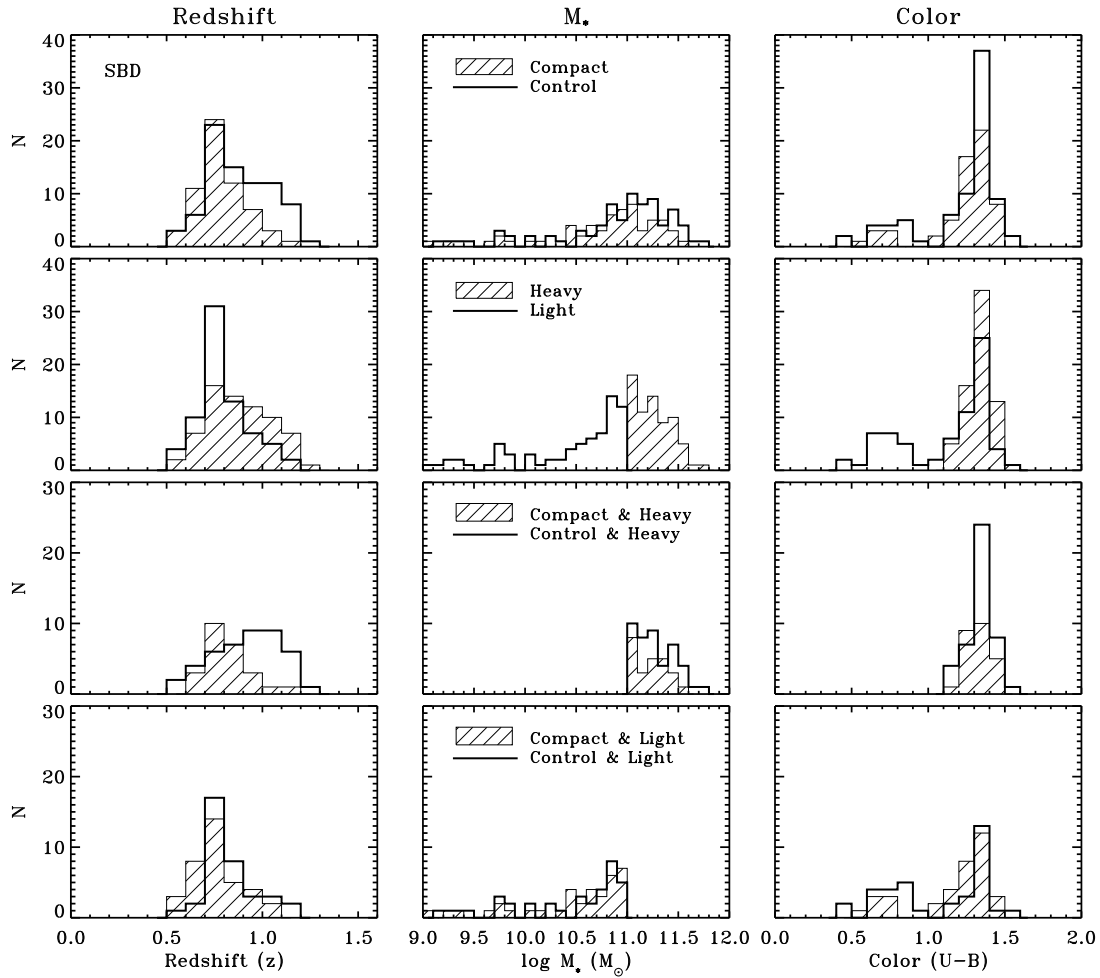


Figure 2.5: Distributions in redshift (first column), stellar mass (second column), and color (third column) for the “Smooth & Bulge Dominated (SBD) Sample”, which implements cuts for $B/T > 0.35$ and $S2 < 0.075$. The compact ($r_e < 2$ kpc) and control ($r_e > 2$ kpc) subsamples are shown in the first row, and the heavy ($M_* > 10^{11} M_\odot$) and light ($M_* < 10^{11} M_\odot$) subsamples are shown in the second row.

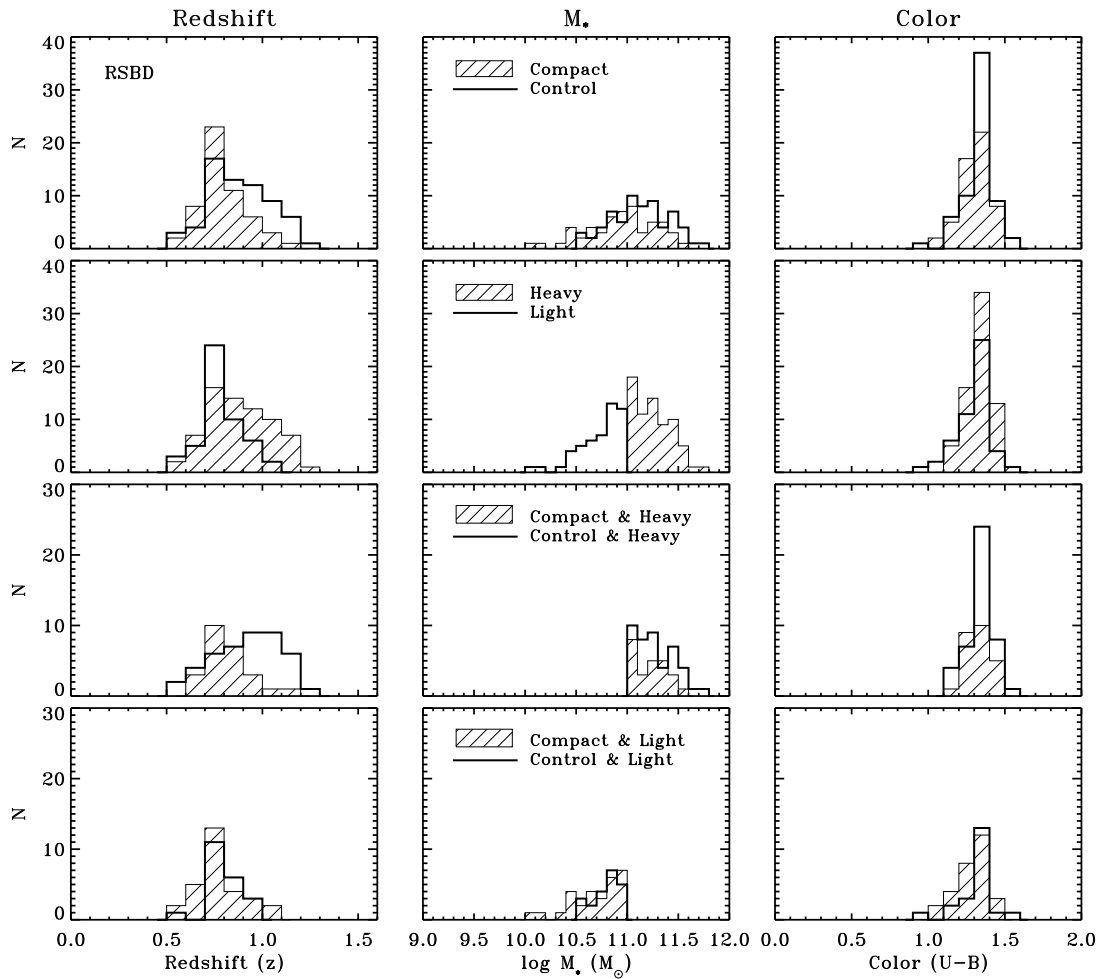


Figure 2.6: Distributions in redshift (first column), stellar mass (second column), and color (third column) for the “Red, Smooth & Bulge Dominated (RSBD) Sample”, which implements cuts for $B/T > 0.35$, $S2 < 0.075$, and $U - B > 0.9$. The compact ($r_e < 2$ kpc) and control ($r_e > 2$ kpc) subsamples are shown in the first row, and the heavy ($M_* > 10^{11} M_\odot$) and light ($M_* < 10^{11} M_\odot$) subsamples are shown in the second row.

Table 2.2 (cont'd)

Sample Name	B/T cut	S2 cut	$U - B$ Cut	Bulge Radius (R_e) cut	Mass cut ($\log M_*$)	# with data at 4130-4160 Å
RSBD, control, heavy	> 0.35	< 0.075	> 0.9	> 2 kpc	> 11	44
RSBD, compact, light	> 0.35	< 0.075	> 0.9	< 2 kpc	< 11	29
RSBD, control, light	> 0.35	< 0.075	> 0.9	> 2 kpc	< 11	21

2.4 Co-Addition of DEEP2 Spectra

Before co-adding, we applied the proprietary flux calibration algorithms, which were kindly provided by Renbin Yan in private communication, to the one-dimensional spectra. The flux calibration is done in two steps. First, the calibration corrects for variations in the quantum efficiency curves of each chip, as well as variations in overall throughput. Next, the spectrum is converted from counts/hr/pixel to erg/s/cm^{-2} . We then converted each spectrum to rest-frame wavelengths and normalized by the mean flux at $4130 < \lambda [\text{\AA}] < 4160$. We chose this normalization range in order to avoid any relevant Lick indices. Spectra which lacked data in the normalization range were excluded from further analysis and did not contribute to the co-addition. The number of galaxies that had data in the normalization range are listed in the last column of Table 2.2. Finally, the spectra were linearly interpolated onto a 0.5 \AA grid.

For each one-dimensional spectrum, there is an associated inverse variance (or noise) spectrum. We normalized the inverse variance spectra by the same factor as the galaxy spectra and interpolated them onto the same grid. The spectra were then co-added, with each pixel \hat{y} weighted according to the inverse variance at that point, as:

$$\hat{y} = \frac{\sum_i y_i / \sigma_i^2}{\sum_i 1 / \sigma_i^2} \quad (2.1)$$

By nature, inverse-variance-weighted co-addition gives a higher weight to brighter objects.

This effect is reflected in the error estimates (see §4.2 and Figures 4.4 and 4.8 in particular for further details and in-depth discussion). However, we note that other stacking methods may yield tighter results. This is explored more in §5.2.

Initial inspection of the co-added spectra revealed apparent contamination of $H\beta$ by the O2 A-band, which falls on the $H\beta$ line for redshifts $z \sim 0.56$. In order to eliminate this (and other) contamination, we masked both the O2 A- and B-bands (7594-7621 Å and 6867-6884 Å respectively) from the rest-frame spectra by setting the inverse variances for those points to zero.

2.5 Systematic Properties of the Samples

Co-addition is susceptible to a number of systematics. In order to understand the systematics of our co-addition, for each point in the co-add we tracked the signal-to-noise spectrum. The signal-to-noise at a given point is defined as:

$$S/N = \frac{f_{co}}{\sigma_{co}} \quad (2.2)$$

where f_{co} is the flux of the co-added spectrum at that point and σ_{co} is the standard deviation of the co-added spectrum at that point:

$$\sigma_{co} = \frac{1}{\sqrt{\sum_i \frac{1}{\sigma_i^2}}} \quad (2.3)$$

We also tracked the mean redshift, the mean stellar mass, and the number of galaxies that contribute to the co-add. Because we are primarily performing differential measurements between our samples, the systematics that co-addition is susceptible to can be minimized by realizing that whichever systematic affects a given co-added sample is similarly affecting the comparative co-added control sample.

Figures 2.7 through 2.17 show the resultant co-added spectra and tracked systematics for the all of the subsamples listed in Table 2.2. The top panels of these figures show the co-added

spectrum of the given subsample of galaxies. All spectra show clear features of older stellar populations, such as the prominent 4000 \AA break. They also feature prominent Balmer lines, which are strongest in the spectra of A-type stars, and indicative of stellar populations that are evolving as a result of a recent burst of star-formation, as well as Ca H- and K-lines, which are strongest in stars cooler than A-types. There are some notable differences in the spectra of the various subsamples: for example, the RBD compact samples (both mass-divided and non-mass-divided) display markedly stronger Balmer lines than the other samples.

Of the non-mass-divided samples, the RBD compact sample also displays the greatest [OIII]-5007 emission. This emission is also particularly strong in the ‘light’ SBD and RSBD samples. [OIII]-5007 is characteristic of active galactic nuclei (AGN) and/or young stellar populations (Kauffmann et al. 2003). We do not have spatially resolved spectra for our sample, but the line fluxes are small. While in principle extended emission line regions could bias our size estimates upward, and weak AGN contamination could bias them downward, at the levels seen in our samples neither effect will be large. The effect of possible emission line infill on our age measurements is investigated in §3.3.

The signal-to-noise is highest where the number of objects contributing to the composite is highest, which occurs typically between $4000 < \text{\AA} < 5000$. In all cases, the Light galaxy spectra are noisier than the Heavy spectra, although this effect is least pronounced in the RBD sample due to the greater number of Light galaxies. For all co-added subsamples, the change in average redshift follows a similar trend, decreasing from $z \sim 1$ to $z \sim 0.6$ from $3500 < \text{\AA} < 5500$. Before subdividing by mass, the Control samples tend to have higher average masses than the Compact samples. Once the samples have been mass-divided, the average mass of the Compact and Control samples show similar trends.

A potential source of systematic error arises from the differences in properties of the samples themselves (for example, if two of the samples we are comparing had wildly different redshift distributions). Returning to Figures 2.4, 2.5, and 2.6, which show the histograms of the distribution in redshift, stellar mass, and color for the subsamples defined in §2.3, we performed

a two-sample Kolmogorov-Smirnov (K-S) test on the each of these pairs of distributions. The K-S test reports a p -value, which is the probability that the two cumulative frequency distributions would be as far apart as they are measured if the two samples were randomly sampled from identical populations. A p -value < 0.05 indicates that the two distributions are likely not drawn from identical distributions. The results of the K-S test for the distribution pairs can be found in Table 2.3. The p -values which are < 0.05 are indicated in bold.

The RBD Compact/Control pair shows a significant difference in stellar mass and color, but not redshift. The opposite is true for the SBD and RSBD Compact/Control pairs: they show a difference in redshift, but not in stellar mass or color. Comparing the Heavy and Light galaxies, the p -values for the stellar mass distributions are very close to zero, as expected because the masses are split at $M_* = 10^{11} M_\odot$. The Heavy/Light comparisons also indicate that the redshift and color distributions tend to different between the Heavy and Light galaxies.

The mass- and radius-divided samples are the most consistent. The RBD Heavy and Compact vs. Heavy and Control samples have no significant differences in redshift, stellar mass, or color. The same is true for the SBD and RSBD Light and Compact vs. Light and Control samples. The SBD/RSBD Heavy and Compact vs. Heavy and Control samples show a difference in the redshift distributions. However, Figure 2.17 shows that once the spectra are co-added, the redshift declines across the wavelength range in a similar fashion.

2.6 Summary

This chapter has detailed the methodology behind our sample selection and our co-adding procedure. We have described the systematics of the co-added spectra and examined some of the differences seen in the resultant co-added spectra of the samples. The following chapter will describe the method we use to characterize the age of the stellar populations in these co-added spectra.

Table 2.3. Kolmogorov-Smirnov results for histogram pairs in Figures 2.4, 2.5, & 2.6

Sample Pair	Redshift <i>p</i> -value	M_* <i>p</i> -value	Color ($U - B$) <i>p</i> -value
RBD Compact/Control	0.409	1.838×10^{-5}	0.00543
RBD Heavy/Light	1.499×10^{-4}	4.204×10^{-43}	0.0204
RBD Heavy & Compact/Heavy & Control	0.356	0.583	0.0676
RBD Light & Compact/Light & Control	0.436	0.00199	0.0658
SBD Compact/Control	0.00419	0.256	0.627
SBD Heavy/Light	0.00396	1.368×10^{-31}	2.945×10^{-5}
SBD Heavy & Compact/Heavy & Control	0.0123*	0.476*	0.835*
SBD Light & Compact/Light & Control	0.102	0.851	0.179
RSBD Compact/Control	0.00514	0.0529	0.161
RSBD Heavy/Light	0.00894	6.89×10^{-26}	0.241
RSBD Heavy & Compact/Heavy & Control	0.0123*	0.476*	0.835*
RSBD Light & Compact/Light & Control	0.319	0.341	0.160

Note. — Bold numbers denote a p -value < 0.05 , which indicates that the distributions being compared are statistically different.

*The SBD and RSBD Heavy samples contain identical galaxies.

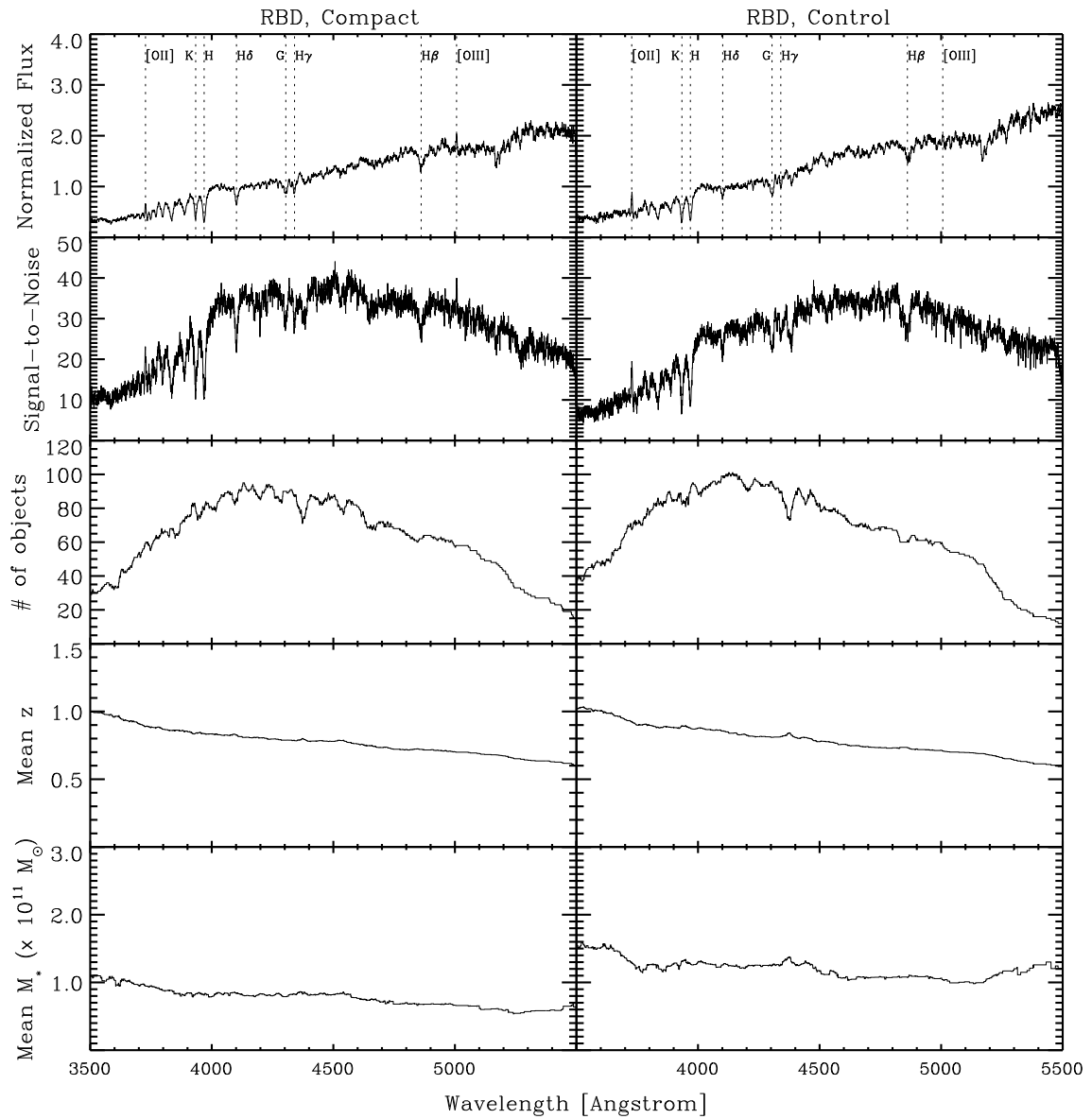


Figure 2.7: The topmost panel shows the co-added spectrum for the compact ($r < 2$ kpc; left column) and control ($r > 2$ kpc; right column) galaxies for our “Red & Bulge Dominated (RBD) Sample” of galaxies (selected by color and bulge-to-total ratio). This sample has not been subdivided by mass. Dotted lines mark the location of spectral features of interest (from left to right: [OII], Ca K and H, H δ , G-band, H β). The panels below display the tracked systematics, including signal-to-noise, the number of objects contributing at each given point in the co-addition, the average redshift, and the average stellar mass.

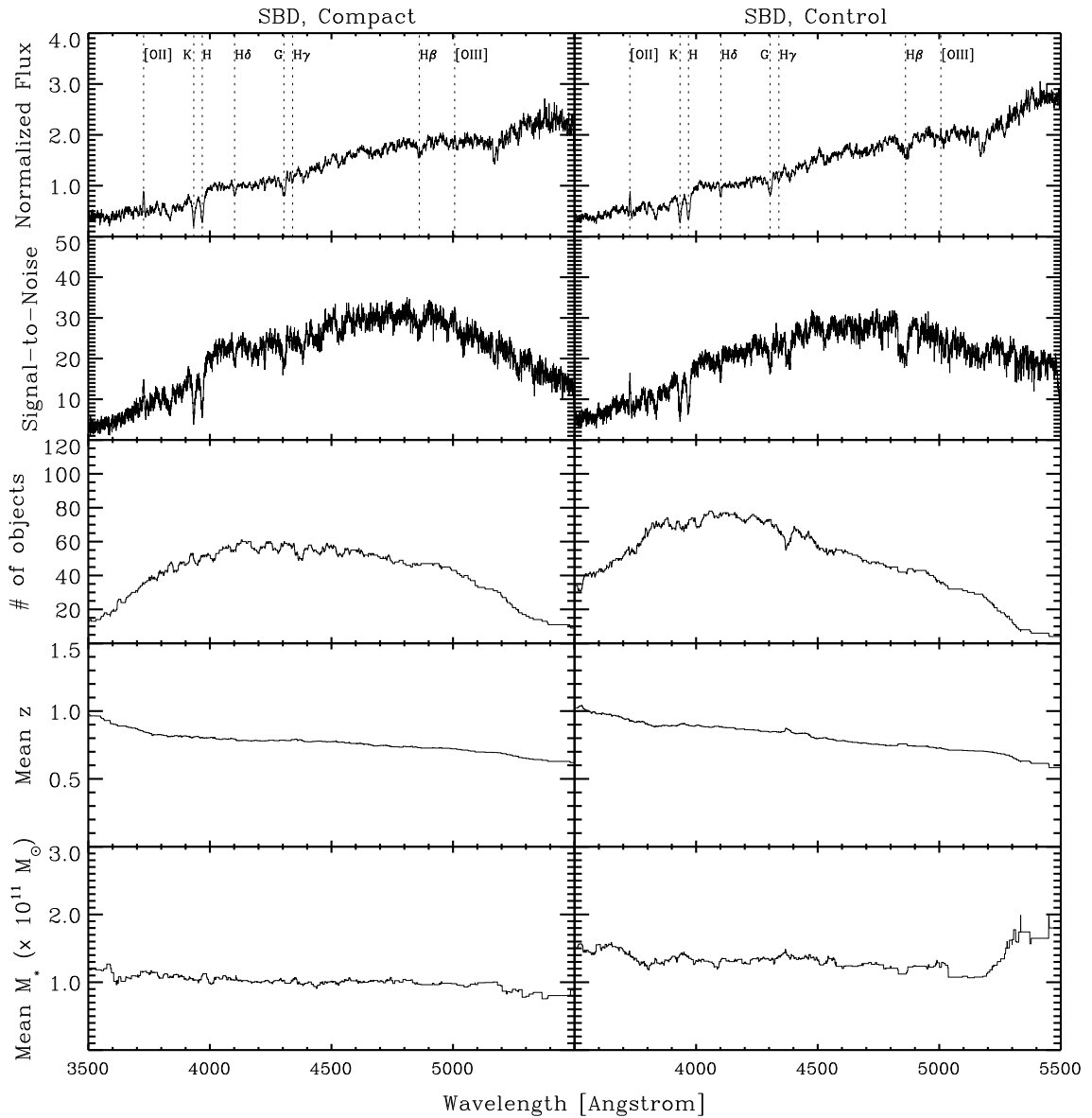


Figure 2.8: The topmost panel shows the co-added spectrum for the compact ($r < 2$ kpc; left column) and control ($r > 2$ kpc; right column) galaxies for our “Smooth & Bulge Dominated (SBD) Sample” of galaxies (selected by image smoothness and bulge-to-total ratio). This sample has not been subdivided by mass. The spectral features (dotted lines) and systematics (lower panels) are tracked as in Figure 2.7.

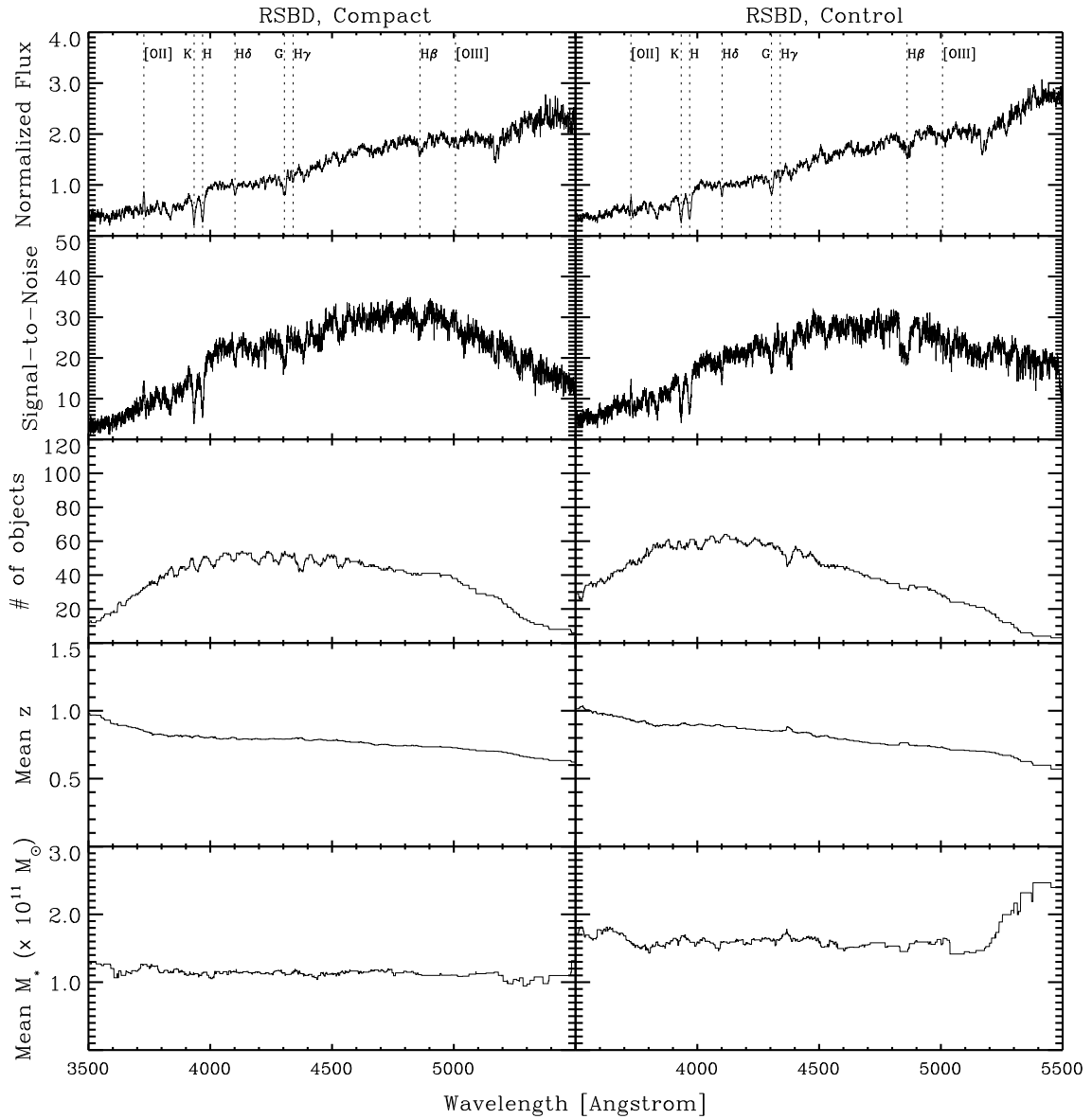


Figure 2.9: The topmost panel shows the co-added spectrum for the compact ($r < 2$ kpc; left column) and control ($r > 2$ kpc; right column) galaxies for our “Red, Smooth & Bulge Dominated (RSBD) Sample” of galaxies (selected by image smoothness, bulge-to-total ratio, and color). This sample has not been subdivided by mass. The spectral features (dotted lines) and systematics (lower panels) are tracked as in Figure 2.7.

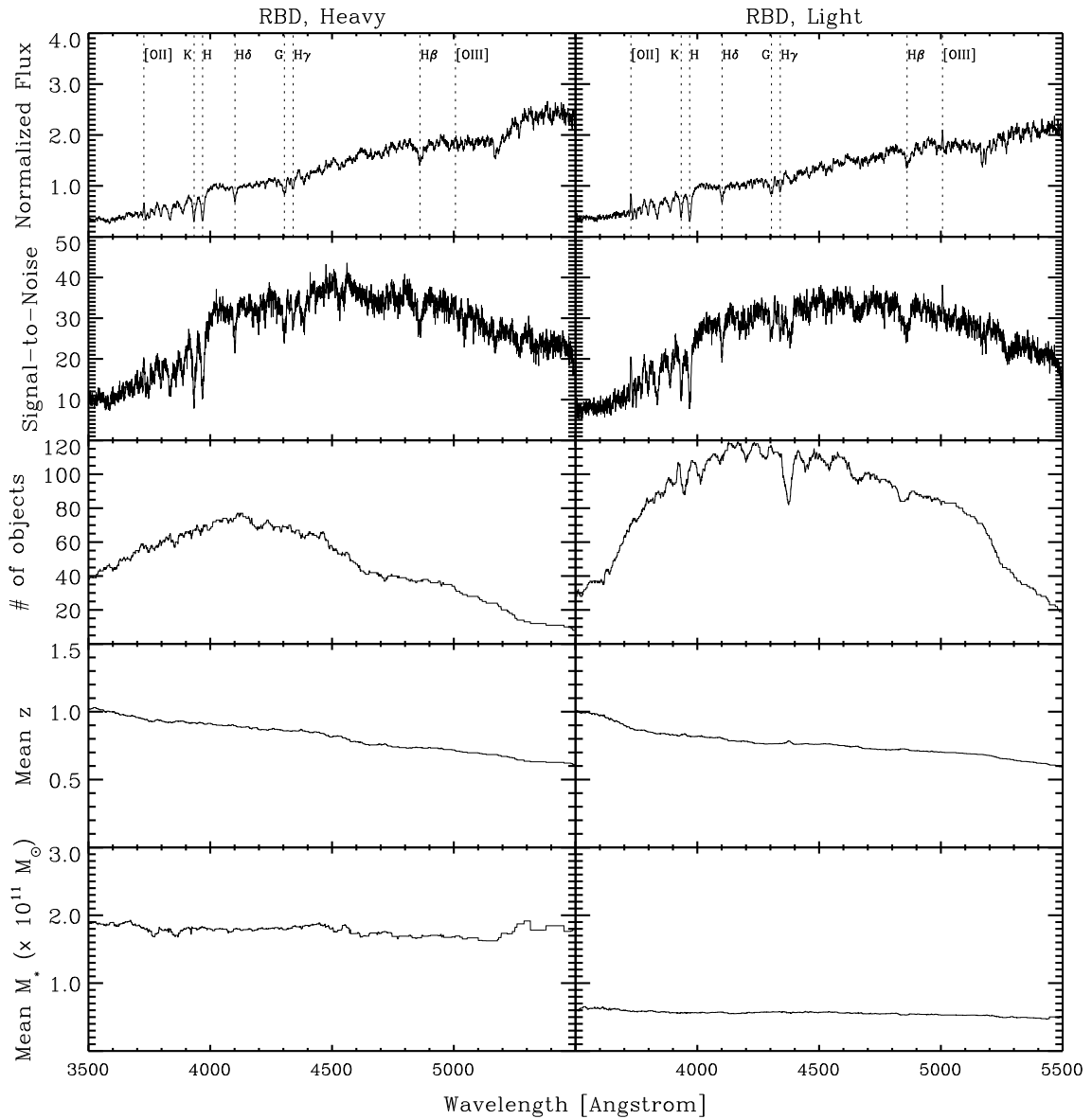


Figure 2.10: The topmost panel shows the co-added spectrum for the heavy ($M_* > 10^{11} M_\odot$; left column) and light ($M_* < 10^{11} M_\odot$; right column) galaxies for our “Red & Bulge Dominated (RBD) Sample” sample of galaxies (selected by color and bulge-to-total ratio). This sample has not been subdivided by size. The spectral features (dotted lines) and systematics (lower panels) are tracked as in Figure 2.7.

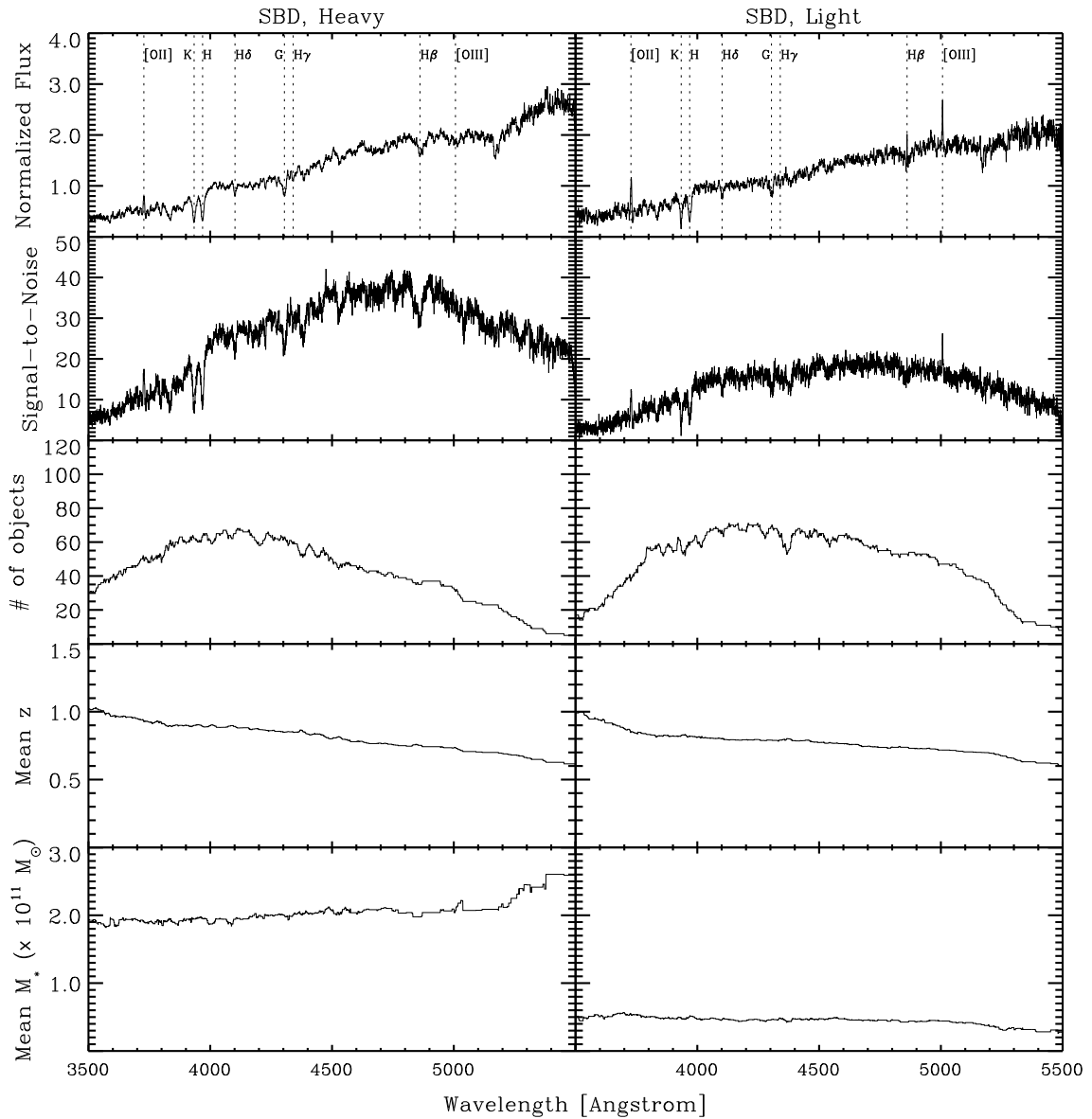


Figure 2.11: The topmost panel shows the co-added spectrum for the heavy ($M_* > 10^{11} M_\odot$; left column) and light ($M_* < 10^{11} M_\odot$; right column) galaxies for our “Smooth & Bulge Dominated (SBD) Sample” sample of galaxies (selected by image smoothness and bulge-to-total ratio). The spectral features (dotted lines) and systematics (lower panels) are tracked as in Figure 2.7.

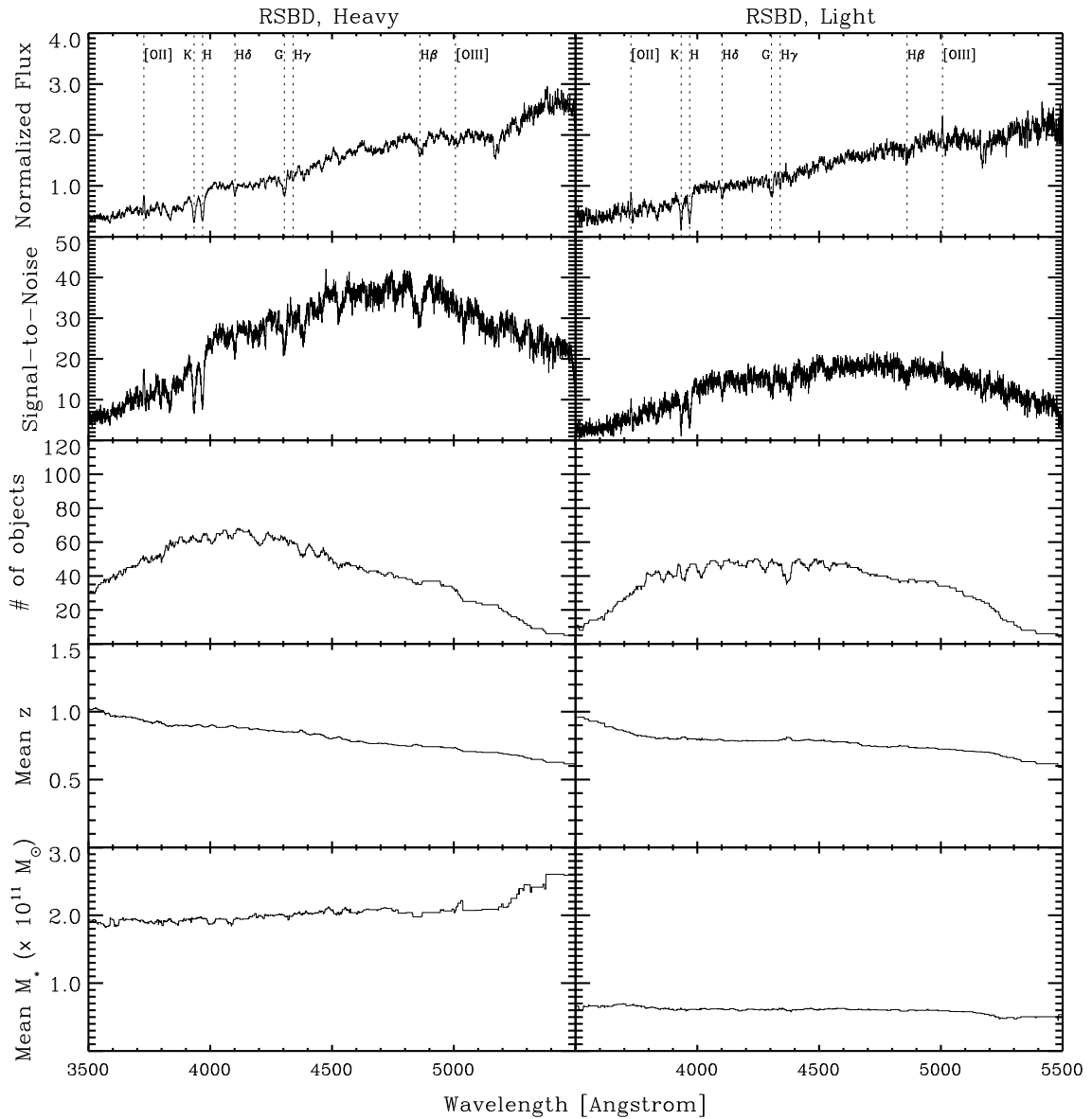


Figure 2.12: The topmost panel shows the co-added spectrum for the heavy ($M_* > 10^{11} M_\odot$; left column) and light ($M_* < 10^{11} M_\odot$; right column) galaxies for our “Red, Smooth & Bulge Dominated (RSBD) Sample” sample of galaxies (selected by image smoothness, bulge-to-total ratio, and color). The spectral features (dotted lines) and systematics (lower panels) are tracked as in Figure 2.7.

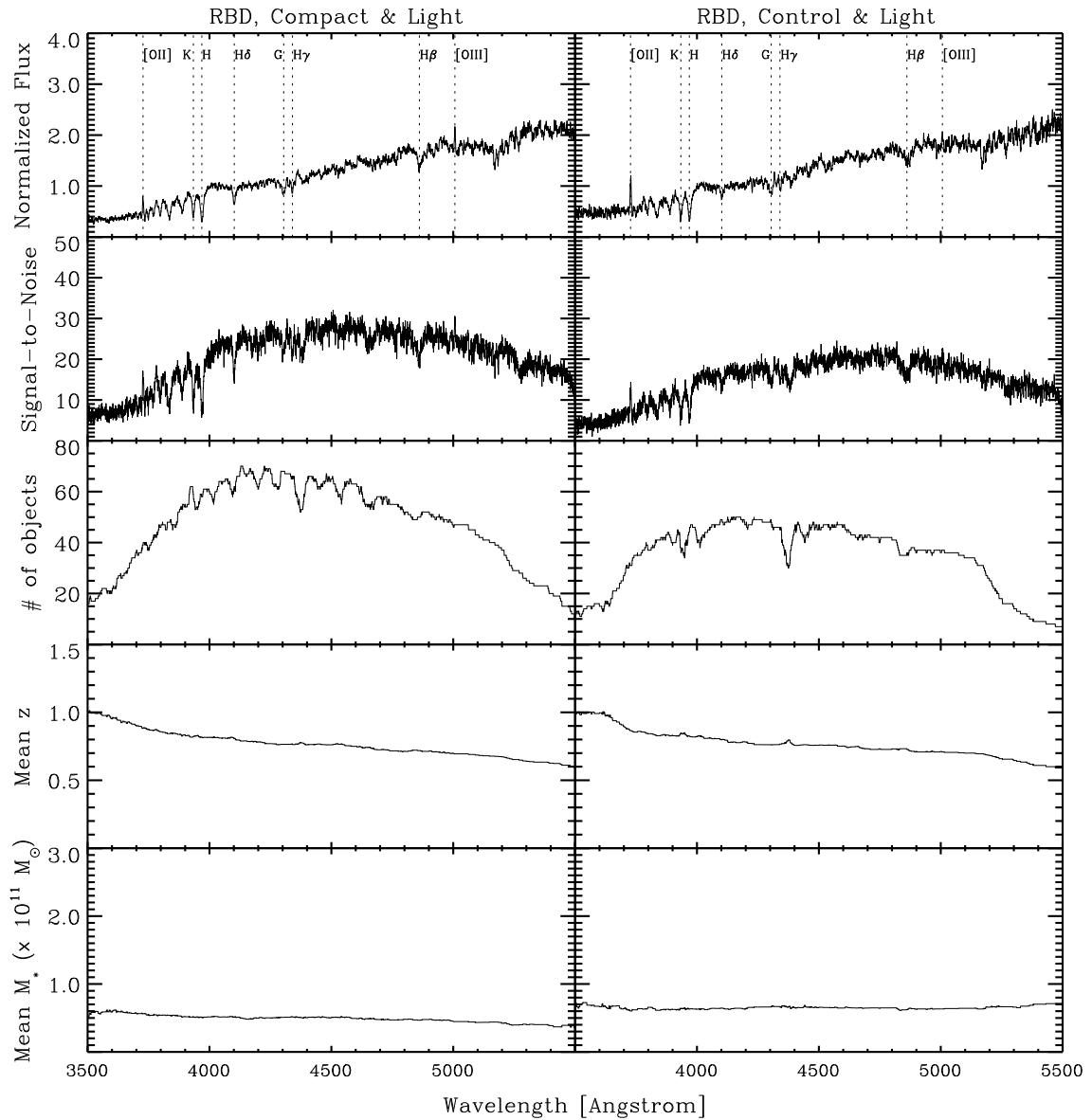


Figure 2.13: The topmost panel shows the co-added spectrum for the light ($M_* < 10^{11} M_\odot$) galaxies in the “Red & Bulge Dominated (RBD) Sample” (selected by color and bulge-to-total ratio), subdivided into compact ($r < 2$ kpc; left column) and control ($r > 2$ kpc; right column) galaxies. The spectral features (dotted lines) and systematics (lower panels) are tracked as in Figure 2.7.

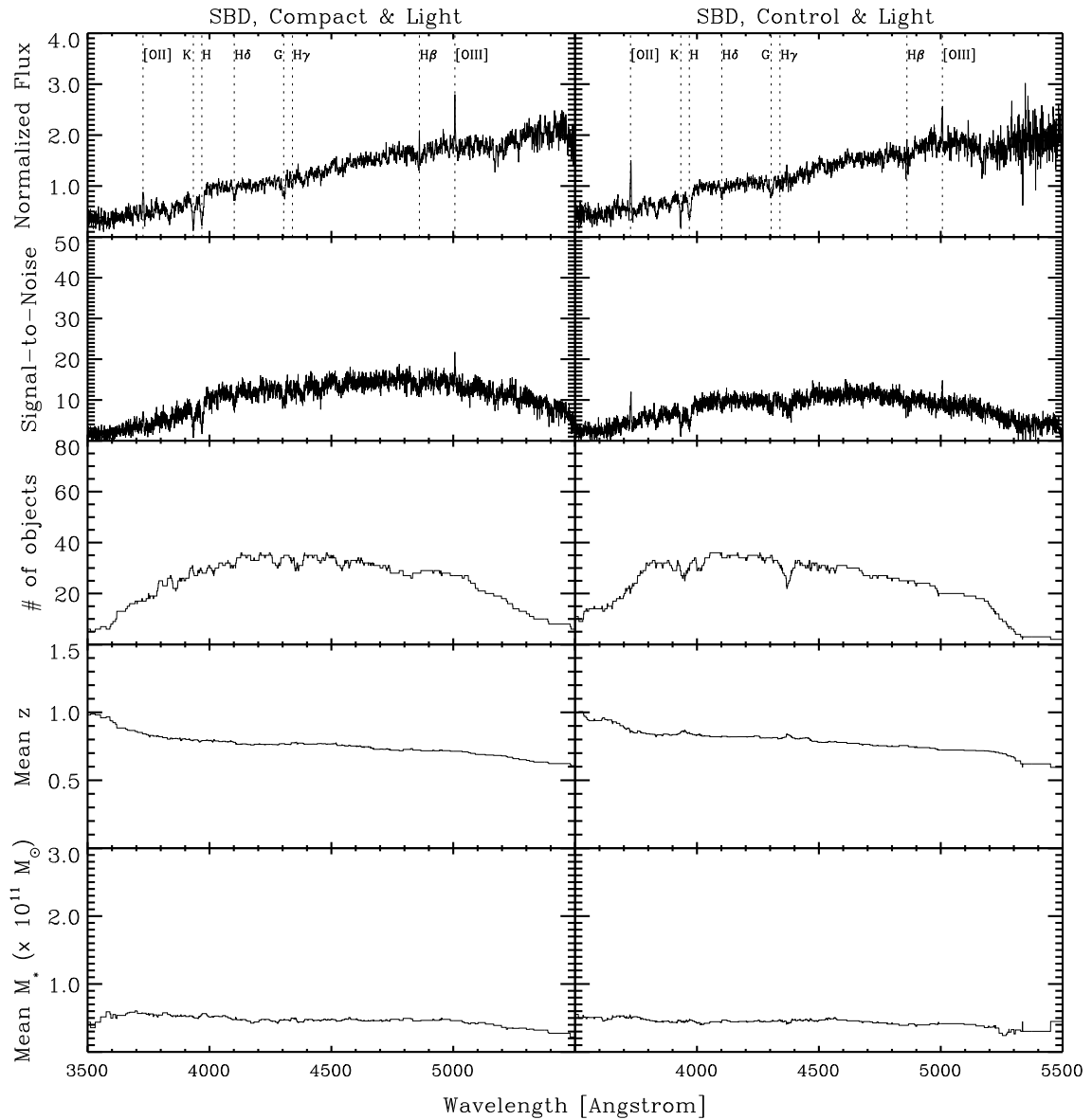


Figure 2.14: The topmost panel shows the co-added spectrum for the light ($M_* < 10^{11} M_\odot$) galaxies in the “Smooth & Bulge Dominated (SBD) Sample” (selected by image smoothness and bulge-to-total ratio), subdivided into compact ($r < 2$ kpc; left column) and control ($r > 2$ kpc; right column) galaxies. The spectral features (dotted lines) and systematics (lower panels) are tracked as in Figure 2.7.

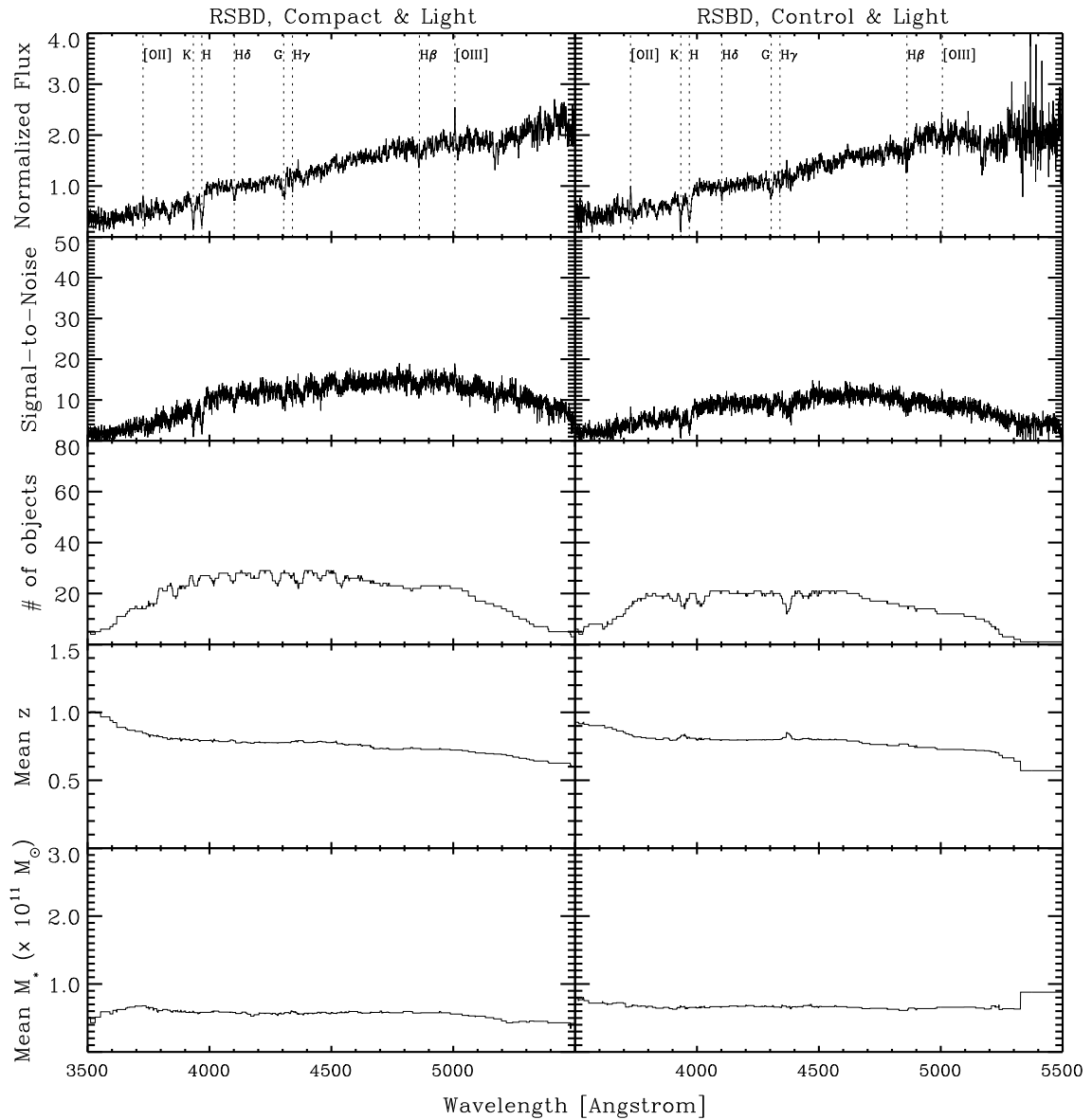


Figure 2.15: The topmost panel shows the co-added spectrum for the light ($M_* < 10^{11} M_\odot$) galaxies in the “Red, Smooth & Bulge Dominated (SBD) Sample” (selected by image smoothness, bulge-to-total ratio, and color), subdivided into compact ($r < 2$ kpc; left column) and control ($r > 2$ kpc; right column) galaxies. The spectral features (dotted lines) and systematics (lower panels) are tracked as in Figure 2.7.

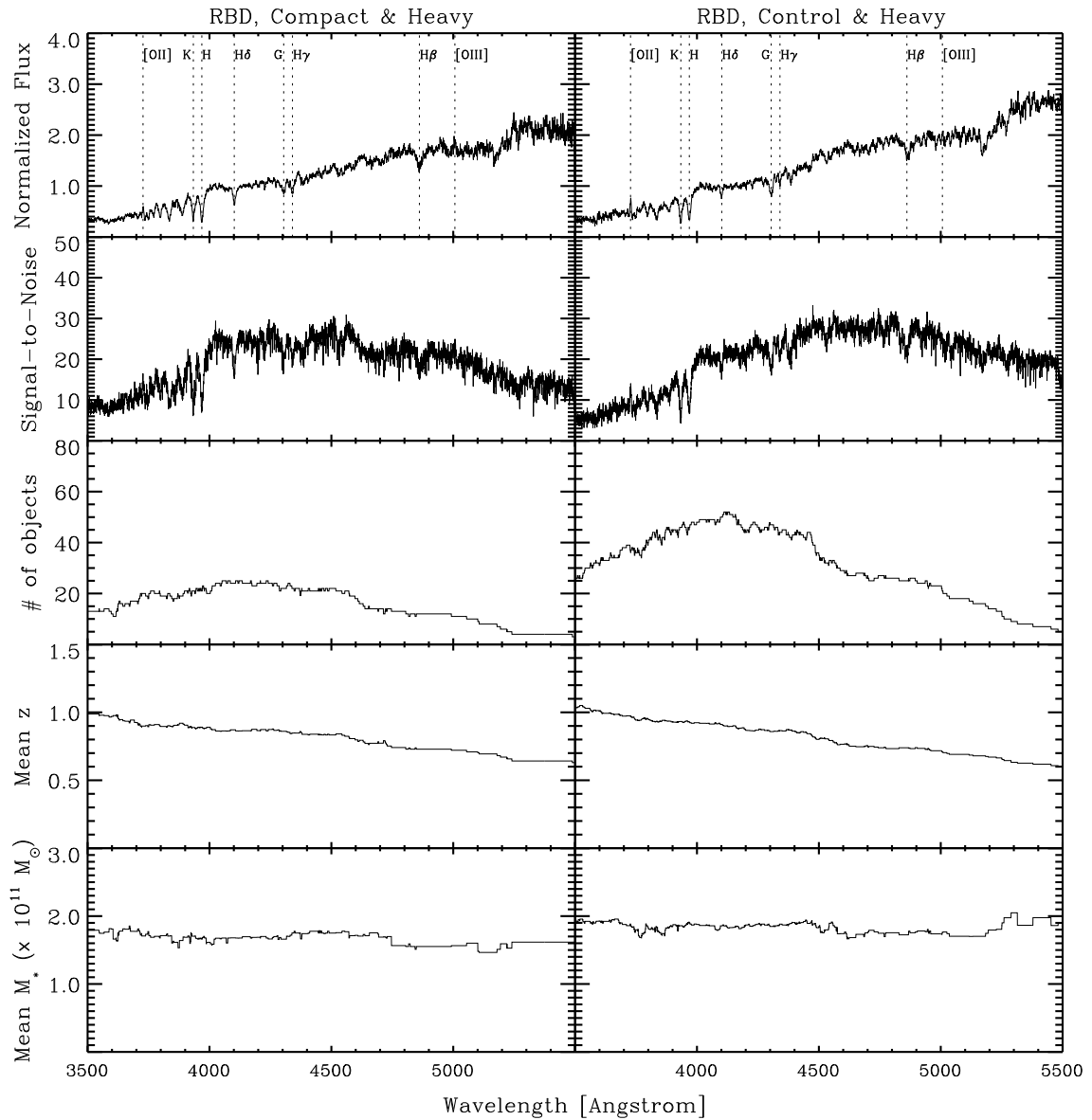


Figure 2.16: The topmost panel shows the co-added spectrum for the heavy ($M_* > 10^{11} M_\odot$) galaxies in the “Red & Bulge Dominated (RBD) Sample” (selected by color and bulge-to-total ratio), subdivided into compact ($r < 2$ kpc; left column) and control ($r > 2$ kpc; right column) galaxies. The spectral features (dotted lines) and systematics (lower panels) are tracked as in Figure 2.7.

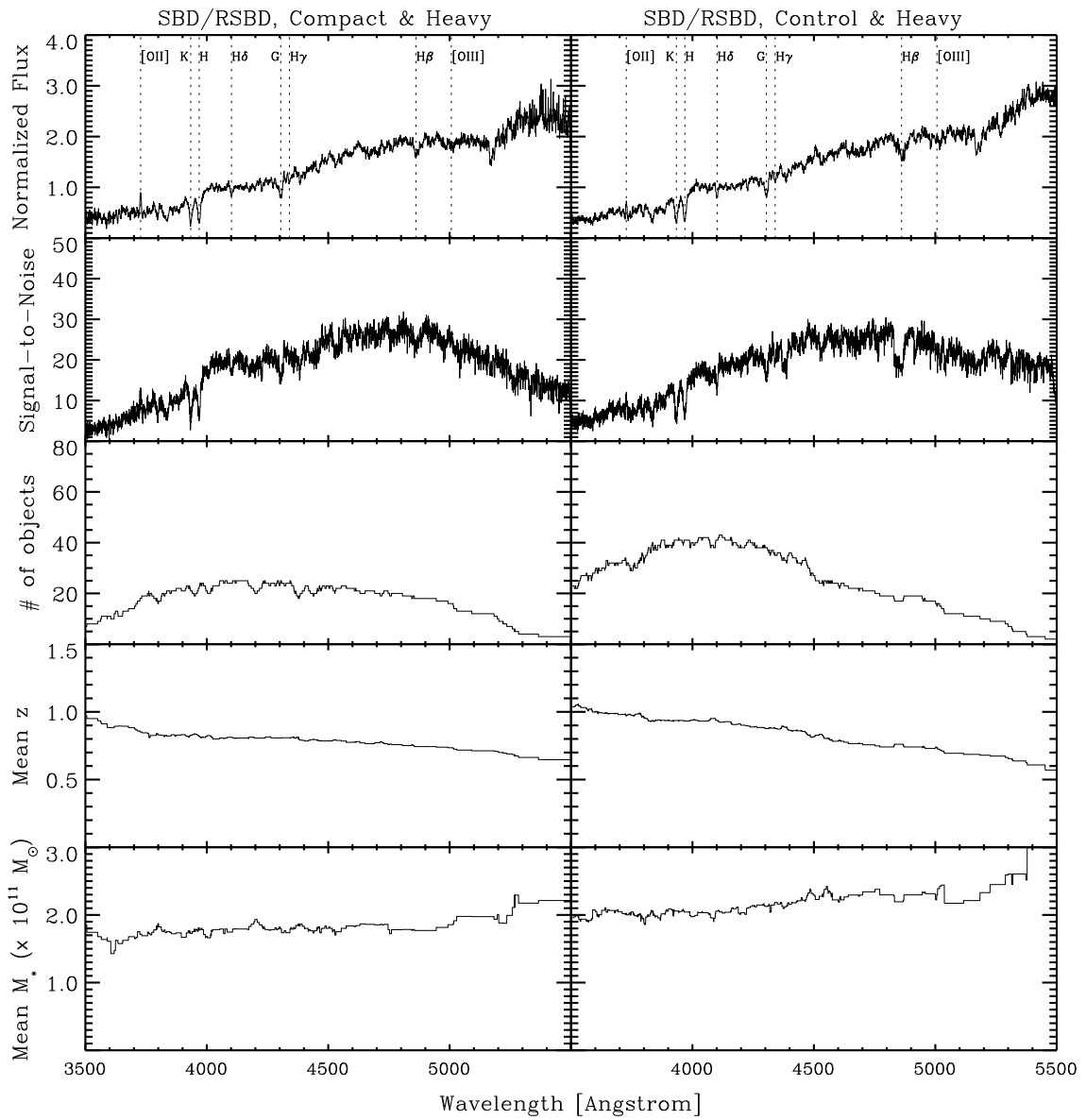


Figure 2.17: The topmost panel shows the co-added spectrum for the heavy ($M_* > 10^{11} M_\odot$) galaxies in the “Smooth & Bulge-Dominated (SBD)” sample (selected by image smoothness and bulge-to-total ratio). Because the addition of the color cut $U - B > 0.9$ removes only the light galaxies from the SBD sample, the heavy RSBD sample (selected by image smoothness, bulge-to-total ratio, and color) is identical to the heavy SBD sample. The galaxies are subdivided by radius into compact ($r < 2$ kpc; left column) and control ($r > 2$ kpc; right column) samples. The spectral features (dotted lines) and systematics (lower panels) are tracked as in Figure 2.7.

Chapter 3

Methodology

3.1 Chapter Overview

In this chapter, we discuss the methodology used for measuring the age of the co-added spectra (§3.2). In §3.3, we examine several potential sources of systematic error on our age measurements. Our method of characterizing the degree of homogeneity of the stellar populations of the co-added spectra is described in §3.4.

3.2 Age Measurements

To measure the light-weighted ages of the co-added spectra, we use the EZ_Ages IDL code package (Graves & Schiavon 2008; Schiavon 2007), which computes the mean, light-weighted stellar population age for unresolved stellar populations, along with $[\text{Fe}/\text{H}]$, and abundance ratios $[\text{Mg}/\text{Fe}]$, $[\text{C}/\text{Fe}]$, $[\text{N}/\text{Fe}]$, and $[\text{Ca}/\text{Fe}]$. For convenience, a brief description of the EZ_Ages algorithm can be found in §1.4.1, but the reader interested in details is referred to Graves & Schiavon (2008) and Schiavon (2007) for an extensive discussion of techniques used to measure light-weighted ages from faint galaxy spectra. In this section, we present the precise methodology and parameters used in our investigations.

First, we measured Lick index line strengths for each co-added spectrum using the automated IDL code `Lick_EW`, available as part of `EZ_Ages`. `Lick_EW` reads in the input spectra along with the associated error spectrum (in our case, the signal-to-noise spectrum). The resolution (in FWHM Angstroms or pixels) and the velocity dispersion of the spectrum must also be specified. We describe how we measure the velocity dispersions of the galaxies in Section 3.2.1.

Next, the main code `EZ_Ages` was used to determine the light-weighted age of each co-added spectrum. (As a reminder, `EZ_Ages` works by taking measured index strengths as input, and compares them to the stellar population synthesis models of Schiavon (2007). If they are provided, `EZ_Ages` uses errors in the Lick index data to estimate the uncertainties in the ages, $[\text{Fe}/\text{H}]$, and abundance ratios. Uncertainties are assumed to be dominated by measurement errors in the line strengths.) In our case, we used the signal-to-noise of each co-added spectrum to determine the errors. The models provide a choice of isochrone: either solar-scale abundances from Girardi et al. (2000) or α -enhanced abundances (average $[\alpha/\text{Fe}] = +0.42$) from Salasnich et al. (2000). However, the models based on the α -enhanced isochrone come with a warning that they are to be used with caution: Weiss et al. (2006) showed that there were problems with the adopted opacity tables which caused the temperatures predicted at the main sequence turnoff and giant branch to be slightly too high. Therefore for all of our age estimations, we use the solar-scale isochrone. Two choices are offered for the IMF exponent: 1.35 (Salpeter) and 0. We use the Salpeter IMF in all our measurements.

For a time, a problem with measuring the ages of early-type galaxies is that the colors and line strengths of most absorption indices change similarly in response to variations of either age or metallicity (Worthey 1994, e.g.). This age-metallicity degeneracy is no longer the dilemma that it once was: Worthey (1994) showed that $\text{H}\beta$ is more sensitive to age than it is to metallicity, and the models were extended toward higher order Balmer lines by Worthey & Ottaviani (1997). `EZ_Ages` uses a Balmer line and an iron line to disentangle the effects of age and metallicity. The default choices for these lines are $\text{H}\beta$ for age-sensitivity and an average of Fe5270 and Fe5335 ($\langle\text{Fe}\rangle$) for $[\text{Fe}/\text{H}]$ sensitivity, although other lines or combinations

of lines can be specified by the user. In Section 3.2.2, we detail how we selected the optimal combination of line indices to ensure accurate age measurements.

3.2.1 Velocity dispersion measurement

The velocity dispersion of the spectrum must be specified when measure the Lick index line strengths in order to correct for the doppler broadening of the lines. To measure the velocity dispersions, we used the cross-correlation method as implemented in the `fv.fxcor` routine in `iraf` (Tonry & Davis 1979). We calculated the cross-correlation function (CCF) between the observed, co-added spectrum and a template spectrum of a single stellar population calculated for solar metallicity and age 2.0 Gyr (from the Schiavon (2007) library of synthetic single stellar population spectra). The width of this CCF is sensitive to the widths of the absorption lines in the target spectrum (which are broadened by the velocity dispersion). This sensitivity was used to estimate the velocity dispersion of the target (e.g. Schiavon et al. 2006). The template was convolved with a range of velocity dispersion values to create a library of sigma-broadened spectra, each of which was then cross-correlated with the original template spectrum. We calculated the full width at half maximum (FWHM) of the CCF peaks and used this to determine the relationship between the FWHM and the velocity dispersion used to broaden the original template spectrum.

Next, we determined the CCF between co-added spectrum and the template spectrum, and the FWHM of this CCF peak was measured. We input this FWHM into the relation derived from the sigma-broadened spectra in order to obtain the velocity dispersion of the co-added spectrum. The resulting velocity dispersions are listed in Table 3.1.

3.2.2 Determining the optimal fitting indices

The full set of Lick indices is not always available in a given set of data. For example, the redshift of a sample may cause some of the lines to be shifted off of the detector, or some instruments may be limited in their observable wavelength range. Fortunately, `EZ_Ages` was

Table 3.1. Sample Velocity Dispersions

Sample Name	σ (km s ⁻¹)
RBD, Compact	226
RBD, Control	278
RBD, Heavy	290
RBD, Light	227
RBD, Compact, Heavy	289
RBD, Control, Heavy	297
RBD, Compact, Light	215
RBD, Control, Light	219
SBD, Compact	265
SBD, Control	311
SBD, Heavy*	296
SBD, Light	176
SBD, Compact, Heavy**	299
SBD, Control, Heavy***	301
SBD, Compact, Light	154
SBD, Control, Light	211
RSBD, Compact	283
RSBD, Control	305
RSBD, Heavy*	296
RSBD, Light	175
RSBD, Compact, Heavy**	299
RSBD, Control, Heavy***	301
RSBD, Compact, Light	175
RSBD, Control, Light	182

*The SBD, Heavy and the RSBD, Heavy samples contain identical galaxies.

**The SBD, Compact, Heavy and the RSBD, Compact, Heavy samples contain identical galaxies.

***The SBD, Control, Heavy and the RSBD, Control, Heavy samples contain identical galaxies.

designed with the option of using multiple, different combinations of Lick indices to fit for the fiducial age and $[\text{Fe}/\text{H}]$ in order to take these or other possible limitations into account. Using EZ_Ages, Graves & Schiavon (2008) derived ages and metal abundances for clusters NGC 6441 and M67 using several different index combinations. They compared the results obtained from each index combination to the results obtained from the other index combinations and to the values from the literature, when available. They found that the majority of index combinations gave ages and abundances that varied by less than ± 0.1 dex.

In this thesis, our primary concern was to ensure the most accurate age determination. To supplement the results from Graves & Schiavon (2008), we constructed a synthetic galaxy spectrum with a simple stellar population of solar metallicity using the GALAXEV code from Bruzual & Charlot (2003). We tested several combinations of Lick indices with EZ_Ages to fit the age of the galaxy at 0.5, 1, 2, 3, 5, and 7 Gyrs. A list of the combinations of weights that were tested are outlined in Table 3.2. We limited the indices that we varied to Balmer and iron lines because these lines are the ones that most affect the measurement of the galaxy's age.

We then compared the ages calculated from EZ_Ages to the true ages of the ideal synthetic spectra. Figures 3.1 and 3.2 show the percent error results for each different index combination in Table 3.2. Each figure shows the percent error in the age fit by EZ_Ages using each individual Balmer line on its own as well as the specific combination of Balmer lines chosen for that combination. We chose the index combination that gave the least average percent error for the Balmer combination as well as the fewest number of dropped fits (EZ_Ages will return a null value for the age if it falls completely off the model grids). The index combination that met these criteria was #7, which consisted of a combination of $H\beta$, $H\gamma_F$, $H\delta_F$ for the Balmer lines and an average of Fe5270 and Fe5335 for the iron lines. We used this set of lines to fit for the age for the rest of our analyses. Table 3.3 lists the age as measured by EZ_Ages and the percent difference from the true age of the simple stellar population for our chosen set of line indices.

Table 3.2. Index Combinations Tested for EZ_Ages Fitting

Index Combination	Balmer Lines	Iron Lines
1	$H\beta$	Fe5270, Fe5335
2	$H\beta, H\gamma_F, H\gamma_A, H\delta_F, H\delta_A$	Fe5270, Fe5335
3	$H\beta$	Fe4383
4	$H\beta, H\gamma_F, H\delta_F$	Fe4383
5	$H\beta, H\gamma_A, H\delta_A$	Fe4383
6	$H\gamma_A, H\delta_A$	Fe4383
7	$H\beta, H\gamma_F, H\delta_F$	Fe5270, Fe5335
8	$H\beta, H\gamma_F, H\delta_F$	Fe4383, Fe5015
9	$H\beta, H\gamma_F, H\delta_F$	Fe4383, Fe5015, Fe5270, Fe5335
10	$H\gamma_F$	Fe5270, Fe5335
11	$H\delta_F$	Fe5270, Fe5335
12	$H\beta, H\gamma_F, H\delta_F$	Fe4383, Fe5270, Fe5335
13	$H\beta, H\delta_A$	Fe4383, Fe5270, Fe5335
14	$H\beta, H\delta_A$	Fe4383
15	$H\delta_A$	Fe4383
16	$H\beta, H\gamma_F, H\gamma_A, H\delta_F, H\delta_A$	Fe4383, Fe5015, Fe5270, Fe5335

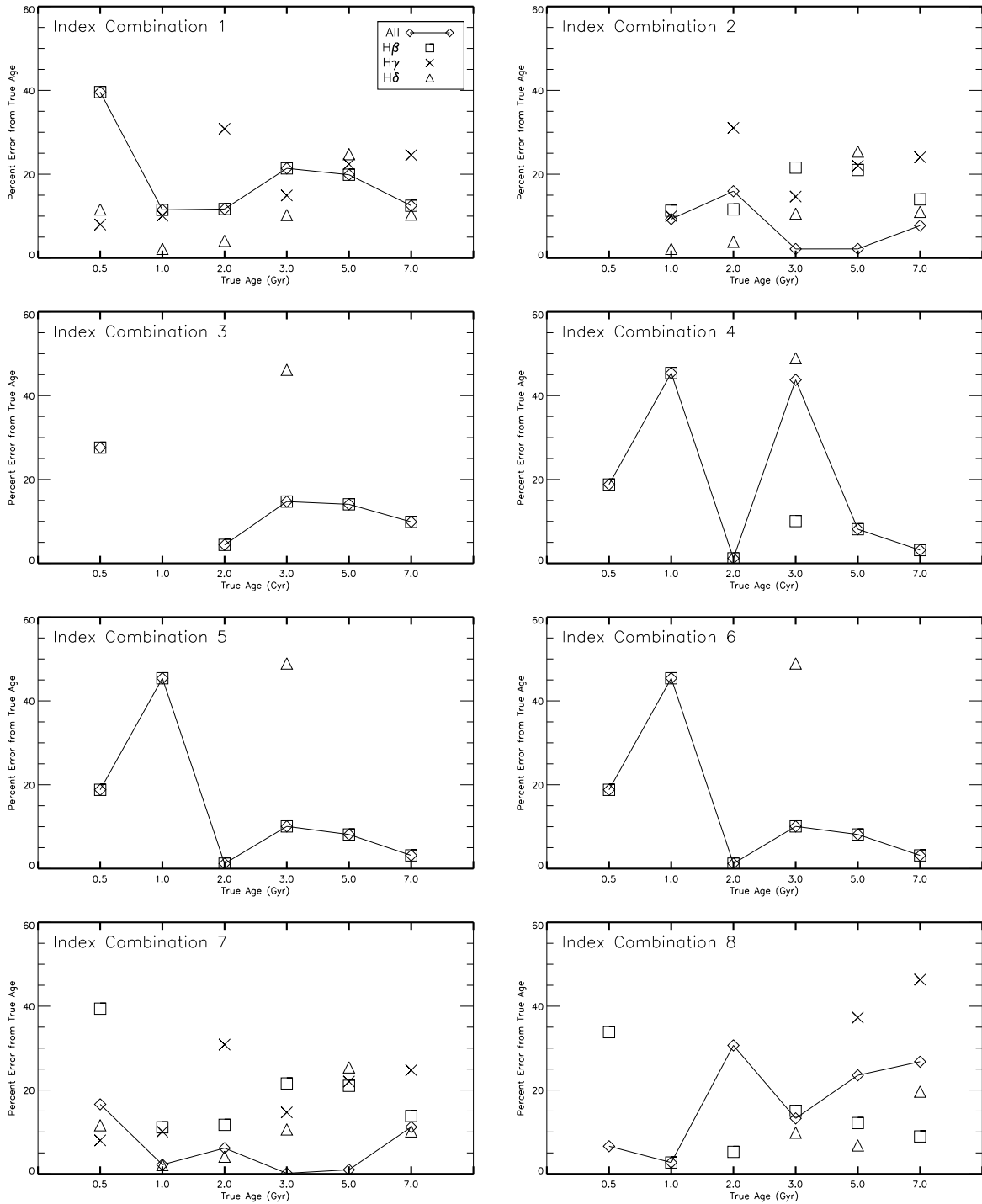


Figure 3.1: Each panel shows the percent error for a different combination of indices used to fit the age of a simple stellar population at various ages (0.5, 1.0, 2.0, 3.0, 5.0, and 7.0 Gyr). The specific indices for each combination are listed in Table 3.2. The symbols indicate the age and subsequent error on the age fit using all of the Balmer indices in a given combination (diamond symbol connected by solid line) and for each individual Balmer index alone ($H\beta$, square; $H\gamma$, cross; and $H\delta$, triangle).

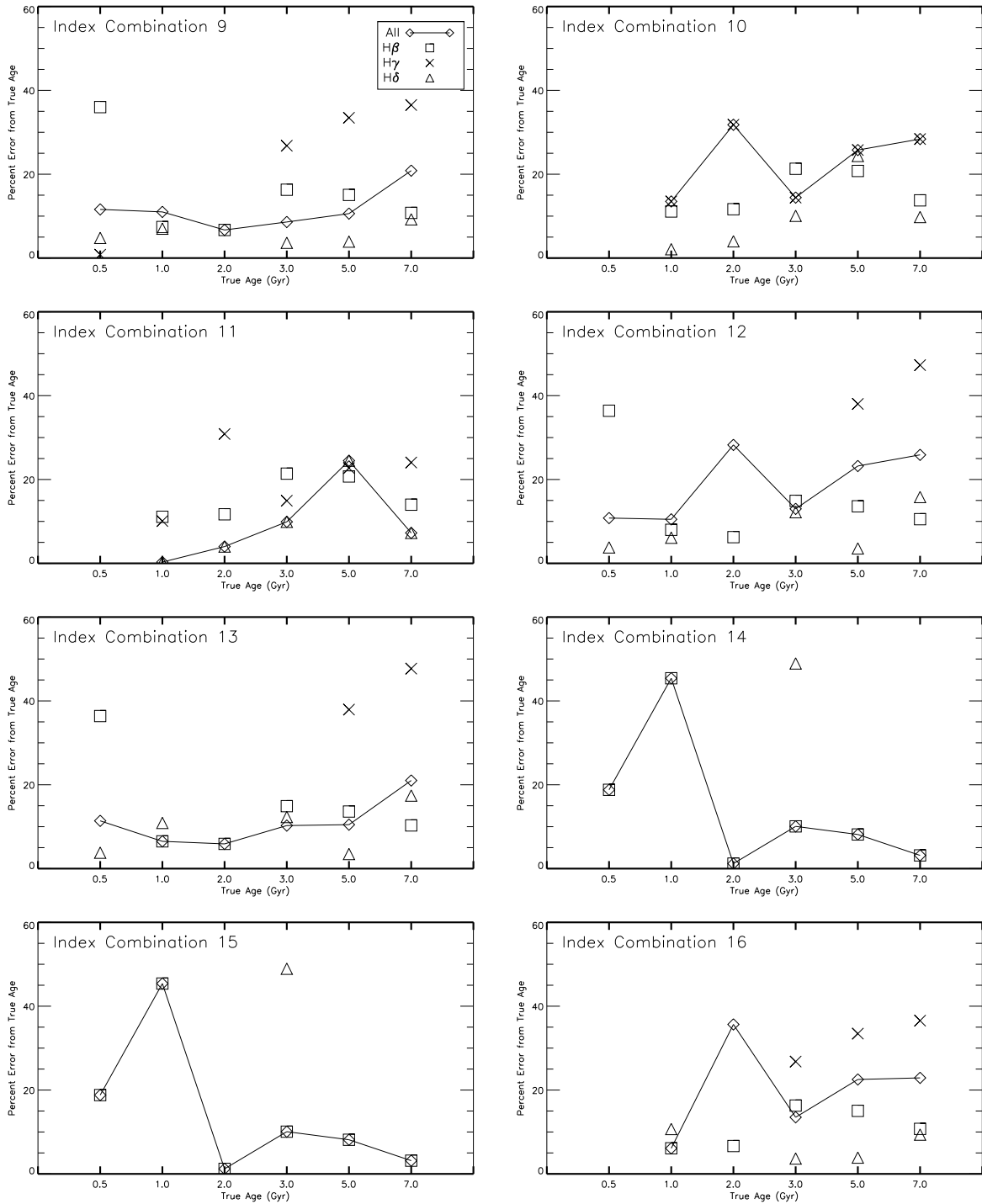


Figure 3.2: A continuation of the previous figure. Each panel shows the percent error for a different combination of indices used to fit the age of a simple stellar population at various ages (0.5, 1.0, 2.0, 3.0, 5.0, and 7.0 Gyr). The specific indices for each combination are listed in Table 3.2. The symbols indicate the age and subsequent error on the age fit using all of the Balmer indices in a given combination (diamond symbol connected by solid line) and for each individual Balmer index alone ($H\beta$, square; $H\gamma$, cross; and $H\delta$, triangle).

Table 3.3. Percent Error for EZ_Ages Indices

SSP Age (Gyr)	Age from EZ_Ages (Gyr)	% Error
0.5	0.58	16.6
1.0	0.98	2.2
2.0	1.88	6.2
3.0	2.99	0.1
5.0	5.05	1.0
7.0	6.21	11.2

Note. — The percent differences are indicative of the achieved accuracy in the ideal case of an SSP.

3.3 Systematic errors on the age measurements

We investigated two potential sources of systematic error on our age measurements: the use of a single template to measure the velocity dispersions and emission line infill of Balmer lines. In principle, neither effect should be large: for one, convolution with a velocity dispersion is a second-order effect on measurements of equivalent width. Next, emission line infill should be small for quiescent galaxies. Furthermore, the relatively weak [OII] emission in the spectra does not necessarily indicate star formation. The ratio between [OII] and $H\beta$ is similar to that seen in low-ionization nuclear emission-line regions (LINERs) or other LINER-like galaxies (Yan et al. 2006; Yan & Blanton 2012). The [OII] emission seen here is likely similar to the extended emission-line region commonly seen by IFU surveys such as SAURON and ATLAS3D in a large fraction of nearby early-type galaxies (Sarzi et al. 2010). Such regions are likely produced by photoionization from old but hot stars, such as post-AGB stars, rather than by star formation. Although we did not expect these potential systematic errors to significantly affect our results,

we believed this was worth verifying.

The effect of template mismatch (and/or velocity dispersion uncertainties) was estimated by altering the measured velocity dispersions by $\pm 10\%$ and $\pm 20\%$ and noting the resulting changes in the ages returned by EZ_Ages. These changes are listed in Table 3.4, and Figures 3.3 through 3.8 show how the change in velocity dispersion affects the samples on an index-index grid of three different Balmer lines and $\langle \text{Fe} \rangle$.

In the RBD samples, the measured ages differed from the nominally measured “true” age by at most 0.67 Gyr, with most differing by ~ 0.2 Gyr. These small differences do not significantly change our conclusions. In the SBD and RSBD samples, the velocity dispersion appeared to have a slightly more exaggerated effect: the measured ages tended to vary by $\sim 1 - 1.5$ Gyr for the more extreme changes to the velocity dispersion ($\pm 20\%$). The most extreme cases included the SBD/RSBD Compact & Heavy sample, where the samples fell off the model grids when the velocity dispersion was reduced by either 10 or 20% (a clear sign that the velocity dispersions were too low). On the other hand, when the SBD/RSBD Compact & Heavy velocity dispersion was increased, the measured ages become older by ~ 1 Gyr, which makes the conclusions described later in §4.2.3 even stronger. Similarly, the RSBD Control & Light sample fell off the model grids when the velocity dispersion was increased by 10 or 20%. Finally, the SBD Control & Light sample, had the largest difference in measured ages at 2 Gyr older than the “true” age when the velocity dispersion was decreased by 20%. This result foreshadows a conclusion that we reach in §4.3: that the “light” subsamples are composed of galaxies with signal-to-noise ratios that are substantially lower than those in the “heavy” subsamples.

We note that in general, a higher velocity dispersion results in younger inferred ages, but the opposite is true for the SBD/RSBD Compact & Heavy sample. The reason for this is evident in Figures 3.6 or 3.8: at the measured velocity dispersion, the SBD/RSBD Compact & Heavy sample is barely on the $H\beta$ vs. $\langle \text{Fe} \rangle$ grid, and is not on the grids of $H\gamma_F$ or $H\delta_F$ at all. When the velocity dispersion is increased (the lightest symbols), the SBD/RSBD Compact & Heavy sample falls on the model with age 7 Gyr for the $H\beta$ and the model with age 10 Gyr for $H\delta_F$.

Since EZ_Ages is weighted to take the average of the Balmer features, the resultant age is therefore older. The comparative SBD/RSBD Control & Heavy sample was better behaved, with a change of ~ 0.4 Gyr for $\sigma \pm 10\%$ and a maximum change of $+1.14$ Gyr for -20% . Our overall conclusion is that template mismatch/velocity dispersion uncertainties are unlikely to significantly impact our conclusions, given the relatively small differences in measured ages for the majority of our samples.

The amount of emission line infill of the Balmer absorption features was characterized by fitting stellar population models to the continua of the co-added spectra using routines adapted from SDSS analysis outlined in Brinchmann et al. (2004); Tremonti et al. (2004). A library of template spectra was generated using Bruzual & Charlot (2003) stellar population synthesis code (BC03). The templates were composed of single stellar population models of 10 different ages (0.005, 0.025, 0.1, 0.2, 0.6, 0.9, 1.4, 2.5, 5.0, and 10.0 Gyr) and three different metallicities (20%, 100%, and 250% Z_{\odot}). The templates were convolved to the appropriate measured velocity dispersion of each co-added sample and re-sampled to match the data, and then a nonnegative least-squares fit was performed to construct the best-fitting model. Once the best-fitting stellar population has been subtracted from the continuum, any remaining residuals were removed, and the nebular features were fit. We then used the infill-corrected Balmer equivalent widths and measured the resulting changes in the ages returned by EZ_Ages. These changes, along with the equivalent widths of the nebular features (negative values indicate emission features), are listed in Table 3.5. This procedure was done with the aid of Jarle Brinchmann, who performed the fitting routines. We performed this procedure only on the subsamples that we detail in Keating et al. (2015), namely the RBD and SBD/RSBD Heavy Compact and Control subsamples (in §4.3, we explain that we removed the “light” galaxies from our analysis in order to keep only the galaxies with the highest signal-to-noise).

The RBD sample ages change by < 0.03 Gyr. The largest change shown is in the RSBD Control & Heavy sample, which gets older by 0.68 Gyr. The RSBD Compact & Heavy sample falls off the model grids and therefore does not have an age estimate. An inspection Figure 3.8

which shows the index-index plot of $\langle \text{Fe} \rangle$ vs. $H\beta$ for this sample reveals that it is just barely outside of the grid boundaries, and lies closest to the models with an ages between 7-10 Gyr. This is consistent with the measured age of the original (non-infill-corrected) sample. Given these small changes, our conclusion is that the amount of infill does not vary enough across our samples to significantly impact the differences between our age measurements.

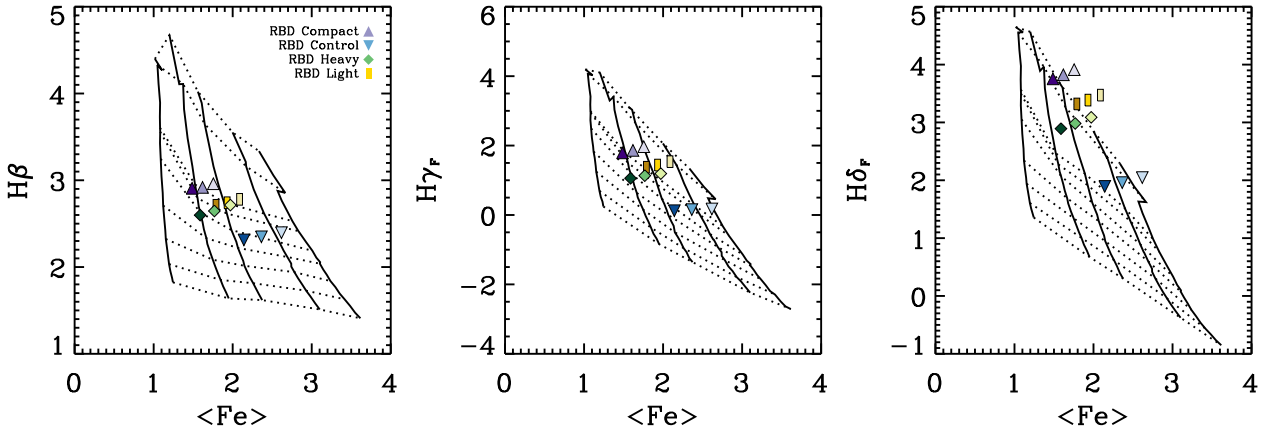


Figure 3.3: Index-index model grids of $H\beta$ and $\langle \text{Fe} \rangle$ (left), $H\gamma_F$ and $\langle \text{Fe} \rangle$ (center), and $H\delta_F$ and $\langle \text{Fe} \rangle$ (right) showing the effects of changing the velocity dispersion by +20% (lightest symbols) and -20% (darkest symbols) for the RBD Compact, Control, Heavy, and Light subsamples. The values at the measured velocity dispersion are denoted by the symbol colors in the legend. Solid lines show constant $[\text{Fe}/\text{H}]$ from left to right of -1.3 , -0.7 , -0.4 , 0.0 , and $+0.2$. Dotted lines show constant age from top to bottom of 1.2, 1.5, 2.5, 2.8, 3.5, 5.0, 7.0, 10.0, and 14.1 Gyr.

3.4 Characterizing the Homogeneity of Co-added Spectra

Our approach to characterizing the age estimates inferred from co-added spectra is based on the central ideas of “bootstrap resampling” (Efron & Tibshirani 1994). An overview of the bootstrap procedure can be found in §1.5. Briefly, the statistical bootstrap technique attempts to reconstruct the shape of an underlying distribution by resampling, with replacement, from observed data. This means that if the original data set has size n , a new, random sample of

Table 3.4. Systematics I: Effect on Age Measurements of Changing Velocity Dispersion

Sample	Age ($\sigma - 20\%$) (Gyr)	Age ($\sigma - 10\%$) (Gyr)	'True' Age (Gyr)	Age ($\sigma + 10\%$) (Gyr)	Age ($\sigma + 20\%$) (Gyr)
RBD, Compact	1.95	1.67	1.54	1.45	1.19
RBD, Control	2.84	2.64	2.36	2.10	2.93
RBD, Heavy	2.45	2.29	2.02	1.82	1.75
RBD, Light	1.86	1.70	1.57	1.30	1.18
RBD, Compact, Heavy	1.83	1.67	1.50	1.35	1.10
RBD, Control, Heavy	3.43	3.00	2.78	2.43	2.92
RBD, Compact, Light	1.87	1.77	1.65	1.55	1.42
RBD, Control, Light	2.44	2.31	2.20	2.05	1.86
SBD, Compact	7.99	7.51	6.97	6.53	5.94
SBD, Control	5.07	4.39	3.81	3.35	3.06
SBD, Heavy*	7.14	6.14	5.68	5.46	5.65
SBD, Light	7.50	7.33	7.18	7.09	6.78
SBD, Compact, Heavy**	N/A	N/A	7.27	8.90	8.39
SBD, Control, Heavy***	4.65	3.96	3.51	3.14	3.28
SBD, Compact, Light	6.30	6.20	6.12	6.05	5.91
SBD, Control, Light	10.25	9.22	8.24	7.50	6.93
RSBD, Compact	7.92	7.41	6.73	6.16	5.52
RSBD, Control	5.37	4.62	4.24	3.71	3.22
RSBD, Heavy*	7.14	6.14	5.68	5.46	5.65
RSBD, Light	7.15	7.13	7.00	6.92	6.71
RSBD, Compact, Heavy**	N/A	N/A	7.27	8.90	8.39
RSBD, Control, Heavy***	4.65	3.96	3.51	3.14	3.28
RSBD, Compact, Light	5.24	5.09	5.04	5.06	4.66
RSBD, Control, Light	8.11	8.20	8.41	N/A	N/A

*The SBD, Heavy and the RSBD, Heavy samples contain identical galaxies.

**The SBD, Compact, Heavy and the RSBD, Compact, Heavy samples contain identical galaxies.

***The SBD, Control, Heavy and the RSBD, Control, Heavy samples contain identical galaxies.

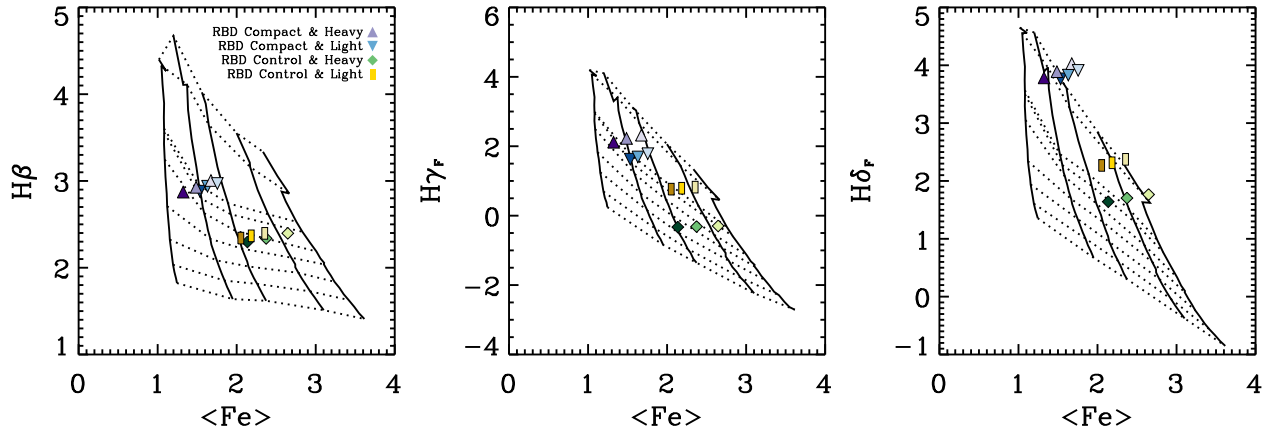


Figure 3.4: Index-index model grids of $H\beta$ and $\langle Fe \rangle$ (left), $H\gamma_F$ and $\langle Fe \rangle$ (center), and $H\delta_F$ and $\langle Fe \rangle$ (right) showing the effects of changing the velocity dispersion by +20% (lightest symbols) and -20% (darkest symbols) for the RBD Compact & Heavy, Compact & Light, Control & Heavy, and Control & Light subsamples.

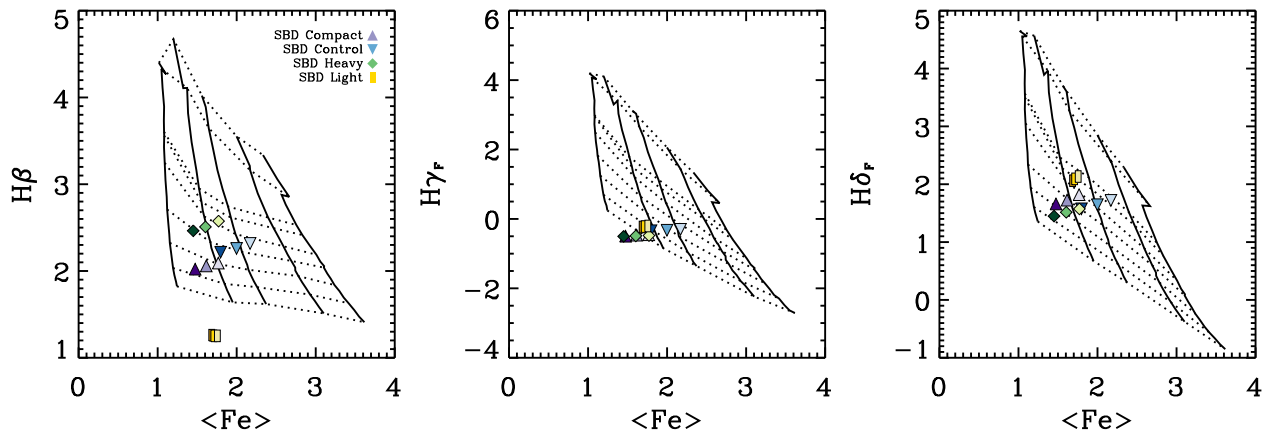


Figure 3.5: Index-index model grids of $H\beta$ and $\langle Fe \rangle$ (left), $H\gamma_F$ and $\langle Fe \rangle$ (center), and $H\delta_F$ and $\langle Fe \rangle$ (right) showing the effects of changing the velocity dispersion by +20% (lightest symbols) and -20% (darkest symbols) for the SBD Compact, Control, Heavy, and Light subsamples.

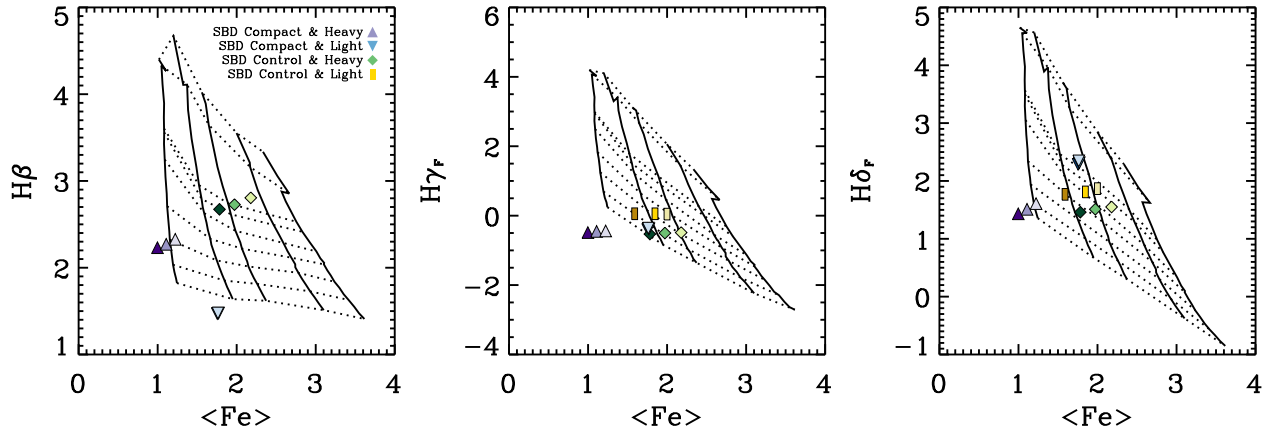


Figure 3.6: Index-index model grids of $H\beta$ and $\langle Fe \rangle$ (left), $H\gamma_F$ and $\langle Fe \rangle$ (center), and $H\delta_F$ and $\langle Fe \rangle$ (right) showing the effects of changing the velocity dispersion by $+20\%$ (lightest symbols) and -20% (darkest symbols) for the SBD Compact & Heavy, Compact & Light, Control & Heavy, and Control & Light subsamples.

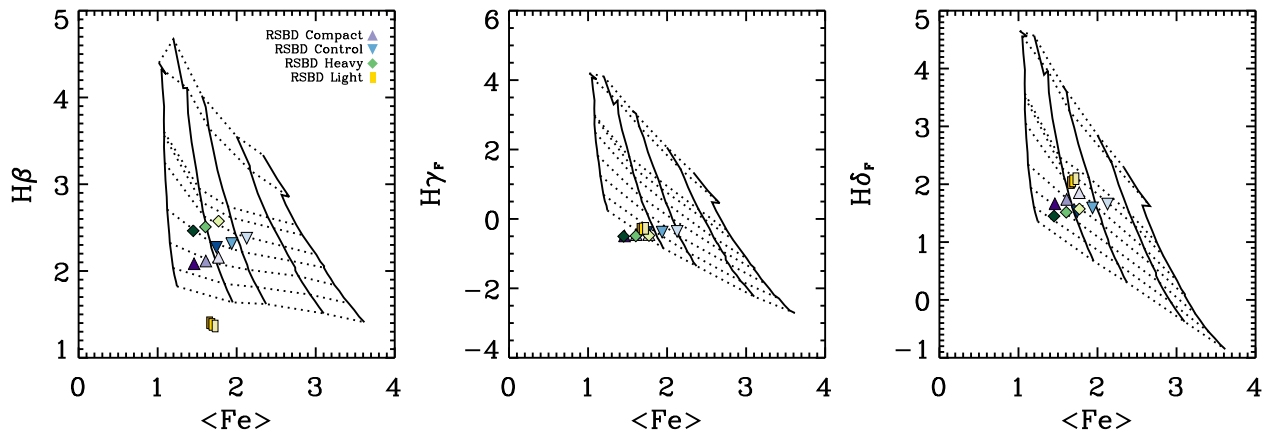


Figure 3.7: Index-index model grids of $H\beta$ and $\langle Fe \rangle$ (left), $H\gamma_F$ and $\langle Fe \rangle$ (center), and $H\delta_F$ and $\langle Fe \rangle$ (right) showing the effects of changing the velocity dispersion by $+20\%$ (lightest symbols) and -20% (darkest symbols) for the RSBD Compact, Control, Heavy, and Light subsamples.

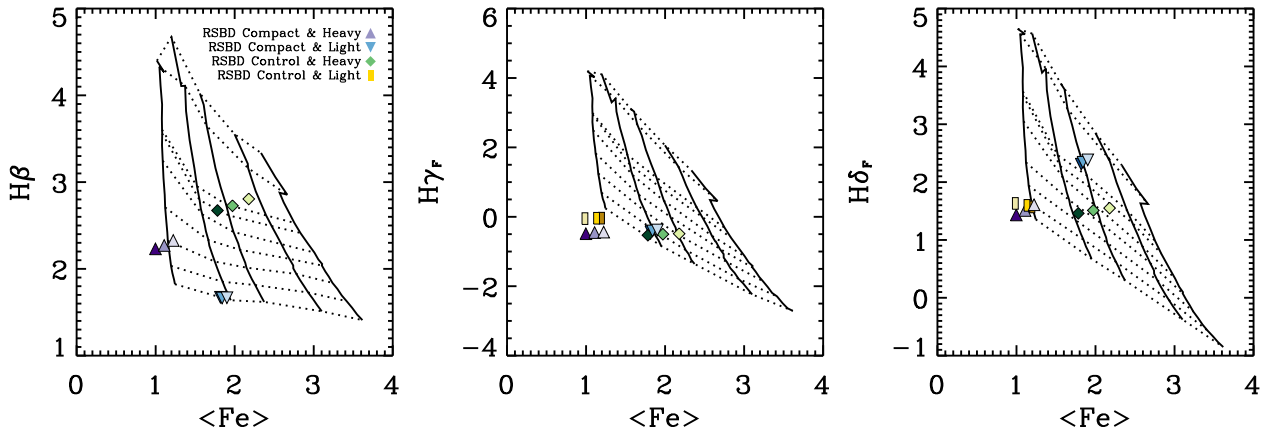


Figure 3.8: Index-index model grids of $H\beta$ and $\langle Fe \rangle$ (left), $H\gamma_F$ and $\langle Fe \rangle$ (center), and $H\delta_F$ and $\langle Fe \rangle$ (right) showing the effects of changing the velocity dispersion by +20% (lightest symbols) and -20% (darkest symbols) for the RSD Compact & Heavy, Compact & Light, Control & Heavy, and Control & Light subsamples.

Table 3.5. Systematics II. Effect on Ages Measurements of Correcting Balmer Line Infill

Sample	Nebular $H\beta$ EW (Å)	Nebular $H\delta_F$ EW (Å)	Nebular $H\gamma_F$ EW (Å)	“True” Age (Gyr)	Infill Age (Gyr)
RBD, Compact, Heavy	0.069	-0.049	0.060	1.50	1.48
RBD, Control, Heavy	-0.110	-0.011	0.081	2.78	2.81
SBD/RSBD, Compact, Heavy	-0.062	0.051	-0.021	7.27	N/A*
SBD/RSBD, Control, Heavy	-0.178	-0.109	-0.050	3.51	4.19

*The SBD/RSBD Compact, Heavy sample fell off the model grids after correcting the Balmer features for emission line infill. An inspection of the index-index plot of $\langle Fe \rangle$ vs. $H\beta$ plot reveals that the sample is just barely outside of the grid boundaries, and is closest to the model with an age just older than 7 Gyr.

size n is drawn from the original sample by allowing the same element to be drawn multiple times. A measurement is made from the new sample (in our case, the age of the co-added spectrum). This process is then repeated a large number of times and the resulting distribution of the measurement's values is computed and used as an estimate of the underlying distribution for the quantity being measured.

The typical use of a bootstrap is to place error estimates on observables, but the technique is actually more general than this, since the shape of the bootstrapped distribution itself can also be used to probe the homogeneity of an underlying sample. We recognize that the galaxy samples we have selected, although chosen to have similar properties, are nevertheless most likely not a homogeneous population. Using the bootstrapping technique allows us to deal with this issue explicitly: if an underlying distribution is multi-modal, a record of this is traced by the modality of the distribution recovered by the bootstrap resampling exercise.

Our application of this useful aspect of the bootstrap is best illustrated using simulations. Using the BC03, we created several synthetic galaxy spectra as comparisons for our co-added DEEP2 spectra. As an initial comparison, we used the simple stellar population models computed using the Salpeter IMF with 40% solar metallicity. We then created synthetic spectra with several different star formation histories. For each star formation history, we bootstrapped three samples: each sample consisted of 60 galaxies (similar to the number of galaxies in our larger samples). Each sample was composed of galaxies that were either 2 Gyr old (“young” galaxies) or 7 Gyr old (“old” galaxies). Sample 1 contained 60 “old” galaxies (all with age 7 Gyr). Sample 2 contained 56 “old” galaxies and 4 “young” galaxies. Sample 3 contained 48 “old” galaxies and 12 “young” galaxies. In order to mimic our real data, each galaxy spectrum was convolved with a Gaussian to simulate a velocity dispersion of 300 km s^{-1} (chosen to match the velocity dispersions of our “Heavy” samples). We added noise to the spectra in the samples to such that each spectrum had signal-to-noise ratio of ~ 5 .

For each star formation history, we performed the bootstrap resampling technique on Samples 1, 2, and 3 by drawing 60 galaxy spectra, with replacement, at random from each sample (note

Table 3.6. Mean Bootstrap Ages for Various Star Formation Histories

SF History	Sample 1 Mean Age (Gyr)	Sample 2 Mean Age (Gyr)	Sample 3 Mean Age (Gyr)
#1: Single burst, 0.5 Gyr	6.40	5.76	4.43
#2: Single burst, 1.0 Gyr	6.19	5.22	4.09
#3: Exp. burst, $\tau = 0.5$	6.60	5.44	3.91
#4: Exp. burst, $\tau = 1.0$	5.13	4.32	3.35
#5: Exp. burst, $\tau = 1.0$, + 0.2 Gyr single burst at $t = 3$ Gyr	4.41	3.82	3.23
#6: Exp. burst, $\tau = 1.0$, + 0.2 Gyr single burst at $t = 2$ Gyr	4.66	4.13	3.16
#7: Exp. burst, $\tau = 0.5$, + 0.2 Gyr single burst at $t = 3$ Gyr	5.18	4.54	3.55
#8: Exp. burst, $\tau = 0.5$, + 0.2 Gyr single burst at $t = 2$ Gyr	5.69	4.87	3.83
#9: Exp. burst, $\tau = 0.2$, + 0.2 Gyr single burst at $t = 3$ Gyr	5.42	4.89	3.94
#10: Exp. burst, $\tau = 0.2$, + 0.2 Gyr single burst at $t = 2$ Gyr	5.93	5.17	4.38
#11: Exp. burst, $\tau = 0.5$, + Exp. burst ^a $\tau = 0.5$ at $t = 3$ Gyr	4.65	4.14	3.45

^aSecond burst has amplitude 0.3.

that for Sample 1, which has an entirely old population, this effect is reduced to drawing galaxies with different added noise rather than different ages). These randomly selected galaxies were then co-added and an age was measured from the resultant spectrum. This process of drawing with replacement from the sample, co-adding the selected galaxies, and then measuring an age was repeated 300 times, which resulted in 300 age measurements for each sample. Table 3.6 lists the mean age for each sample for each of the 11 different star formation histories examined. Figures 3.9 – 3.19 show the star formation history used to generate the synthetic spectra (top panel) and the histogram of the ages obtained from the bootstrapping procedure (bottom panels).

For each star formation history, Sample 1 has the highest median and mean age, followed by Sample 2 and Sample 3 respectively. Such a result indicated that the bootstrap technique

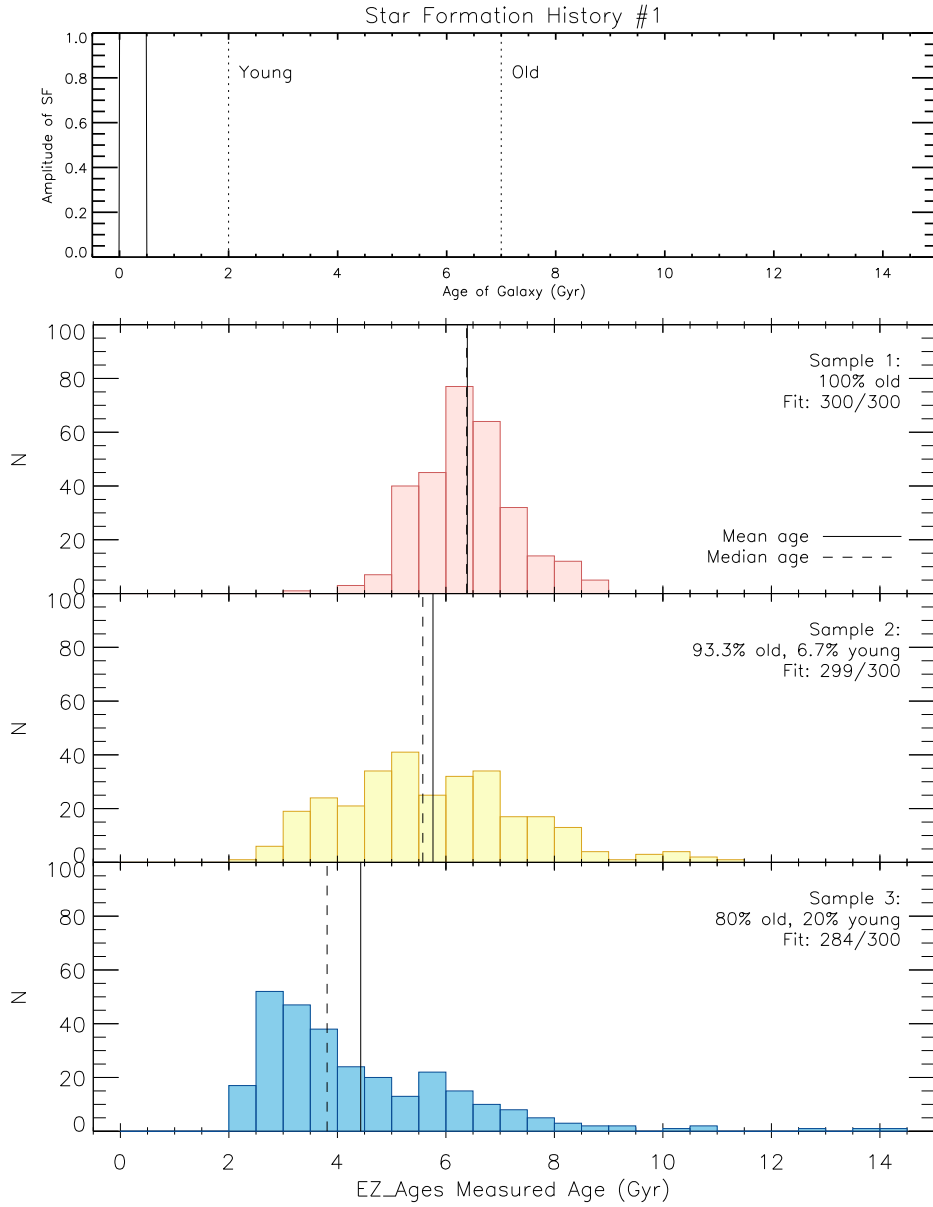


Figure 3.9: Top panel depicts the star formation history used to generate the synthetic galaxy spectra: a single burst 0.5 Gyr in duration. The dotted lines mark the ages of the “young” (2 Gyr) and “old” (7 Gyr) galaxies used in the bootstrap procedure. The bottom three panels display age histograms generated from 300 bootstrap resamplings of the synthetic galaxy spectra drawn from three sample parent populations: Sample 1 contained 60 galaxies with age 7 Gyr, Sample 2 contained 56 galaxies with age 7 Gyr and 4 galaxies with age 2 Gyr, and Sample 3 contained 48 galaxies with age 7 Gyr and 12 galaxies with age 2 Gyr. The histogram has bin size 0.25 Gyr. The mean age of each histogram is marked by a solid line and the median age by a dotted line.

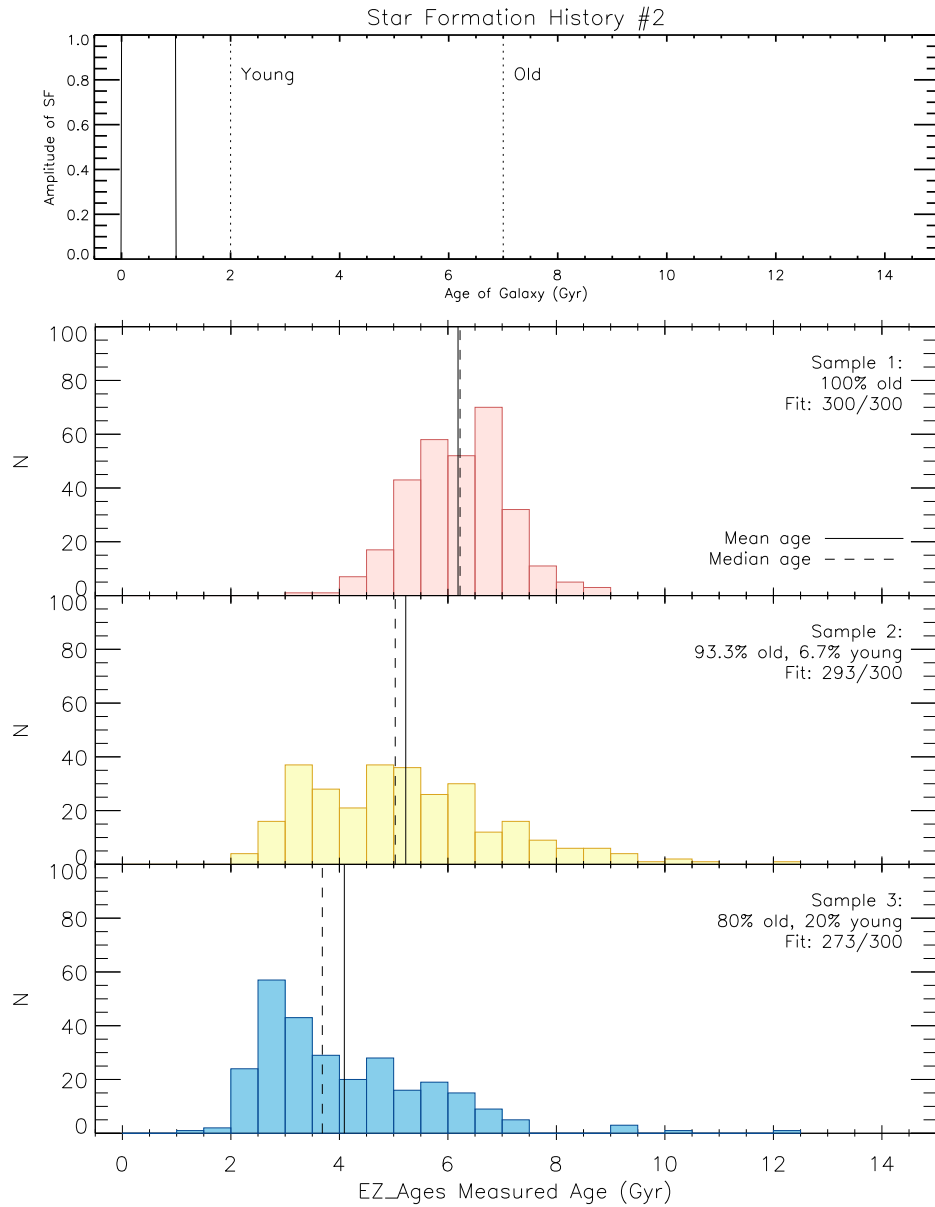


Figure 3.10: Top panel depicts the star formation history used to generate the synthetic galaxy spectra: a single burst 1.0 Gyr in duration. The dotted lines mark the ages of the “young” (2 Gyr) and “old” (7 Gyr) galaxies used in the bootstrap procedure. The bottom three panels display age histograms generated from 300 bootstrap resamplings of the synthetic galaxy spectra drawn from three sample parent populations: Sample 1 contained 60 galaxies with age 7 Gyr, Sample 2 contained 56 galaxies with age 7 Gyr and 4 galaxies with age 2 Gyr, and Sample 3 contained 48 galaxies with age 7 Gyr and 12 galaxies with age 2 Gyr. The histogram has bin size 0.25 Gyr. The mean age of each histogram is marked by a solid line and the median age by a dotted line.

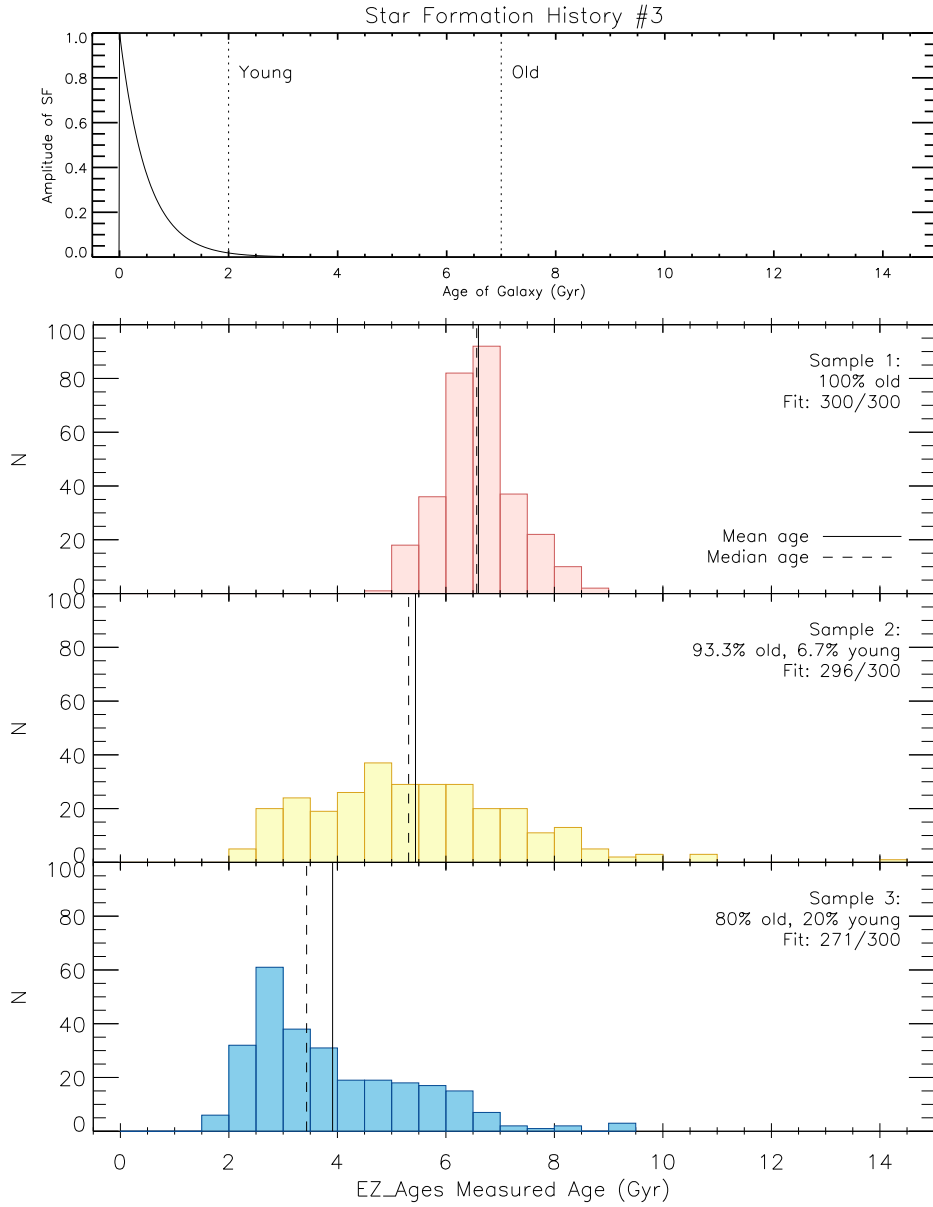


Figure 3.11: Top panel depicts the star formation history used to generate the synthetic galaxy spectra: exponentially declining with e -folding timescale $\tau = 0.5$ Gyr. The dotted lines mark the ages of the “young” (2 Gyr) and “old” (7 Gyr) galaxies used in the bootstrap procedure. The bottom three panels display age histograms generated from 300 bootstrap resamplings of the synthetic galaxy spectra drawn from three sample parent populations: Sample 1 contained 60 galaxies with age 7 Gyr, Sample 2 contained 56 galaxies with age 7 Gyr and 4 galaxies with age 2 Gyr, and Sample 3 contained 48 galaxies with age 7 Gyr and 12 galaxies with age 2 Gyr. The histogram has bin size 0.25 Gyr. The mean age of each histogram is marked by a solid line and the median age by a dotted line.

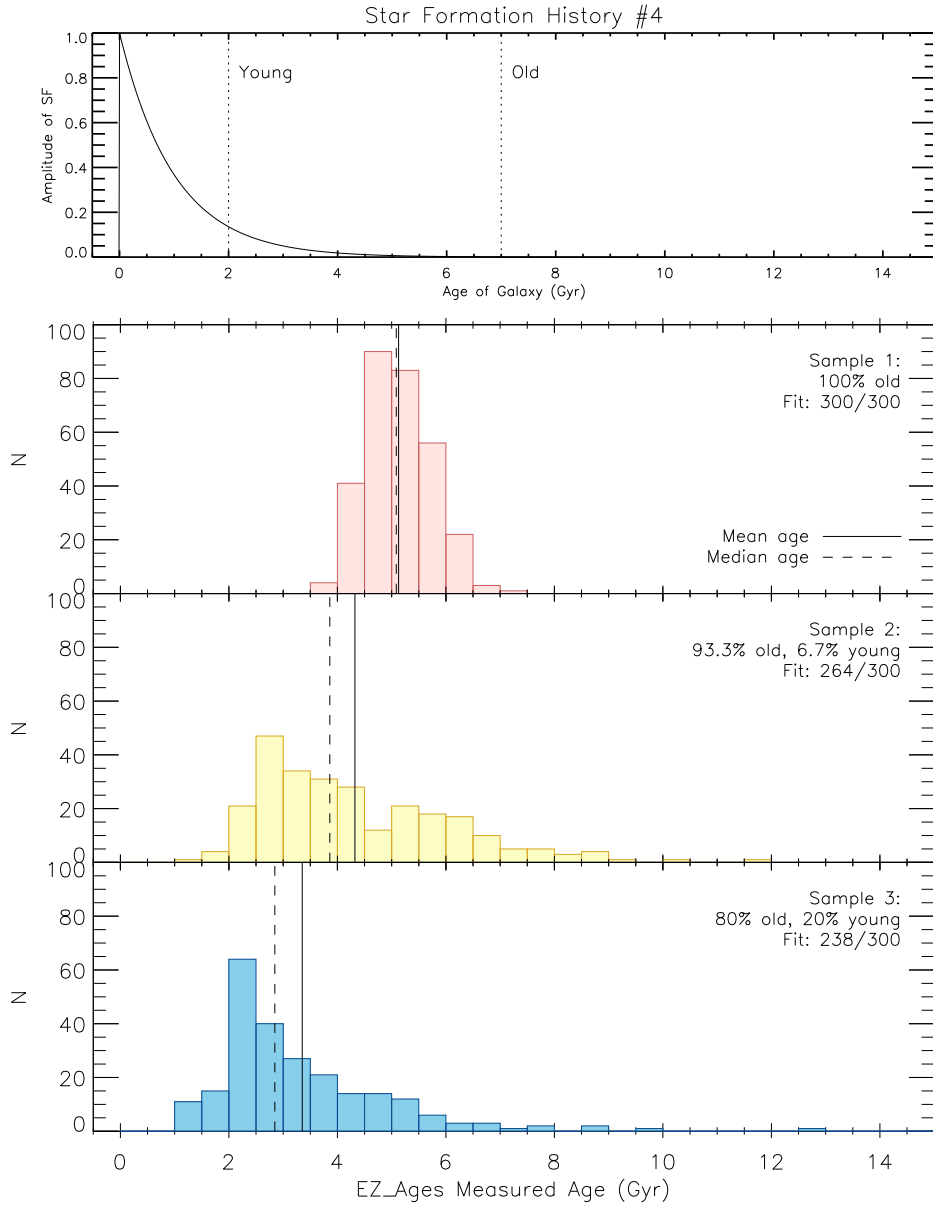


Figure 3.12: Top panel depicts the star formation history used to generate the synthetic galaxy spectra: exponentially declining with e -folding timescale $\tau = 1.0$ Gyr. The dotted lines mark the ages of the “young” (2 Gyr) and “old” (7 Gyr) galaxies used in the bootstrap procedure. The bottom three panels display age histograms generated from 300 bootstrap resamplings of the synthetic galaxy spectra drawn from three sample parent populations: Sample 1 contained 60 galaxies with age 7 Gyr, Sample 2 contained 56 galaxies with age 7 Gyr and 4 galaxies with age 2 Gyr, and Sample 3 contained 48 galaxies with age 7 Gyr and 12 galaxies with age 2 Gyr. The histogram has bin size 0.25 Gyr. The mean age of each histogram is marked by a solid line and the median age by a dotted line.

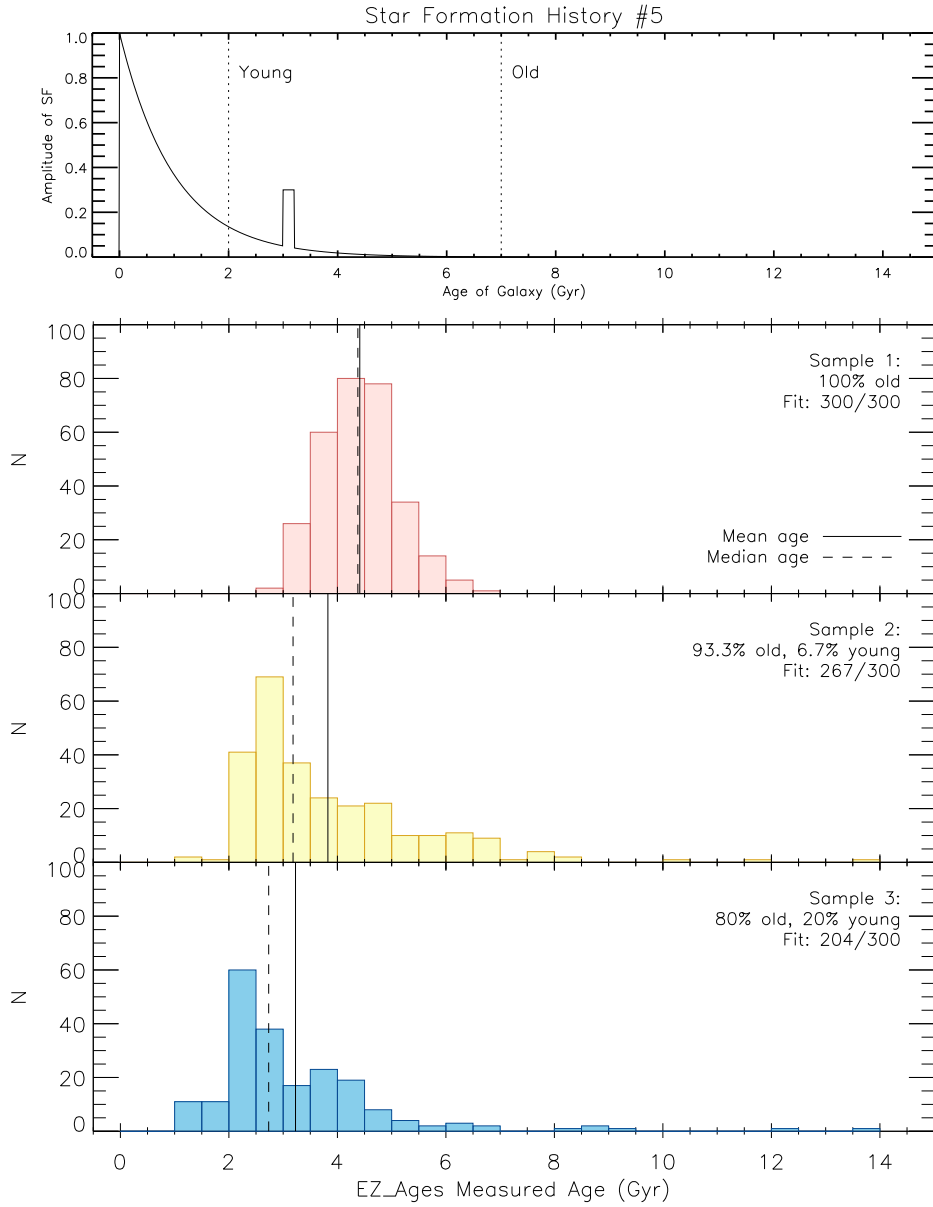


Figure 3.13: Top panel depicts the star formation history used to generate the synthetic galaxy spectra: exponentially declining with e -folding timescale $\tau = 1.0$ Gyr, followed by a 0.2 Gyr long single burst at $t = 3$ Gyr. The dotted lines mark the ages of the “young” (2 Gyr) and “old” (7 Gyr) galaxies used in the bootstrap procedure. The bottom three panels display age histograms generated from 300 bootstrap resamplings of the synthetic galaxy spectra drawn from three sample parent populations: Sample 1 contained 60 galaxies with age 7 Gyr, Sample 2 contained 56 galaxies with age 7 Gyr and 4 galaxies with age 2 Gyr, and Sample 3 contained 48 galaxies with age 7 Gyr and 12 galaxies with age 2 Gyr. The histogram has bin size 0.25 Gyr. The mean age of each histogram is marked by a solid line and the median age by a dotted line.

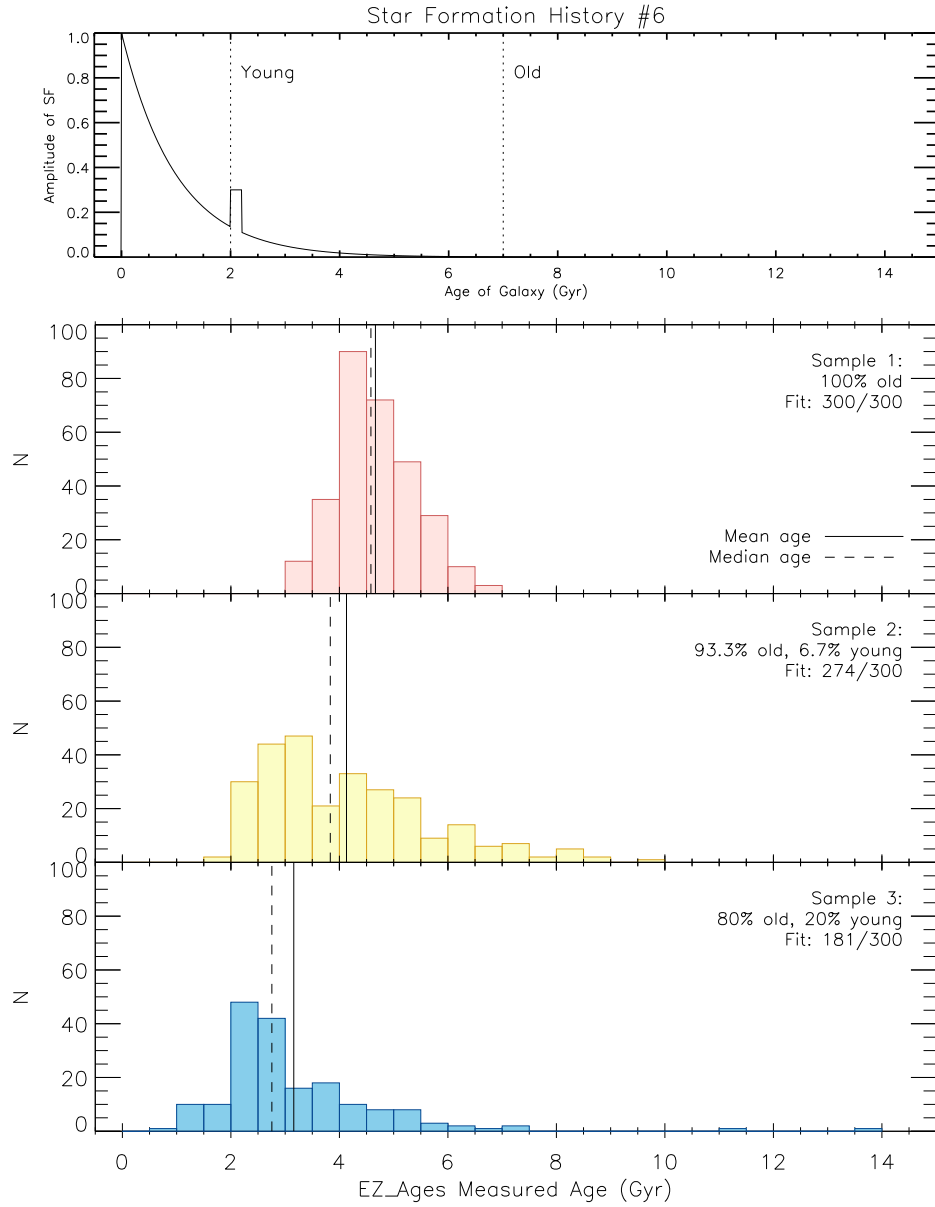


Figure 3.14: Top panel depicts the star formation history used to generate the synthetic galaxy spectra: exponentially declining with e -folding timescale $\tau = 1.0$ Gyr, followed by a 0.2 Gyr long single burst at $t = 2$ Gyr. The dotted lines mark the ages of the “young” (2 Gyr) and “old” (7 Gyr) galaxies used in the bootstrap procedure. The bottom three panels display age histograms generated from 300 bootstrap resamplings of the synthetic galaxy spectra drawn from three sample parent populations: Sample 1 contained 60 galaxies with age 7 Gyr, Sample 2 contained 56 galaxies with age 7 Gyr and 4 galaxies with age 2 Gyr, and Sample 3 contained 48 galaxies with age 7 Gyr and 12 galaxies with age 2 Gyr. The histogram has bin size 0.25 Gyr. The mean age of each histogram is marked by a solid line and the median age by a dotted line.

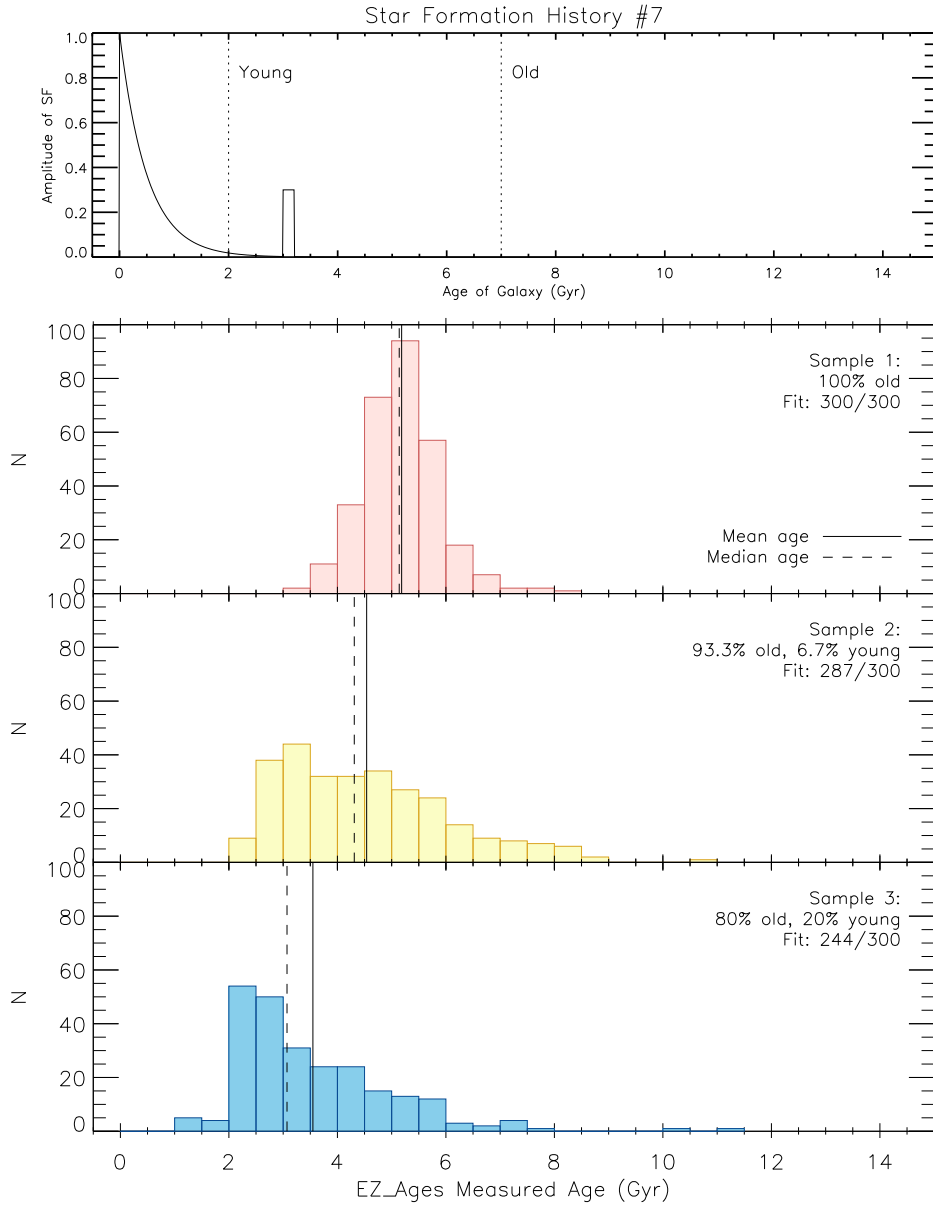


Figure 3.15: Top panel depicts the star formation history used to generate the synthetic galaxy spectra: exponentially declining with e -folding timescale $\tau = 0.5$ Gyr, followed by a 0.2 Gyr long single burst at $t = 3$ Gyr. The dotted lines mark the ages of the “young” (2 Gyr) and “old” (7 Gyr) galaxies used in the bootstrap procedure. The bottom three panels display age histograms generated from 300 bootstrap resamplings of the synthetic galaxy spectra drawn from three sample parent populations: Sample 1 contained 60 galaxies with age 7 Gyr, Sample 2 contained 56 galaxies with age 7 Gyr and 4 galaxies with age 2 Gyr, and Sample 3 contained 48 galaxies with age 7 Gyr and 12 galaxies with age 2 Gyr. The histogram has bin size 0.25 Gyr. The mean age of each histogram is marked by a solid line and the median age by a dotted line.

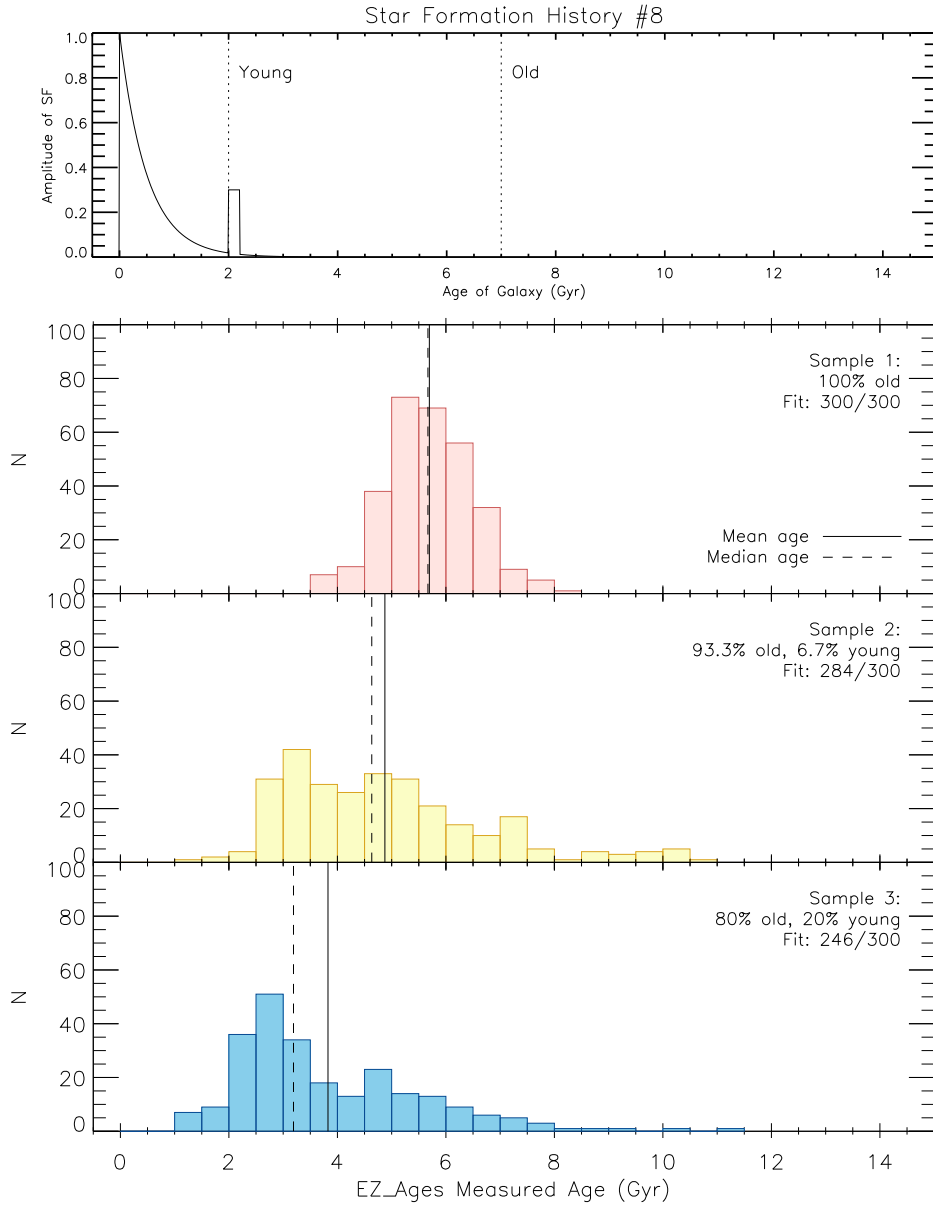


Figure 3.16: Top panel depicts the star formation history used to generate the synthetic galaxy spectra: exponentially declining with e -folding timescale $\tau = 0.5$ Gyr, followed by a 0.2 Gyr long single burst at $t = 2$ Gyr. The dotted lines mark the ages of the “young” (2 Gyr) and “old” (7 Gyr) galaxies used in the bootstrap procedure. The bottom three panels display age histograms generated from 300 bootstrap resamplings of the synthetic galaxy spectra drawn from three sample parent populations: Sample 1 contained 60 galaxies with age 7 Gyr, Sample 2 contained 56 galaxies with age 7 Gyr and 4 galaxies with age 2 Gyr, and Sample 3 contained 48 galaxies with age 7 Gyr and 12 galaxies with age 2 Gyr. The histogram has bin size 0.25 Gyr. The mean age of each histogram is marked by a solid line and the median age by a dotted line.

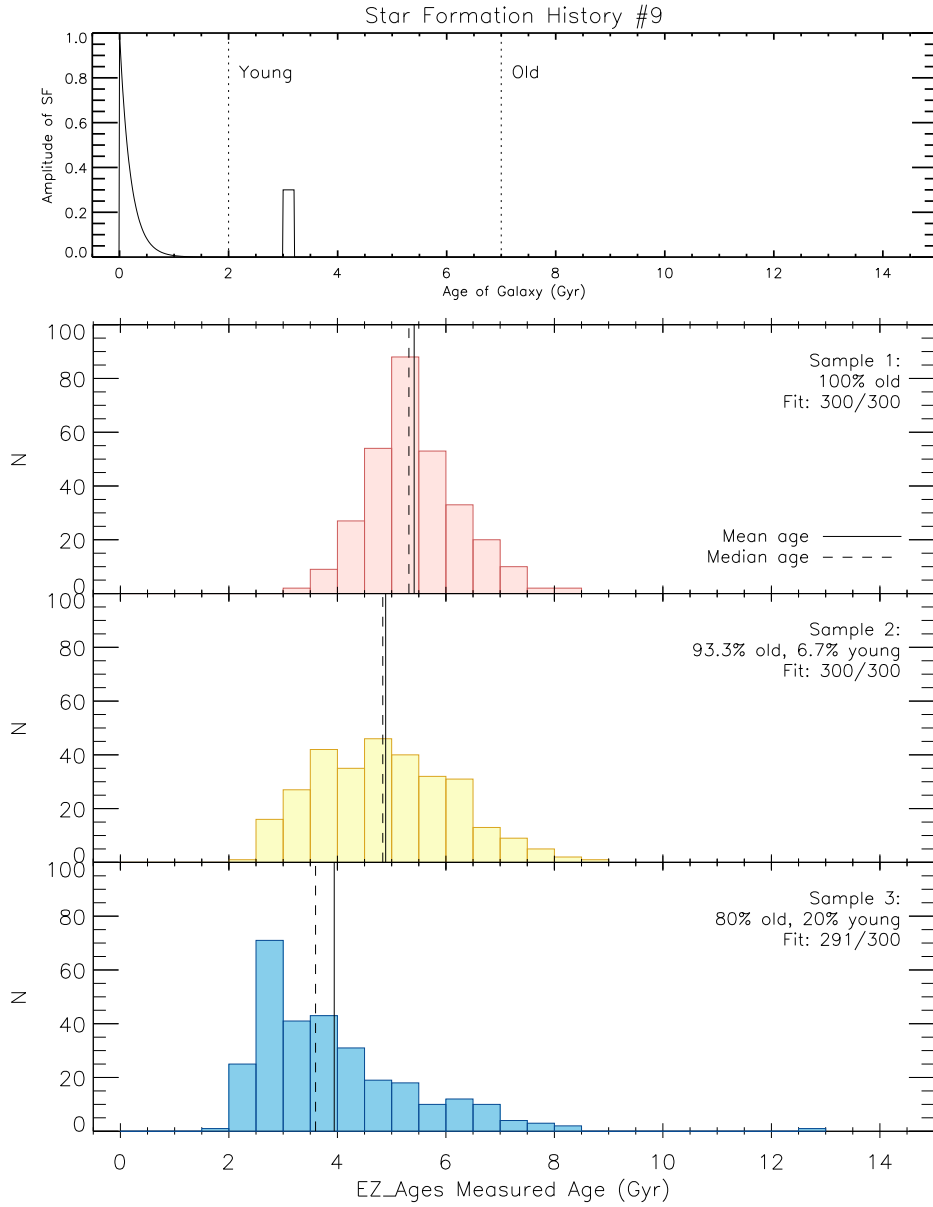


Figure 3.17: Top panel depicts the star formation history used to generate the synthetic galaxy spectra: exponentially declining with e -folding timescale $\tau = 0.2$ Gyr, followed by a 0.2 Gyr long single burst at $t = 3$ Gyr. The dotted lines mark the ages of the “young” (2 Gyr) and “old” (7 Gyr) galaxies used in the bootstrap procedure. The bottom three panels display age histograms generated from 300 bootstrap resamplings of the synthetic galaxy spectra drawn from three sample parent populations: Sample 1 contained 60 galaxies with age 7 Gyr, Sample 2 contained 56 galaxies with age 7 Gyr and 4 galaxies with age 2 Gyr, and Sample 3 contained 48 galaxies with age 7 Gyr and 12 galaxies with age 2 Gyr. The histogram has bin size 0.25 Gyr. The mean age of each histogram is marked by a solid line and the median age by a dotted line.

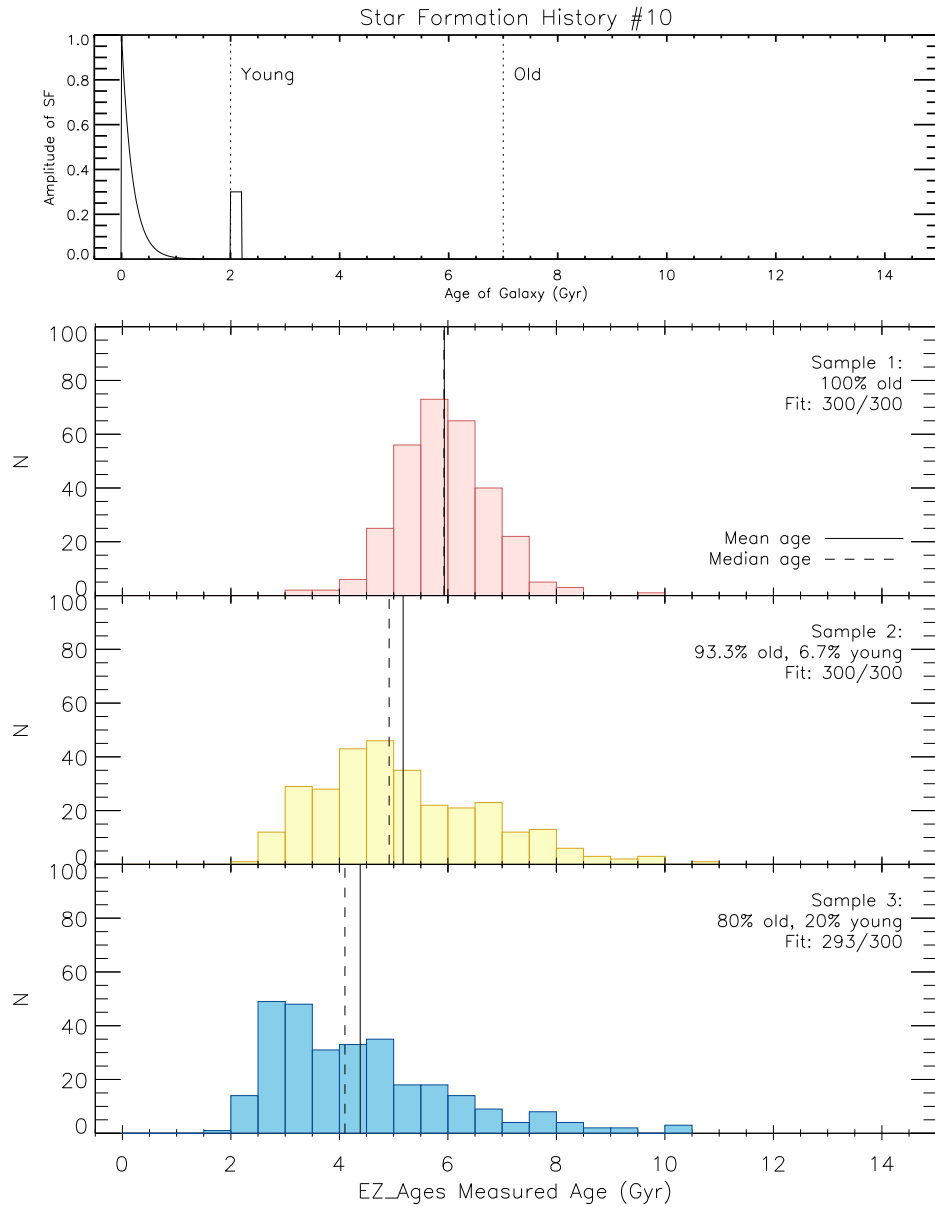


Figure 3.18: Top panel depicts the star formation history used to generate the synthetic galaxy spectra: exponentially declining with e -folding timescale $\tau = 0.2$ Gyr, followed by a 0.2 Gyr long single burst at $t = 2$ Gyr. The dotted lines mark the ages of the “young” (2 Gyr) and “old” (7 Gyr) galaxies used in the bootstrap procedure. The bottom three panels display age histograms generated from 300 bootstrap resamplings of the synthetic galaxy spectra drawn from three sample parent populations: Sample 1 contained 60 galaxies with age 7 Gyr, Sample 2 contained 56 galaxies with age 7 Gyr and 4 galaxies with age 2 Gyr, and Sample 3 contained 48 galaxies with age 7 Gyr and 12 galaxies with age 2 Gyr. The histogram has bin size 0.25 Gyr. The mean age of each histogram is marked by a solid line and the median age by a dotted line.

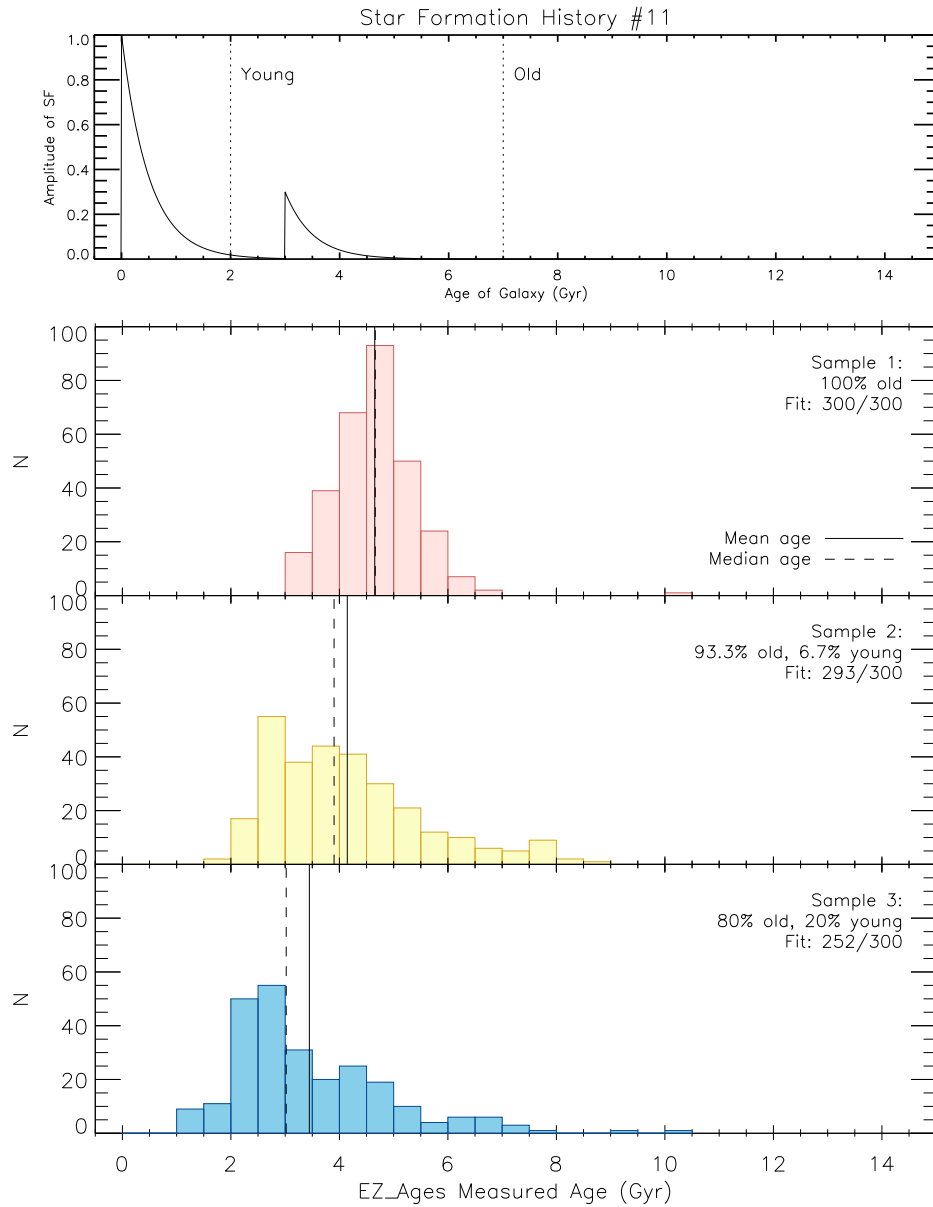


Figure 3.19: Top panel depicts the star formation history used to generate the synthetic galaxy spectra: exponentially declining with e -folding timescale $\tau = 0.5$ Gyr, followed by another exponentially declining burst with $\tau = 0.5$ Gyr and amplitude 0.3 at $t = 3$ Gyr. The dotted lines mark the ages of the “young” (2 Gyr) and “old” (7 Gyr) galaxies used in the bootstrap procedure. The bottom three panels display age histograms generated from 300 bootstrap resamplings of the synthetic galaxy spectra drawn from three sample parent populations: Sample 1 contained 60 galaxies with age 7 Gyr, Sample 2 contained 56 galaxies with age 7 Gyr and 4 galaxies with age 2 Gyr, and Sample 3 contained 48 galaxies with age 7 Gyr and 12 galaxies with age 2 Gyr. The histogram has bin size 0.25 Gyr. The mean age of each histogram is marked by a solid line and the median age by a dotted line.

was, at least on a very basic level, doing what it should, as Sample 1 had the largest number of old galaxies, and Sample 3 had the smallest. It is difficult to draw significant conclusions from the small number (300) of bootstraps done. Instead, we used these brief simulations to roughly quantify how much of an effect the star formation history had on the shapes of the bootstrap distributions. The histogram shapes indicated to us that the star formation history did not have a significant effect, as the shapes are all generally similar between samples with the same homogeneity. Consequently, we chose to use a simple stellar population as the basis of comparison to synthetic spectra in our subsequent analyses.

Having laid out the basic idea using these very simple models, we now go on to apply the concept to more realistic representations of our data. We created synthetic spectra to resample 4000 times, which is the number of times we resample our real data. The new synthetic spectra were produced by using simple stellar populations with 20% solar metallicity ($Z = 0.004$), once again with ages of 2 Gyr (the “young” galaxy) and of 7 Gyr (the “old” galaxy). The spectra were convolved with a Gaussian to simulate a velocity dispersion of 300 km s^{-1} .

We created six new parent galaxy populations comprised of 25 galaxies each, chosen to mimic our smallest (and therefore most uncertain) sample of galaxies. We added noise to each galaxy spectrum in the parent populations such that each spectrum had a signal-to-noise ratio of ~ 5 . The number of “young” spectra relative to “old” spectra in the parent populations was increased in steps of 5: the first parent population 25 noise realizations of young galaxy; the second parent population contains 5 noise realizations of the old galaxy and 20 noise realizations of the young galaxy; the third has 10 noise realizations of the old galaxy and 15 noise realizations of the young galaxy; and so forth, with the final parent population containing 25 noise realizations of the old galaxy. For each parent population, we co-added the galaxies and measured the nominal light-weighted age, marked by the diamonds in Figure 3.20. Next, on each parent sample, we used the bootstrap resampling technique as described earlier, resulting in 4000 different age measurements for each parent population.

The age histograms for the six parent populations with differing percentages of 7 Gyr

old galaxies and 2 Gyr old galaxies can be seen in Figure 3.20. Given that Lick indices have a non-linear response to age, we plot our histograms in log-age, with a bin size of 0.02 in $\log(\text{age}(\text{Gyr}))$. We note that when we have more homogeneous populations (the young population with 0% old galaxies and the old population with 100% old galaxies), we recover a more Gaussian distribution of ages centred roughly around the age of the input spectra. In the mixed populations, we see tails develop particularly towards older ages.

To explore how far we could recover a mixed population, we created an additional parent population with 25 total galaxies: 15 galaxies of 7 Gyr age, and 5 galaxies each with 5 Gyr and 2 Gyr age. This “mixed” parent population would, potentially, display a three-peaked histogram. Figure 3.21 shows the age histogram for the “mixed” parent population. We do not clearly recover three distinct peaks, but the population is distinctively less Gaussian than our homogeneous populations. It closely resembles the synthetic population with 15 galaxies of 7 Gyr age and 10 galaxies of 2 Gyr age, which is unsurprising.

We note that another informative test of this procedure would be to perform the bootstrap resampling a number of times on synthetic spectra with random age distributions instead of two distinct ages. However, we performed this initial simpler test to determine if the procedure could pick out distinct populations if they existed. These simple synthetic galaxy comparisons have shown that mixed populations leave an imprint in the bootstrap-resampled age histograms, but that it is difficult to tell precisely what the degree of heterogeneity is within the stellar population ages. Our approach in the next chapter is to therefore exploit this information to qualitatively characterize the homogeneity of galaxy populations.

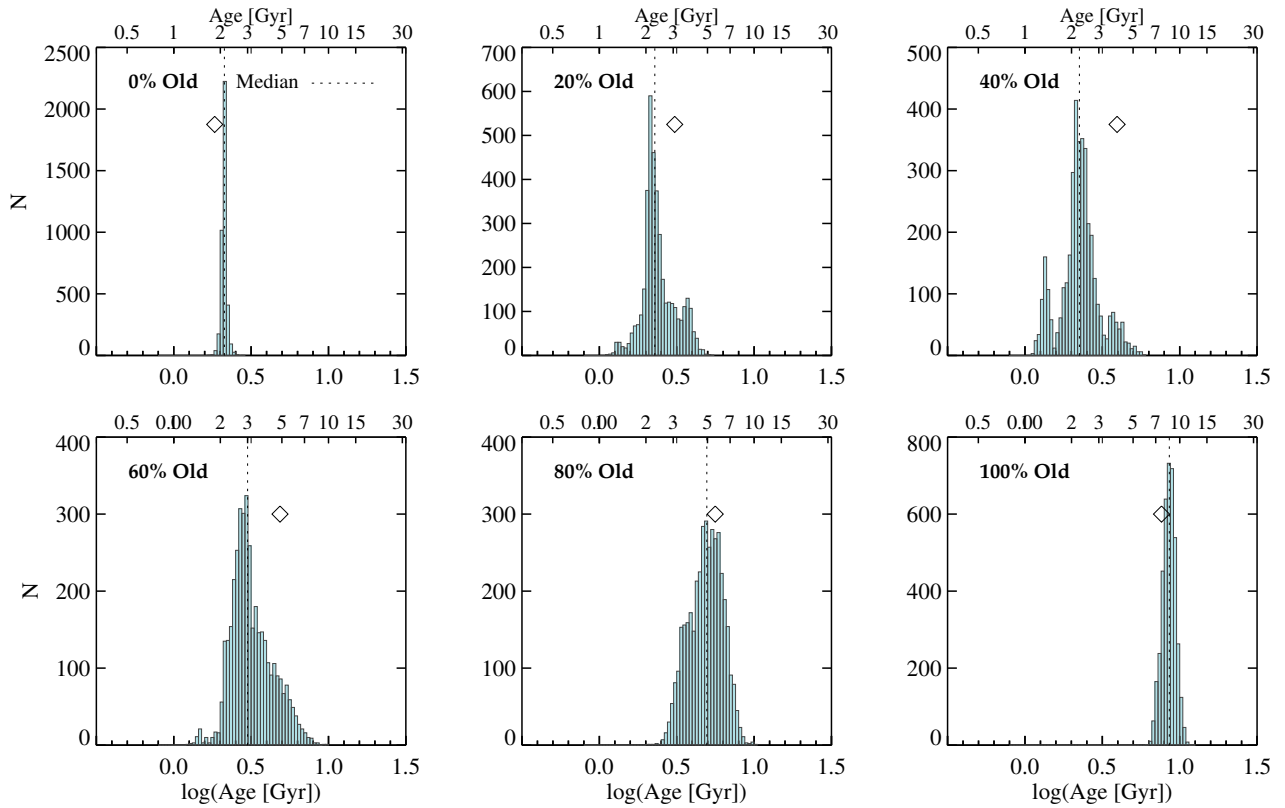


Figure 3.20: Age histograms generated from 4000 bootstrap resamplings of the synthetic galaxy spectra drawn from parent populations with differing numbers of “young” (2 Gyr) and “old” (7 Gyr) spectra. The histograms have bin size 0.02 in $\log(\text{age (Gyr)})$. The median \log age is marked in each histogram by a dotted line. Black diamonds denote the nominal light-weighted age for each parent population. The homogeneous populations (0% old and 100% old) have Gaussian distributions, whereas the mixed populations have more skewed distributions.

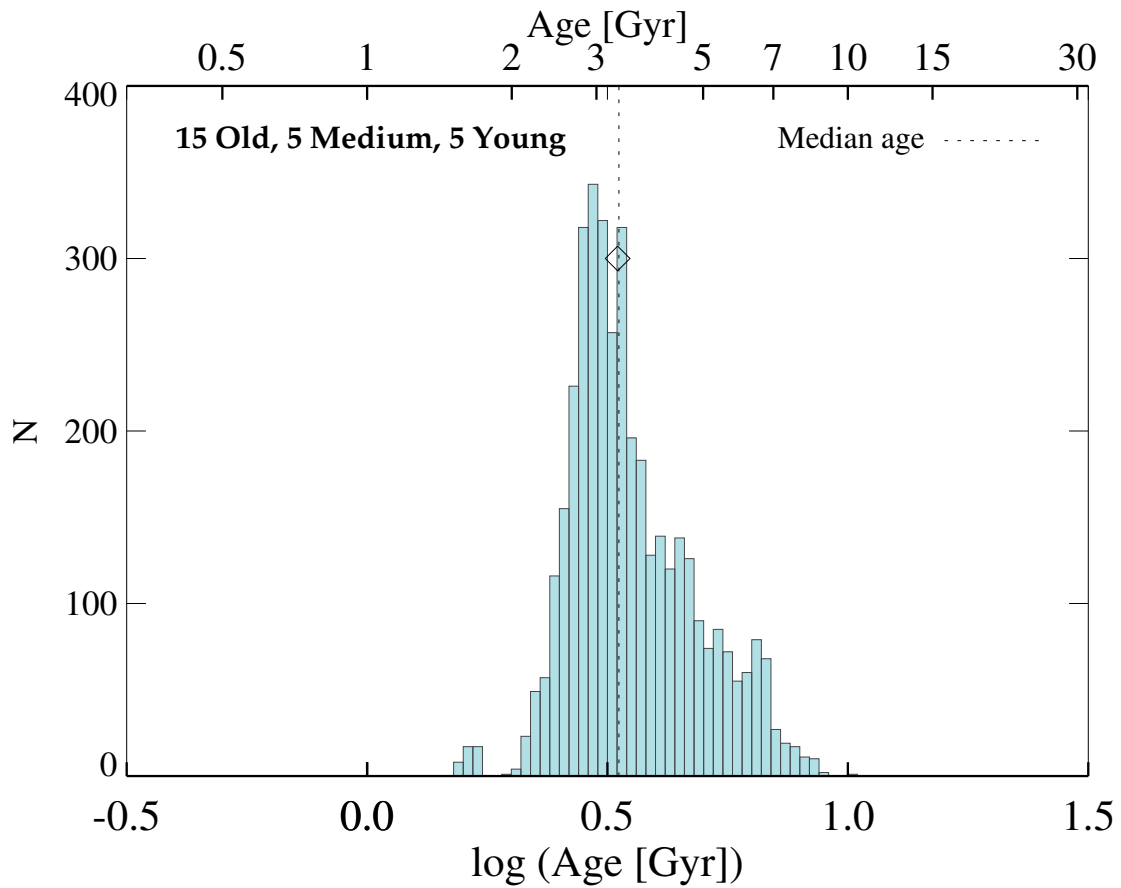


Figure 3.21: Age histograms generated from 4000 bootstrap resamplings of the synthetic galaxy spectra drawn from a parent population with 15 galaxies of 7 Gyrs age, 5 galaxies of 5 Gyrs age, and 5 galaxies of 2 Gyrs age. The histogram has bin size 0.02 in $\log(\text{age (Gyr)})$. The median \log age is marked by a dotted line. The black diamond denotes the nominal light-weighted age.

Chapter 4

Results

4.1 Chapter Overview

This chapter describes the results of our analysis of the diversity of the stellar populations that go into our co-added spectra, using the bootstrap-based approach to spectral co-addition. In §4.2, we describe the application of the bootstrapping technique to our samples, and show the histograms of the ages obtained by bootstrapping. Section 4.3 provides a brief overview of the main points to take away from the results. We find a correlation between a galaxy’s smoothness and its measured age, which is discussed in §4.5. In §4.4, we investigate whether certain galaxies are found to contribute significantly more or less to each histogram.

4.2 Nominal ages and bootstrap resampling

In this section, we describe our application of the bootstrapping technique to the samples of early-type galaxies defined in §2.3. To start, we measured the nominal age of each sample, which is the age of the original co-added sample (see Figures 2.7 – 2.17) before the bootstrap resampling is performed. Next, we drew galaxies at random with replacement from each of the subsamples. The total number of galaxies drawn is equal to the size of the given subsample: for example, for the RBD, Compact subsample, we draw 97 galaxies each time, but for the RBD,

Compact, Heavy sample we draw 25 galaxies. We co-added the randomly drawn galaxies and then measured the resultant age with EZ_Ages. This procedure was repeated 4000 times for each subsample of galaxies, giving almost 4000 estimates for each sample's age.

4.2.1 Velocity Dispersion Shortcut

Due to the time-intensive process of measuring the velocity dispersions using the IRAF cross-correlation technique, we did not measure the velocity dispersion of each new co-added spectrum in our bootstrap. Instead, the velocity dispersion for each of the new bootstrapped co-added spectra was assumed to be the same as the measured velocity dispersion of the original sample from which we performed the resampling (see Table 3.1). To determine how much error this might introduce into our age measurements, we performed a small number of bootstrap co-additions (300 resamplings), measuring the velocity dispersion for each co-addition and then using the velocity dispersion to measure the age for each resampling. We performed the same analysis with another 300 resamplings, this time assuming the velocity dispersion for each co-add was the same as the velocity dispersion measured in the original sample. Figure 4.1 shows the results of these two scenarios. There was negligible difference in shape between the two bootstrap distributions, and both have nearly the same median age, indicating that we could safely assume a single velocity dispersion for our larger bootstrap resamplings.

The histograms showing the measured age distributions inferred from the bootstrap resamplings are shown in Figures 4.2 through 4.12. The nominal age measurements for each of the original co-added samples are shown in Table 4.1, along with the median, mean, and modal ages from the bootstrap resampling.

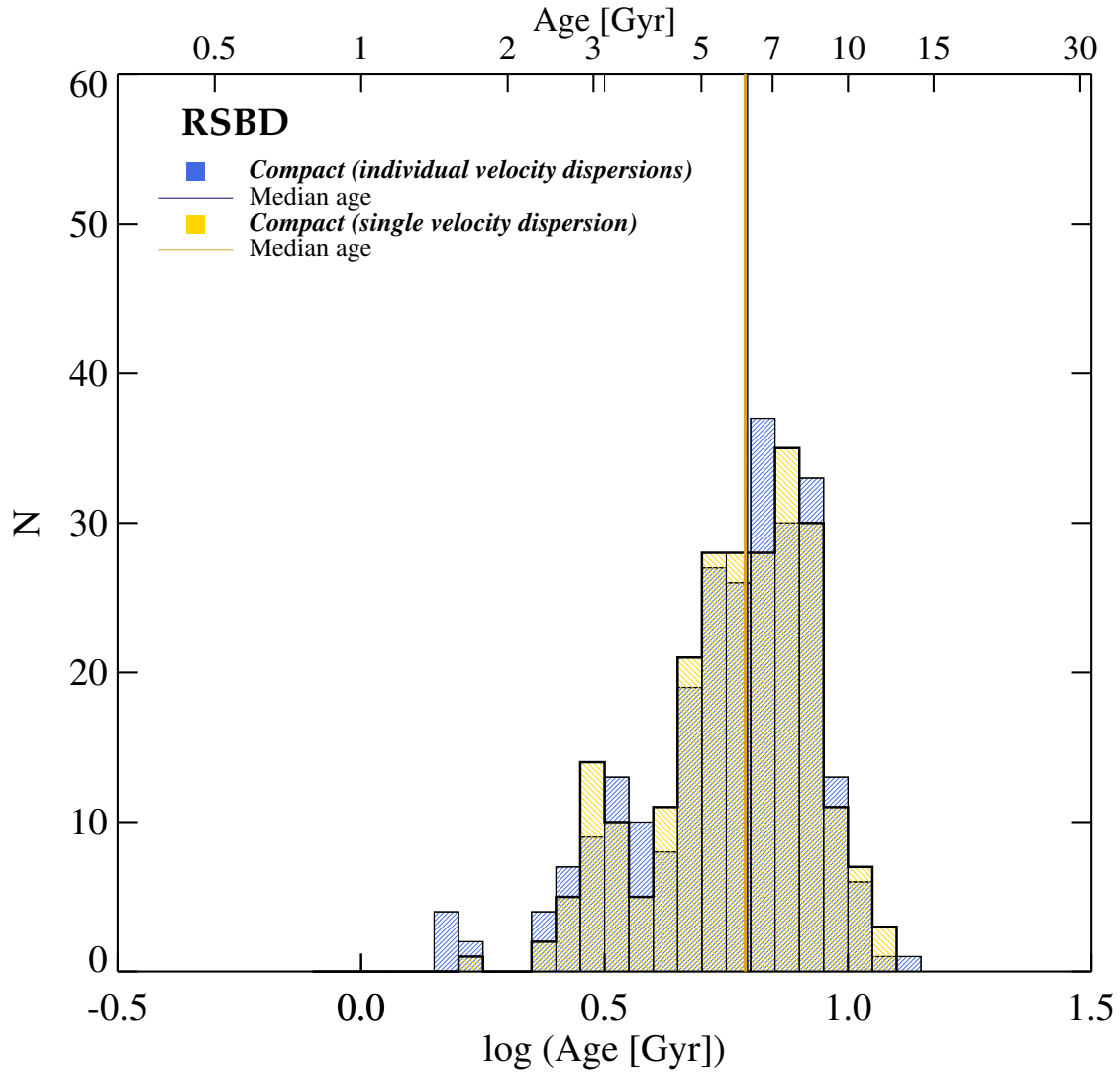


Figure 4.1: Age histograms generated from bootstrapping the Compact subsample of the “Red, Smooth & Bulge-Dominated (RSBD) Sample”. The blue histogram shows the results for the case where the velocity dispersions for each randomly co-added spectrum were measured individually. The yellow histogram shows the results for the case where a single velocity dispersion is assumed for the entire sample. The histograms have bin size 0.05 in $\log(\text{age (Gyr)})$. The median ages of the histograms are marked with a solid line of the same color as the histogram it is measured from.

Table 4.1. Measured Ages

Sample Name	Nominal Age (Gyr)	Median Bootstrap Age (Gyr)	Mean Bootstrap Age (Gyr)	Modal Bootstrap Age (Gyr)
RBD, Compact	1.54	1.56	1.81	1.20
RBD, Control	2.36	2.81	3.10	2.78
RBD, Heavy	2.02	2.21	2.52	2.05
RBD, Light	1.57	1.98	2.11	2.09
RBD, Compact and Heavy	1.50	1.62	2.15	1.12
RBD, Control and Heavy	2.78	3.42	4.10	2.98
RBD, Compact and Light	1.65	1.94	2.21	1.17
RBD, Control and Light	2.20	2.60	2.99	2.26
SBD, Compact	6.97	4.83	5.22	3.41
SBD, Control	3.81	4.31	4.82	2.94
SBD, Heavy	5.68	4.77	5.06	3.00
SBD, Light	7.18	6.47	6.81	5.21
SBD, Compact and Heavy	7.27	6.69	6.70	6.80
SBD, Control and Heavy	3.51	3.68	4.32	2.97
SBD, Compact and Light	6.12	4.96	5.58	2.96
SBD, Control and Light	8.24	6.73	7.18	5.33
RSBD, Compact	6.73	4.86	5.20	3.00
RSBD, Control	4.24	4.56	4.98	3.15
RSBD, Heavy	5.68	4.97	5.30	3.00
RSBD, Light	7.00	6.33	6.62	5.10
RSBD, Compact and Heavy	7.27	6.69	6.70	6.80

Table 4.1 (cont'd)

Sample Name	Nominal Age (Gyr)	Median Bootstrap Age (Gyr)	Mean Bootstrap Age (Gyr)	Modal Bootstrap Age (Gyr)
RSBD, Control and Heavy	3.51	3.68	4.32	2.97
RSBD, Compact and Light	5.04	4.54	5.13	2.99
RSBD, Control and Light	8.41	4.83	5.74	3.30

The central findings that emerge from these figures is that massive compact early-type galaxies selected on the basis of red color and high bulge-to-total ratio are *younger* than similarly-selected larger galaxies, suggesting that size growth in these objects is *not* driven mainly by progenitor bias, and that individual galaxies grow as their stellar populations age. However, compact early-type galaxies selected on the basis of image smoothness and high bulge-to-total ratio (as well as red color) are older than a control sample of larger galaxies.

The basis for these results, organized by parent samples, is as follows:

4.2.2 Red and Bulge-Dominated Galaxies

The histograms for this sample (selected on the basis of high bulge-to-total ratio and red color) are shown in Figures 4.2 – 4.5. Looking first at Figure 4.2, which compares the Compact and Control subsamples with no mass division, we obtained a nominal age of 1.5 Gyr for the compact galaxies and a nominal age of 2.4 Gyr for the control galaxies. The histograms for these subsamples are markedly different. The Compact subsample displays multiple peaks, the most prominent at ~ 1.2 Gyr, with a secondary one at ~ 2.3 Gyrs. The median age is 1.56 Gyr. The Control subsample, on the other hand, only displays one prominent peak close to the median age of 2.81 Gyr. We note here a possibility of contamination from AGN, as the RBD Compact sample displays some [OIII]-5007 emission, which is characteristic of AGN

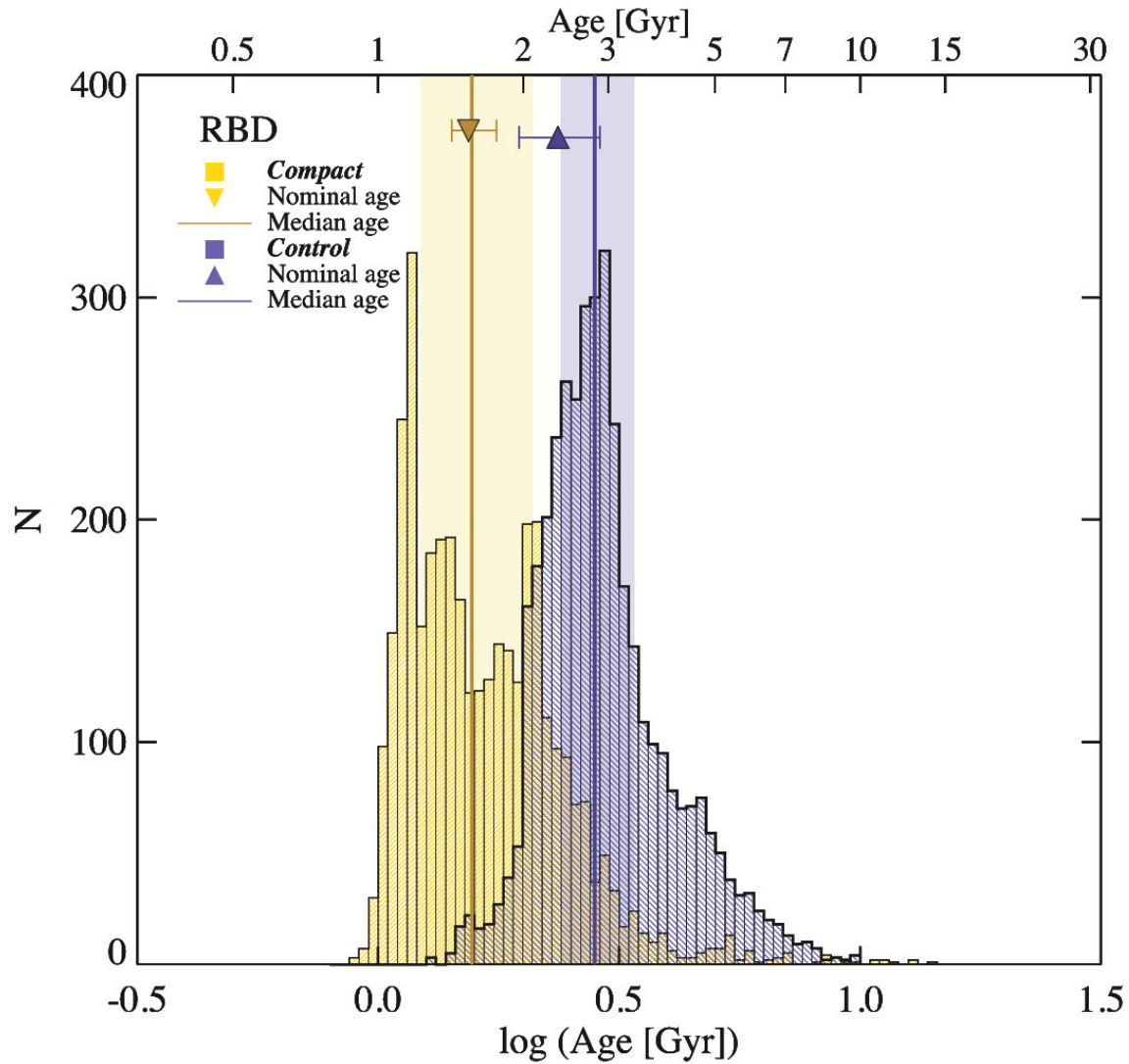


Figure 4.2: Age histograms generated from bootstrapping the Compact (yellow) and Control (purple) galaxies in the “Red & Bulge-Dominated (RBD) Sample” 4000 times each. The histograms have bin size 0.02 in $\log(\text{age (Gyr)})$. The median ages of the histograms are marked with a solid line of the same color as the histogram it is measured from. The interquartile range, a measure of dispersion which encompasses 25% of the data points on either side of the median age, is shown by a semi-transparent band in the same color as the histogram. Measured nominal ages from the original (non-resampled) co-added subsamples are demarcated by symbols of the same colors with errors estimated by `EZ_Ages` using the signal-to-noise spectrum to determine the measurement error of the Lick index line strengths.

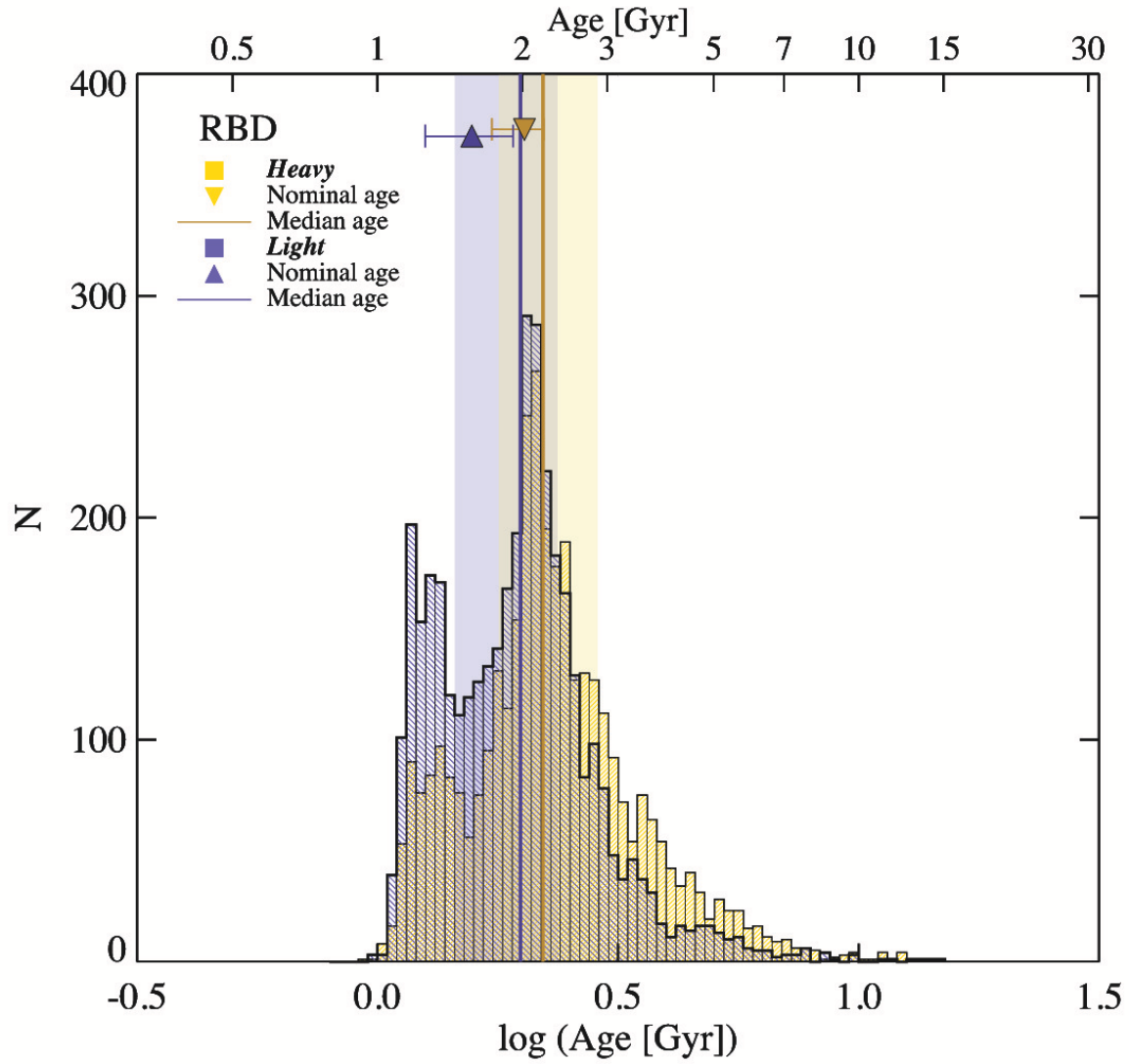


Figure 4.3: Age histograms generated from bootstrapping the Heavy (yellow) and Light (purple) galaxies in the “Red & Bulge-Dominated (RBD) Sample” 4000 times each. The histograms have bin size 0.02 in $\log(\text{age (Gyr)})$. Symbols are as described in Figure 4.2.

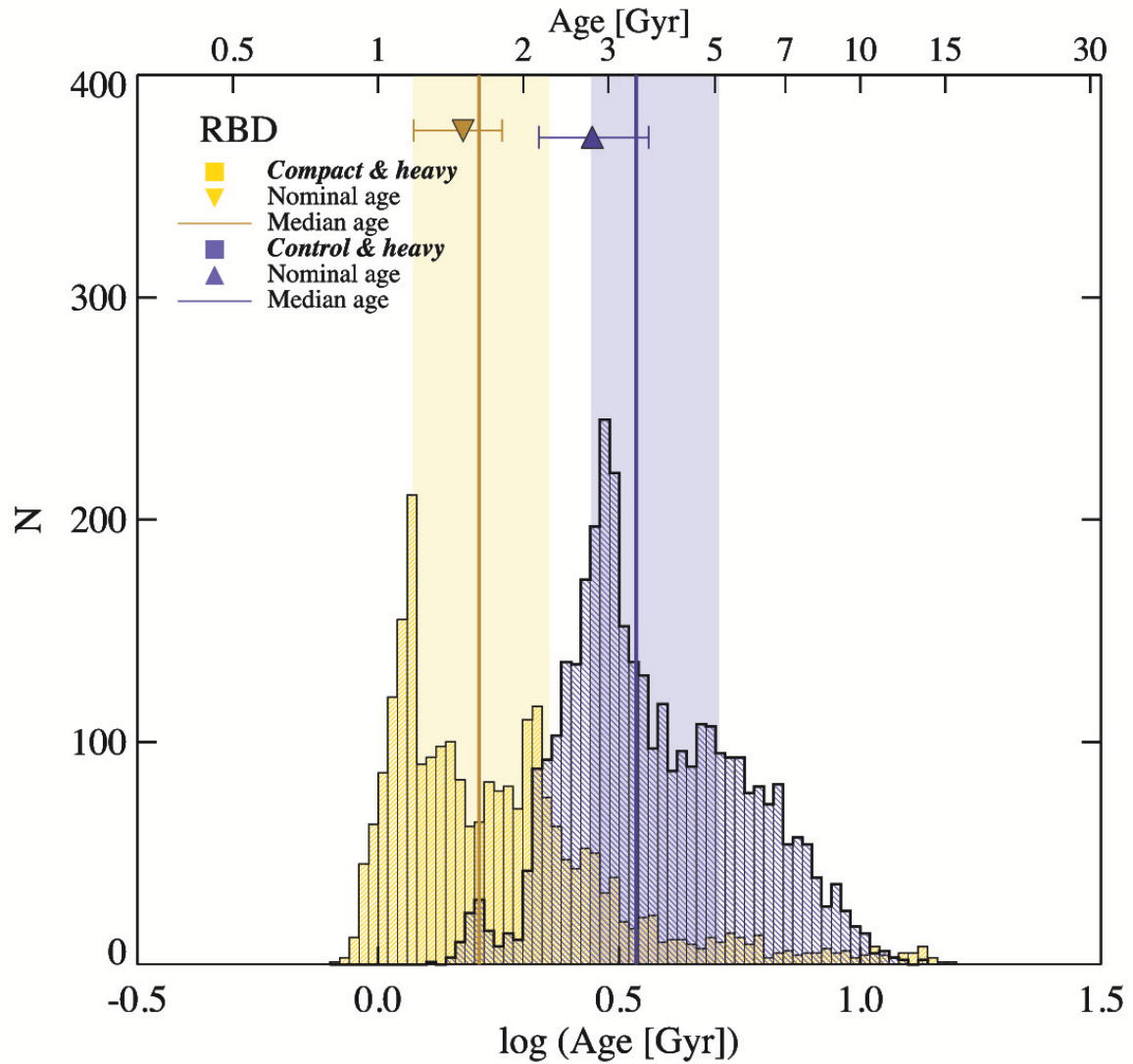


Figure 4.4: Age histograms generated from bootstrapping the Compact and Heavy (yellow) and Control and Heavy (purple) galaxies in the “Red & Bulge-Dominated (RBD) Sample” 4000 times each. The histograms have bin size 0.02 in $\log(\text{age (Gyr)})$. Symbols are as described in Figure 4.2.

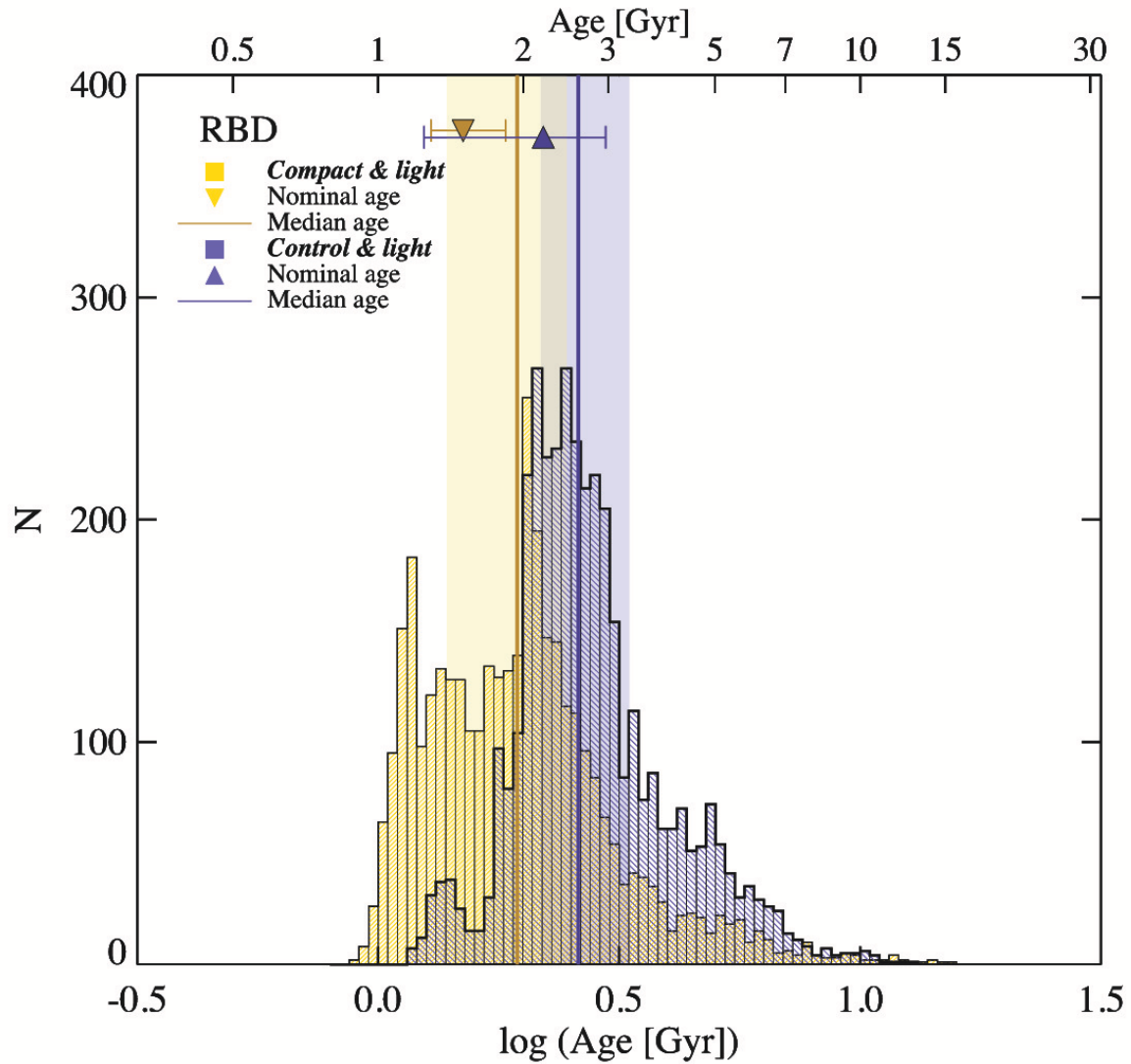


Figure 4.5: Age histograms generated from bootstrapping the Compact and Light (yellow) and Control and Light (purple) galaxies in the “Red & Bulge-Dominated (RBD) Sample” 4000 times each. The histograms have bin size 0.02 in $\log(\text{age (Gyr)})$. Symbols are as described in Figure 4.2.

with young stellar populations. However, we did not apply any correction for emission infill, as the results of §3.3 imply that the impact of emission infill on our age measurements is minimal. Furthermore, the presence of such infill would skew the results towards older ages, not younger.

The Compact and Control subsamples can be contrasted with the Heavy and Light subsamples in Figure 4.3, which have histograms that are fairly similar in shape. There is significant overlap between the interquartile ranges, and the median ages of both of the histograms fall within the overlap of the interquartile ranges. This indicates that there isn't a significant difference in the stellar populations of the galaxies when they are separated only by mass.

Of the four subsample comparisons in the RBD sample, the Compact & Heavy and Control & Heavy distributions in Figure 4.4 show the greatest difference in median age. We obtain a nominal age of 1.5 Gyr for the Compact & Heavy galaxies and 2.8 Gyr for the Control & Heavy galaxies. The median ages measured from the bootstrap resample histograms are 1.62 and 3.42 Gyr respectively. The age histogram of the Control & Heavy subsample has a shape that is very similar to our synthetic population with 60% 7 Gyr old galaxies and 40% 2 Gyr old galaxies or that of the distribution with three different ages. We acknowledge that such similarities are, of course, not conclusive – any number of other combinations of galaxy ages could produce similarly-shaped distributions. It is clear, however, that the distribution is not Gaussian. The Compact & Heavy subsample has an age histogram which looks unlike any of our synthetic distributions. It has two distinct peaks: a primary peak at just slightly > 1 Gyr, and a secondary peak at slightly > 2 Gyr. The peaks are followed by an extensive tail towards older ages. Given that our synthetic distributions shown in §3.4 were created by sampling galaxies with only two age variations, we conclude that the compact sample, with a histogram that displays such a long tail towards older ages is likely to represent a population with a broader range of ages than the control sample.

The Compact & Light and Control & Light histograms shown in Figure 4.5 display significant overlap in their interquartile ranges, much like the Heavy & Light subsamples. The error bars are also the largest of any of our subsamples. This is not surprising, as the signal-to-noise

of the galaxies with $M_* < 10^{11} M_\odot$ is significantly lower than the signal-to-noise of the higher mass galaxies.

4.2.3 Smooth & Bulge-Dominated Galaxies

The results for this sample (selected on the basis of high bulge-to-total ratio and smooth morphology) are shown in Figures 4.6 through 4.9.

Figure 4.6 shows the Compact and Control subsamples, which have similar, overlapping histograms and overlapping interquartile ranges. The Compact subsample, which has a nominal age of 6.97 Gyr, displays three main peaks in its histogram: the first at ~ 3.2 Gyr, the second (most prominent) at ~ 5 Gyr, and the third at ~ 7 Gyr. The Control subsample has a nominal age of 3.81 Gyr (note that the error bars for the nominal ages overlap by about 1 Gyr). It displays two main peaks: the first prominent one at ~ 3 Gyr and the second at ~ 5 Gyr.

The Heavy and Light subsamples, shown in Figure 4.7 also have overlapping histograms and interquartile ranges. Interestingly, the nominal age and error on the nominal age for the Heavy subsample falls almost entirely within the lower error bar for the nominal age of the Light subsample.

Figure 4.8 shows the Compact & Heavy and Control & Heavy subsamples for the SBD and RSBD samples (when the mass division was implemented, these samples contained identical Heavy galaxies). The Compact & Heavy sample has a nominal age of 7.27 Gyr and a median age of 6.69 Gyr. The Control & Heavy sample has a nominal age of 3.51 Gyr, over 3.75 Gyr younger than the Compact & Heavy subsample, and a median age of 3.68. Although there is some overlap between the interquartile ranges of the histograms and between the error bars for the nominal ages, the histogram shapes are very distinct. The Compact & Heavy galaxies show three peaks: a very small one at ~ 1.8 Gyr, a slightly higher one at ~ 3 Gyr, and the highest one near the nominal/median age of ~ 7 Gyr. The Control & Heavy galaxies have the same small peak at ~ 1.8 Gyr, and a larger prominent peak around ~ 3 Gyr. This is followed by a tail with what could be considered two smaller peaks at ~ 5 and ~ 6 Gyrs.

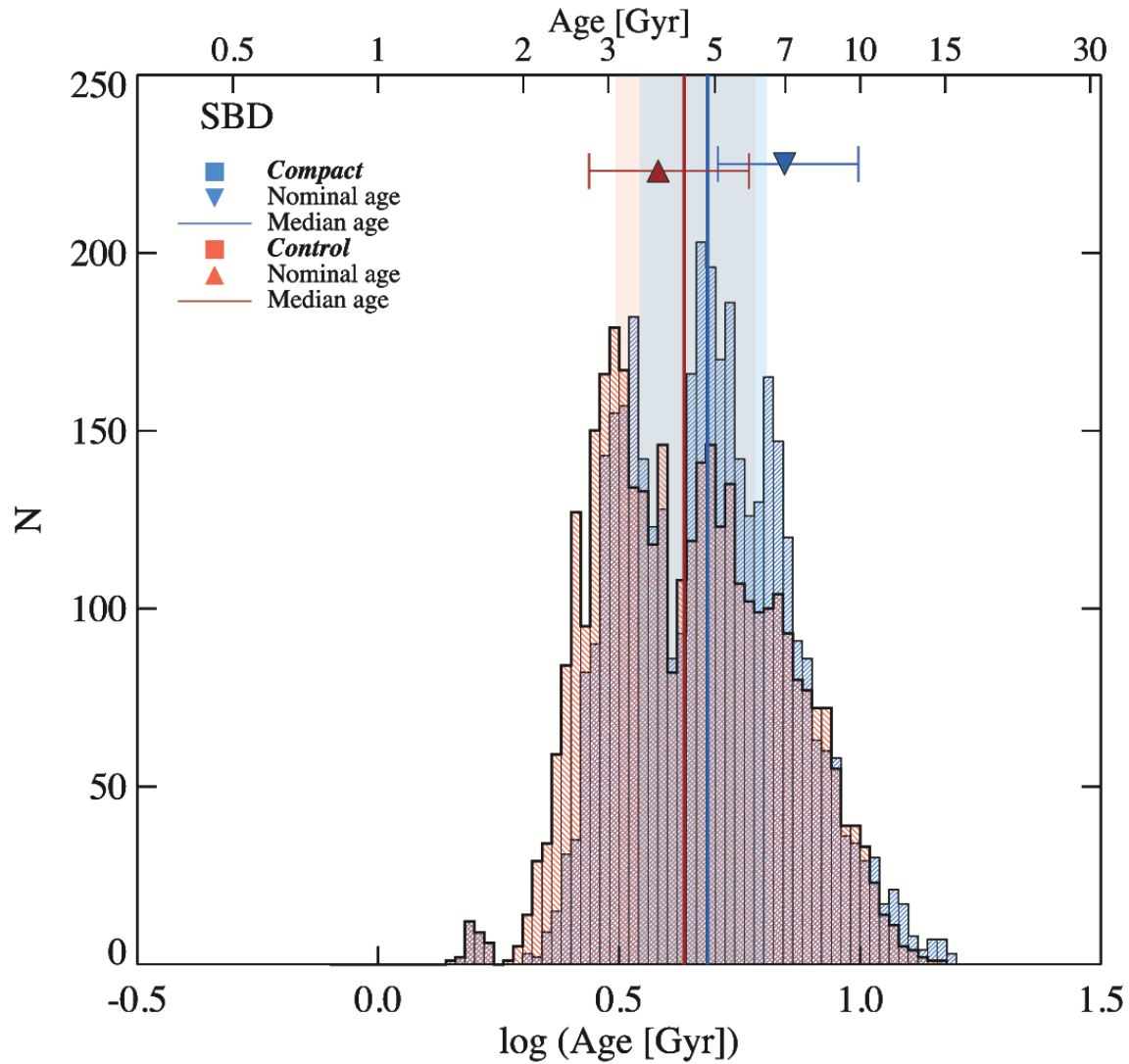


Figure 4.6: Age histograms generated from bootstrapping the Compact (blue) and Control (red) galaxies in the “Smooth, & Bulge-Dominated (SBD) Sample” 4000 times each. The histograms have bin size 0.02 in $\log(\text{age (Gyr)})$. The median ages of the histograms are marked with a solid line of the same color as the histogram it is measured from. The interquartile range, a measure of dispersion which encompasses 25% of the data points on either side of the median age, is shown by a semi-transparent band in the same color as the histogram. Measured nominal ages from the original (non-resampled) co-added subsamples are demarcated by symbols of the same colors with errors estimated by `EZ_Ages` using the signal-to-noise spectrum to determine the measurement error of the Lick index line strengths.

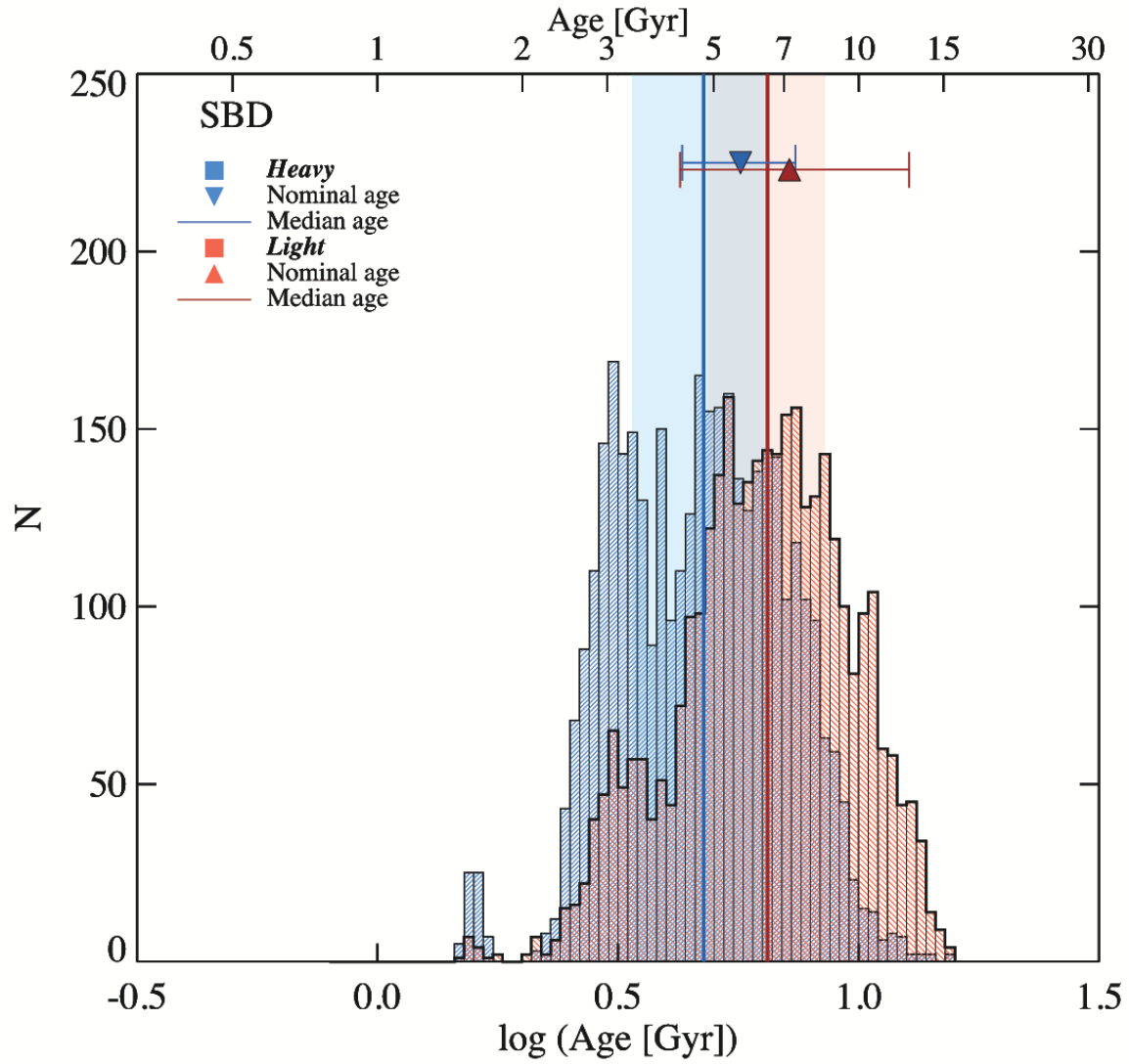


Figure 4.7: Age histograms generated from bootstrapping the Heavy (blue) and Light (red) galaxies in the “Smooth, & Bulge-Dominated (SBD) Sample” 4000 times each. The histograms have bin size 0.02 in $\log(\text{age (Gyr)})$. Symbols are as described in Figure 4.6.

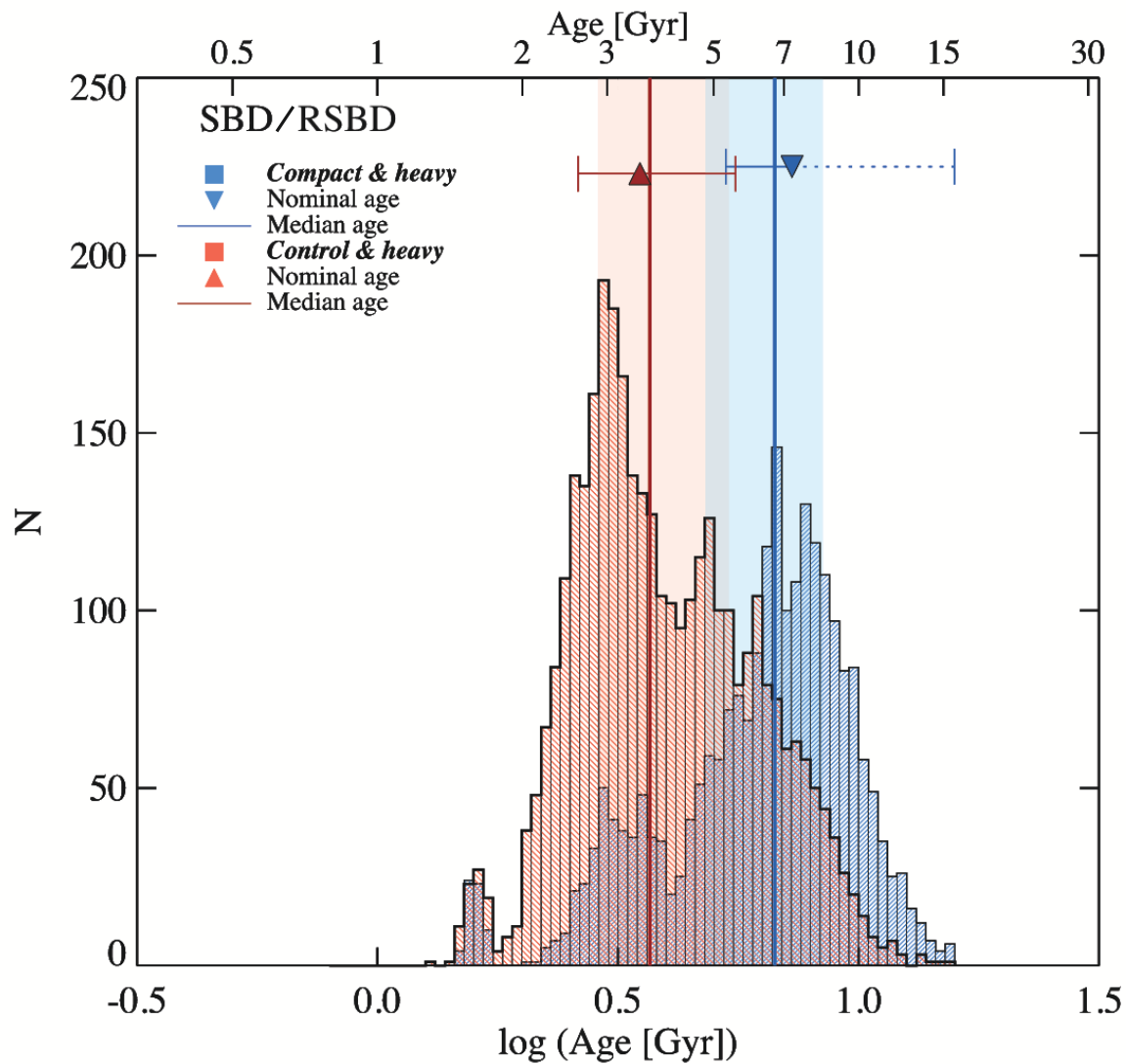


Figure 4.8: Age histograms generated from bootstrapping the Compact and Heavy (blue) and Control and Heavy (red) galaxies in the “Smooth, & Bulge-Dominated (SBD) Sample” and the “Red, Smooth, & Bulge-Dominated (RSBD) Sample” 4000 times each. The histograms have bin size 0.02 in $\log(\text{age (Gyr)})$. Symbols are as described in Figure 4.6. The positive age limit for the Compact and Heavy sample cannot be calculated by EZ_Ages because it exceeds the maximum 15.8 Gyr age of the models.

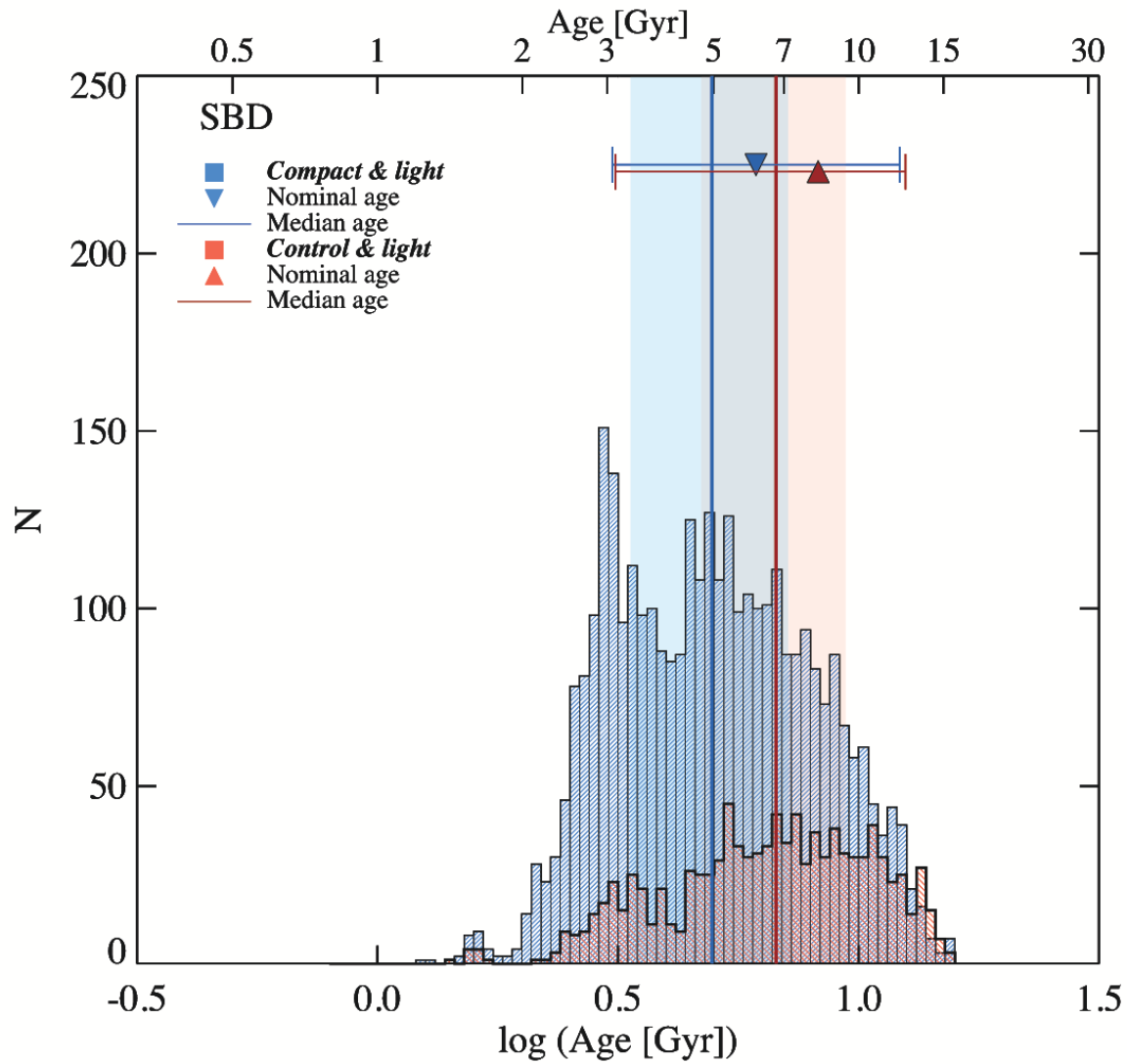


Figure 4.9: Age histograms generated from bootstrapping the Compact and Light (blue) and Control and Light (red) galaxies in the “Smooth, & Bulge-Dominated (SBD) Sample” 4000 times each. The histograms have bin size 0.02 in $\log(\text{age (Gyr)})$. Symbols are as described in Figure 4.6.

Finally, in Figure 4.9, we see that the histograms from the Compact & Light and Control & Light subsamples are quite broad and overlap significantly. Both nominal ages for these subsamples have very large errors. We again conclude that the poor signal-to-noise for the Light galaxies makes it difficult to draw conclusions from the bootstrapping procedure.

4.2.4 Red, Smooth & Bulge-Dominated Galaxies

The results for this sample (selected on the basis of high bulge-to-total ratio, smooth morphology, and red color) are shown in Figures 4.10 through 4.12, as well as Figure 4.8.

Figure 4.10 shows the Compact and Control subsamples, which have nearly identical histogram shapes and large overlap between their interquartile ranges. The nominal age of the Compact subsample is 6.73 Gyr, and the nominal age for the Control subsample is 4.24. There is also overlap between the lower error of the Compact nominal age and the upper error of the Control nominal age.

Both subsequent histogram comparisons (of the Heavy and Light subsamples in Figure 4.11 and the Compact & Light and Control & Light subsamples in Figure 4.12) show similar results, with overlapping, similarly-shaped histograms and nominal ages that have large errors. The Control & Light subsample shows a particularly broad histogram, much like its counterpart in the SBD sample. Indeed, the only subsample comparison that shows a marked difference in histogram shape and nominal age measurement is the one shown earlier in Figure 4.8.

4.3 Overview of the Results

The previous section illuminated two important facts:

1. Low mass galaxies ($M_* < 10^{11} M_\odot$) simply have too low a signal-to-noise ratio to let us draw significant conclusions from them, even with our co-adding/bootstrapping procedure.
2. We are able to make meaningful inter-comparisons between two subsamples of massive galaxies: (a) RBD Compact & Heavy vs. RBD Control & Heavy (Figure 4.4); and (b)

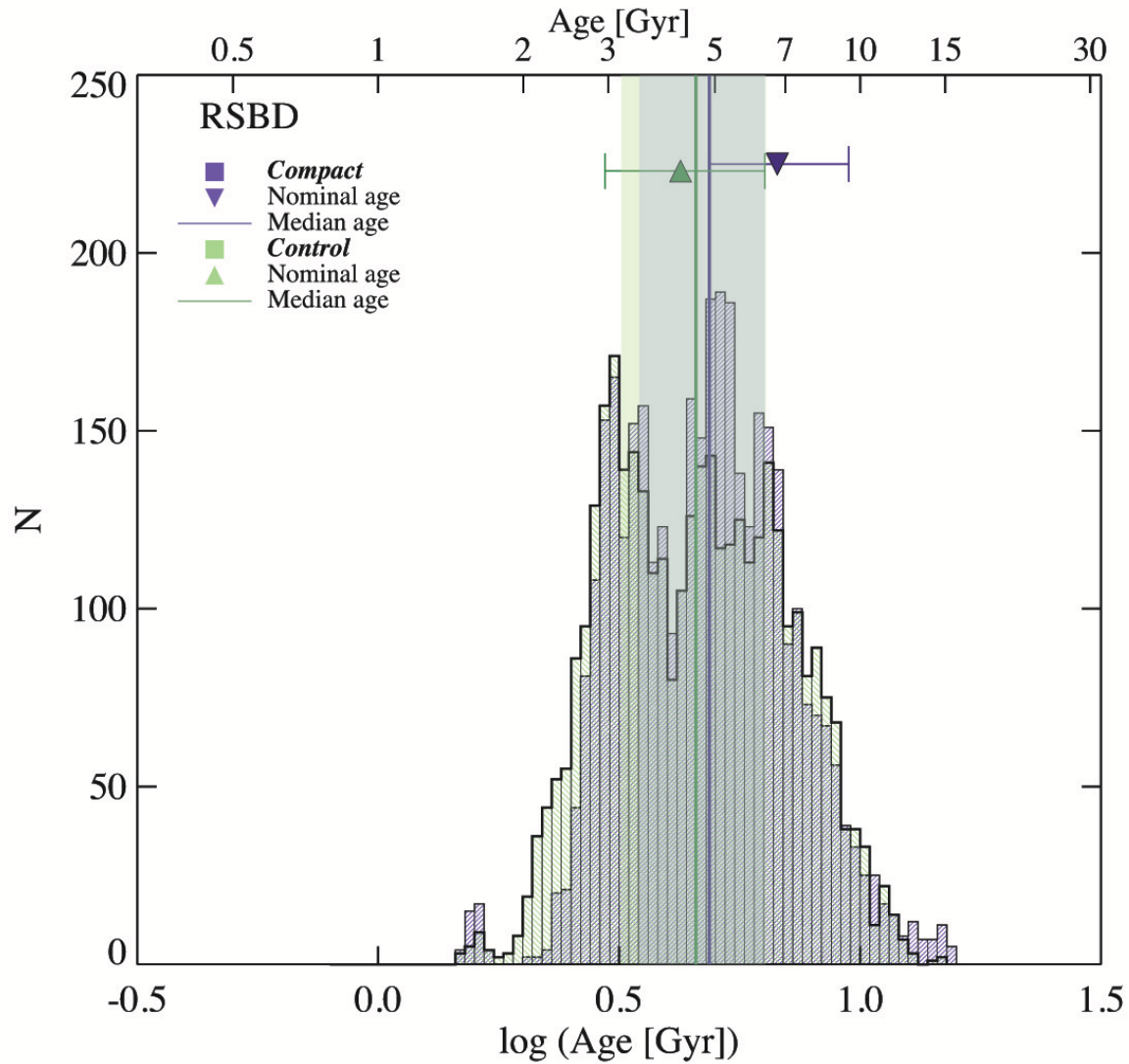


Figure 4.10: Age histograms generated from bootstrapping the Compact (purple) and Control (green) galaxies in the “Red, Smooth, & Bulge-Dominated (RSBD) Sample” 4000 times each. The histograms have bin size 0.02 in $\log(\text{age (Gyr)})$. The median ages of the histograms are marked with a solid line of the same color as the histogram it is measured from. The interquartile range, a measure of dispersion which encompasses 25% of the data points on either side of the median age, is shown by a semi-transparent band in the same color as the histogram. Measured nominal ages from the original (non-resampled) co-added subsamples are demarcated by symbols of the same colors with errors estimated by `EZ_Ages` using the signal-to-noise spectrum to determine the measurement error of the Lick index line strengths.

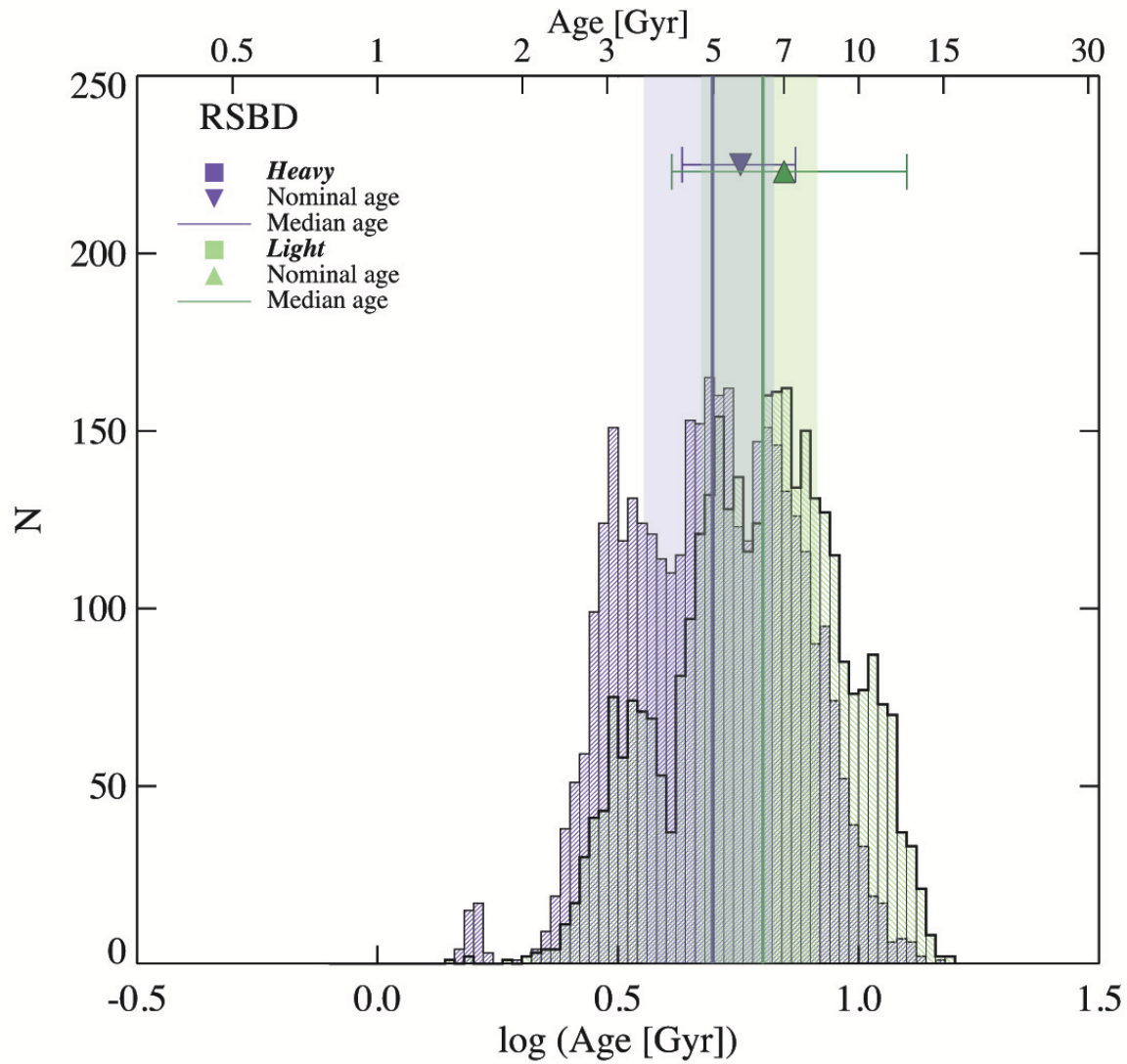


Figure 4.11: Age histograms generated from bootstrapping the Heavy (purple) and Light (green) galaxies in the “Red, Smooth, & Bulge-Dominated (RSBD) Sample” 4000 times each. The histograms have bin size 0.02 in $\log(\text{age (Gyr)})$. Symbols are as described in Figure 4.10.

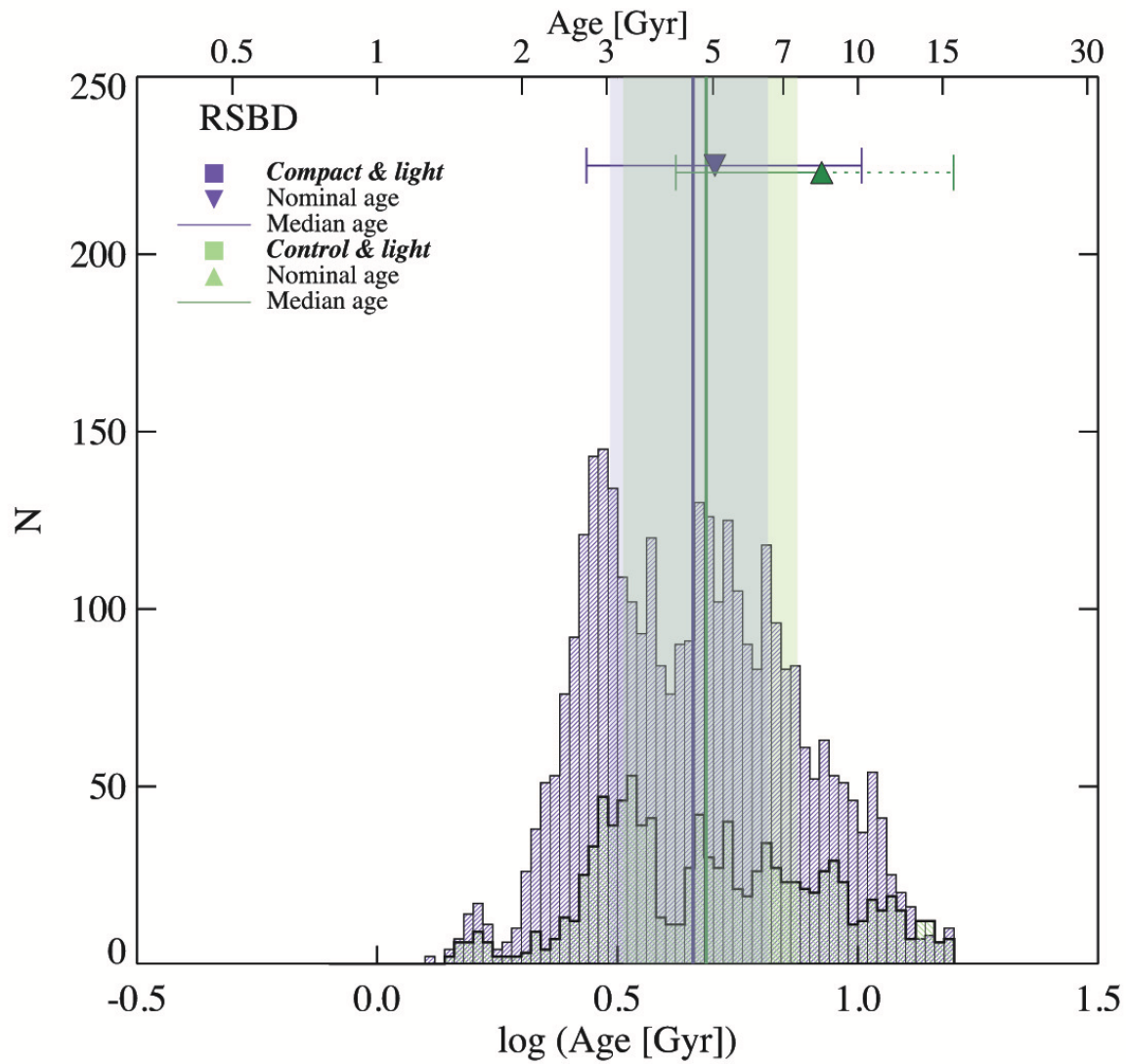


Figure 4.12: Age histograms generated from bootstrapping the Compact and Light (purple) and Control and Light (green) galaxies in the “Red, Smooth, & Bulge-Dominated (RSBD) Sample” 4000 times each. The histograms have bin size 0.02 in $\log(\text{age (Gyr)})$. Symbols are as described in Figure 4.10. The positive age limit for the Control and Light sample cannot be calculated by EZ_Ages because it exceeds the maximum 15.8 Gyr age of the models.

SBD/RSBD Compact & Heavy vs. SBD/RSBD Control & Heavy (Figure 4.8). These figures can be considered our most compelling results, and we will the focus of our analysis and discussion for the remainder of this thesis.

A Kolmogorov-Sminrov test indicates that for both the RBD and the RSBD Heavy samples there is $< 1\%$ likelihood that the null hypothesis – that the compact and control subsamples come from the same population – is correct. However, because of the overlap between the interquartile ranges of the RSBD subsample, we are cautious in interpreting the results as being indicative of significant differences in the mean ages of the populations. The story these figures tell is of significant differences in the diversity of the subsamples, where in this context we refer to ‘diversity’ to mean a mix in the star formation histories of the galaxies defining the subsets.¹

It is tempting to attribute the age difference between the SBD/RSBD Compact & Heavy and Control & Heavy samples to the fact that the two samples have statistically different redshift distributions before the co-addition was performed (see, for reference, Table 2.3 and row 3 in Figure 2.5). However, Figure 2.17 makes the important point that at the wavelengths of most key spectral features (e.g. $H\beta$ and $\langle Fe \rangle$) the mean redshift of the co-added galaxies is very similar for both samples, so that once the galaxies have been co-added (after appropriate normalization) the initial differences in the redshift distributions are not very meaningful.

Nevertheless, as a sanity check, we performed the bootstrap resampling on a subset of the Control & Heavy sample which was more matched in redshift to the Compact & Heavy sample. To do this, we reduced the number of galaxies at $z > 0.8$ in the Control & Heavy sample such that the two distributions are the same from $0.8 < z < 1.3$. The result of bootstrapping this new Control subset in comparison to the Compact & Heavy can be seen in Figure 4.13. Figure 4.14 shows the histogram of ages for the original Control & Heavy subset overlaid with the new redshift-matched subset. The nominal age of the redshift-matched Control & Heavy sample was 5.45 Gyr, or 1.9 Gyr older than the nominal age of the original Control & Heavy sample.

¹We should also note that the range of recovered ages extends beyond the age of the Universe over the redshift range of several of the samples, as the age of the Universe is ~ 8.6 Gyr at the lowest redshift of 0.5.

The median age of the bootstrap resample did not change as drastically, increasing only by 0.75 Gyr. The shape of the histogram was not significantly altered, either. We therefore conclude that the redshift differences are responsible for some, but not all, of the age differences seen in this sample.

Next, we note that although the nominal age for the SBD/RSBD Control & Heavy sample is ~ 0.7 Gyr older than the nominal age for the RBD Control & Heavy sample, the bootstrap resampling age histograms for both of these control samples are similar. The control histograms show a tiny peak at ~ 1.5 Gyr, and then a strong peak at its modal age, with a declining tail to older ages. This looks much like our synthetic population with 60% 7 Gyr old galaxies and 40% 2 Gyr old galaxies.

The SBD/RSBD Compact & Heavy sample, on the other hand, does not share a distribution shape that is distinctly similar to any of the synthetic populations: although the synthetic distribution with 40% old galaxies displays three peaks, its peaks are located at different ages and have differing heights. We believe this implies that the stellar populations of the compact galaxies are less homogeneous than that of the control galaxies, but this conjecture remains mostly at a qualitative level.

The main important point that emerges from Figures 4.4 and 4.8 is the fact that whether the compact galaxies are older or younger than the control galaxies depends on the method used to define that sample of early-type galaxies. This result echoes that of Moresco et al. (2013), who reached similar conclusions coming from a completely different direction, using photometric data from zCOSMOS 20-k sample.

4.4 Characterizing the contributing galaxies

As a sanity check, we looked at the number of times each galaxy in a given subsample contributed to one of the co-added spectra. As the number of bootstraps increase, we would expect any given galaxy to contribute roughly the same number of times as any other given galaxy. However, because co-added spectra that fall off the model grids are excluded from our age analysis, this

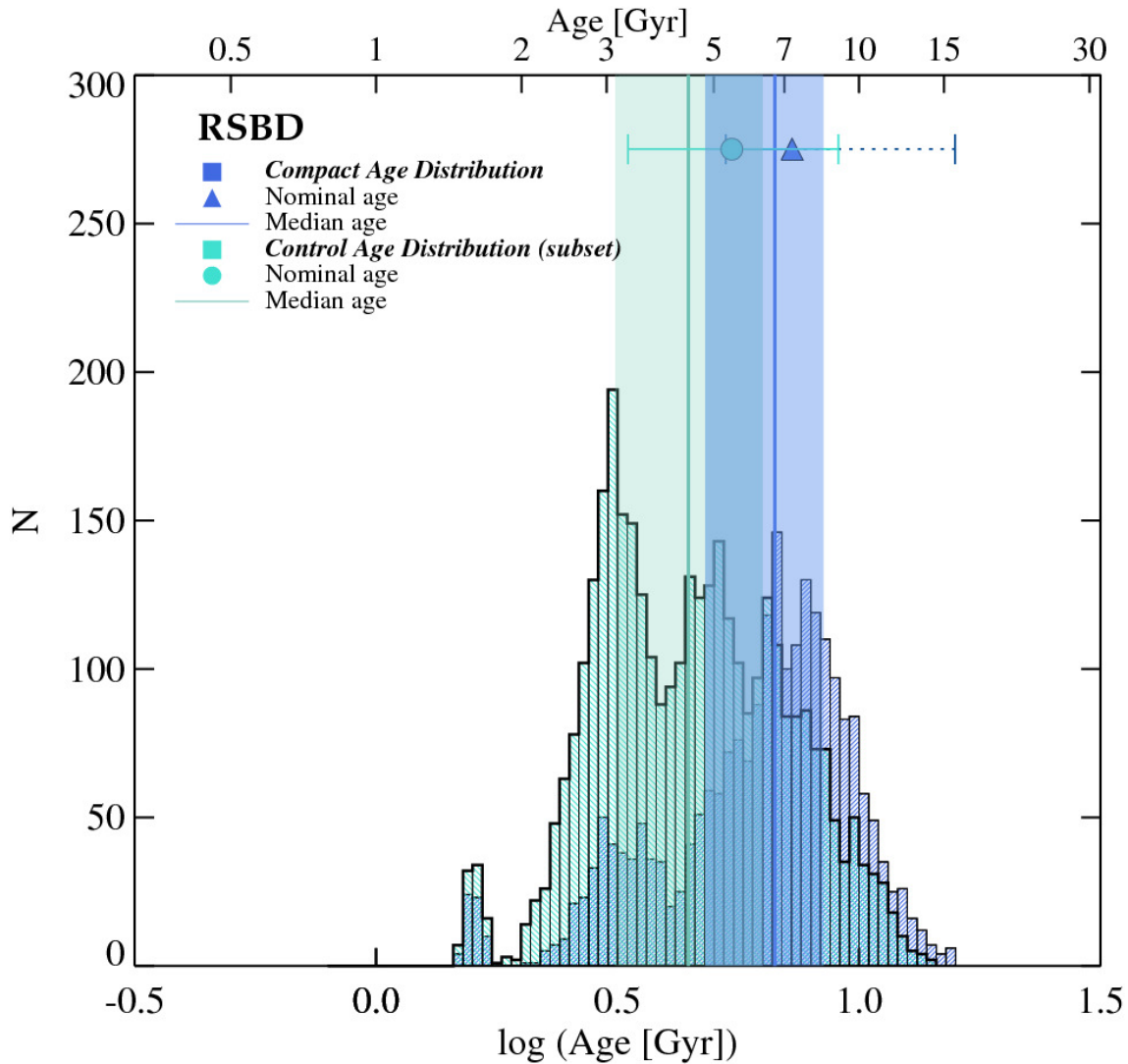


Figure 4.13: Age histograms generated from bootstrapping the Compact (blue) and a redshift-matched subset of the Control (teal) galaxies in the “Red, Smooth, & Bulge-Dominated (RSBD) Sample” 4000 times each. The histograms have bin size 0.02 in $\log(\text{age (Gyr)})$. Measured nominal ages from the original (non-resampled) co-added subsamples are demarcated by symbols of the same colors. The errors are estimated by `EZ_Ages` using the signal-to-noise spectrum to determine the measurement error of the Lick index line strengths. The positive age limit for the Compact sample cannot be calculated by `EZ_Ages` because it exceeds the maximum 15.8 Gyr age of the models. The median ages from the bootstrap resamples are marked with a solid line of the same color as in the histogram. The interquartile range, a measure of dispersion which encompasses 25% of the data points on either side of the median age, is shown by a semi-transparent band in the same color as the histogram it is measured from.

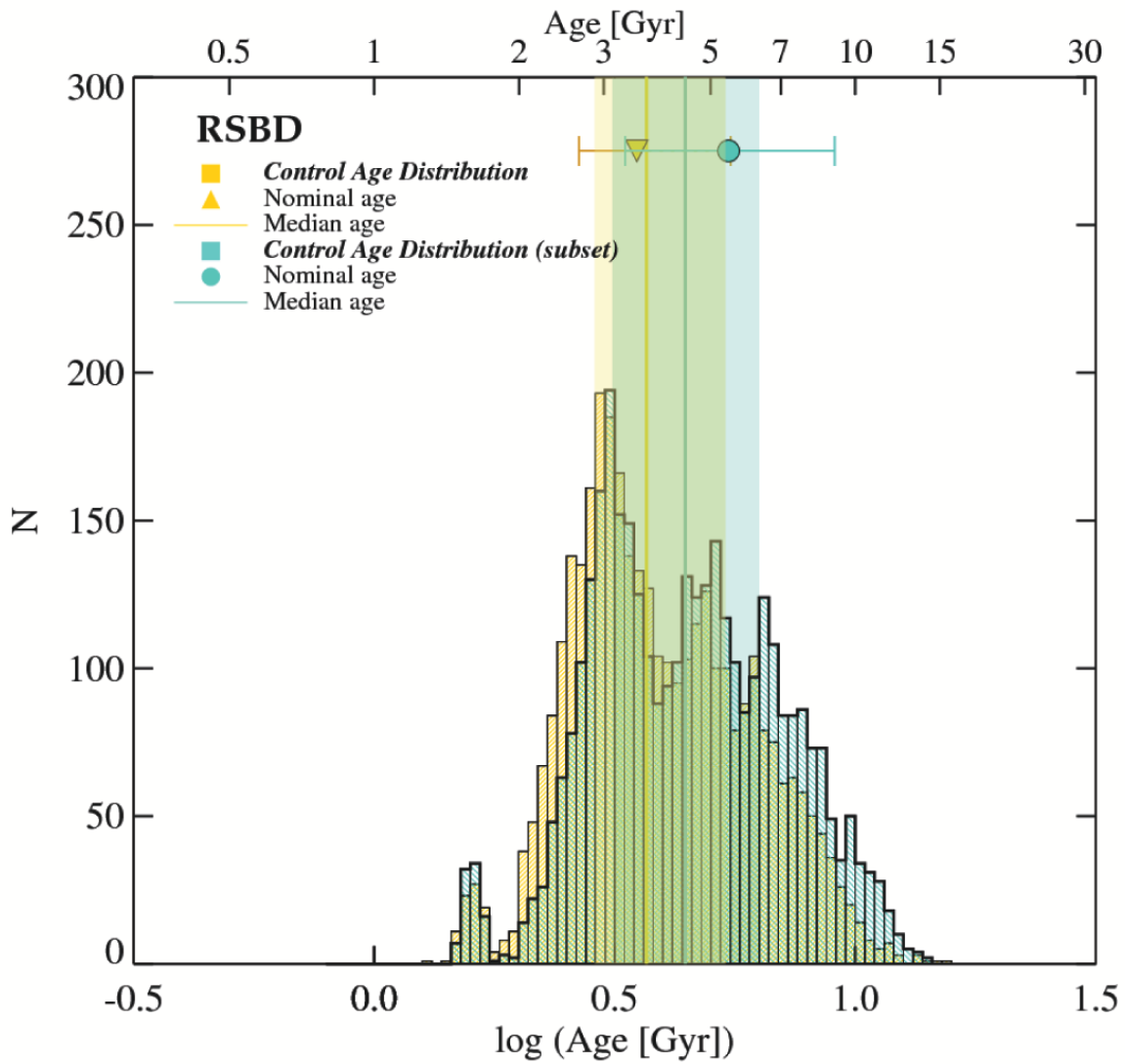


Figure 4.14: Comparison of the age histograms generated from bootstrapping the entire set of Control galaxies (yellow) and a subset of the Control galaxies which have been matched in redshift to Compact galaxies (teal) in the “Red, Smooth, & Bulge-Dominated (RSBD) Sample” 4000 times each. Symbols as described in Figure 4.13.

introduces opportunity for certain galaxies to appear more or less often than others. For the RBD and RSBD Compact & Heavy and Control & Heavy subsamples, we examine the galaxies that contribute to the entire histogram of bootstrap ages (with age < 15 Gyr) as well as only those spectra with ages measured above the median bootstrap age and below the median bootstrap age. The full results are shown in Appendix B. Here, we show only the the RSBD Control & Heavy results for ages above and below the median bootstrap age (Figures 4.15 and 4.16). In each figure, the 8-digit DEEP ID of the galaxy is labeled on the x-axis. The dotted and dashed lines indicate 1σ and 3σ variations respectively from the average number of contributing galaxies, which is indicated by the solid line.

Galaxy 12016360 (shown in Figure 4.17 is of particular interest: it contributes both weakly to the SBD/RSBD Control & Heavy bootstraps with ages less than the median age, and strongly to the same subsamples when ages are greater than the median age. We can conclude, then, that this galaxy almost certainly contains a predominantly old stellar population.

4.5 Correlation between “smoothness” and age

When we compare the measured ages of our samples defined without a measure of image smoothness (Red, Bulge-Dominated sample) to those selected with the smoothness criterion (Red, Smooth, & Bulge-Dominated sample), the ages of both the compact and control subsamples of the RBD subsamples are younger than the ages of both the compact and control RSBD subsamples, although the ages of the RBD and RSBD Control samples are consistent with each other within a $1-\sigma$ uncertainty. However, the significant age difference between the Compact samples reveals a correlation between the “smoothness” and age (at least for compact galaxies): smoother galaxies are older than clumpier ones.

Such a result is not unexpected, as the RSBD sample was particularly chosen to minimize contamination from S0/Sa type galaxies; as such, we considered the possibility that such galaxies are contaminating the population selected in the RBD sample. We visually inspected images of the galaxies in both of our samples in order to discern whether we had such contamination.

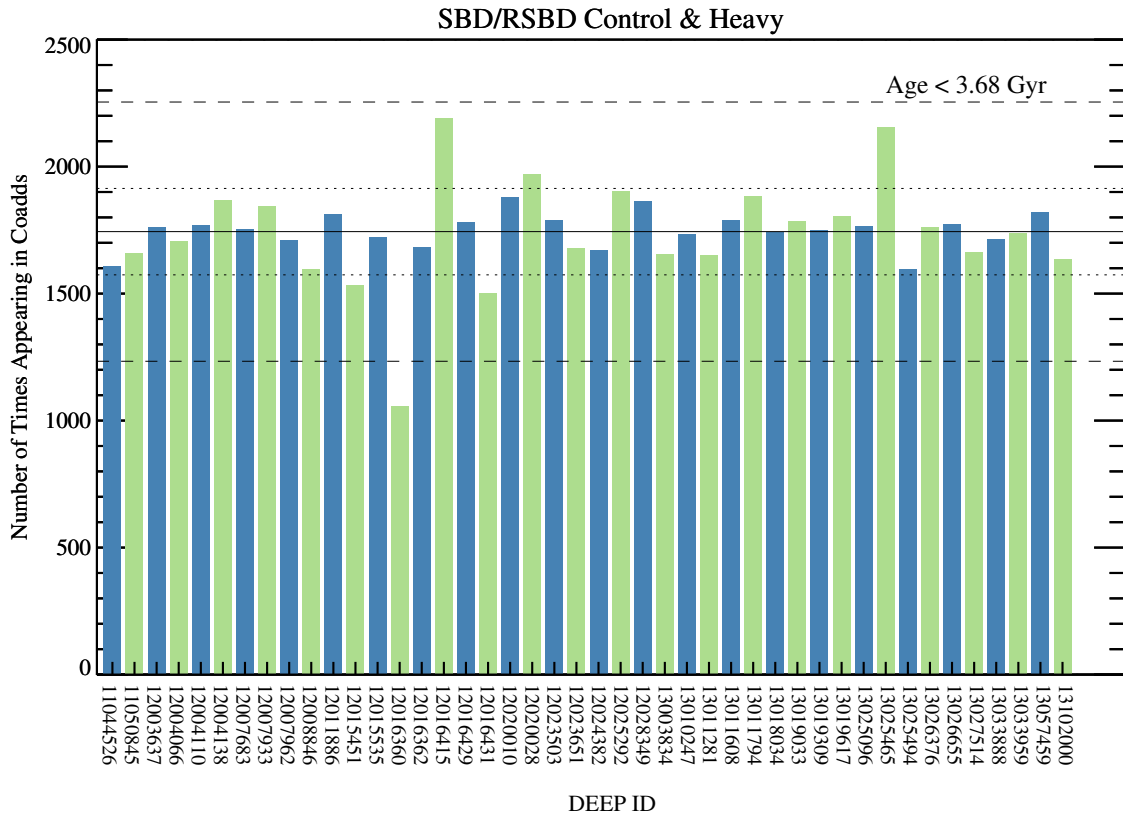


Figure 4.15: The number of galaxies contributing to the co-added bootstrapped spectra for the SBD/RSBD Control & Heavy subsample for ages < 3.68 Gyr, the median bootstrap age. The solid line denotes the mean number of contributing galaxies. The dotted and dashed lines indicate 1 and 3σ variations respectively from the average number of contributing galaxies. Here, one galaxy (with DEEP ID 12016360) contributes fewer than the mean minus 3σ. Note that this is the same galaxy which also under-contributed to the RBD Control & Heavy subsample with ages less than the median bootstrap age.

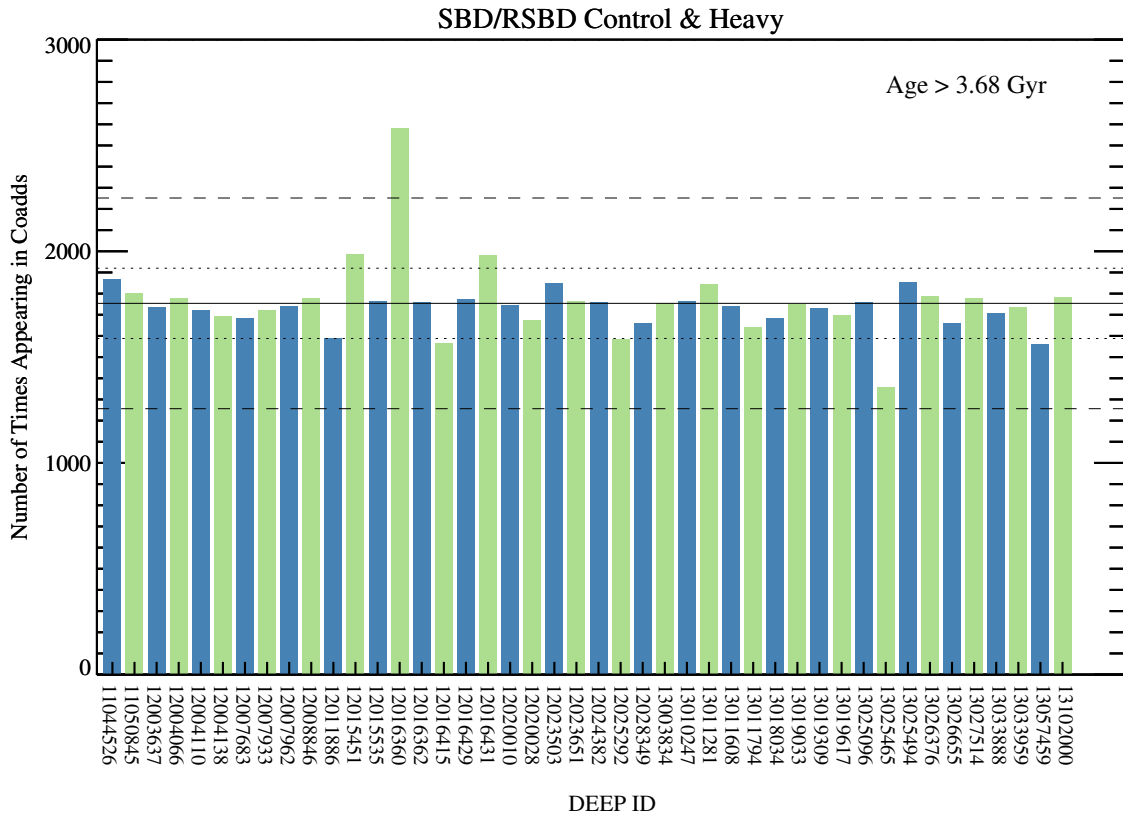


Figure 4.16: The number of galaxies contributing to the co-added bootstrapped spectra for the SBD/RSBD Control & Heavy subsample for ages > 3.68 Gyr, the median bootstrap age. The solid line denotes the mean number of contributing galaxies. The dotted and dashed lines indicate 1 and 3 σ variations respectively from the average number of contributing galaxies. Here, one galaxy (with DEEP ID 12016360) contributes more than 3 σ over the mean. Note that this is the same galaxy which under-contributed to this sample when the ages were less than the median age, and also over-contributed to the RBD Control & Heavy subsample with ages great than the median bootstrap age.

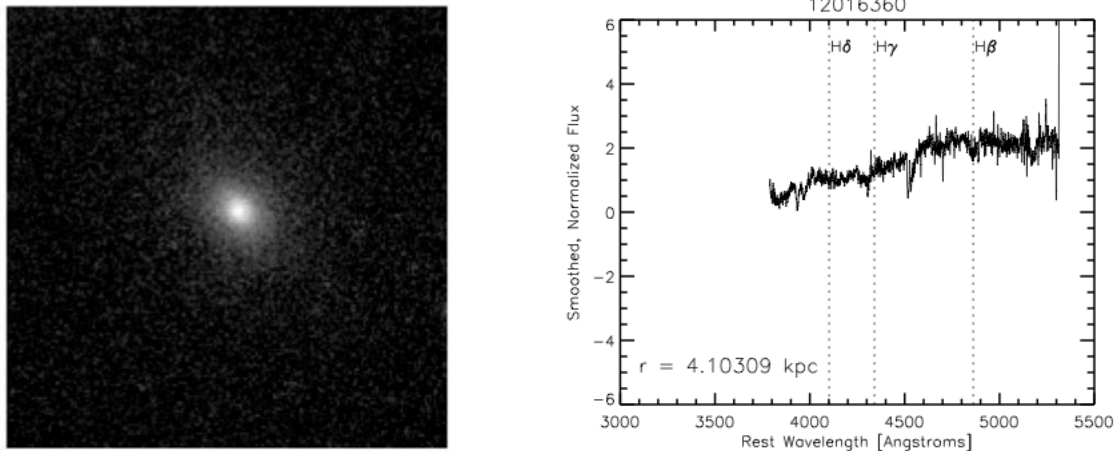


Figure 4.17: DEEP ID 12016360 (image on the left, spectrum on the right) contributes strongly to the co-additions with ages greater than the median age for the RBD, SBD, and RSBD Control & Heavy subsample, and also contributes weakly to co-additions with ages less than the median age for the same subsamples.

The following fractions of galaxies were identified to be probably spiral or lenticular galaxies: $\frac{2}{25}$ (8%) in the RBD Compact & Heavy subsample, $\frac{6}{53}$ (11.3%) in the RBD Control & Heavy subsample; $\frac{1}{25}$ (4%) in the RSBD Compact & Heavy subsample, and $\frac{2}{44}$ (4.5%) in the RSBD Control & Heavy sample. Images and spectra for these galaxies, along with average representative images and spectra, are attached in Appendix A. The higher percentage of galaxies identified as non-ellipticals in the RBD sample confirms that there is a degree of contamination that is less present in the RSBD sample, and at least partially explains the younger overall ages of the RBD subsamples. The RBD Compact & Heavy galaxies tend to have a slightly higher redshift than the RSBD Compact & Heavy galaxies, which may partially explain their older ages. However, a K-S test between these two distributions indicates that they are not statistically different. Furthermore, the redshift for both samples declines in a similar way within the co-added spectra, as seen in Figures 2.16 and 2.17. We therefore conclude that this is unlikely to explain much of the age difference.

In effect, our results are consistent with the simple idea that adding a disk component to a galaxy decreases its smoothness, and since the disk is likely to be younger than the bulge of

the galaxy, adding a disk also lowers the galaxy's mean age. However, it is harder to explain why the effect appears to be differential in nature, with the ages of larger early-type galaxies being relatively insensitive to smoothness. The addition of a small disk might be expected to make a bigger difference to the observed size and clumpiness of a compact galaxy than it would to a relatively large galaxy, which might explain at least part of this effect. In any case, higher resolution observations of compact galaxies that clearly show the existence of disks in these systems and allow their sizes to be measured as part of a multi-component model would allow these ideas to be tested.

Chapter 5

Conclusions & Future Work

5.1 Conclusions

5.1.1 Defining an “early-type galaxy” and the influence of “progenitor bias”

It is clear from the differing age measurements obtained in our samples that investigations of stellar populations at high redshifts must be very careful in definitions of what is meant by an ‘early-type galaxy’ in order to avoid bias. Morphology matters, in addition to color. Yet few of the studies mentioned in the introduction (§1.1 – 1.3; e.g. Trujillo et al. (2011); Chevance et al. (2012); Whitaker et al. (2012); Huertas-Company et al. (2013)) employ a measure of image smoothness in their sample selection. Our Red and Bulge-Dominated sample is closer than our Red, Smooth, and Bulge-Dominated sample to the selection generally used by investigations which discuss the size evolution of massive galaxies, as most of the studies employ some measure of morphology (but rarely smoothness) and/or color in selecting their samples.

For example, Chevance et al. (2012), who investigated the structure of compact massive quiescent galaxies at $z \sim 2$, used the same $B/T > 0.5$ and $S2 \leq 0.075$ cuts as our RSBD sample (though without the color cut), but only for selecting their local early-type galaxy sample. For their high redshift sample, they utilized the color-selected samples of van der Wel et al. (2011)

and a variety of surveys compiled by Damjanov et al. (2011) which provides an overview of the selection criteria used by each. Of the 16 spectroscopic surveys examined in Damjanov et al. (2011), eight are spectroscopically selected objects with old stellar populations (Saglia et al. 2010; van der Wel et al. 2008; Longhetti et al. 2007; Damjanov et al. 2011; 2009; Cimatti et al. 2008; Daddi et al. 2005; van Dokkum et al. 2008), four are morphologically selected ETGs (Schade et al. 1999; Treu et al. 2005; Bundy et al. 2007; Newman et al. 2010; Gargiulo et al. 2011; Saracco et al. 2011), and four are quiescent galaxies selected by color (Rettura et al. 2010; Ryan et al. 2012; Carrasco et al. 2010; Cassata et al. 2010).

Trujillo et al. (2011), who observe that that smaller galaxies (at fixed stellar mass) are *not* older than the larger galaxies, use a sample of visually-classified ETGs from the GOODS and SDSS datasets. Whitaker et al. (2012) used color cuts to isolate samples of recently-quenched galaxies from the NEWFIRM Medium-Band Survey, and found that younger quiescent galaxies are not larger, and in fact may be somewhat smaller, than older galaxies at a fixed redshift. Huertas-Company et al. (2013) studied morphologically-selected quiescent ETGs from the COSMOS survey from $z \sim 1$ to the present and found that galaxy size-mass relation and size growth do not depend on environment. Most recently, Morishita et al. (2014) select quiescent galaxies from the MOIRCS Deep Survey and *HST*/WFC3 CANDELS data in the GOODS-N region using rest-frame colors and find the size growth for massive quiescent galaxies to be consistent with previous studies, at a factor of ~ 2.5 increase from $z \sim 2.5$ to $z \sim 0.5$ at a given stellar mass. Using spectroscopy and photometry from 3D-HST and imaging from CANDELS, van der Wel et al. (2014) used rest-frame colors to isolate quiescent galaxies and showed that the number density of small, compact ETGs strongly decreases between $z \sim 1.5$ and the present.

Other studies have concluded that the method of choosing ‘early-type’ galaxies is important. Our central idea is consistent with Bernardi et al. (2010), who compared samples selected using photometric and spectroscopic information with those based on morphological information and find that samples selected on the basis of colors alone run the risk of being highly contaminated by edge-on disks, which are the reddest objects at intermediate luminosities or stellar masses.

They suggest that the additional requirement of an axis ratio selection $b/a \geq 0.6$ would provide a simple way to select relatively clean early-type samples in high redshift datasets. We find our results are in strong agreement with Moresco et al. (2013): they selected six samples of early-type galaxies up to $z = 1$ from the zCOSMOS-20k spectroscopic survey and analyzed the samples' photometric, spectroscopic, and morphological properties. Their samples were based on morphology, optical colours, specific star formation rate, a best-fit to the observed spectral energy distribution, and a criterion which combined morphological, spectroscopic, and photometric information. They found that the level of contamination from blue, star-forming, or otherwise non-passive outliers was highly dependent on the method by which the sample was selected. The sample selected by morphological criteria (a combination of principal component analysis of five nonparametric diagnostics of galaxy structure and a parametric description of galaxy light) displayed the highest percentage of contamination and showed significant emission lines in the median stacked spectra. The sample that displayed the least amount of contamination was the one selected to be 'purely passive' by combining multiple selection criteria using morphology, spectroscopy, and photometry. They also found a strong dependence of the contamination on stellar mass, and concluded that regardless of the adopted selection criteria, a significantly purer sample can be obtained with a cut at $M > 10^{10.75} M_{\odot}$.

As described earlier, massive compact early-type galaxies selected on the basis of red colors and high B/T ratios display younger ages than the control sample of larger galaxies at similar redshifts and in a similar mass bin. As 'progenitor bias' posits that younger galaxies are larger at fixed mass, we therefore conclude that progenitor bias cannot account for the size growth of compact galaxies, as defined by our RBD selection, and that the individual galaxies experience growth as their stellar populations age. However, the RBD sample is only one reasonable way to isolate early-type galaxies. Using other approaches, we arrive at a different conclusion.

Compact galaxies which are selected on the basis of image smoothness and high B/T ratios display older ages than the control sample of larger galaxies, a result which is consistent with the size growth explanation of progenitor bias. In their recent paper, Carollo et al. (2013) use

the large COSMOS survey to argue that progenitor bias can explain most of the observed size growth of compact galaxies, with size changes due to merging and other processes being of secondary importance, particularly for objects with masses below $10^{11}M_{\odot}$. We conclude that progenitor bias can indeed play a significant role in explaining the apparent size growth of early-type galaxies, but only if they are selected on the basis of the smoothness of their light distributions. The importance of progenitor bias in driving the growth of galaxies is surprisingly sensitive to these sorts of details.

5.2 Future Work and Directions

5.2.1 Determining the local nugget fraction

One of the principal next steps is to more completely characterize the change in number density of compact systems with redshift. Recent searches for local compact galaxies have shown some differing results. Initial investigations by Trujillo et al. (2009) and Taylor et al. (2010) using SDSS suggest that at $z < 0.2$, the number density of compact galaxies is more than three orders of magnitude smaller than at $z \sim 2$. However, Valentinuzzi et al. (2010b) found that in the nearby ($z \sim 0.05$) WINGS galaxy cluster sample, compact massive galaxies represent nearly 22 % of all cluster members with stellar mass range $3 \times 10^{10} \leq M_{*/M_{\odot}} \leq 4 \times 10^{11}$, and they derive a lower limit on the number density which is comparable to the number density at high redshift. Using PM2GC, Poggianti et al. (2013b;a) suggest that there is little difference between the number density of compact galaxies in the field at $0.03 < z < 0.11$ and the number density at high redshift. Using a sample of ~ 200 compact galaxies drawn from the Baryon Oscillation Spectroscopic Survey (BOSS), Damjanov et al. (2014) find that the abundance of compact quiescent galaxies at $0.2 < z < 0.6$ is consistent with the number densities of the most massive compact systems at high redshift. Looking next at the COSMOS field, Damjanov et al. (2015) find that the compact galaxy number density is constant in the interval $0.2 < z < 0.8$, and that the number density is similar to estimates at $z > 1$.

If, as Carollo et al. (2013) suggests, many local compact galaxies are indeed simply misclassified or missing from the Sloan Digital Sky Survey due to seeing, this would not be the case with data from the Canada-France-Hawaii Telescope Legacy Survey (CFHTLS). CFHTLS has a wide area and sufficient resolution to complement the analyses based on HST imaging. We suggest an analysis of the local fraction of compact early-type galaxies in a survey such as CFHTLS would be a useful addition to the studies outlined above.

5.2.2 High Quality Spectra, Measuring Chemical Abundances, and Star Formation History

Obtaining extremely high quality spectra of massive compact galaxies is extremely difficult, yet it is crucial to understanding their place in our schema of galaxy evolution. Some spectroscopy has already been done: Belli et al. (2014a) used the Keck LRIS spectrograph to obtain high signal-to-noise spectra of 62 massive ($\log M_*/M_\odot > 10.7$) galaxies at $1 < z < 1.6$. Their sample includes several compact galaxies, although it is not biased towards them. They reconstructed the star formation histories of the galaxies and determined that the number density evolution of quiescent galaxies matched that of independent deep photometric surveys. Furthermore, they found that the largest galaxies are the youngest at a given redshift (a result consistent with the result we obtained in our RSBD sample). They calculate that only half the increase in average size can be attributed to contribution from recently-quenched galaxies, with the remainder of the size evolution arising from a genuine growth of the quiescent galaxies.

It is clear that high signal-to-noise spectra open the door to many things, one of which is measuring chemical abundances that can enable us to draw detailed conclusions about their star formation histories.

Chemical abundances play a key role in our ability to trace the star formation history of a galaxy. A standard method of studying the abundance profiles of a stellar system is to measure optical absorption features using the Lick system (Worthey et al. 1994; Worthey & Ottaviani 1997). A measurement of heavy elements relative to hydrogen can provide a gauge as to the

progress of chemical evolution in a galaxy: the production rates of individual elements by a grouping of stars is a function of the initial mass function of the stars and the history of star formation in the group (Henry & Worthey 1999). Thus the ratios of two heavy elements can provide information about the differential rate that such elements are produced by stars. Some features and their uses are described below:

1. **Magnesium and Calcium:** The strength of a magnesium feature (typically measured using the Mg b index) relative to an average iron feature (usually measured from $\langle \text{Fe} \rangle$, an average of indices Fe5270 and Fe5335) can reveal enrichment from various types of supernovae. Fe is produced primarily from Type Ia supernovae, while Mg is from Type II, thus an enhanced measure of $[\text{Mg}/\text{Fe}]$ suggests more Type II enrichment than Type Ia enrichment. $[\text{Mg}/\text{Fe}]$ is above solar in the centres of massive early-type galaxies (Worthey et al. 1992, e.g), and Mg_2 is tightly correlated with velocity dispersion, with the largest galaxies having higher Mg_2 , as well as metallicity (e.g., Jørgensen (1999); Trager et al. (2000); Schiavon (2007); Smith et al. (2009)). This implies a regulation or balance between Mg and Fe enrichment. Possible scenarios to explain this include a short star-formation timescale, a top-heavy IMF, and selective winds (Faber et al. 1992; Schiavon 2010).
2. **Nitrogen and Carbon:** Measurements of nitrogen- and carbon-sensitive indices have shown that early-type galaxies tend to have super-solar $[\text{N}/\text{Fe}]$ and $[\text{C}/\text{Fe}]$. Furthermore, these abundance ratios are strongly correlated with velocity dispersion and metallicity (Schiavon 2007; Graves et al. 2007; Smith et al. 2009). A steep slope in $[\text{N}/\text{Fe}]-\sigma$ indicates secondary enrichment of nitrogen by stars around mass $4 - 8M_{\text{sun}}$, which last for $\sim 10^8$ years. A secondary nitrogen enrichment may place constraints on the lower limit for the duration of star formation in the systems in which the stars formed, and may also constrain their characteristic masses (Schiavon 2007; 2010).

Unfortunately, constraining these abundances requires obtaining high quality individual spectra: with the current generation of ground-based 8-10m telescopes, this requires extremely

long integration times. For example, the stacked spectrum of 13 ETGs presented by Cimatti et al. (2008) has an equivalent integration time of 480 hours. Compact massive galaxies are therefore an ideal subject for deep, multiband surveys that can be performed by the next generation of space and ground-based telescopes such as the *James Webb Space Telescope (JWST)*, *Thirty Meter Telescope (TMT)*, and *European Extremely Large Telescope (E-ELT)*. *JWST*, for instance, will be equipped with a spectrograph capable of obtaining 100 spectra simultaneously, and *TMT* will have nearly 10 times the light-collecting area compared to one of the Keck telescopes. This will provide a three times better improvement on the signal-to-noise ratio, corresponding to approximately one magnitude per unit of integration time.

5.3 Thesis Summary

By exploiting the statistical technique of bootstrap resampling, we have explored a method for characterizing the distribution of stellar populations in co-added spectra and investigated the importance of progenitor bias in explaining the rarity of compact massive galaxies in the local universe. We looked for systematic differences in the stellar populations of compact early-type galaxies in the DEEP2 survey as a function of size by comparing the light-weighted ages of compact early-type galaxies at redshifts $0.5 < z < 1.4$ to those of a control sample of larger galaxies at similar redshifts and in similar mass bins. All galaxies in our sample are selected with the same red color cut. Massive compact early-type galaxies selected on the basis of high bulge-to-total ratio are found to be younger than similarly selected larger galaxies, suggesting that size growth in these objects is *not* driven mainly by progenitor bias. In this sample, the bulk of the size growth is consistent with individual galaxies growing with time. However, massive compact early-type galaxies *selected on the basis of image smoothness*, in addition to high bulge-to-total ratio, are older than a control sample of larger galaxies. Progenitor bias could well play a significant role in defining apparent size changes in populations of these objects. An important outcome of our study is therefore the surprising sensitivity of conclusions

regarding progenitor bias to the definitions used in selecting early-type galaxy populations. This result echoes that of Moresco et al. (2013), who also found that the properties of high-redshift early-type galaxy populations are highly sensitive to the definitions used in defining the samples.

Bibliography

Abraham, R. G., et al. 2007, ApJ, 669, 184

Adelman, S. J., & Leckrone, D. S. 1985, in Horizontal-Branch and UV-Bright Stars, ed. A. G. D. Philip, 75–83

Andredakis, Y. C., & Sanders, R. H. 1994, MNRAS, 267, 283

Barro, G., et al. 2013, ApJ, 765, 104

Belli, S., Newman, A. B., & Ellis, R. S. 2014a, ArXiv e-prints

—. 2014b, ApJ, 783, 117

Bernardi, M., Shankar, F., Hyde, J. B., Mei, S., Marulli, F., & Sheth, R. K. 2010, MNRAS, 404, 2087

Bezanson, R., van Dokkum, P., van de Sande, J., Franx, M., & Kriek, M. 2013, ApJ Letters, 764, L8

Bezanson, R., van Dokkum, P. G., Tal, T., Marchesini, D., Kriek, M., Franx, M., & Coppi, P. 2009, ApJ, 697, 1290

Blumenthal, G. R., Faber, S. M., Primack, J. R., & Rees, M. J. 1984, Nature, 311, 517

Booth, J. G., & Sarkar, S. 1998, The American Statistician, 52, 354

Borch, A., et al. 2006, AAp, 453, 869

- Brinchmann, J., Charlot, S., White, S. D. M., Tremonti, C., Kauffmann, G., Heckman, T., & Brinkmann, J. 2004, *MNRAS*, 351, 1151
- Bruce, V. A., et al. 2012, *MNRAS*, 427, 1666
- Bruzual, G., & Charlot, S. 2003, *MNRAS*, 344, 1000
- Buitrago, F., Trujillo, I., Conselice, C. J., Bouwens, R. J., Dickinson, M., & Yan, H. 2008, *ApJ Letters*, 687, L61
- Bundy, K., Treu, T., & Ellis, R. S. 2007, *ApJ*, 665, L5
- Bundy, K., et al. 2006, *ApJ*, 651, 120
- Carollo, C. M., et al. 2013, *ApJ*, 773, 112
- Carrasco, E. R., Conselice, C. J., & Trujillo, I. 2010, *MNRAS*, 405, 2253
- Cassata, P., et al. 2008, *A&A*, 483, L39
- . 2010, *ApJ*, 714, L79
- . 2011, *ApJ*, 743, 96
- Chabrier, G. 2003, *PASP*, 115, 763
- Chang, Y.-Y., van der Wel, A., Rix, H.-W., Wuyts, S., Zibetti, S., Ramkumar, B., & Holden, B. 2013, *ApJ*, 762, 83
- Chernick, M. R. 1999, *Bootstrap methods: a practitioner's guide*, Wiley series in probability and statistics (Wiley)
- Cheung, E., et al. 2012, *ApJ*, 760, 131
- Chevance, M., Weijmans, A.-M., Damjanov, I., Abraham, R. G., Simard, L., van den Bergh, S., Caris, E., & Glazebrook, K. 2012, *ApJL*, 754, L24

Cimatti, A., et al. 2008, *A&A*, 482, 21

Cooper, M. C., et al. 2012, *MNRAS*, 419, 3018

Daddi, E., et al. 2005, *ApJ*, 626, 680

Damjanov, I., Chilingarian, I., Hwang, H. S., & Geller, M. J. 2013, *ApJ Letters*, 775, L48

Damjanov, I., Geller, M. J., Zahid, H. J., & Hwang, H. S. 2015, *ArXiv e-prints*

Damjanov, I., Hwang, H. S., Geller, M. J., & Chilingarian, I. 2014, *ApJ*, 793, 39

Damjanov, I., et al. 2009, *ApJ*, 695, 101

—. 2011, *ApJ Letters*, 739, L44

Davis, M., Gerke, B. F., Newman, J. A., & Deep2 Team. 2005, in *Astronomical Society of the Pacific Conference Series*, Vol. 339, *Observing Dark Energy*, ed. S. C. Wolff & T. R. Lauer, 128

Davis, M., et al. 2003, in *Society of Photo-Optical Instrumentation Engineers (SPIE) Conference Series*, Vol. 4834, *Society of Photo-Optical Instrumentation Engineers (SPIE) Conference Series*, ed. P. Guhathakurta, 161–172

Davis, M., et al. 2007, *ApJ Letters*, 660, L1

Davison, A., & Hinkley, D. 1997, *Bootstrap Methods and Their Application*, *Cambridge Series in Statistical and Probabilistic Mathematics* (Cambridge University Press)

de Vaucouleurs, G. 1948, *Annales d'Astrophysique*, 11, 247

Dick, S. 2013, *Discovery and Classification in Astronomy: Controversy and Consensus*

Dressler, A., Oemler, Jr., A., Poggianti, B. M., Smail, I., Trager, S., Shectman, S. A., Couch, W. J., & Ellis, R. S. 2004, *ApJ*, 617, 867

- Efron, B. 1979, *The annals of Statistics*, 1
- Efron, B., & Tibshirani, R. 1994, *An Introduction to the Bootstrap*, Chapman & Hall/CRC
Monographs on Statistics & Applied Probability (Taylor & Francis)
- Efstathiou, G. 2000, *MNRAS*, 317, 697
- Eggen, O. J., Lynden-Bell, D., & Sandage, A. R. 1962, *ApJ*, 136, 748
- Faber, S. M., Worthey, G., & Gonzales, J. J. 1992, in *IAU Symposium*, Vol. 149, *The Stellar Populations of Galaxies*, ed. B. Barbuy & A. Renzini, 255
- Faber, S. M., et al. 2003, in *Society of Photo-Optical Instrumentation Engineers (SPIE) Conference Series*, Vol. 4841, *Society of Photo-Optical Instrumentation Engineers (SPIE) Conference Series*, ed. M. Iye & A. F. M. Moorwood, 1657–1669
- Fabian, A. C. 2012, *ARA&A*, 50, 455
- Fan, L., Lapi, A., Bressan, A., Bernardi, M., De Zotti, G., & Danese, L. 2010, *ApJ*, 718, 1460
- Fan, L., Lapi, A., De Zotti, G., & Danese, L. 2008, *ApJ Letters*, 689, L101
- Ferrarese, L., & Merritt, D. 2000, *ApJ*, 539, L9
- Fontana, A., et al. 2004, *AAp*, 424, 23
- Gallazzi, A., Brinchmann, J., Charlot, S., & White, S. D. M. 2008, *MNRAS*, 383, 1439
- Gargiulo, A., Saracco, P., & Longhetti, M. 2011, *MNRAS*, 412, 1804
- Girardi, L., Bressan, A., Bertelli, G., & Chiosi, C. 2000, *A&AS*, 141, 371
- Graves, G. J., Faber, S. M., Schiavon, R. P., & Yan, R. 2007, *ApJ*, 671, 243
- Graves, G. J., & Schiavon, R. P. 2008, *ApJS*, 177, 446
- Henry, R. B. C., & Worthey, G. 1999, *PASP*, 111, 919

- Hopkins, P. F., Bundy, K., Murray, N., Quataert, E., Lauer, T. R., & Ma, C.-P. 2009a, *MNRAS*, 398, 898
- Hopkins, P. F., Cox, T. J., Younger, J. D., & Hernquist, L. 2009b, *ApJ*, 691, 1168
- Hopkins, P. F., et al. 2010, *ApJ*, 724, 915
- Huang, S., Ho, L. C., Peng, C. Y., Li, Z.-Y., & Barth, A. J. 2013a, *ApJL*, 768, L28
- . 2013b, *ApJ*, 766, 47
- Hubble, E. P. 1926, *ApJ*, 64, 321
- . 1936, *Realm of the Nebulae*
- Huertas-Company, M., et al. 2013, *MNRAS*, 428, 1715
- Ishibashi, W., Fabian, A. C., & Canning, R. E. A. 2013, *MNRAS*, 431, 2350
- Jørgensen, I. 1999, *MNRAS*, 306, 607
- Kauffmann, G., et al. 2003, *MNRAS*, 341, 33
- Keating, S. K., Abraham, R. G., Schiavon, R., Graves, G., Damjanov, I., Yan, R., Newman, J., & Simard, L. 2015, *ApJ*, 798, 26
- Kent, S. M., Dame, T. M., & Fazio, G. 1991, *ApJ*, 378, 131
- Khochfar, S., & Silk, J. 2006, *ApJ Letters*, 648, L21
- Kormendy, J., & Richstone, D. 1995, *ARA&A*, 33, 581
- Kriek, M., van Dokkum, P. G., Franx, M., Illingworth, G. D., & Magee, D. K. 2009, *ApJ*, 705, L71
- Law, D. R., Steidel, C. C., Shapley, A. E., Nagy, S. R., Reddy, N. A., & Erb, D. K. 2012, *ApJ*, 745, 85

- Longhetti, M., et al. 2007, MNRAS, 374, 614
- López-Sanjuan, C., et al. 2012, A&A, 548, A7
- Magorrian, J., et al. 1998, AJ, 115, 2285
- Maltby, D. T., et al. 2010, MNRAS, 402, 282
- Mancini, C., et al. 2010, MNRAS, 401, 933
- Marconi, A., & Hunt, L. K. 2003, ApJ, 589, L21
- McKee, C. F., & Ostriker, J. P. 1977, ApJ, 218, 148
- McLure, R. J., et al. 2013, MNRAS, 428, 1088
- Mo, H., van den Bosch, F. C., & White, S. 2010, Galaxy Formation and Evolution
- Moresco, M., et al. 2013, A&A, 558, A61
- Morishita, T., Ichikawa, T., & Kajisawa, M. 2014, ApJ, 785, 18
- Naab, T. 2013, in IAU Symposium, Vol. 295, IAU Symposium, ed. D. Thomas, A. Pasquali, & I. Ferreras, 340–349
- Naab, T., Johansson, P. H., Ostriker, J. P., & Efstathiou, G. 2007, ApJ, 658, 710
- Nayakshin, S., & Zubovas, K. 2012, MNRAS, 427, 372
- Newman, A. B., Ellis, R. S., Bundy, K., & Treu, T. 2012, ApJ, 746, 162
- Newman, A. B., Ellis, R. S., Treu, T., & Bundy, K. 2010, ApJL, 717, L103
- Newman, J. A., et al. 2013, ApJS, 208, 5
- Oser, L., Naab, T., Ostriker, J. P., & Johansson, P. H. 2012, ApJ, 744, 63
- Oser, L., Ostriker, J. P., Naab, T., Johansson, P. H., & Burkert, A. 2010, ApJ, 725, 2312

- Ostriker, J. P. 1980, *Comments on Astrophysics*, 8, 177
- Papovich, C., et al. 2012, *ApJ*, 750, 93
- Patel, S. G., Holden, B. P., Kelson, D. D., Franx, M., van der Wel, A., & Illingworth, G. D. 2012, *ApJ*, 748, L27
- Patel, S. G., et al. 2013, *ApJ*, 766, 15
- Poggianti, B. M., Moretti, A., Calvi, R., D'Onofrio, M., Valentinuzzi, T., Fritz, J., & Renzini, A. 2013a, *ApJ*, 777, 125
- Poggianti, B. M., et al. 2013b, *ApJ*, 762, 77
- Ragone-Figueroa, C., & Granato, G. L. 2011, *MNRAS*, 414, 3690
- Raichoor, A., et al. 2012, *ApJ*, 745, 130
- Rettura, A., et al. 2010, *ApJ*, 709, 512
- Reynolds, J. H. 1920, *MNRAS*, 80, 746
- Roberts, M. S., & Haynes, M. P. 1994, *ARA&A*, 32, 115
- Ryan, Jr., R. E., et al. 2012, *ApJ*, 749, 53
- Saglia, R. P., et al. 2010, *A&A*, 524, A6
- Salasnich, B., Girardi, L., Weiss, A., & Chiosi, C. 2000, *A&A*, 361, 1023
- Saracco, P., Longhetti, M., & Gargiulo, A. 2011, *MNRAS*, 412, 2707
- Sarzi, M., et al. 2010, *MNRAS*, 402, 2187
- Schade, D., et al. 1999, *ApJ*, 525, 31
- Schiavon, R. P. 2007, *ApJS*, 171, 146

—. 2010, *Publication of Korean Astronomical Society*, 25, 83

Schiavon, R. P., et al. 2006, *ApJ*, 651, L93

Schweizer, F. 1986, *Science*, 231, 227

Sersic, J. L. 1968, *Atlas de galaxias australes*

Shankar, F., & Bernardi, M. 2009, *MNRAS*, 396, L76

Shankar, F., Marulli, F., Bernardi, M., Dai, X., Hyde, J. B., & Sheth, R. K. 2010, *MNRAS*, 403, 117

Silk, J., & Rees, M. J. 1998, *A&A*, 331, L1

Simard, L., et al. 2002, *ApJS*, 142, 1

—. 2009, *A&A*, 508, 1141

Smith, R. J., Lucey, J. R., Hudson, M. J., & Bridges, T. J. 2009, *MNRAS*, 398, 119

Szomoru, D., Franx, M., Bouwens, R. J., van Dokkum, P. G., Labbé, I., Illingworth, G. D., & Trenti, M. 2011, *ApJ Letters*, 735, L22

Szomoru, D., Franx, M., & van Dokkum, P. G. 2012, *ApJ*, 749, 121

Szomoru, D., et al. 2010, *ApJ Letters*, 714, L244

Taylor, E. N., Franx, M., Glazebrook, K., Brinchmann, J., van der Wel, A., & van Dokkum, P. G. 2010, *ApJ*, 720, 723

Toft, S., et al. 2007, *ApJ*, 671, 285

Tonry, J., & Davis, M. 1979, *AJ*, 84, 1511

Toomre, A., & Toomre, J. 1972, *ApJ*, 178, 623

- Trager, S. C., Faber, S. M., Worthey, G., & González, J. J. 2000, *AJ*, 119, 1645
- Tremonti, C. A., et al. 2004, *ApJ*, 613, 898
- Treu, T., et al. 2005, *ApJ*, 633, 174
- Trujillo, I., Carrasco, E. R., & Ferré-Mateu, A. 2012, *ApJ*, 751, 45
- Trujillo, I., Cenarro, A. J., de Lorenzo-Cáceres, A., Vazdekis, A., de la Rosa, I. G., & Cava, A. 2009, *ApJ Letters*, 692, L118
- Trujillo, I., Conselice, C. J., Bundy, K., Cooper, M. C., Eisenhardt, P., & Ellis, R. S. 2007, *MNRAS*, 382, 109
- Trujillo, I., Ferreras, I., & de La Rosa, I. G. 2011, *MNRAS*, 415, 3903
- Valentinuzzi, T., et al. 2010a, *ApJL*, 721, L19
- . 2010b, *ApJ*, 712, 226
- van der Wel, A., Bell, E. F., van den Bosch, F. C., Gallazzi, A., & Rix, H.-W. 2009, *ApJ*, 698, 1232
- van der Wel, A., Holden, B. P., Zirm, A. W., Franx, M., Rettura, A., Illingworth, G. D., & Ford, H. C. 2008, *ApJ*, 688, 48
- van der Wel, A., et al. 2011, *ApJ*, 730, 38
- . 2014, *ApJ*, 788, 28
- van Dokkum, P. G., & Franx, M. 2001, *ApJ*, 553, 90
- van Dokkum, P. G., et al. 2008, *ApJ Letters*, 677, L5
- . 2010, *ApJ*, 709, 1018
- Varga, J., Csabai, I., & Dobos, L. 2012, *MNRAS*, 426, 833

Vulcani, B., et al. 2011, MNRAS, 412, 246

Weiss, A., Salaris, M., Ferguson, J. W., & Alexander, D. R. 2006, ArXiv Astrophysics e-prints

Whitaker, K. E., Kriek, M., van Dokkum, P. G., Bezanson, R., Brammer, G., Franx, M., & Labbé, I. 2012, ApJ, 745, 179

Whitaker, K. E., et al. 2013, ApJ Letters, 770, L39

White, S. D. M., & Rees, M. J. 1978, MNRAS, 183, 341

Williams, R. J., Quadri, R. F., Franx, M., van Dokkum, P., & Labbé, I. 2009, ApJ, 691, 1879

Worthey, G. 1994, ApJS, 95, 107

Worthey, G., Faber, S. M., & Gonzalez, J. J. 1992, ApJ, 398, 69

Worthey, G., Faber, S. M., Gonzalez, J. J., & Burstein, D. 1994, ApJS, 94, 687

Worthey, G., & Ottaviani, D. L. 1997, ApJS, 111, 377

Yan, R., & Blanton, M. R. 2012, ApJ, 747, 61

Yan, R., Newman, J. A., Faber, S. M., Konidaris, N., Koo, D., & Davis, M. 2006, ApJ, 648, 281

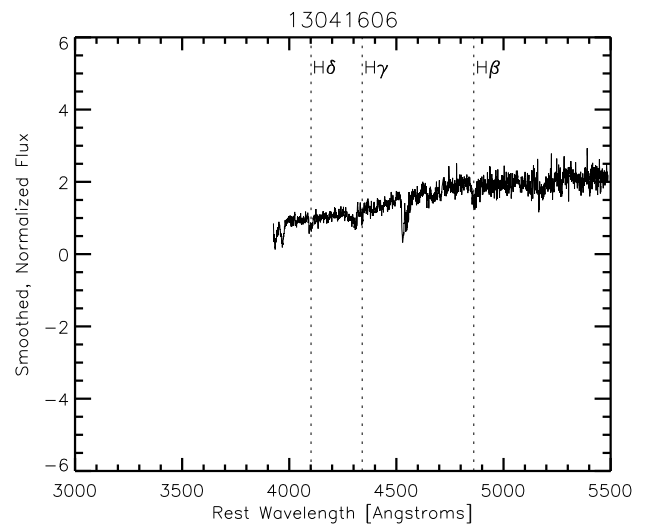
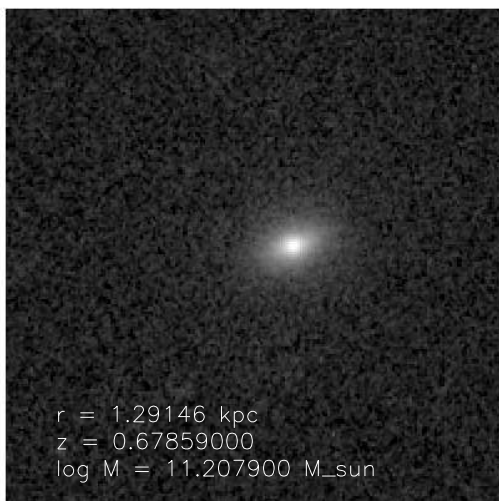
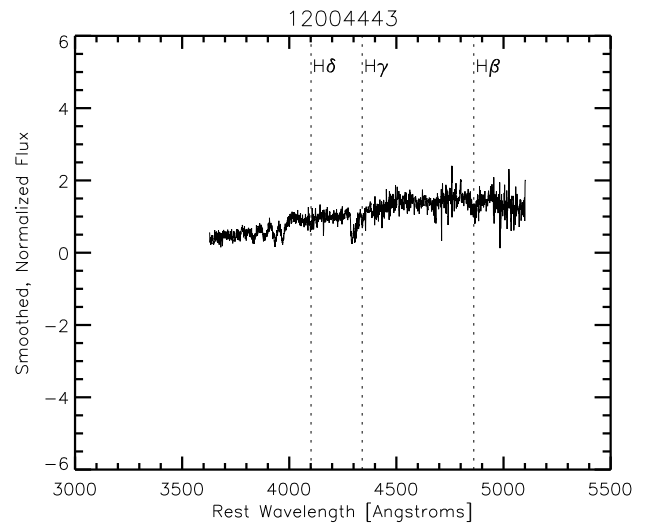
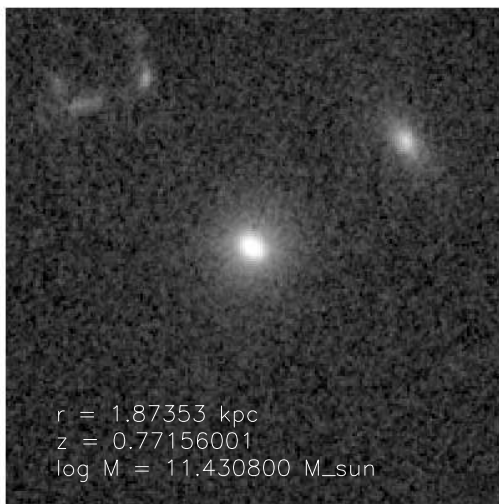
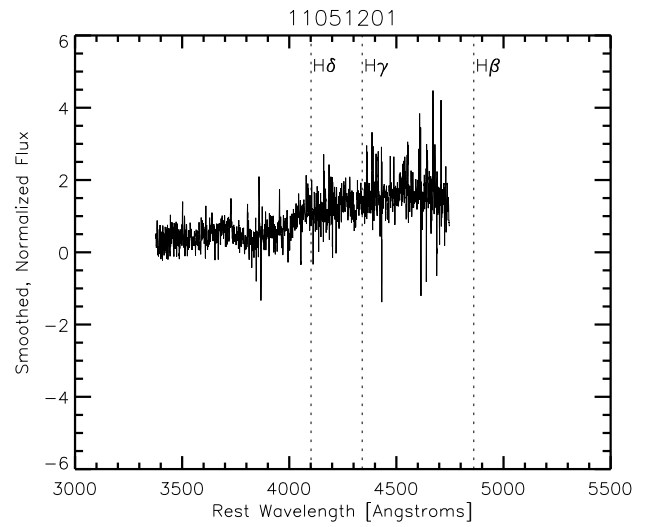
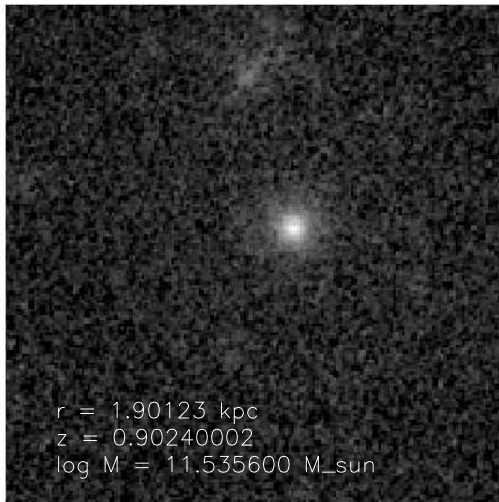
Zirm, A. W., et al. 2007, ApJ, 656, 66

Appendices

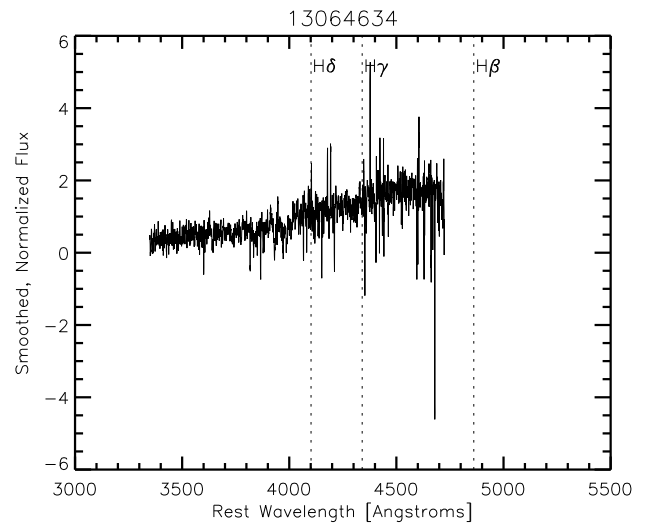
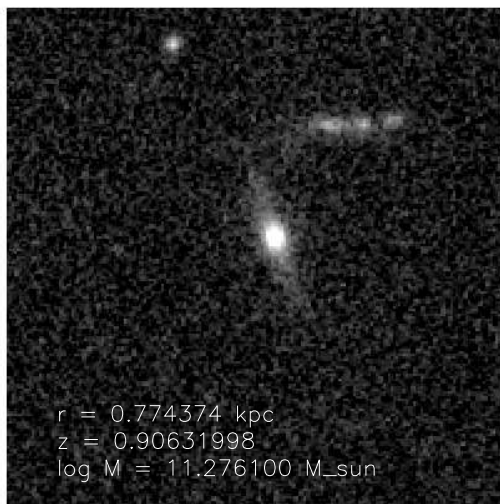
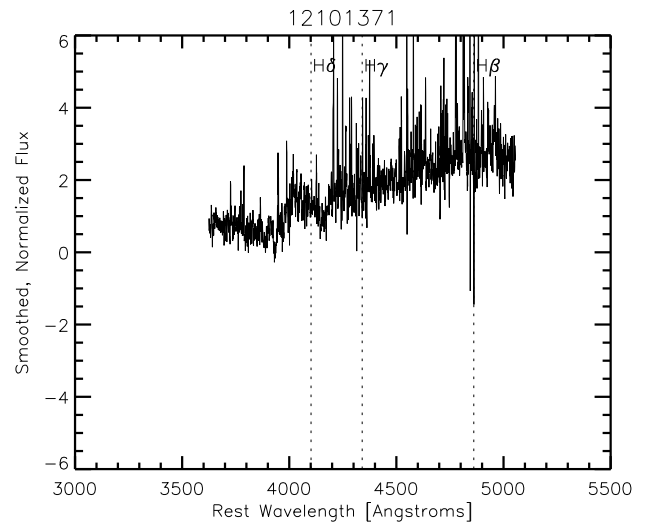
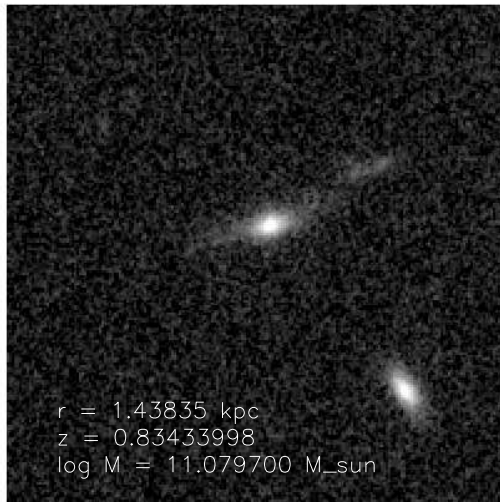
Appendix A

In this appendix we present representative images and spectra of each the RBD and SBD/RSBD Compact & Heavy and Control & Heavy samples. We also present the images of the galaxies that we have visually examined and identified as likely to be non-early-type galaxies. Listed in the bottom left corner of each image is the radius, redshift, and mass of the galaxy.

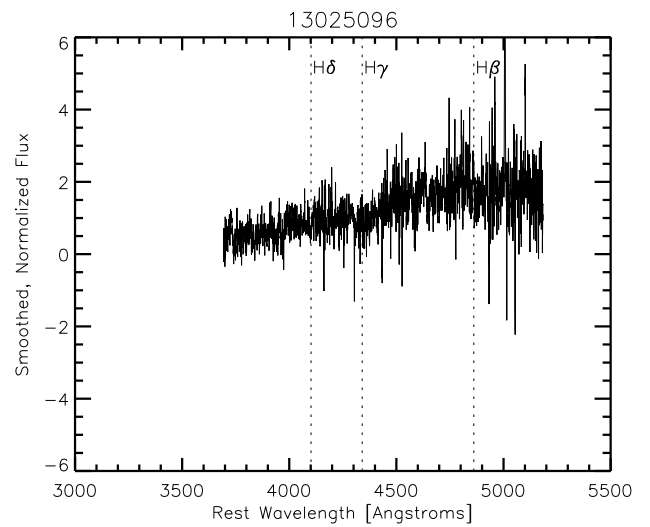
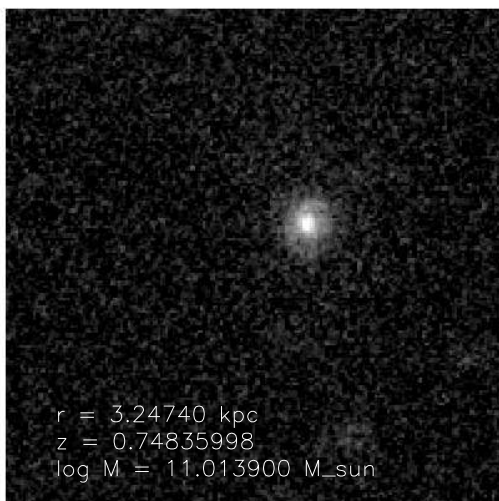
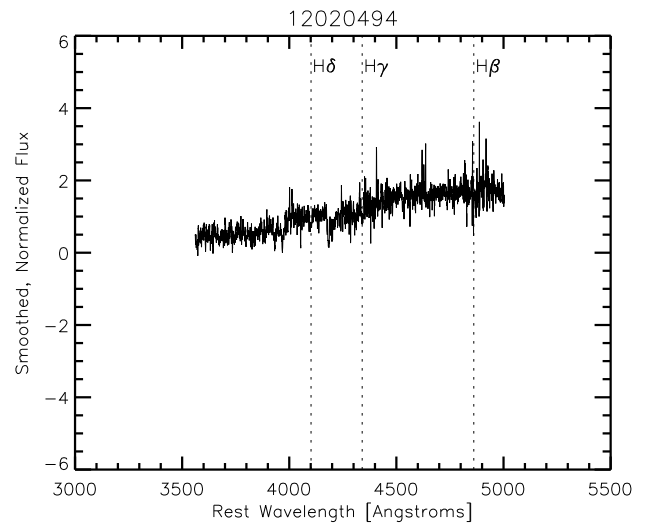
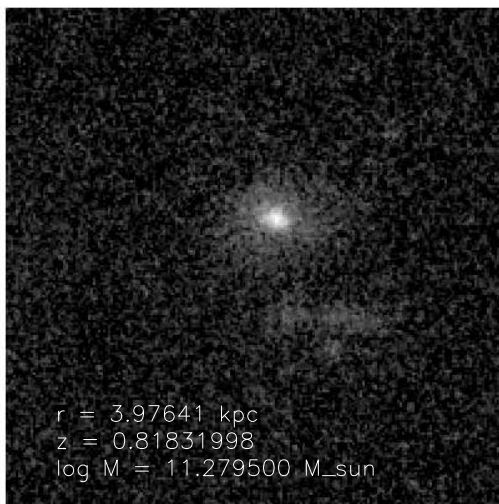
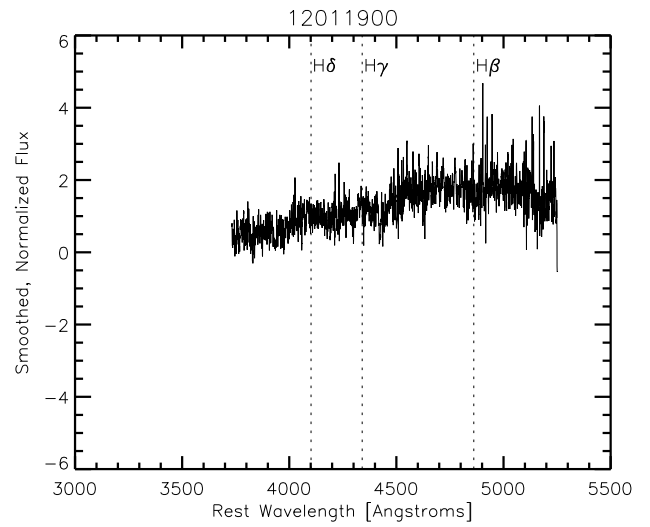
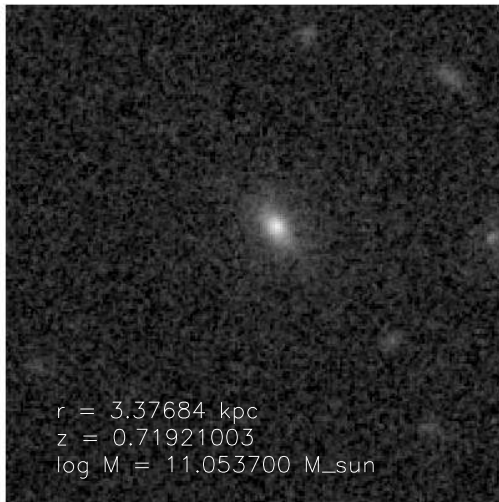
A.1 RBD, Compact & Heavy: Representative Galaxies



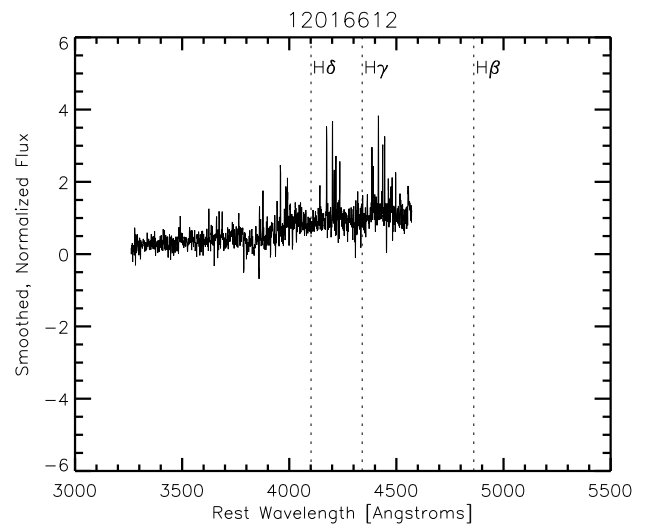
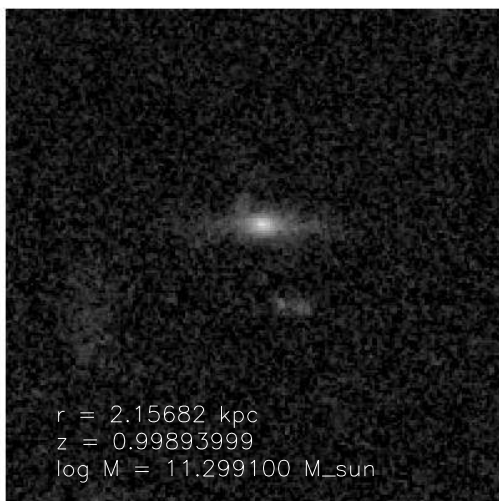
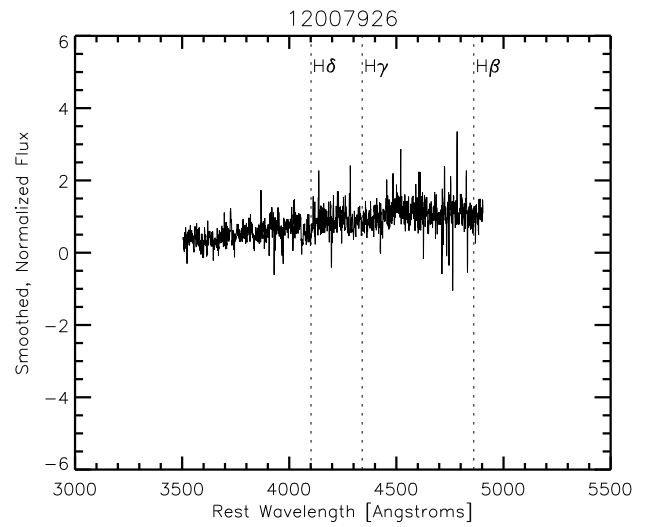
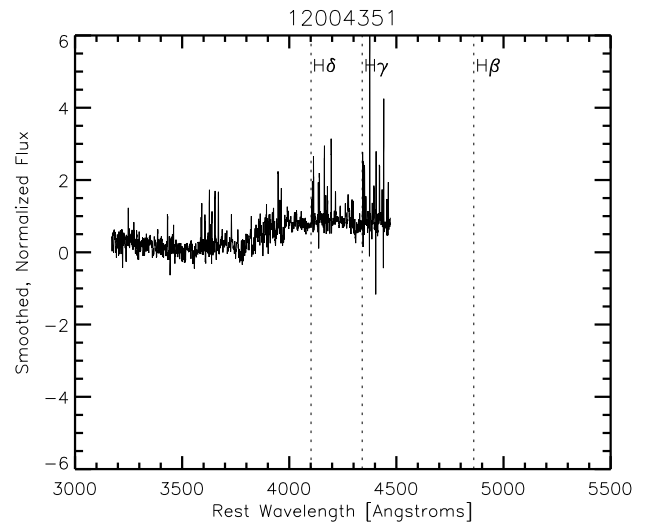
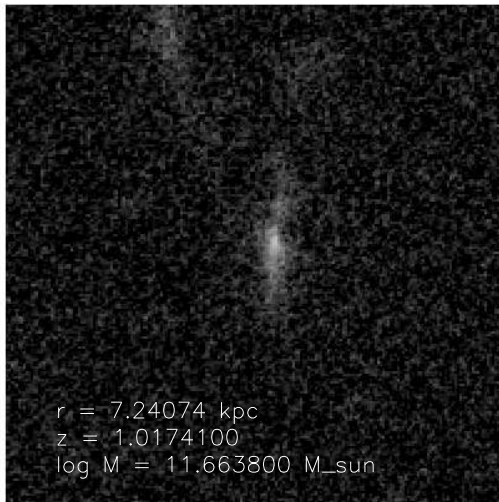
A.2 RBD, Compact & Heavy: non-ETGs

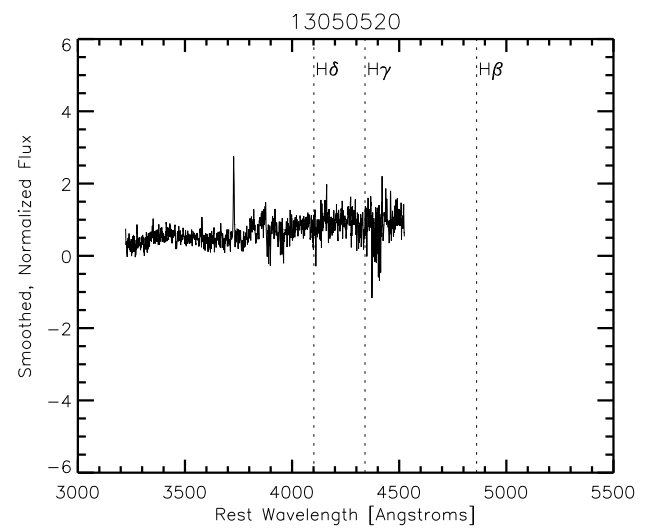
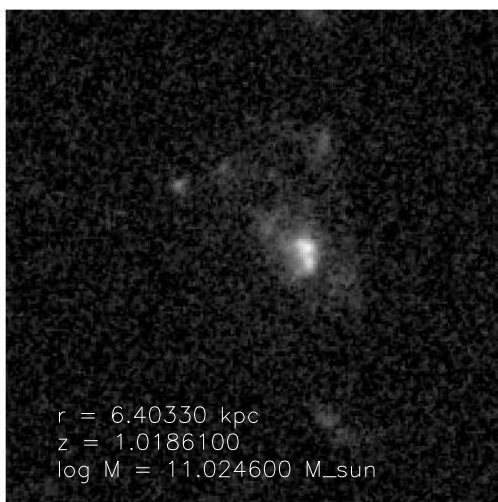
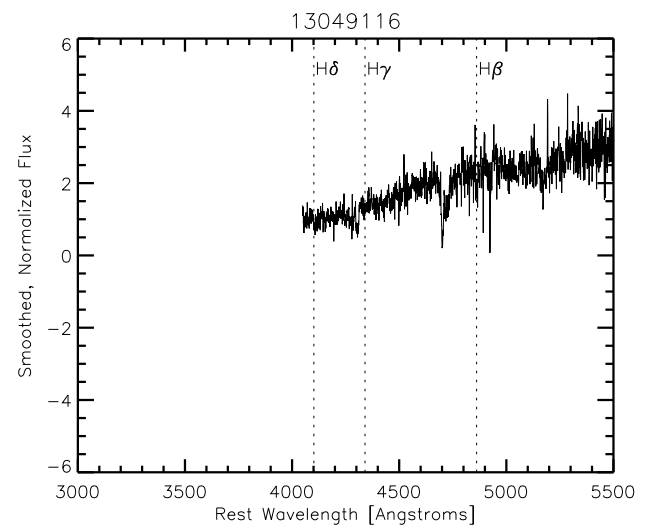
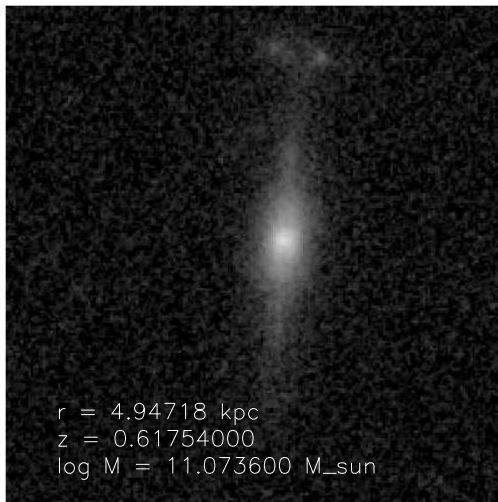
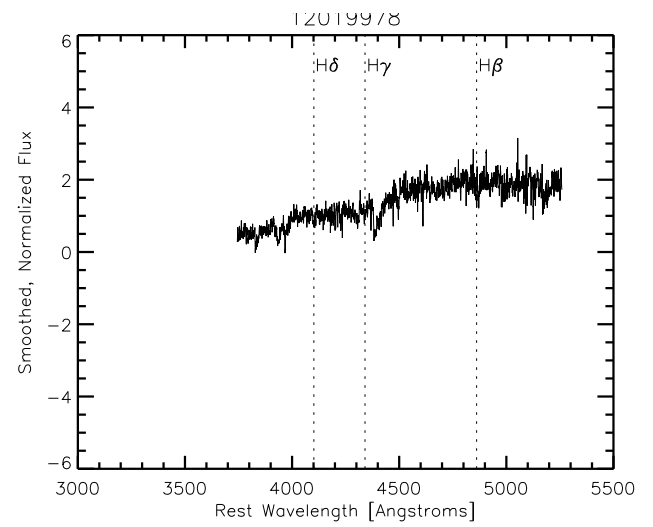
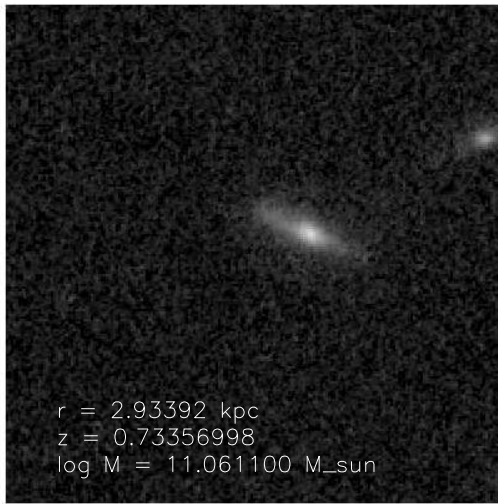


A.3 RBD, Control & Heavy: Representative Galaxies

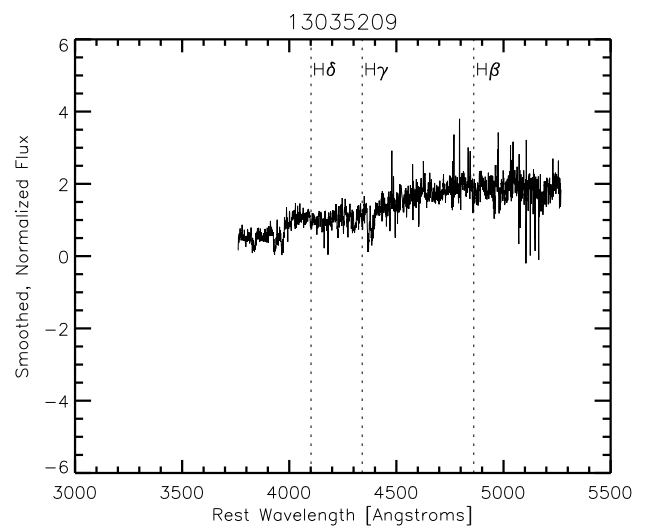
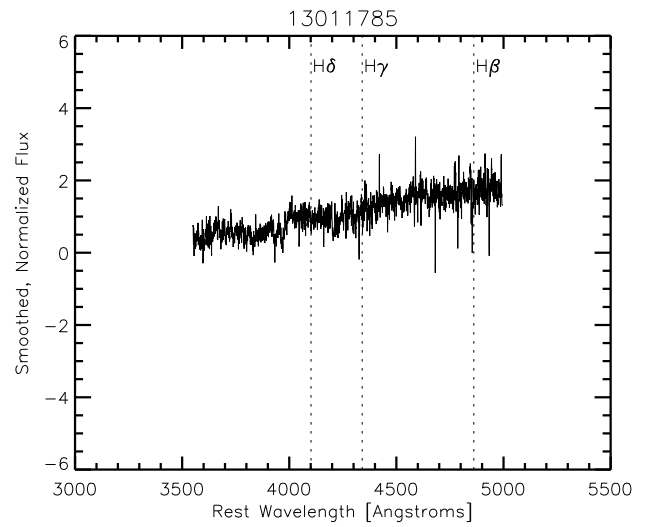
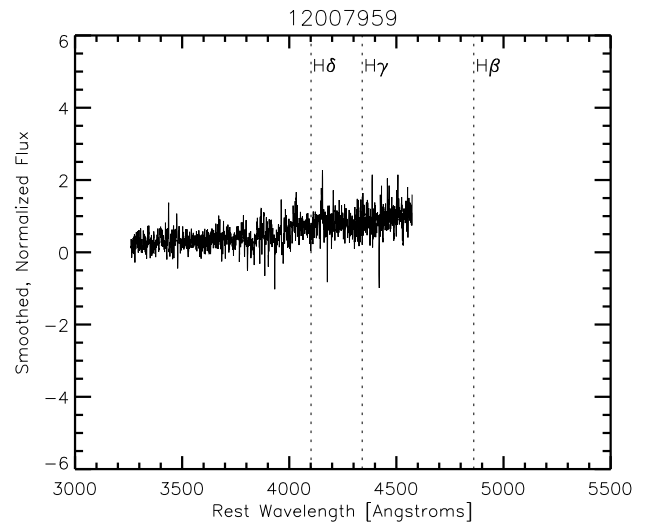
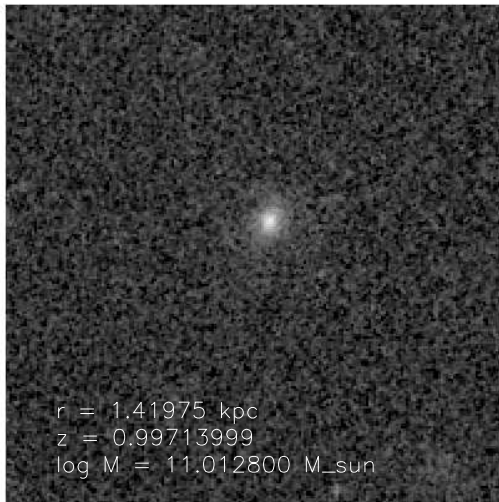


A.4 RBD, Control & Heavy: non-ETGs

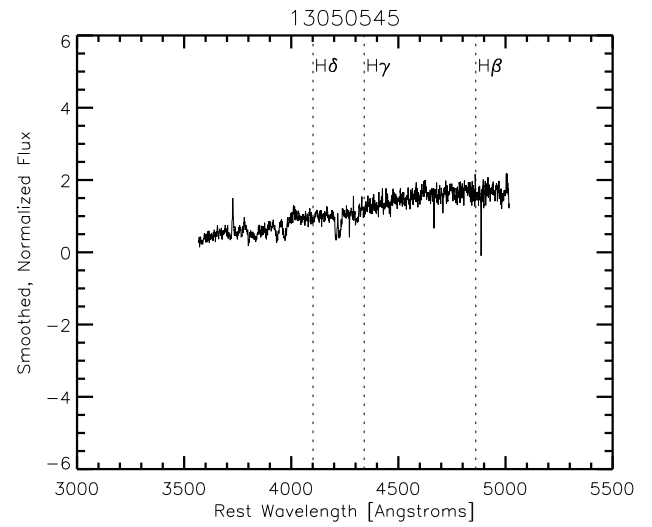
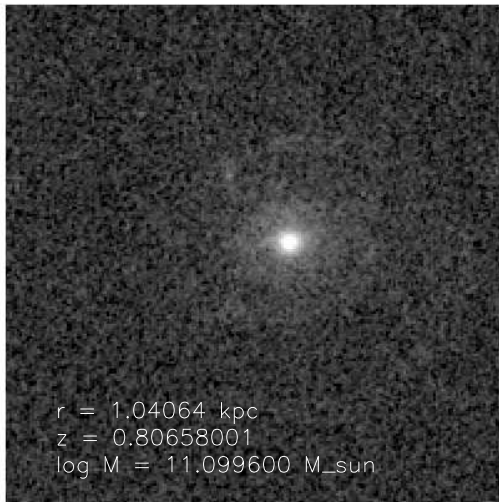




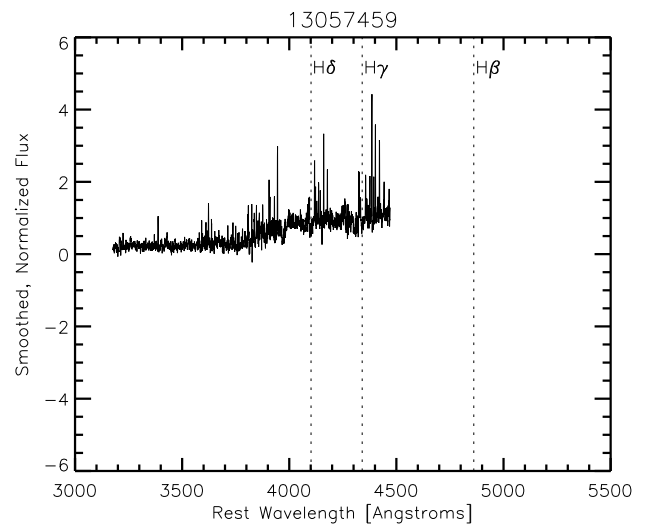
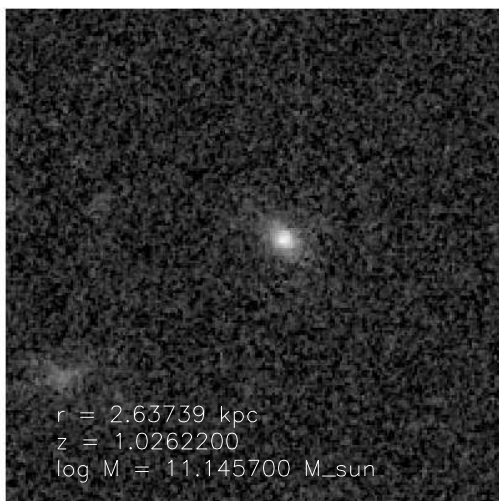
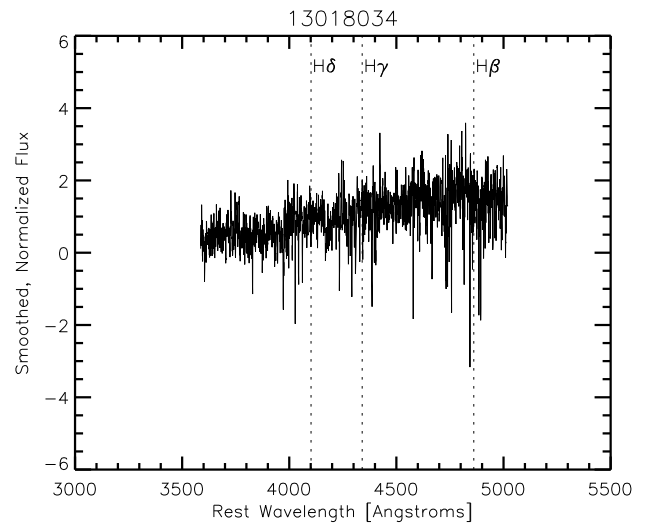
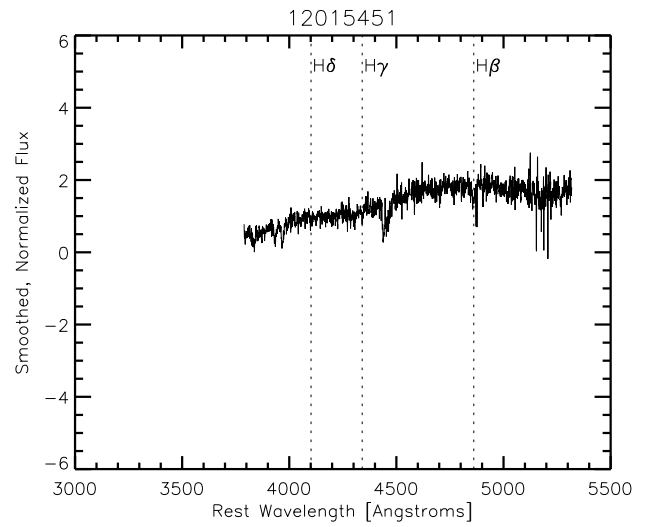
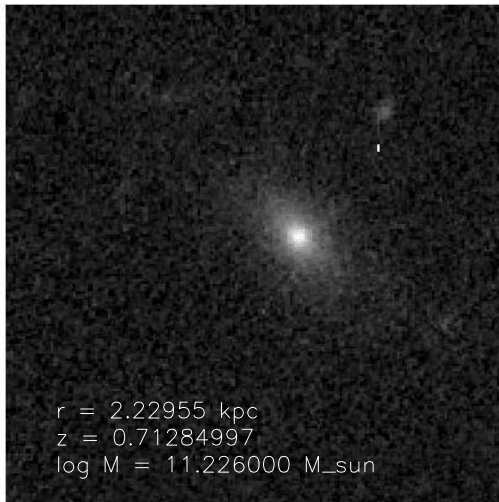
A.5 RSBD, Compact & Heavy: Representative Galaxies



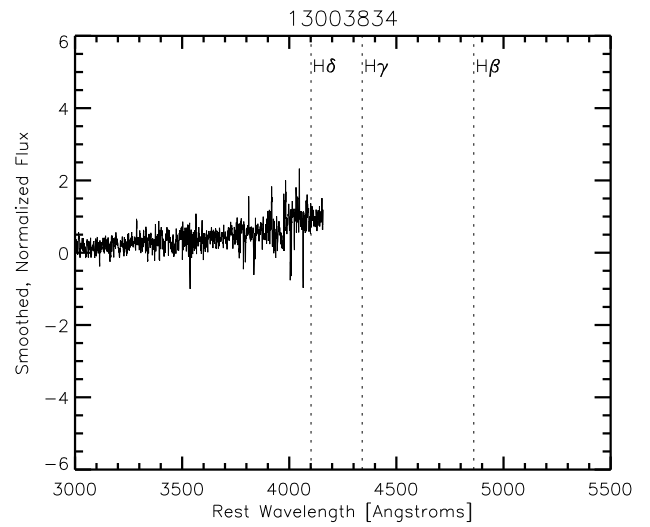
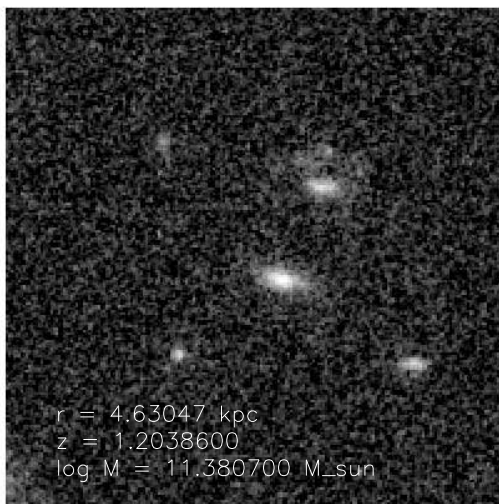
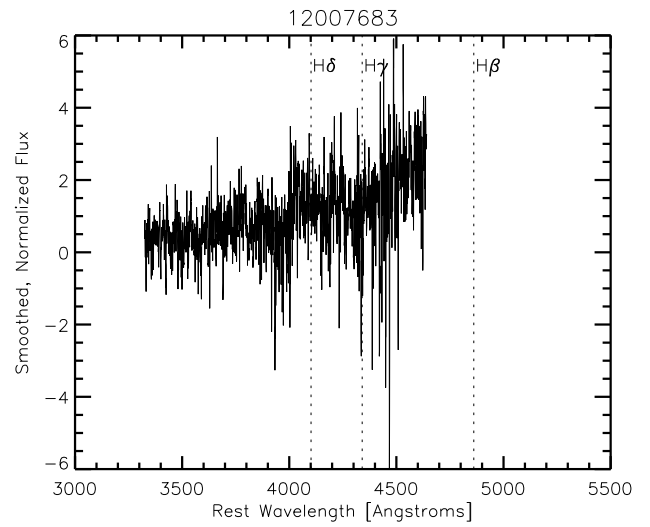
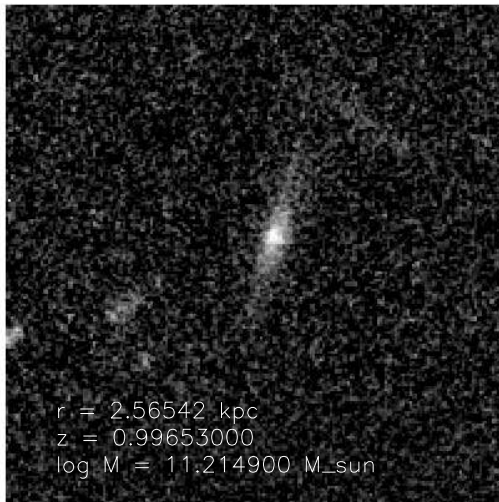
A.6 RSBD, Compact & Heavy: non-ETGs



A.7 RSBD, Control & Heavy: Representative Galaxies



A.8 RSBD, Control & Heavy: non-ETGs



Appendix B

This appendix contains the histograms displaying the number of times an individual DEEP2 galaxy in a given subsample contributed to one of the co-added spectra. We examine the galaxies that contribute to the entire histogram of bootstrap ages (with age < 15 Gyr) as well as only those spectra with ages measured above the median bootstrap age and below the median bootstrap age. In each figure, the 8-digit DEEP ID of the galaxy is labeled on the x-axis. The dotted and dashed lines indicate 1σ and 3σ variations respectively from the average number of contributing galaxies, which is indicated by the solid line.

Of particular note are the galaxies which over- or under-contribute once the histograms are divided by the median age. For the RBD Compact & Heavy subsample, the galaxy with DEEP ID 12008605, shown in Figure B.13, contributes strongly to the co-additions that measured younger ages. On the other hand, galaxy 13034447, shown in Figure B.14, has a very weak contribution to the co-additions that measured older ages. We might conclude from this information that both of these galaxies are have younger stellar populations. Galaxy 12016360, shown in Figure B.15, is of particular interest: it contributes both strongly to the RBD and SBD/RSBD Control & Heavy bootstraps with ages greater than the median age, and weakly to the same subsamples when ages are less than the median age. We can conclude, then, that this galaxy almost certainly contains a predominantly old stellar population.

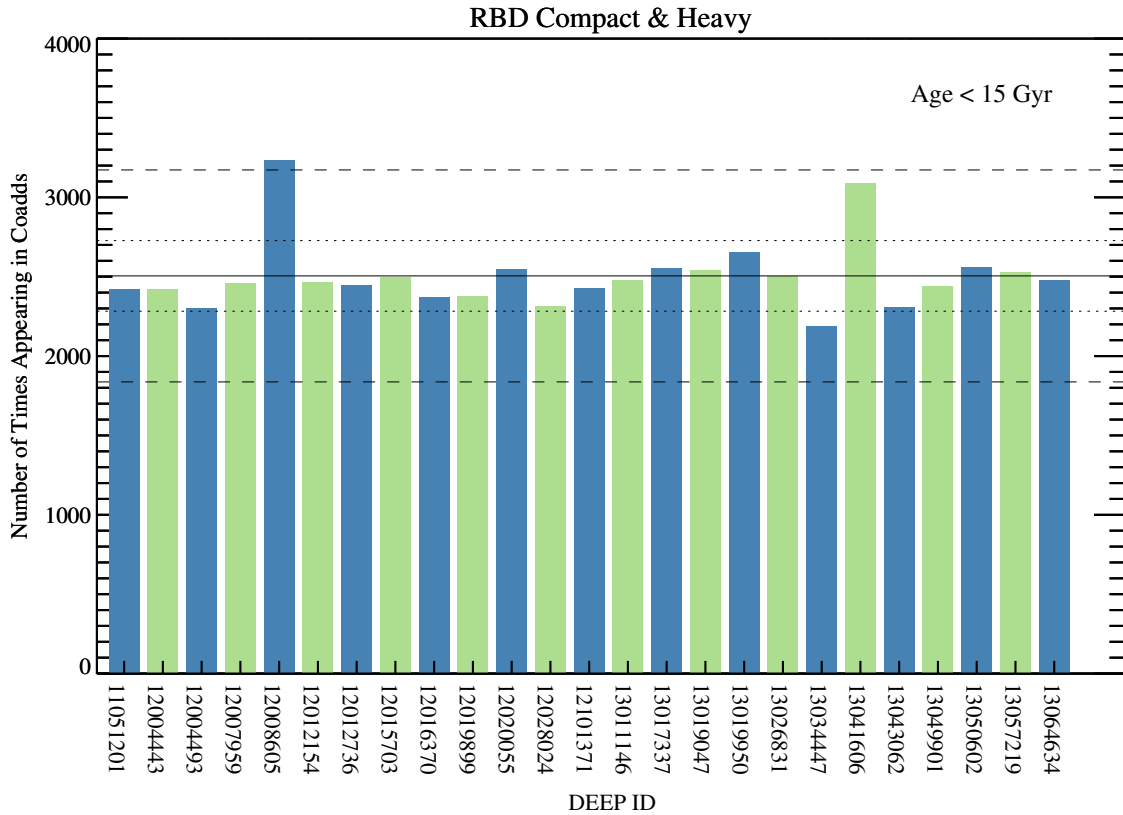


Figure B.1: The number of galaxies contributing to the co-added bootstrapped spectra for the RBD Compact & Heavy subsample for all ages < 15 Gyr. The solid line denotes the mean number of contributing galaxies. The dotted and dashed lines indicate 1 and 3σ variations respectively from the average number of contributing galaxies. Here, one galaxy (with DEEP ID 12008605) contributes more than the mean plus 3σ .

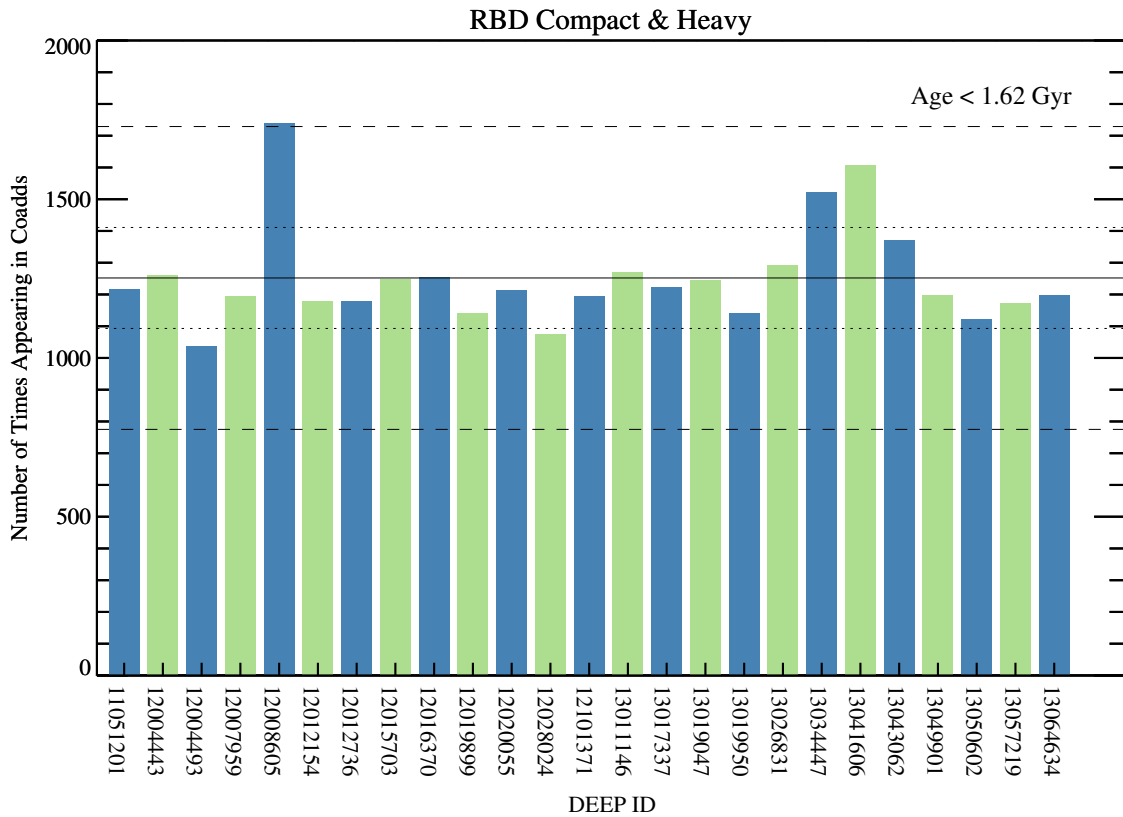


Figure B.2: The number of galaxies contributing to the co-added bootstrapped spectra for the RBD Compact & Heavy subsample for ages < 1.62 Gyr, the median bootstrap age. The solid line denotes the mean number of contributing galaxies. The dotted and dashed lines indicate 1 and 3σ variations respectively from the average number of contributing galaxies. Here again, one galaxy (with DEEP ID 12008605) contributes more than the mean plus 3σ .

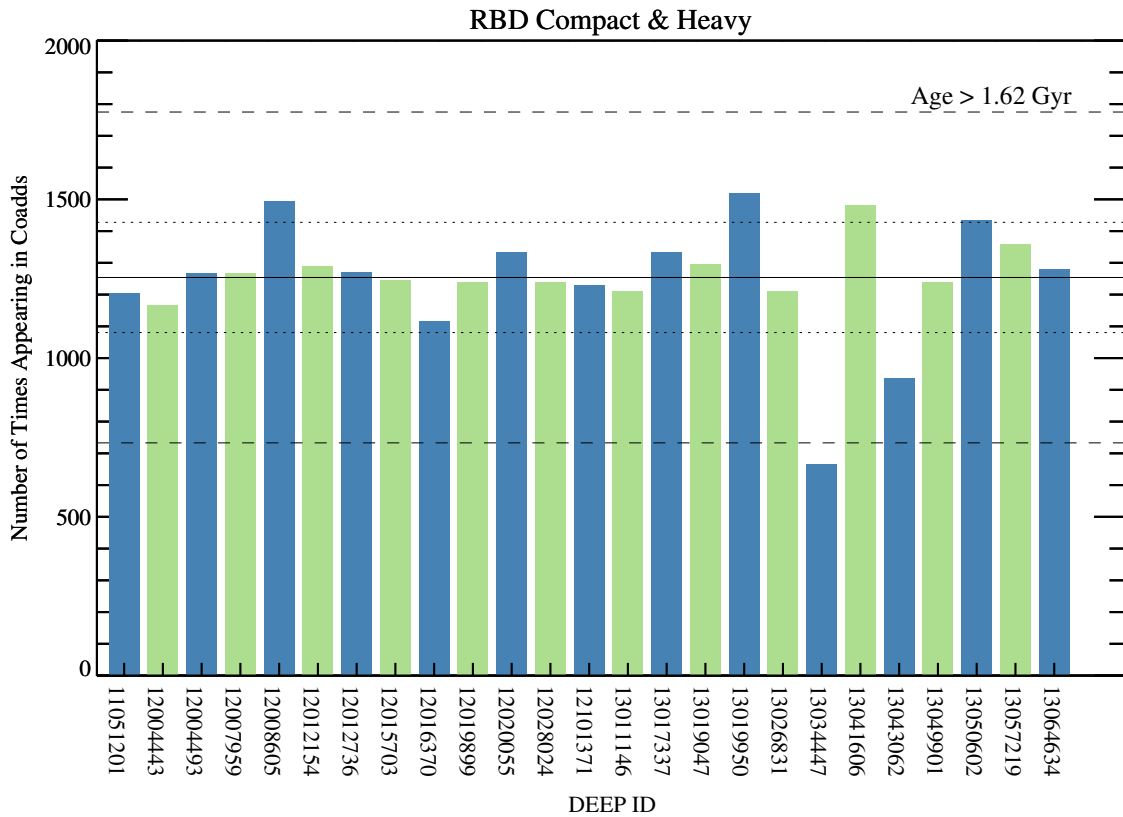


Figure B.3: The number of galaxies contributing to the co-added bootstrapped spectra for the RBD Compact & Heavy subsample for ages > 1.62 Gyr, the median bootstrap age. The solid line denotes the mean number of contributing galaxies. The dotted and dashed lines indicate 1 and 3σ variations respectively from the average number of contributing galaxies. Here, one galaxy (with DEEP ID 13034447) contributes fewer than the mean minus 3σ .

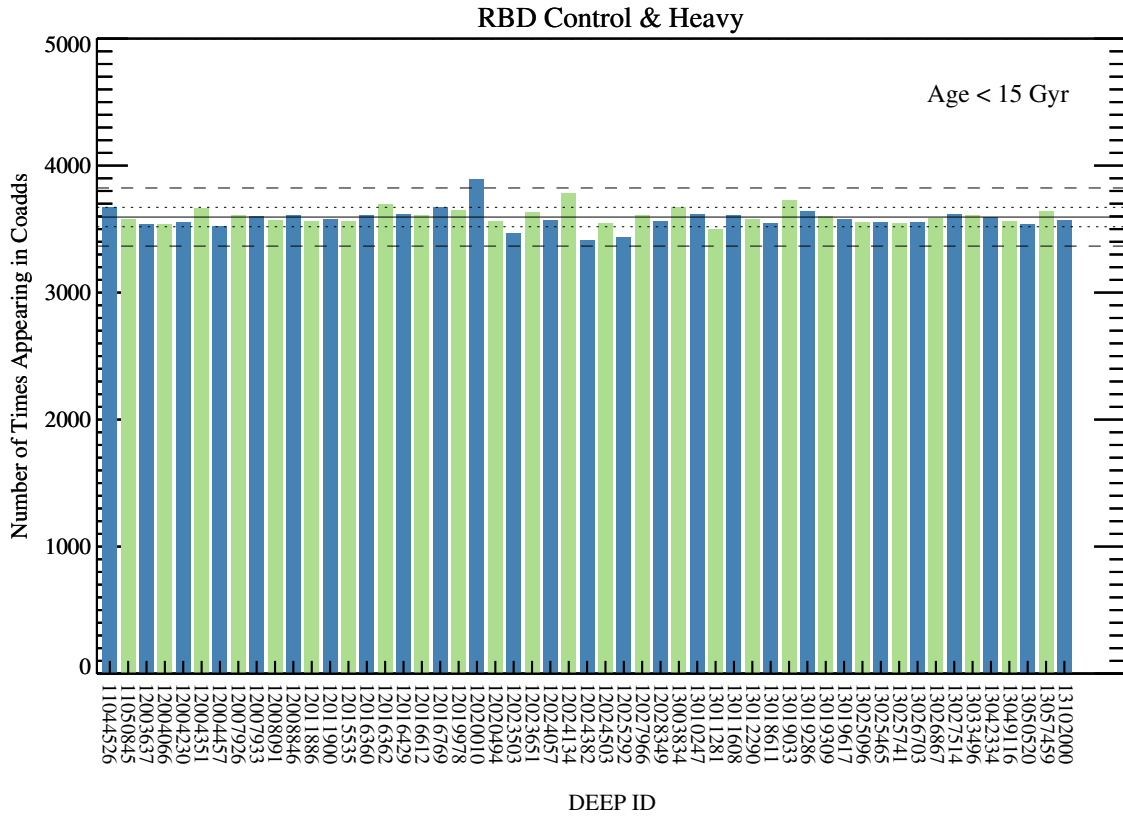


Figure B.4: The number of galaxies contributing to the co-added bootstrapped spectra for the RBD Control & Heavy subsample for all ages < 15 Gyr. The solid line denotes the mean number of contributing galaxies. The dotted and dashed lines indicate 1 and 3 σ variations respectively from the average number of contributing galaxies. Here, one galaxy (with DEEP ID 12020010) contributes more than the mean plus 3 σ .

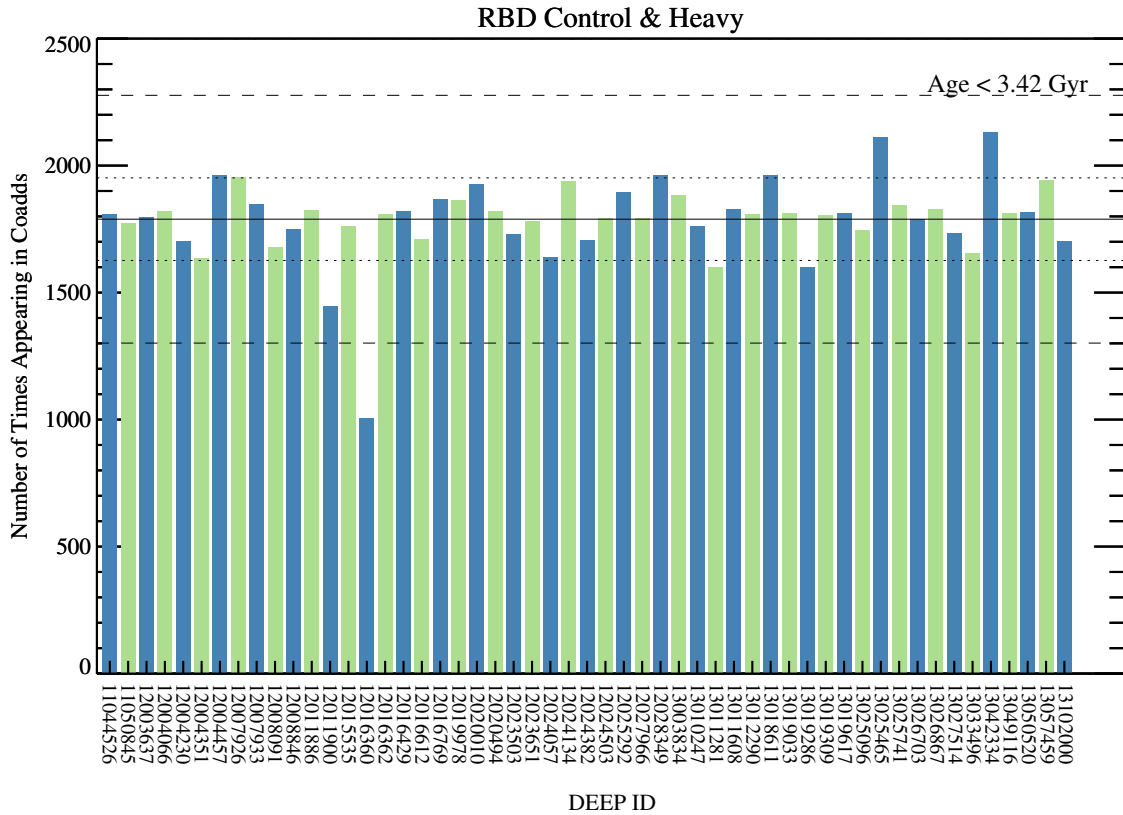


Figure B.5: The number of galaxies contributing to the co-added bootstrapped spectra for the RBD Control & Heavy subsample for ages < 3.42 Gyr, the median bootstrap age. The solid line denotes the mean number of contributing galaxies. The dotted and dashed lines indicate 1 and 3σ variations respectively from the average number of contributing galaxies. Here, one galaxy (with DEEP ID 12016360) contributes fewer than the mean minus 3σ .

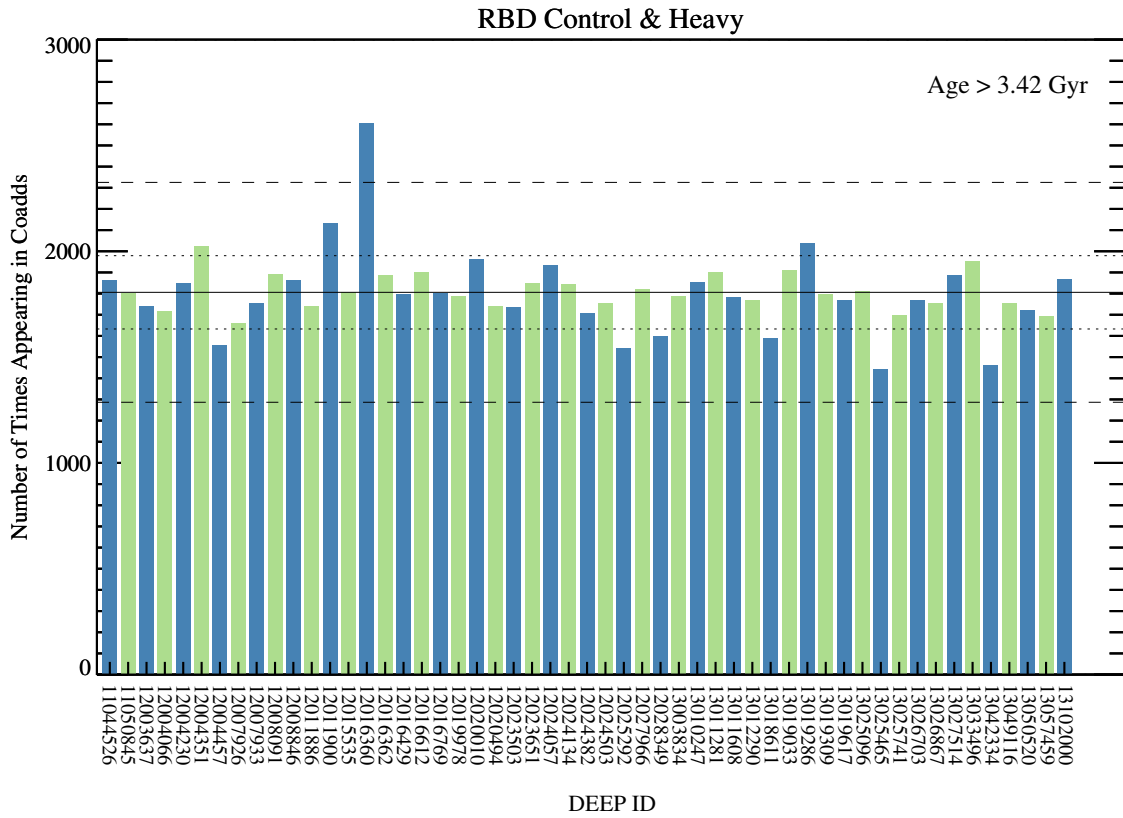


Figure B.6: The number of galaxies contributing to the co-added bootstrapped spectra for the RBD Control & Heavy subsample for ages > 3.42 Gyr, the median bootstrap age. The solid line denotes the mean number of contributing galaxies. The dotted and dashed lines indicate 1 and 3σ variations respectively from the average number of contributing galaxies. Here, one galaxy (with DEEP ID 12016360) contributes more than 3σ over the mean. Note that this galaxy is the same one which contributed less often to the bootstrap resampling when the age was less than the median bootstrap age.

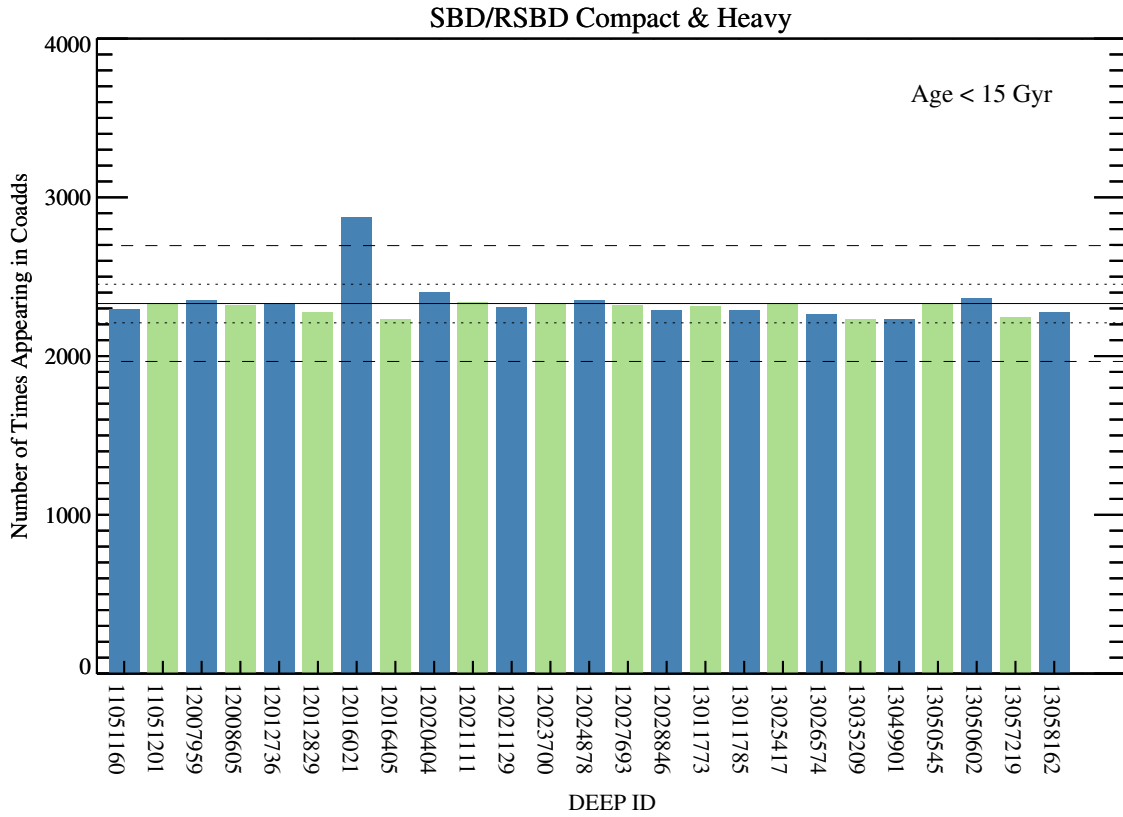


Figure B.7: The number of galaxies contributing to the co-added bootstrapped spectra for the SBD/RSBD Compact & Heavy subsample for all ages < 15 Gyr. The solid line denotes the mean number of contributing galaxies. The dotted and dashed lines indicate 1 and 3 σ variations respectively from the average number of contributing galaxies. Here, one galaxy (with DEEP ID 12016021) contributes more than the mean plus 3 σ .

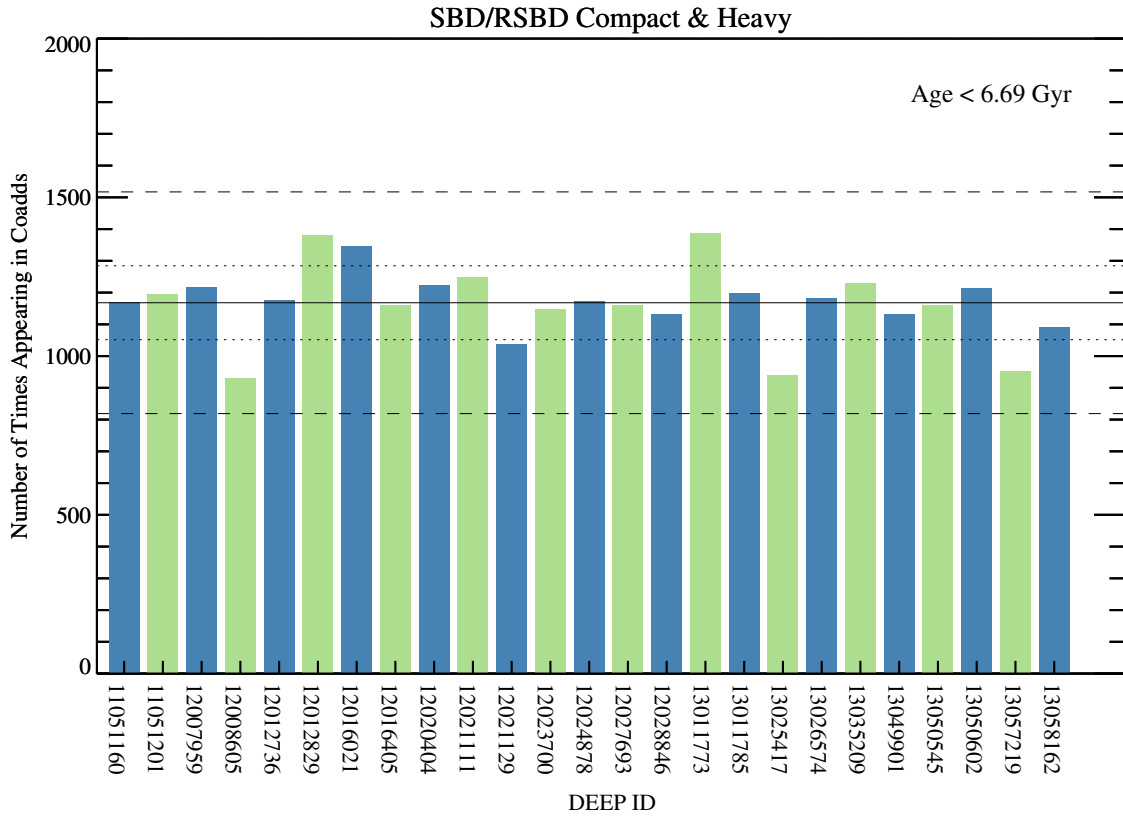


Figure B.8: The number of galaxies contributing to the co-added bootstrapped spectra for the SBD/RSBD Compact & Heavy subsample for ages < 6.69 Gyr, the median bootstrap age. The solid line denotes the mean number of contributing galaxies. The dotted and dashed lines indicate 1 and 3 σ variations respectively from the average number of contributing galaxies. Here no galaxies contribute more or less than 3 σ from the mean.

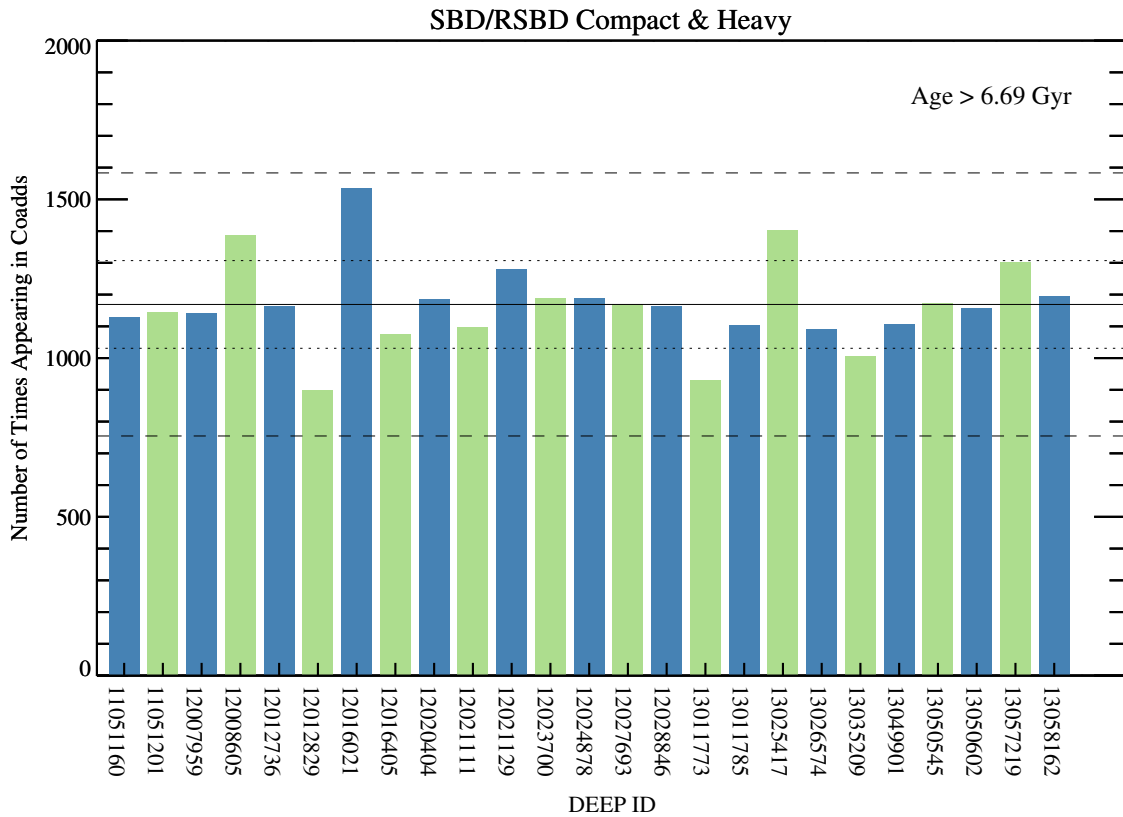


Figure B.9: The number of galaxies contributing to the co-added bootstrapped spectra for the SBD/RSBD Compact & Heavy subsample for ages > 6.69 Gyr, the median bootstrap age. The solid line denotes the mean number of contributing galaxies. The dotted and dashed lines indicate 1- and 3- σ variations respectively from the average number of contributing galaxies. Here no galaxies contribute more or less than 3 σ from the mean.

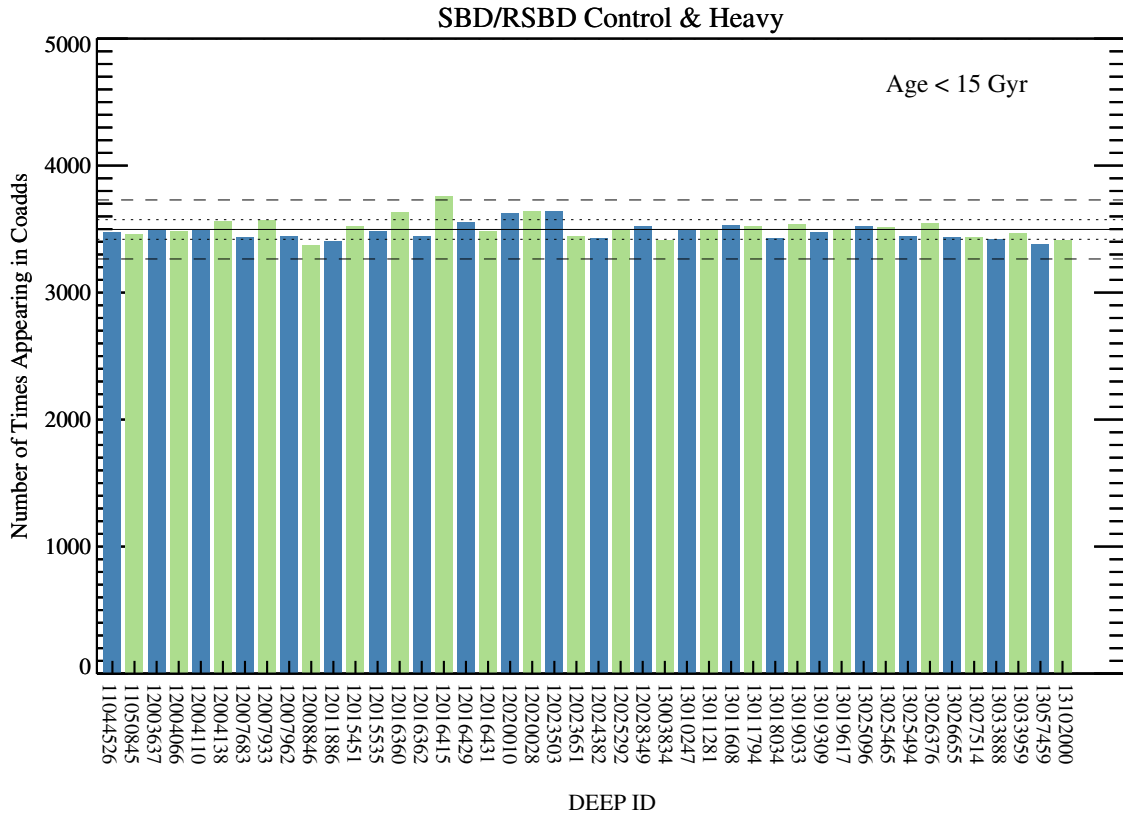


Figure B.10: The number of galaxies contributing to the co-added bootstrapped spectra for the SBD/RSBD Control & Heavy subsample for all ages < 15 Gyr. The solid line denotes the mean number of contributing galaxies. The dotted and dashed lines indicate 1 and 3 σ variations respectively from the average number of contributing galaxies. Here, one galaxy (with DEEP ID 12016415) contributes more than the mean plus 3 σ .

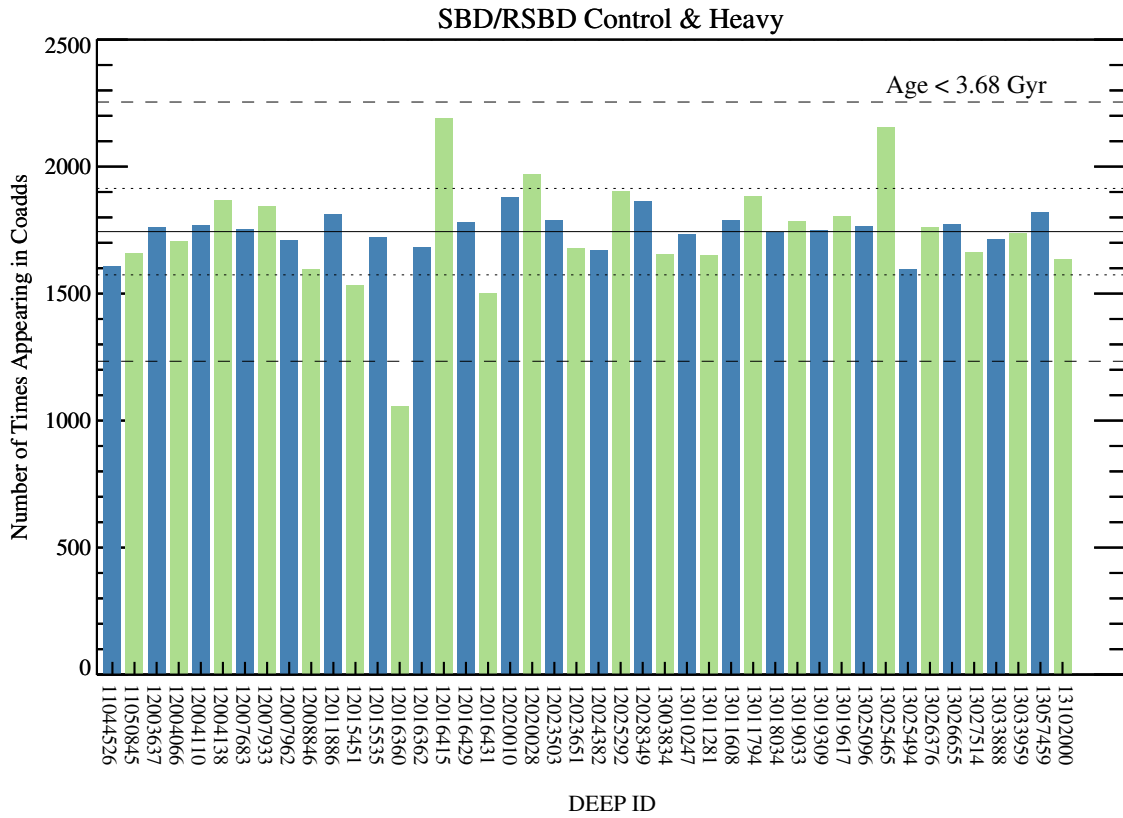


Figure B.11: The number of galaxies contributing to the co-added bootstrapped spectra for the SBD/RSBD Control & Heavy subsample for ages < 3.68 Gyr, the median bootstrap age. The solid line denotes the mean number of contributing galaxies. The dotted and dashed lines indicate 1 and 3σ variations respectively from the average number of contributing galaxies. Here, one galaxy (with DEEP ID 12016360) contributes fewer than the mean minus 3σ. Note that this is the same galaxy which also under-contributed to the RBD Control & Heavy subsample with ages less than the median bootstrap age.

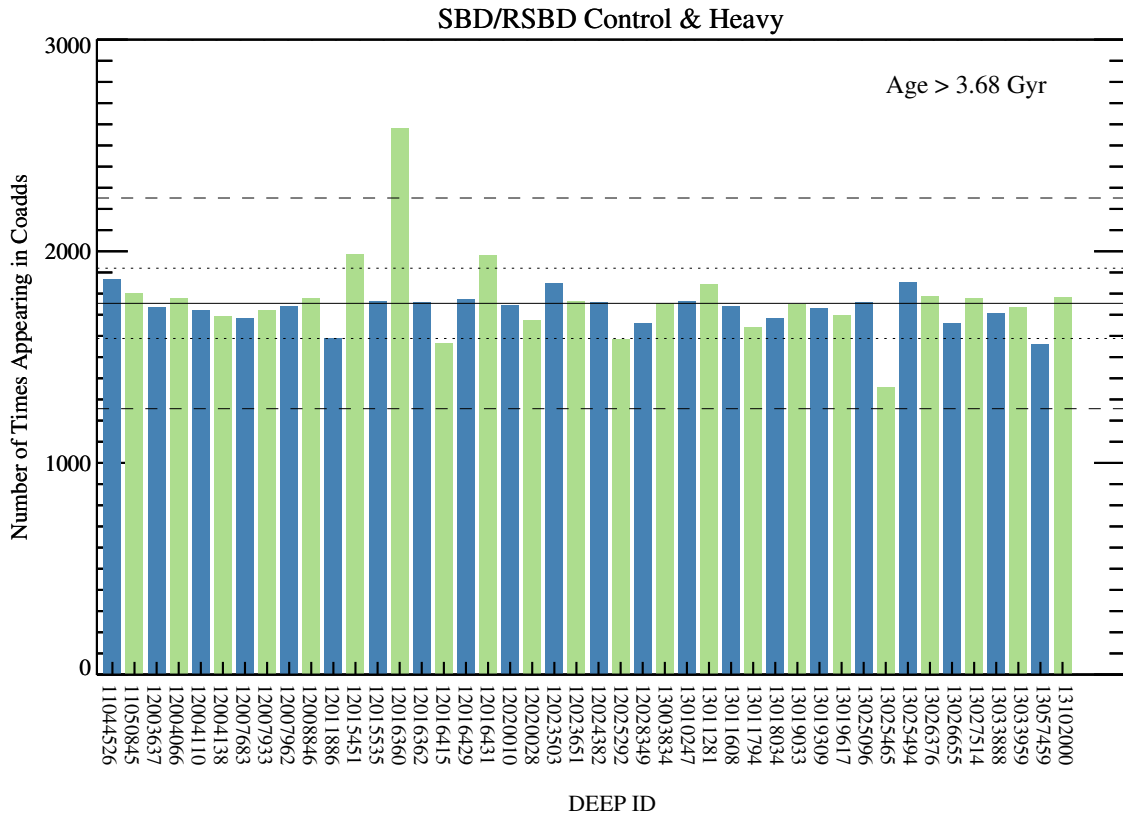


Figure B.12: The number of galaxies contributing to the co-added bootstrapped spectra for the SBD/RSBD Control & Heavy subsample for ages > 3.68 Gyr, the median bootstrap age. The solid line denotes the mean number of contributing galaxies. The dotted and dashed lines indicate 1 and 3 σ variations respectively from the average number of contributing galaxies. Here, one galaxy (with DEEP ID 12016360) contributes more than 3 σ over the mean. Note that this is the same galaxy which under-contributed to this sample when the ages were less than the median age, and also over-contributed to the RBD Control & Heavy subsample with ages great than the median bootstrap age.

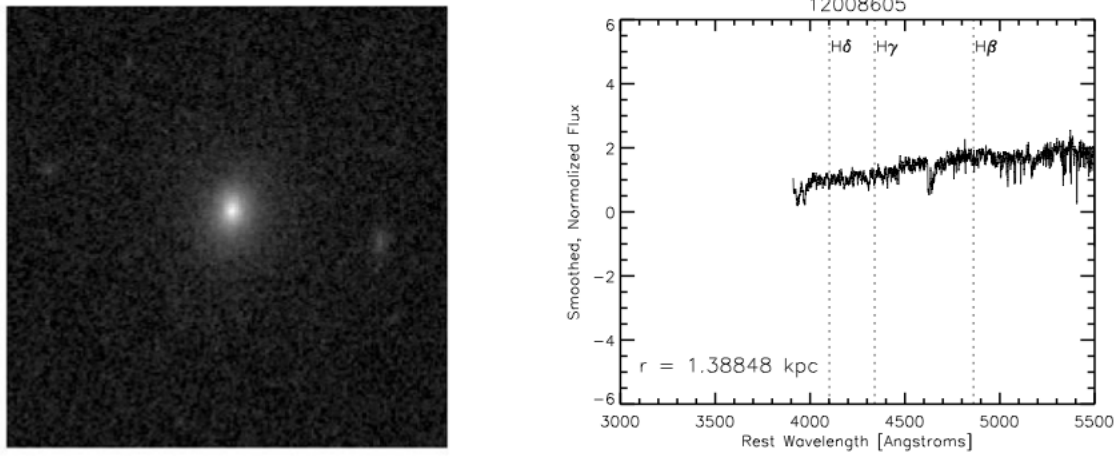


Figure B.13: DEEP ID 12008605 (image on the left, spectrum on the right) contributes strongly to the co-additions with ages younger than the median age for the RBD Compact & Heavy subsample.

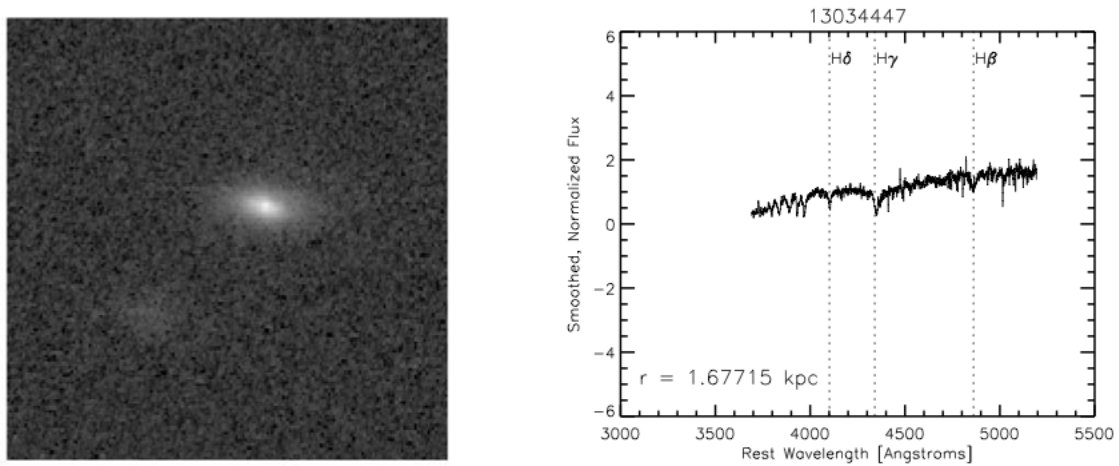


Figure B.14: DEEP ID 13034447 (image on the left, spectrum on the right) contributes weakly to the co-additions with ages older than the median age for the RBD Compact & Heavy subsample.

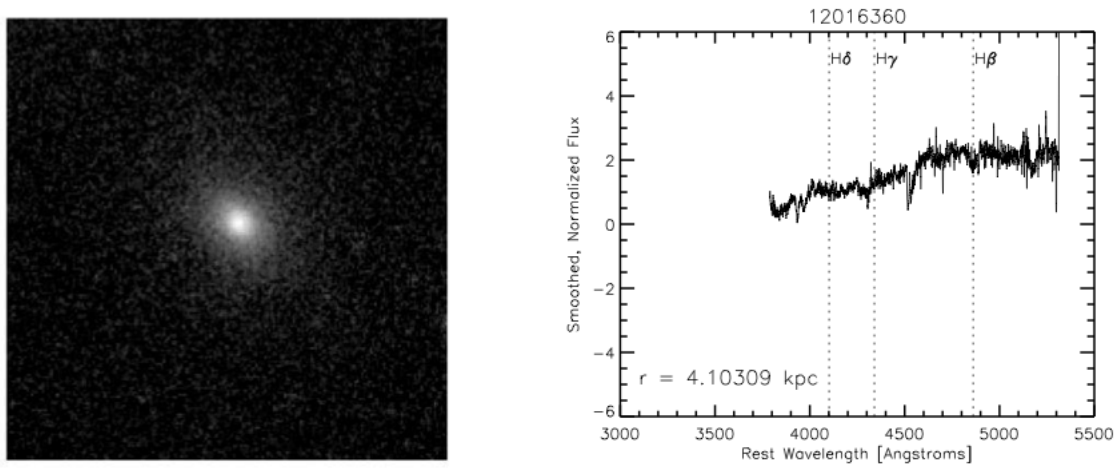


Figure B.15: DEEP ID 12016360 (image on the left, spectrum on the right) contributes strongly to the co-additions with ages greater than the median age for the RBD, SBD, and RSBD Control & Heavy subsample, and also contributes weakly to co-additions with ages less than the median age for the same subsamples.